Vortex and texture defects in radiation and matter wavefields

---

Gary Ruben
BE, MEngSc(Cwk&MinThes), GradDipSc, BSc(Hons)

School of Physics, Monash University

June 21, 2010

Contents

Contents i

List of Figures iii

Acronyms vi

Abstract vii

Disclosure ix

Acknowledgements x

1 Introduction 1
- 1.1 A focused history of vortex production from wave interference 3
- 1.2 Applications of quantised phase vortices 5
- 1.3 Phase vortices defined 8
- 1.4 Some topological aspects of defects 12
- 1.5 Phase vortices from the interference of three plane waves 15
- 1.6 Outline of the thesis 18

2 Three-wave interference beyond plane waves 21
- 2.1 Young's interference experiment revisited 21
- 2.2 Previous work related to the three-pinhole interferometer 23
- 2.3 Phase vortices from the interference of three spherical waves 24
- 2.4 Linear interference of Gaussian waves 50
- 2.5 Summary 56

3 Propagation of a vortical beam through a ground glass plate 57
- 3.1 Laguerre-Gauss beams 57
- 3.2 Laguerre-Gauss beam and ground glass plate model 60
- 3.3 Results from the model 62
- 3.4 Summary 67

4 Vortices from interference in nonlinear fields 69

4.1 Bose-Einstein condensates 69
4.2 Interference of a three-way segmented BEC 72
4.3 Numerical modelling of nonlinear BEC dynamics 75
4.4 Results from the three-way segmented pancake-BEC 87
4.5 3D simulations of the trapped BEC 110
4.6 Summary 122

5 Texture defects from interference in multicomponent fields 125
5.1 Introduction 126
5.2 Modelling a known two-component 3D system 132
5.3 Texture defect lattice formation in the untrapped two-component BEC 134
5.4 Texture defects in the trapped two-component BEC 148
5.5 Summary 157

6 Conclusions 159

Bibliography 165

Appendices 176

A Detecting vortices and nodal lines in phase data 177

B Three spherical waves reconsidered as one perturbed spherical wave 181

C Mathematica GPE derivations 183
C.1 Dimensioned 3D to 2D to dimensionless 2D route 184
C.2 Dimensioned 3D to dimensionless 3D to 2D route 186
C.3 Reduction to 2D by evaluation of the 3D GPE in the z=0 plane 188
C.4 Reduction to 2D of coupled GPEs in the absence of an axial trap 190

D Contents of optical disk 193

E Publications arising from thesis 195
E.1 Paper: Phase vortices from a Young's three-pinhole interferometer 196
E.2 Erratum: Phase vortices from a Young's three-pinhole interferometer 207
E.3 Conference paper: Phase vortices from the interference of three spherical waves 208
E.4 Paper: Vortex-lattice formation and melting in a nonrotating Bose-Einstein condensate 210

List of Figures

1.1 Vortex definition and structure 10
1.2 Helicoidal nodal line wavefront 12
1.3 Mapping from physical to order parameter space 14
1.4 Phasor diagram for three interfering spherical waves 16
1.5 Vortex lattice from three interfering plane waves 18

2.1 Interference pattern from Young's two-pinhole interferometer 22
2.2 Schematic of a Young's three-pinhole interferometer 24
2.3 Polar coordinate system for the Young's three-pinhole interferometer 25
2.4 Schematic showing two vortices from one (n, m) pair 28
2.5 Properties of parameter-space ellipses 32
2.6 Amplitude and phase for three interfering spherical waves 34
2.7 More examples for three interfering spherical waves 35
2.8 Parameter-space ellipses corresponding to Figs 2.6 and 2.7 36
2.9 Ellipses generating different numbers of vortices and antivortices 40
2.10 Vortex trajectories for varying source phases 42
2.11 Vortex motion along hyperbola trajectories 44
2.12 Hyperbolas for $\theta_3 = 90°$ 44
2.13 Simulations of nodal lines from three spherical waves and three pinholes 48
2.14 Symmetric near-field nodal line structure from three spherical waves 49
2.15 Experimental nodal line structure from three interfering Gaussians 52

3.1 Laguerre-Gauss modes 59
3.2 Helicoidal wavefronts for different beam vortex charges 60
3.3 Schematic of an LG beam passing through a ground glass plate 61
3.4 Key indicating the region of computed results in subsequent figures 63
3.5 Key indicating locations (z_0) at which subsequent results are computed 64
3.6 Simulation results for GGP height $h = \lambda/\ell - 50\%$ 65
3.7 Simulation results for GGP height $h = \lambda/\ell + 50\%$ 65
3.8 Simulation results for $\ell = 2$ with w_0 halved 66

4.1 Vortex production from the snake instability 72

4.2 Schematic of a three-piece BEC experiment 73
4.3 Selected frames from a temporal sequence of a segmented BEC 74
4.4 Harmonic trap, damping function, and aliasing effect 86
4.5 Phasor diagrams with nonlinear contributions 89
4.6 Simulation results for a BEC initially segmented into equal-phase pieces 91
4.7 The 2D harmonic trap potential with superposed three-way light sheet 92
4.8 A linear model of interfering Gaussian wavepackets 93
4.9 Simulation of a BEC initially segmented into pieces with a phase winding 96
4.10 Results for traps with lower barriers and additional partition geometries 97
4.11 Vorticity plots comparing selected BEC segmentation schemes 98
4.12 Crystallographic description of the lattice formed from Gaussian sources 100
4.13 Simulation of the Henderson et al. (2009) experiment 102
4.14 Vortex interaction dynamics 105
4.15 Simulation results for segmented BECs of ^{23}Na 108
4.16 Image of the 3D trap potential and in-situ ground-state condensate 113
4.17 Probability density visualisations of 3D simulations 114
4.18 Nodal line structures within a pancake condensate 115
4.19 Probability density and nodal lines of a 3D BEC in a spherical trap 117
4.20 Projected probability density for a BEC in a divided, spherical trap 118
4.21 Order parameter and nodal lines of a BEC in an oblate spheroidal trap 119
4.22 Projected probability density for a BEC in an oblate spheroidal trap 120
4.23 Vortex structure detail in the oblate-spheroidally-trapped system 120
4.24 Nodal lines in the oblate-spheroidally-trapped system 121
4.25 Randomly colourised nodal lines of the honeycomb lattice 121

5.1 Hyperfine levels of ^{87}Rb 127
5.2 Bloch sphere 129
5.3 Mollweide projection of prototypical baby skyrmion 130
5.4 Projected probability densities of the Mertes et al. (2007) experiment 134
5.5 Bloch vector visualisation of the Mertes et al. (2007) experiment 135
5.6 A slice showing the order parameter and its Mollweide projection 136
5.7 Hyperfine level coupling via two lasers 137
5.8 Combining honeycomb lattices with different relative phases 138
5.9 Planar defect Bloch vector representation 139
5.10 Ballistic expansion behaviour of the nonlinear coupling term 140
5.11 Lattices in the two level ^{87}Rb system 142
5.12 Texture defects in the two level ^{87}Rb system 143
5.13 Identification of texture defect types 144

5.14 Mollweide plots of meron and planar defects 145
5.15 Translated lattices in the two-level ^{87}Rb system 146
5.16 Texture defects in the translated two-level ^{87}Rb system 147
5.17 Vortex-skyrmion 149
5.18 Evolution of the trapped two-component condensate 151
5.19 Meron defect types 152
5.20 Examples of defect clusters 154
5.21 Meron pair classification 155

A.1 Phase unwrapping in 2D 177
A.2 Phase unwrapping in 3D 179

Acronyms

1D	one dimensional
2D	two dimensional
3D	three dimensional
(1+1)D	one spatial dimension and one time dimension
(2+1)D	two spatial dimensions and one time dimension
(3+1)D	three spatial dimensions and one time dimension
BEC	Bose-Einstein condensate
BKT	Berezinskii-Kosterlitz-Thouless
FWHM	full width at half maximum
GGP	ground glass plate
GPE	Gross-Pitaevskii equation
LG	Laguerre-Gauss
KZ	Kibble-Zurek
NLSE	nonlinear Schrödinger equation
OAM	orbital angular momentum
OVC	optical vortex coronagraph
PDE	partial differential equation
RDS	ring dark soliton
RF	radio frequency
RK4IP	fourth-order Runge-Kutta in the interaction picture
SLM	spatial light modulator
TF	Thomas-Fermi
VA	vortex-antivortex
VD	vortex-antivortex dipole
$\mathbb{Z}$	The set of all integers

Abstract

In this thesis the features that arise from the interference of simple coherent waves are described, namely the topological defects of phase known as phase vortices permeating such wavefields. Phase vortices are associated with the rotation of energy and mass and arise naturally in regions containing coherent light and/or matter.

The simplest possible system exhibiting these defects is that of three linearly interfering plane waves, described using the classical theory of monochromatic complex scalar wavefields. We explore the related case of three outgoing waves produced by point sources, such as a laser-illuminated screen that has been punctured by three pinholes. We develop a description of the resulting vortex structure in the optical far-field, and relate this to the source arrangement and parameters. This allows an estimate of the number and positions of the vortices, and leads to connections to particular results from information theory and number theory. Numerical simulations of the near-field defect structure are also presented. Findings from this study are then applied to the time evolution of a nonlinear Bose-Einstein condensate of atoms, which shares the property of coherence that enables its description by a related model of interfering Gaussian wavepackets. Numerical modelling of the nonlinear system is performed for both trapped and untrapped Bose-Einstein condensates (BECs) in two and three spatial dimensions, for BEC pieces initially positioned at the three corners of an equilateral triangle. We demonstrate the production of a distorted honeycomb vortex-antivortex lattice, due to wavepacket interference. The wavepacket expansion is halted by the presence of a magnetic trap, causing the lattice to melt and providing a population of mobile vortices and antivortices. The addition of nonlinearity in this system over the linear case leads to the formation of vortex clusters, whose dynamics we investigate.

A model of a Laguerre-Gauss laser beam, which carries a phase vortex along its axis, is studied following its interaction with a ground-glass plate. We present preliminary results showing that the beam acquires interference-generated vortices whose number density evolves as a function of propagation distance and beam topological charge, due to interaction with the roughened glass.

Beyond the nonlinear coherent wavefields applied to the description of Bose-

condensed gases, a pseudo-spinor system described as a nonlinear coupled system of two complex scalar fields is studied. Such systems admit the existence of *texture* defects similar to those that exist in ferromagnetic systems. We numerically model a pseudo-spinor system that we arrange to generate carefully aligned honeycomb vortex-antivortex lattices in the coupled components. We find that this corresponds to a texture defect lattice and identify its constituent texture defects as merons and a type of planar defect. Following the analogy with the single component BEC, we also study texture defects and clusters in the trapped pseudo-spinor system.

Disclosure

This thesis contains no material which has been accepted for the award of any other degree or diploma in any university or other institution. To the best of my knowledge the thesis contains no material previously published or written by another person, except where due reference is made in the text of the thesis.

Gary Ruben

Acknowledgements

First and foremost, I thank my supervisor David Paganin. David's talent for teaching, depth and breadth of knowledge, and skilful guidance combined to make him a wonderful supervisor. At the end of my PhD I also feel he has provided me with a reserve of useful advice to draw upon in future. I also sincerely thank Michael Morgan for sharing his wisdom and insight. Since agreeing to cosupervise with David, Michael's suggestions have visibly influenced the research path I followed over the last few years. Having two such enthusiastic and supportive supervisors has made my personal PhD experience more satisfying than I imagined it would be at the outset.

I am extremely grateful to Miles Padgett for his invitation and generous support of my visit to the University of Glasgow optics group. The welcoming culture within the group helped make it a wonderful experience for me. Amongst the group members, Kevin O'Holleran must be singled out for thanks. The confluence of our research areas and his good nature made the visit both enjoyable and useful; not to mention all that he taught me about vortices and optics in general. Thanks also to other members and visitors in the group with whom I became friends; Alasdair Hamilton, Barry Jack, Alison Yao, Johannes Courtial, Aline Vernier, Bhuvanesh Sundar, Lucy Murray, Daryl Preece, Stephen Keen, Eric Yao, Sonja Franke-Arnold, Jonathan Leach, Graham Gibson, and Martin Lavery. Thanks also to those who hosted my visits to their universities; Aidan Arnold from Strathclyde, Mark Dennis from Bristol, and Rob Sewell from Imperial.

Given that we must trust to luck the people we share our time with whilst PhD students I consider myself fortunate that I can count so many of my fellow postgraduate students as friends. For their support over the last few years, thanks to Sally Irvine, Shekhar (Shakes) Chandra, Nadia Zatsepin, Naomi Schofield, Kathryn Spiers, Kaye Morgan, Shane Kennedy, David Vine, John Gillam, John Daniels, and Ivan Williams.

Thanks to Lincoln Turner for generously supporting my visit to the Beyond Bells workshop. Thanks also to Lincoln and Andy Martin for their help and encouragement with all manner of BEC-related help. Without this, I could not have gotten so far.

Special thanks to Anne Eastaugh for her friendship and support. Many others

have helped me in numerous ways. Thanks to Jean Pettigrew, David Jesson, Simon Clarke, Robert Bartnik, Helen Faulkner, Russell Anderson, Chris Ticknor, Ricardo Carretero, and Kristian Helmerson.

I have benefited from the existence of a variety of free open source software during my PhD. In particular, I am grateful to the many developers of Python, NumPy, SciPy, matplotlib, Mayavi, VTK, and XmdS. I have received financial assistance under an Australian Postgraduate Award.

Finally, thanks to my family for all the support and encouragement; Viv, Danny, Mum and Dad. I regret that my father did not live to see this completed and I dedicate this thesis to him.

1 Introduction

Oh, what a void there is in things.

— Persius

Waves abound in nature, lying at the heart of quantum mechanics and therefore our understanding of the fundamental forces, light and matter. One reason for the ubiquity of waves as the building blocks of so many successful physical models is thanks to Joseph Fourier who showed that we can decompose descriptions of objects and fields into their component waves. Yet the objects and fields need not be smooth and continuous in all their aspects. In particular, at points of zero amplitude, the phase is undefined, and is said to be *singular* at such points.

Continuity of the wavefunction ensures that the phase is continuous in the immediate non-zero amplitude neighbourhood of these singularities. Consequently, measurement of the phase over a path encircling the singularity reveals that it cycles s times through all possible 2π values, where s is an integer indicating the singularity *strength* or *topological charge*. A probability current of energy or matter is associated with the phase gradient so that energy or matter swirls around the singularities, in amounts quantised by s. They are *quantised vortices* of light or matter, known variously as optical vortices, phase vortices, optical phase vortices, phase singularities, quantised vortices, quantum vortices, nodal points, nodal lines, vortex lines, wave dislocations, and cosmic strings (Dennis et al., 2009). We will mostly refer to them as vortices or nodal lines.

Optical vortices are associated with an orbital angular momentum (OAM) carried by the photons in the vicinity of the vortex core, distinct from the photons' intrinsic spin angular momentum (Allen et al., 1992). Photons in the field around a strength-s vortex typically each carry $s\hbar$ of OAM. Much of the interest in optical vortices has been attributed to the recognition of this property.

There are many familiar examples of vortices in nature. Cyclonic weather systems are visible as spiralling cloud formations, tornadoes and waterspouts, and

in the great red spot of Jupiter. Smoke rings propagating in air are vortex loops, and eddies in streams are indicators of turbulence. Less familiar are the aforementioned vortices in light, in the eigenstates of the Hydrogen atom, in superfluid Helium, cosmic strings and neutron stars. Our focus is on vortices of this less familiar type, which exist in coherent wavefields. They differ from the former examples in classical systems, by virtue of the quantisation of the vortical flows of matter or optical energy.

We will be concerned with quantised vortices both in linear optical systems and also nonlinear systems of matter waves which take the form of the laboratory ensembles of cold atoms known as Bose-Einstein condensates (BECs) (Pethick and Smith, 2008). In particular, we will examine the creation of vortices produced by the interference of small numbers of simple, non-vortical waves, described by complex scalar wavefunctions in both linear and nonlinear media. Our work is motivated by developments from the field of *singular optics*, which typically deals with all aspects of vortices in wave optics, but also with polarization singularities of the vector electromagnetic theory, and with caustics, which are the singularities of ray (geometric) optics.

Three noteworthy reviews of the field of singular optics have been published in the series Progress in Optics; by Soskin and Vasnetsov (2001), Desyatnikov et al. (2005), and Dennis et al. (2009). The introductory chapters of the PhD theses of Dennis (2001) and O'Holleran (2008) also provide helpful reviews. Nye (1999) provides a comprehensive treatment of *wave dislocations* as singularities of wave optics; he presents these alongside caustics and polarization singularities. Andrews (2008) is a general introduction focused on vortex-carrying beams, with particular emphasis on the angular momentum property of the field surrounding a vortex, the application of this property to the manipulation of matter, and the transmission of information. The approach taken in Chap. 2 of this thesis follows Paganin (2006, Chap. 5), which also provides a general introduction to optical vortices.

In discussing phase vortices as singularities of complex scalar fields describing electromagnetic wave optics, it is important to remember that this model sits between geometric or ray optics and quantum optics, and is itself a simplified model that ignores the vector nature of electromagnetism, which incorporates polarization. Singularities exist within all of these models of light. Polarization singularities arise in electromagnetic fields at points of pure linear or pure circular polarization (Nye, 1999). Points of pure linear polarization occur over surfaces in 3D and lines in 2D, and are known as L lines. Points of pure circular polarization occur over lines in 3D and points in 2D, and are known as C points. The singularities of geometric optics are *caustics*, which are points or curves of infinite intensity

under that theory (Nye, 1999; Dennis et al., 2009). Caustic singularities are *tamed* by describing the same system using a more general theory such as wave optics; they do not arise in the wave model. Vacuum fluctuations arise within the fully-quantised quantum electrodynamical model of light. Just as a system described with the ray theory may contain singularities which are removed by reformulation using the wave theory, so too do vacuum fluctuations tame the singularities of the wave theory in the vicinity of the dark core of an optical vortex (Berry and Dennis, 2004; Berry, 2007; Barnett, 2008).

Vortices are discussed in most general texts and reviews of BECs due to an early realisation of their importance in understanding the fundamental physics that these systems reveal (Dalfovo et al., 1999; Leggett, 2001, 2006; Pethick and Smith, 2008). BECs are one member of a group of related nonlinear systems in which vortices play a significant role; other members of which include superfluids, superconductors, nonlinear optics, and cosmic strings (Pismen, 1999; Kivshar and Agrawal, 2003). Vortices also play a central role in *quantum turbulence* studies, recently reviewed by Kasamatsu and Tsubota (2009).

1.1 A focused history of vortex production from wave interference

The demonstration of the wave nature of light by Thomas Young stands amongst the most famous experiments in the history of physics (Young, 1804; Born and Wolf, 1999). Young divided a coherent polychromatic source of light into two secondary sources and showed that the resulting recombination exhibited a pattern of dark and bright fringes consistent with the superposition of waves. With the discovery of quantum mechanics, the simplicity of the Young experiment made it an obvious choice for reinterpretation and exposition of wave-particle duality and cemented its place as the prototype for many related experiments in modern physics. Yet despite the prominence of Young's experiment, most people are surprised to discover that adding a third source of waves transforms the well-known pattern from fringes into a lattice of vortices at which the intensity falls to zero and around which energy or matter flows. It is perhaps equally surprising that vortex production from wave interference is not a recent idea.

Vortices have appeared in many physical models throughout the history of physics. They were a fundamental feature of Descartes's ideas on the nature of matter from the early 1600s, describing the nature and motion of planets by analogy with whirlpools in water (Ball, 1960). In 1867, Lord Kelvin (Sir William Thomson),

inspired by Helmholtz's observation of vortex rings in incompressible fluids (e.g. smoke rings), proposed an atomic model of "knotted or knitted vortex atoms" which he noted were localised and topological in nature; their different configurations were thus a possible source of different observed spectra (Thomson, 1867). James Clerk Maxwell was strongly influenced by Kelvin's ideas associating vorticity with magnetic fields, and incorporated them into his vortex model of the aether, helping to cement his thinking about electromagnetism (Cushing, 1998).

Singularities in wavefields, which we now know are associated with optical vortices, also have a long history. William Rowan Hamilton discovered polarization singularities in 1832 (Soskin and Vasnetsov, 2001). As noted by Berry (1981), the first experimental recognition of a phase singularity occurred when Whewell (1836) took timed measurements of the tides at coastal points around the North Sea, effectively measuring the constant-phase wavefronts of the tides. Whewell's observations required the existence of a central point of undefined phase, called an *amphidromic point*, at which the ocean height remains constant. Later, Dirac (1931) considered the singularities of a complex scalar wavefunction for a particle in an electromagnetic field. He noted the line-like nature of these singularities in 3D and associated their ends with point singularities of the electromagnetic field, which he identified as magnetic monopoles.

The first recognition of an optical vortex in a complex scalar wavefield was made by Wolter (1950) who modelled internal reflection from a glass-air interface as an interference process by four plane waves. We are largely concerned with three-wave interference in this thesis. It is therefore notable that soon afterwards, Braunbek (1951) was the first to realise that the superposition of three defect-free waves is sufficient to create phase singularities and to remark that consequently they should be ubiquitous in interfering wavefields.

A revival of interest in optical vortices has occurred since the publication by Nye and Berry (1974) of the first directed efforts toward the understanding of phase singularities in fields, arising in particular due to the interference of small numbers of waves. Noting the ubiquity of these "dislocations in wave trains," the importance of phase singularities as general features of wavefields was established. The description of defects in crystals provided a natural analogue for this early work, where atomic planes took the place of wavefronts.

Nicholls and Nye (1987) made the first investigation of singularities produced by the superposition of three fundamental waves. They studied the evolution and spatial-dependence of the singularities produced by the interference of three wave pulses and showed that a regular lattice of singularities is produced. Later, Masajada and Dubik (2001) studied the interference of three plane-waves and the

related vortex lattice, echoing Braunbek (1951) by noting that this is the minimum number of waves required for lattice formation. They employed a phasor approach to determine the vortex locations; a version of which we will apply to the different cases of three interfering spherical, pinhole, and Gaussian waves.

We have presented a very narrow view of the history of optical vortex production, focusing on the important developments that led directly to the point at which the next chapter picks up, namely the study of the vortices produced by the interference of three spherical waves.

1.2 Applications of quantised phase vortices

A surprising diversity of applications have been proposed or realised for vortices. For applications in which a small number of vortices is to be deliberately engineered, a common method is to pass radiation from a coherent source – such as a laser, x-ray synchrotron beam, or electron beam – through a spiral phase plate to confer a desired transverse phase profile on the resulting beam (Beijersbergen et al., 1993; Peele and Nugent, 2003; Okamoto and Sasada, 2005; Kotlyar et al., 2006). A spiral phase plate is a helical ramp designed to retard the phase of light of a given wavelength by a fraction of 0 to 2π, where the fraction increases monotonically from zero to a nonzero integer around the beam axis. Passing a beam through a spiral phase plate generates a beam containing a vortex lying along the propagation axis. If the illuminating beam is Gaussian, the result is a Laguerre-Gauss (LG) beam, which we study in Chap. 3. Alternatively, illuminating a forked diffraction grating generates vortical beams in the off-axis orders, where the number of 2π traversals of phase around the beam, equal to the topological charge, corresponds to the diffraction order (Bazenhov et al., 1990). Such gratings may be constructed with fixed dimensions corresponding to a particular wavelength or may be implemented using spatial light modulators (SLMs) (Kishima et al., 2006). Kim et al. (1997) generated optical vortices in Gaussian laser beams using curved glass plates, which are easier to manufacture than optical-wavelength spiral phase plates. Vortical Bessel beams have a vortex that lies along the beam axis (Herman and Wiggins, 1991). Certain modes of laser cavities also generate vortical beams directly (Vaughan and Willetts, 1979).

Applications have been proposed in areas such as photonics, sensors and storage technologies (Desyatnikov et al., 2005). The topological charge of optical and BEC vortices has been proposed as a possible qubit element in quantum computing and communications (Mair et al., 2001; Molina-Terriza et al., 2007). Manipulating the vortex charge has been demonstrated as a means to transmit information

securely (Gibson et al., 2004). In this scheme, SLMs are employed in the production and detection of vortex-carrying beams and potential eavesdroppers are unable to decode data encoded in the beam. The cores of optical vortex tubes may be used to transport BECs in atom optics systems where electromagnetic fields function as waveguides (Xu et al., 1999; Arlt et al., 2000; Rhodes, 2005). Similarly, optical vortex solitons in nonlinear media may be used as reconfigurable photonic waveguides (Carlsson et al., 2000; Law et al., 2000).

Interferometry applications exploit the position dependence of vortices to determine the positions and phase dependence of the contributing sources (Masajada et al., 2002). Certain imaging applications create vortices in the optical path of instruments such as microscopes and telescopes. In microscopy, the addition of a forked diffractive element to the optical path allows additional edge enhancement of imaged objects and also allows interferometrically generated surface contours to distinguish between raised and depressed surface features (Fürhapter et al., 2005b,a). The optical vortex coronagraph (OVC) is a device for optically removing high intensity starlight from astronomical telescope images to aid extrasolar planet finding (Swartzlander, 2001, 2009). The direct observation of distant planets is difficult due to their proximity to the bright star they orbit. By designing an optical system with a vortex coinciding with the star's position, light can be "spun out" of the field of view of interest rendering any dimly reflecting orbiting planet visible.

The angular momentum generated in the vicinity of the vortex has also found applications. The selective trapping and manipulation of small amounts of matter with light is possible with optical tweezer systems (He et al., 1995; Gahagan and Swartzlander, 1996; Grier, 2003). These permit fine control over the forces involved and have application in manipulating mesoscopic matter. They are employed in the measurement of the mechanical properties of polymers and biological structures such as bacteria and other cells, down to the chromosomal level. Conventional optical tweezers have been developed without vortices, but the ability to introduce angular momentum into a focused region via an optical vortex permits new capabilities in these systems. When applied in this way, an optical vortex is known as an optical spanner. Optical spanners exert a torque on a small object by illuminating it with a vortical beam (Friese et al., 1998; Nieminen et al., 2004). These can power micro-machine components, such as gears, or spin ensembles of particles, transporting and mixing small fluid volumes, which are otherwise resistant to mixing, within microfluidic or *lab-on-a-chip* systems. These technologies find application in such areas as medical and pathology diagnostics, chemical and environmental sampling and drug discovery. The radius of influence of an optical spanner may be changed by varying the vortex charge. Furthermore, by controlling the

polarization, the optical spanner can transfer both spin and OAM to illuminated particles. Reflective, absorptive or low-dielectric constant objects are not suitable for trapping by conventional optical tweezers, yet optical-vortex-based tweezers permit trapping of these types of objects (He et al., 1995).

Vortices arise naturally in a variety of linear and nonlinear physical systems that may be described via complex fields, including the angular-momentum eigenstates of the hydrogen atom (Messiah, 1961, pp. 412–420), the Meissner state of type-II superconductors (Abrikosov, 1957; Tilley and Tilley, 1990), vortex states of superfluids (Feynman, 1955; Pismen, 1999) and BECs (Pitaevskii and Stringari, 2003), optical vortex solitons (Desyatnikov et al., 2005), propagating electron wavefunctions diffracting through crystalline slabs (Allen et al., 2001), Gaussian random wavefields (Berry, 1978), and optical speckle fields (Freund et al., 1993). A primary motivation for the study of phase singularities in wavefields is that they form a nodal-line *skeleton*, which when combined with knowledge of the local field configuration around the nodal-lines, provides an alternative description of the field structure (Berry and Dennis, 2001; Dennis et al., 2009). The semiconductor Quantum Hall effect, trapped flux tubes in superconductors and vortices in superfluids are all closely related, albeit with different wave equations governing their evolution, and with order-parameter fields replacing wavefunctions (Pismen, 1999). The study of the associated singularities in BECs has application to phenomena in condensed matter systems; a prominent example being type-II (high temperature) superconductivity. Related to this is the area of quantum turbulence (Tsubota, 2009) and its connection with turbulence in classical fluids (Yepez et al., 2009). The understanding of the transition of fluids to superfluids is closely connected to the formation of ensembles of quantised vortices into clusters. Superfluid models arise in connection with models of neutron stars and quantised vortices are fundamental to the understanding of their behaviour and dynamics (Epstein and Baym, 1992). Cosmic strings in cosmological models are quantum vortices of complex scalar field models (Hindmarsh and Kibble, 1995; Pismen, 1999).

In linear optical systems, diffraction leads to bright and dark field regions evolving under propagation. Although diffraction-free beams, such as Bessel beams, are a propagation-invariant counter-example to this statement, they are non-square-integrable and hence nonphysical (Montgomery, 1967). In contrast, nonlinear systems support field structures called solitons, whose shapes are resistant to change under propagation through space or time (Kivshar and Agrawal, 2003).[1] In the case of propagation through space, the nonlinear term offsets the

[1] In our discussions of solitons, we allow them to be stable over short timescales. Some authors impose a stricter criterion and require them to be unconditionally stable (see Konotop, 2008).

effect of diffraction to keep the field shape somewhat constant. Nonlinear self-focusing and defocusing effects can conspire to create bright and dark solitons, respectively. Dark solitons containing one or more nodal lines along their axis are *vortex solitons* (Proukakis et al., 2004; Desyatnikov et al., 2005). They are simply vortices in self-defocusing nonlinear media. As we will see in Chap. 4, the defocusing effect corresponds to a positive nonlinearity in the corresponding nonlinear term in the nonlinear Schrödinger equation (NLSE). The NLSE models the propagation of nonlinear optical systems through space, and the propagation of BECs through time. The other solitonic structure of interest to us is the *dark stripe soliton*, which is unstable and decays via a mechanism known as the *snake instability*, into an alternating series of vortices and antivortices. We discuss this further in §4.1.1.

Speckle fields contain large numbers of vortices and are generated when waves propagate through media with fluctuating refractive index, such as the atmosphere or biological tissue, or through optical glass elements with roughened surfaces (Goodman, 2007; O'Holleran, 2008). The solution of inverse problems in which one has a diffraction pattern containing vortex-laden speckle provides further motivation for understanding vortices (Allen et al., 2001). The related inverse problem of determining the diffractive objects from a diffraction pattern often relies on phase retrieval algorithms, which can behave poorly in the presence of vortices (Ghiglia and Pritt, 1998). Understanding of vortices may lead to improved methods for solving this important practical problem.

The applications of vortices are clearly diverse, as are the mechanisms by which they form. Before proceeding to describe the formation of vortices by wave interference, we first introduce their general properties in the following section.

1.3 Phase vortices defined

Consider a monochromatic scalar plane-wave wavefunction

$$\Psi(\mathbf{r}, t) = \rho e^{i(\mathbf{k}\cdot\mathbf{r}-\omega t)}, \tag{1.1}$$

coordinatised by the general position vector $\mathbf{r}$ and time t. It is specified by an amplitude $\rho = \sqrt{I}$ corresponding to intensity $I = \Psi^*\Psi$, a wavevector $\mathbf{k}$, and an angular frequency ω. This wavefunction is a solution to the d'Alembert wave equation $\nabla^2\Psi - c^{-2}\partial_t^2\Psi = 0$, where c is the wave speed, ∇^2 is the 3D Laplacian and $\partial_t \equiv \partial/\partial t$ is a partial differential operator operating with respect to time. We will mostly be concerned with the spatial part of the non time-varying solution of the

associated (time independent) Helmholtz equation $\nabla^2\Psi + k^2\Psi = 0$, namely,

$$\Psi(\mathbf{r}) = \xi + i\vartheta = \rho e^{i\chi}, \tag{1.2}$$

where the field is represented at every point by two values; its real and imaginary parts, ξ and ϑ, or its amplitude ρ and phase χ. Later we will consider Gaussian and LG beams, which are solutions of the related paraxial wave equation, and BECs, which are solutions of the related NLSE called the Gross-Pitaevskii equation (GPE). In general, complex scalar fields composed of such plane waves may be used to describe a single polarization state of a field, or unpolarized radiation fields in the absence of current and charges for an "image formed with a source of natural light by an optical system of moderate numerical aperture" (Born and Wolf, 1999, §8.4). With this description, a complex scalar plane wave has only two degrees of freedom so that it is uniquely specified by the amplitude and phase (ρ, χ), or alternatively its real and imaginary parts (ξ, ϑ), at every location.

Figure 1.1 shows the amplitude (a) and associated phase (b-d) of the field resulting from the superposition of a small number of plane waves, imaged over a plane. Three integration contours in Fig. 1.1(c) surround (i) a vortex, (ii) an antivortex which is a vortex whose phase winds in the opposite sense, and (iii) a vortex-free region. Continuity of the wavefunction in the immediate neighbourhood of the singularity ensures that the phase may only change by an integer multiple of 2π around any closed contour. The phase gradient is related to the current $\mathbf{j} = \mathrm{Im}\,(\Psi^*\nabla\Psi) = \xi\nabla\vartheta - \vartheta\nabla\xi = I\,\nabla\chi$ of energy or matter (for a matter wavefield), which circulates around the singularity, hence the name *vortex*.[2] More formally, in order to determine whether a vortex exists at a particular point in a plane over which a field is observed, we perform a contour integration over the phase gradient about that point. As shown by the three examples in Fig. 1.1(c), each contour is chosen to be small enough to avoid encompassing any other nearby singularities which may be present. The integral is evaluated over a smooth simple closed contour Γ in the conventional sense shown,

$$\oint_\Gamma d\chi = \oint_\Gamma \nabla\chi \cdot \mathbf{t}\, dl = 2\pi s, s \in \mathbb{Z}, \tag{1.3}$$

where $\mathbf{t}$ is a unit tangent vector to the contour Γ and dl is an infinitesimal line element along Γ. The resulting index s corresponds to the number of 2π phase windings encountered in traversing the contour once, and is referred to as the *strength*, *topological charge*, or simply the *charge* of the vortex (Dennis et al., 2009).

[2] A full derivation of the current may be found in Paganin (2006, Eq. 5.17); the final expression being $\mathbf{j} = \alpha I\,\nabla\chi$, where α is a real constant of proportionality that we set to 1.

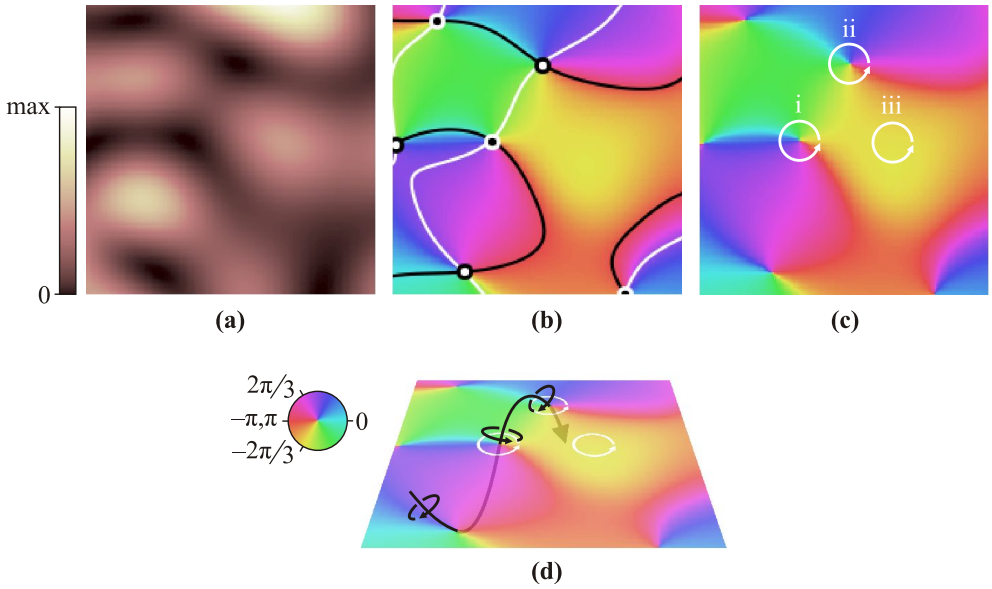

Figure 1.1: (a) Intensity I and (b–d) phase χ of a random wavefield $\Psi = \xi + i\vartheta$ imaged over a plane. (b) Vortices (black circle with white edge) and antivortices (white circle with black edge) lie at zeros of the intensity in (a). Zero-contours of the real part ξ (black) and imaginary part ϑ (white) intersect at (anti)vortex locations. (c) Three contours over which integrals of the phase gradient are calculated indicate (i) $s = 1$ (vortex), (ii) $s = -1$ (antivortex), and (iii) no phase singularity. (d) A nodal line piercing the plane has a sense indicated by the arrowhead and corresponding to a right-hand rule, indicated by the black circles. At the vortex, this sense matches the sense of contour (i), whereas at the antivortex the sense is opposite that of contour (ii). Image after O'Holleran (2008).

Its sign (sgn s) represents whether the singularity is a vortex (sgn $s = +1$) or antivortex (sgn $s = -1$). Thus zero windings indicates that there is no vortex at the point, whereas a non-zero result indicates the presence of a vortex of charge s.

Phase singularities exist at locations in the field at which the complex amplitude is 0, corresponding to the intersection of zero contours of the real and imaginary parts individually, as shown in Fig. 1.1(b). These contours are lines in 2D and surfaces in 3D. Thus vortices are points in 2D and lines in 3D, these lines being infinitely long or forming closed loops in free space. They can also terminate on sharply-bounded scattering surfaces. Furthermore these loops may be linked with other loops or lines or may even form knots (Berry and Dennis, 2001; Dennis et al., 2010). For the examples shown here, the vortices are all charge $s = +1$ or $s = -1$. Higher charge vortices correspond to points at which multiple zero contours of ξ and ϑ converge. Typically, field perturbations will cause these higher charge vortices to separate into some number of charge-one vortices and antivortices,

whose total charge must be conserved. For example, an $s = +2$ vortex might explode into three $s = +1$ vortices and one $s = -1$ antivortex (Freund, 1999). Also visible in Fig. 1.1(b) is Freund's *sign principle*, which explains that, except when there are saddle points, in traversing any of the zero contours of ξ or ϑ the vortices encountered always alternate in sign (Freund and Shvartsman, 1994).

Since the amplitude is zero, the phase ceases to have a physical meaning at the vortex core (Dirac, 1931). As shown in Fig. 1.1(d), vortices in the 2D plane correspond to nodal lines in 3D. Because the field is complex, for it to vanish requires two conditions (i.e., the real and imaginary parts must individually vanish). In the language of geometric topology, a vortex is thus a codimension-2 defect of the field. The codimension describes the dimensionality of the defect relative to the space from which it is viewed, so the vortex has dimension $2 - 2 = 0$ in 2D and $3 - 2 = 1$ in 3D. Complex scalar fields also support a codimension-1 defect called a *vortex sheet* (Wang et al., 2008), which disintegrates into nodal lines when perturbed. Measured across a vortex sheet, the phase changes discontinuously by π. These take the form of concentric cylinders (whose radius increases with z) between Airy rings in the diffraction pattern of a finite lens, and between concentric regions of certain LG laser modes.

The nodal line shown in Fig. 1.1(d) has a sense determined by the direction of the phase winding, as indicated by the black loops. Using the right-hand screw rule gives the sense of the nodal line, indicated by its arrowhead. This sense can be locally determined on the nodal line by the vorticity vector $\mathbf{\Omega} \equiv \frac{1}{2}\nabla \times \mathbf{j} = (\nabla\xi \times \nabla\vartheta)|_{\xi=0,\vartheta=0}$ (Dennis et al., 2009). This relation has the intuitive interpretation that the direction is tangential to both zero contours of ξ and ϑ, which in turn have orientations determined by their gradients, evaluated at zero.

If the sense matches that of the contour where it pierces the observation plane, the singularity is a vortex at that point and an antivortex otherwise. The white integration contours in Fig. 1.1(d) have a sense determined by the right-hand screw rule for a z-axis perpendicular to the plane and pointing up toward the reader. If the observation plane is oriented away from the reader, the contour sense is reversed and consequently the vortex sign reverses. That is, the white loops reverse but the black loops, which are independent of the observer, do not; vortices become antivortices and antivortices become vortices, with the distinction depending on the observer.

Figure 1.1(d) also indicates that the vortex (i) and antivortex (ii) are not independent but can be thought of as connected via the nodal line (Berry, 1998). If the observation plane is translated upwards until it is a tangent to the nodal line, the corresponding vortex and antivortex move together until they are collocated,

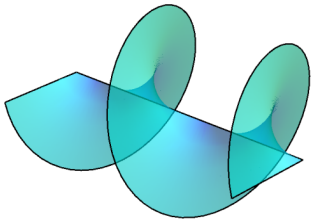

Figure 1.2: The constant-phase wavefront of $\Psi = (x + iy)\exp(ikz)$ is a helicoid for a nodal line lying parallel to the field propagation direction.

when they merge and annihilate. This occurs regardless of the plane orientation. Similarly, for a fixed observation plane in a time-varying field, if the nodal line moves downwards, provided the integrity of this line is maintained, meaning that it does not break and reconnect with any neighbouring nodal lines, the vortex and antivortex annihilate.

The name *wave dislocations* hints at the connection between the defects of the wavefronts and those described in crystallography, namely screw, edge, and mixed screw-edge dislocations (Nye and Berry, 1974; Dennis, 2009; Dennis et al., 2009). For example, the simplest wavefunction containing a phase vortex is generated by the function (Berry, 1981; Freund, 1999):

$$\Psi(\mathbf{r}) = (x + iy)\exp(ikz), \tag{1.4}$$

which, although not square integrable and hence nonphysical, acts as a prototypical charge $s = +1$ vortex revealing the local wavefront structure as a helicoid, as shown in Fig 1.2, where the nodal line lies along the z-axis, parallel to the field propagation direction. When it lies perpendicular, the analogy is with a pure edge dislocation, and other orientations correspond to the mixed screw-edge case. Furthermore, the Burgers vector – used to define dislocations in crystallography – may be evaluated in optical wavefields in terms of a local metric of phase gradient for each singularity (Dennis, 2009).

1.4 Some topological aspects of defects

The phase vortex is a type of topological defect; one of a family of such defects arising in fields. In this section we briefly introduce topological defects and discuss vortices as a prototypical example arising in complex scalar fields, which have two internal dimensions; one for each of the real and imaginary parts. In Chap. 5 we expand the discussion to include skyrmions and merons, which are topological defects of fields with more than two internal dimensions. There are many books

on topology as a mathematical topic, but condensed matter texts address topology along with related aspects with which we are concerned; the mapping between the physical space (also called the configuration space) and the so-called *order-parameter space* is largely ignored by the more mathematical texts, but is important for the physical picture. The best exposition of the relevant physics is by Mermin (1979). Another nice, slightly gentler introduction is provided by Sethna (2006).

Sethna (2006, p.198, §9.4) states that "A defect is a tear in the order parameter field. A topological defect is a tear that cannot be patched." Furthermore "*Topology* is the study of curves and surfaces where bending and twisting is ignored." The point is that topology is blind to bending or twisting of the fields we deal with, but *not blind* to the defects or singularities. In order to show that some region of a field contains a topological defect, the relevant property must be mapped to a special space (the order-parameter space) in such a way that any bending or twisting distortions are removed. Once mapped, the topology of any defect may be classified according to the number of times it covers this space. The area of mathematics that deals with this classification is called homotopy theory (see, e.g., Gowers et al., 2008, §IV.6).

An order parameter describes the essential physical properties of the field at each location in space. In the linear scalar optics case, the physical field is described using a complex scalar wavefunction. Because the defects exist in the phase of this field, the corresponding order parameter is chosen to be the phase. In the case of BECs, we use the GPE which also models the underlying physics as a complex scalar field Ψ. This is itself an order parameter and it is usually referred to as such, but it is not the order parameter that concerns us when looking for vortices; the relevant order parameter is the phase of Ψ. In Chap. 5 we deal with a pseudo-spinor that combines the individual complex scalar order parameters Ψ_1 and Ψ_2 of a two-component BEC. In that chapter we look at baby-skyrmion and meron *texture defects*. These are defects of an order parameter field of normalised spin vectors. For baby-skyrmions and merons, the order parameter is the 2D field of 3-vectors obtained by combining two 2D complex scalar fields.

Mathematicians distinguish between the surface of a sphere and its interior volume by calling the former a *sphere* and the latter a *ball*.[3] The number of dimensions d required to locate a point is also required for the description. Thus, the surface of a spherical apple is called the 2-sphere S^2, where 2 refers to the number of dimensions required to parameterise a point on its surface, and the pulp is the 3-ball B^3. We cannot directly visualise the 3-sphere S^3 from our 3D vantage.

[3] See http://mathworld.wolfram.com/Ball.html (Weisstein, 2009).

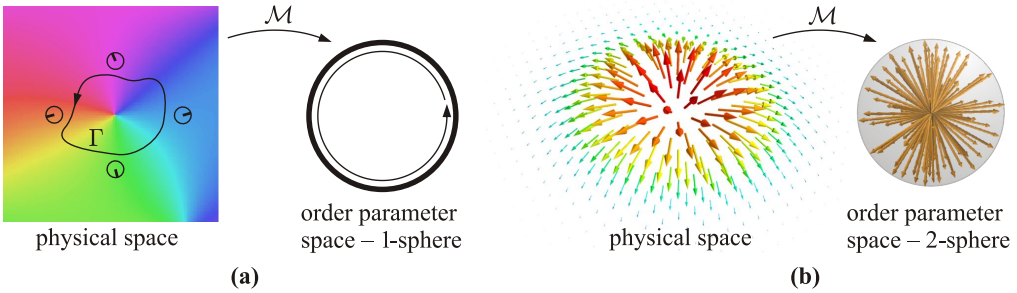

Figure 1.3: Schematic examples of mappings from physical to order parameter spaces. (a) The phase encountered along a contour Γ is mapped to an S^1 space. (b) The normalised 3-vectors encountered within a region are mapped to an S^2 space.

Luckily, the order-parameter spaces we are concerned with are S^1 and S^2.[4] A unit 1-sphere is a circle; only one number is required to parameterise a position on a circle. More generally, the spaces of algebraic topology are often d-dimensional spheres or tori with one or more holes. Figure 1.3 shows schematic examples of the phase along a contour mapped to S^1 and of a field of 3-vectors mapped to S^2; the latter example being relevant to texture defects, which we introduce in Chap. 5.

Because phase is a single number modulo 2π, the corresponding order parameter space is the unit circle. The mapping $\mathcal{M}$ from the physical space to the order parameter space samples the phase along a closed contour. The corresponding path followed in the order parameter space on the circle may meander back and forth but continuity of the order parameter field in physical space ensures that it will start and end at the same point in the order parameter space. Any distortion of the contour that does not cross the enclosed singularities will not change the number of times that the circle is completely covered, although the meanderings on the circle may change. This number is an integer, known as the *winding number*, that measures the topology. It is equal to the total signed charge of the singularities enclosed by the contour. For higher dimensional order parameter spaces, the number of coverings of the d-sphere is called the *wrapping number*. The topological essence of the singularities is reduced to a single integer by this method.

[4] Some might argue that visualising the 2-sphere S^2 on a 2D piece of paper is pushing things, but we are used to applying tricks like shading and perspective representation to help us.

1.5 Phase vortices from the interference of three plane waves

Consider the following superposition of three complex scalar plane waves coordinatised by the general position vector $\mathbf{r}$:

$$\Psi(\mathbf{r}) = \sum_{j=1}^{3} A_j \exp\left[i\left(\mathbf{k}_j \cdot \mathbf{r} + \phi_j\right)\right], \tag{1.5}$$

where the non-negative real constants A_j denote the amplitude of the jth wave, $\mathbf{k}_j$ are wavevectors corresponding to the same wavelength $\lambda_0 = 2\pi/|\mathbf{k}_j|$ and ϕ_j are phase factors, relative to some global phase. Despite the constituent plane waves not having a vortical character, the above superposition generates an array of straight, parallel nodal lines (Nicholls and Nye, 1987; Masajada and Dubik, 2001; Vyas and Senthilkumaran, 2007). If a fourth wave is introduced, as its amplitude is increased the nodal lines evolve progressively into helices, jagged lines, and ultimately loops (O'Holleran et al., 2006). When non-plane-waves interfere, the resulting nodal lines are in general curved. For spherical and Gaussian waves, the straight lines become curves with more complicated analytical forms. As more waves are introduced the curves become convoluted, allowing them to form loops or knots.

Here we introduce the method in Masajada and Dubik (2001) and Paganin (2006) for describing the creation of a vortex lattice from three interfering plane waves. In the next chapter, we follow this method for the three spherical wave and three Gaussian wave cases. To determine the location of the resulting vortices, the knowledge that vortex cores lie at points of zero amplitude is used. Given that the problem is restricted to two degrees of freedom, a geometric phasor diagram can be constructed with one phasor per plane wave [Fig. 1.4(a)]. For a resultant zero amplitude the phasors must sum to zero when placed tip to tail.

This condition is met by the degenerate case of two antiparallel phasors of equal amplitude. Such a case describes a two pinhole interferometer in which the sources have equal amplitude and their phases differ by π. The field cancels completely along a single plane of zero amplitude that bisects the sources. This plane corresponds to a vortex-sheet or *domain-wall* defect rather than a vortex. Vortex formation from linear superposition of greater than three sources has also been demonstrated, corresponding to a loop of four or more phasors (O'Holleran et al., 2006).

For the case of three plane waves, following Paganin (2006), a coordinate system is established with respect to the wavevector $\mathbf{k}_1 \equiv (k_{1x}, k_{1y}, k_{1z})$ such that it

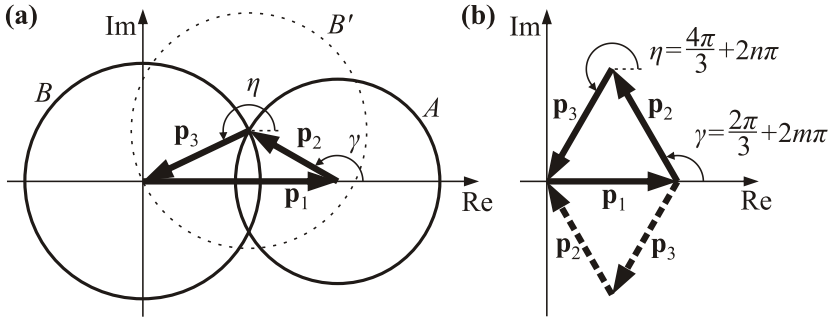

Figure 1.4: Phasor diagram from which vortex solutions are established. Three phasors $\mathbf{p}_1, \mathbf{p}_2, \mathbf{p}_3$ correspond to the three respective terms on the right side of Eqs (1.7) or (2.2), and form a closed triangle corresponding to a resultant zero amplitude. Two angles γ and η arise in the construction. (a) In the case of arbitrary amplitudes for $\mathbf{p}_1$, $\mathbf{p}_2$ and $\mathbf{p}_3$, the tip of $\mathbf{p}_2$ is constrained to lie on circle A of radius $|\mathbf{p}_2|$, with the tail of $\mathbf{p}_3$ being constrained to lie on circle B of radius $|\mathbf{p}_3|$. (b) For equal amplitudes $|\mathbf{p}_1| = |\mathbf{p}_2| = |\mathbf{p}_3|$ an equilateral triangle is formed. The dashed construction represents another of the six equivalent alternatives formed by permutating the phasor order.

has only a non-zero k_{1z} component. The coordinate system is rotated such that $\mathbf{k}_2$ has only non-zero k_{2x} and k_{2z} components. This leaves $\mathbf{k}_3$ with all non-zero k_{3x}, k_{3y} and k_{3z} components. Ψ is then

$$\begin{aligned}\Psi = A_1 \exp\left[i(kz + \phi_1)\right] + A_2 \exp\left[i\left(k_{2x}x + z\sqrt{k^2 - {k_{2x}}^2} + \phi_2\right)\right] \\ + A_3 \exp\left[i\left(k_{3x}x + k_{3y}y + z\sqrt{k^2 - {k_{3x}}^2 - {k_{3y}}^2} + \phi_3\right)\right]\end{aligned} \tag{1.6}$$

where $k^2 \equiv {k_1}^2 = {k_{1x}}^2 + {k_{1y}}^2 + {k_{1z}}^2$. Without loss of generality, we can set $\phi_1 = 0$. This is equivalent to saying that the phase is defined to within a global phase factor. At points of zero amplitude along the $z = 0$ plane,

$$0 = A_1 + A_2 \exp\left[i(k_{2x}x + \phi_2)\right] + A_3 \exp\left[i(k_{3x}x + k_{3y}y + \phi_3)\right]. \tag{1.7}$$

Figure 1.4(a) is constructed by establishing a coordinate system such that the relative phase of the first plane wave is designated as zero. The circle B' represents the possible phasor orientations constrained by the tip of phasor $\mathbf{p}_2$. The zero sum condition is easier to construct if $\mathbf{p}_3$ is flipped and the circle B drawn constrained by the tail of $\mathbf{p}_1$. The resulting solutions are shown in the phasor diagram as the intersection of the circles A and B. Note that there are two intersections and hence two solutions, corresponding to a vortex and antivortex pair.

The arguments of the two exponentials in Eq. (1.7) are identified in the phasor diagram as γ and η, respectively. For simplicity, here and elsewhere in this thesis,

we assume that the sources are all of equal amplitude. For the three-pinhole interferometer treated in the next chapter, such a case corresponds to a uniformly illuminated screen punctured by three pinholes, where the pinholes are secondary sources. The angles γ and η are thus uniquely defined to within an integer multiple of 2π. Stated another way, rotating either of $\mathbf{p}_2$ or $\mathbf{p}_3$ by a multiple of 2π generates the same phasor diagram. Thus we have

$$\gamma = \frac{2\pi}{3} = k_{2x}x + \phi_2 + 2m\pi \tag{1.8a}$$

and

$$\eta = \frac{4\pi}{3} = k_{3x}x + k_{3y}y + \phi_3 + 2n\pi, \tag{1.8b}$$

where $m, n \in \mathbb{Z}$.

These equations can be solved to determine the vortex coordinates (x, y) in terms of the source wave components $\mathbf{k}_j$ and phases ϕ_j, and pairs of indices (m, n) that uniquely index each vortex:

$$\begin{aligned} x &= \frac{2\pi/3 - (\phi_2 + 2m\pi)}{k_{2x}}, \\ y &= \frac{k_{2x}\left[4\pi/3 - (\phi_3 + 2n\pi)\right] - k_{3x}\left[2\pi/3 - (\phi_2 + 2m\pi)\right]}{k_{2x}k_{3y}}. \end{aligned} \tag{1.9}$$

A numerical example of three superposed plane waves is given in Fig. 1.5, corresponding to the parameters $A_1 = A_2 = A_3 = 1$ and $\phi_1 = \phi_2 = \phi_3 = 0$, with all fields being evaluated over the plane $z = 0$. This example illustrates the three interfering plane waves giving rise to an infinitely extended lattice of straight, parallel nodal lines. These are shown intersecting the plane $z = 0$, at locations that are visible as vortices in the phase map. In the amplitude plot, the vortices lie at points where $|\Psi| = 0$, which coincide with the intersections of the zero contours. For this case of symmetrically arranged sources, the lattice has a honeycomb symmetry and contains equal numbers of vortices and antivortices, as it must in order to conserve the zero angular momentum of the unsuperposed source waves. The honeycomb lattice is composed of two interleaved lattices with hexagonal or triangular symmetry; one containing vortices and one containing antivortices.

The OAM associated with an area of the field may be related to the transverse component of the linear momentum density, which is proportional to the probability current in that area (Courtial et al., 2006). This knowledge could be applied to various areas of the field in Fig. 1.5. One obvious example might be a hexagonal unit cell of the honeycomb lattice, whose vertices coincide with the vortex cores. Placing the origin at the cell centre makes it immediately apparent,

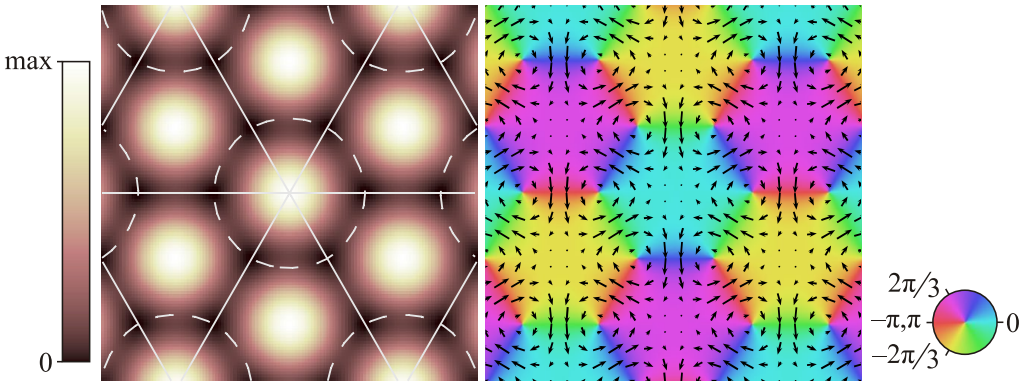

Figure 1.5: Intensity (left) and phase (right) of three interfering plane waves observed over the plane $z = 0$. An infinite, regular lattice of vortices arises. Here the wavevectors are oriented symmetrically with respect to the z axis, with $\mathbf{k}_1 = (\sqrt{3}, -1, 10), \mathbf{k}_2 = (-\sqrt{3}, -1, 10)$ and $\mathbf{k}_3 = (0, 2, 10)$. Zero contours of the real (dashed lines) and imaginary (solid lines) parts are overlaid on the intensity plot. These intersect at intensity zeros which are also vortex locations. Probability current $\mathbf{j}$ is shown overlaying the phase. Current flows counter-clockwise around vortices and clockwise around anti-vortices.

from the three-fold rotational symmetry of the current vectors, that OAM is zero within such a bounded area. The lattice symmetry of this example allows us to translate the coordinate system origin by one lattice cell without consequence, and because there are no discontinuities on the cell boundary, we can infer that the total OAM of the field is zero.

The topological charge s of each of these point defects is seen to be ± 1. In this context, we note that higher-charge vortices are not observed with three sources. To form a charge s nodal line in a field locally obeying the Helmholtz equation, $s(s+1)/2$ complex conditions must be specified (Berry and Dennis, 2001). This corresponds to $s(s+1)$ conditions, if the real and imaginary parts of the conditions are considered separately. Evidently, a minimum of five point sources lying in a plane, requiring a total of seven coordinates for the specification of their position (up to irrelevant translations and rotations), is the minimum requirement to form $s = 2$ vortices.

1.6 Outline of the thesis

We have demonstrated the superposition of three plane waves which generates a lattice of parallel nodal lines; when viewed in a plane, they are observed as zeros of intensity corresponding to a honeycomb lattice of vortices and antivortices (Nicholls and Nye, 1987; Masajada and Dubik, 2001). This simple idea of the

generation of a lattice of vortices from the interference of three waves motivates much of the remainder of this thesis.

In Chap. 2 we generalize the study of linear three-wave interference to the superposition of three expanding spherical waves, three illuminated-pinhole secondary-sources modelled using a Rayleigh-Sommerfeld propagator with delta-function sources, and three Gaussian wavepackets. Approximate analytical expressions are derived for the vortex locations in the optical far field and compared with numerical simulations for all these cases. For the spherical wave case, a representation in terms of a certain parameter space arises, allowing estimates of the number of vortices, description of a natural coordinate system for the vortices at the intersections of a family of hyperbolas, and a surprising link to the information capacity of the diffracted field. The 3D nodal line structure is also studied numerically in the near field for this case and for the pinhole interferometer. The case of interfering Gaussian waves is shown to give rise to an infinitely extended vortex-antivortex lattice embedded in a Gaussian intensity envelope.

In Chap. 3 we present a model of a vortex-carrying LG laser beam as it propagates and is diffracted through a ground glass plate (GGP), generating a speckled field in the process. We observe that the field vorticity achieves a maximum at a characteristic distance from the plate.

In Chap. 4 we apply our knowledge of the three-pinhole Young's interferometer to the analogous nonlinear case of three initially localised, BEC wavepackets. With numerical 2D and 3D simulations, we demonstrate the production of a honeycomb vortex-antivortex (VA) lattice that is predicted to form by analogy with the linear case. Suggestions are provided for modifications to previous experiments which have failed to observe this lattice. The vortex creation mechanism is explained with relation to the linear expanding Gaussian wavepacket model presented in Chap. 2. We develop a crystallographic model of the vortex locations in this lattice, which compare favourably with the results of a recent experiment (Henderson et al., 2009). If the BEC remains magnetically trapped after the pieces interfere, the vortices and antivortices formed in the lattice become motile and interact chaotically. We describe the resulting interactions within the now-turbulent BEC.

In Chap. 5 we study texture defects, which are topological defects that exist for certain configurations of the field within bounded regions of the physical space. Their order parameter space is S^2 or S^3, in contrast with the S^1 space corresponding to topological phase defects. By allowing the atoms in a BEC to be excited to a second internal hyperfine state, sufficient additional internal degrees of freedom are available to support the existence of texture defects. A strong connection exists between vortices and certain texture defects. With numerical models of

the two-component BEC, we apply our findings explaining the lattice translation as a result of initial BEC segment phases, to the creation of two honeycomb VA lattices; one for each population of atoms in each of the two internal states. The relationship between vortices and texture defects applied to the suitably aligned lattices generates a lattice of texture defects. We identify the defects as merons and a certain type of planar defect. By analogy with the chaotic dynamics observed in the single-component trapped BEC, we then seek to generate texture defects in the turbulent trapped two-component BEC into which vortices have been seeded. Using a model of a 2D two-component BEC, we again find, by virtue of the strong connection between vortices and certain texture defects, that such a system naturally generates texture defects.

Finally, in Chap. 6 we discuss some ideas for future directions that build on the work developed in this thesis.

2 Three-wave interference beyond plane waves

> Nothing's beautiful from every point of view.
>
> — Horace

In this chapter the superposition of three plane waves, which generates an infinite lattice of phase vortices, is generalized to the cases of (i) three distinct monochromatic expanding spherical waves interfering in space, and (ii) three Gaussian wavepackets interfering as they undergo propagation through time. We describe the application of a phasor approach to these cases, applied in the far-field region asymptotically far from the sources. Approximate analytical expressions are derived for the vortex locations. For the spherical wave case, a representation in terms of a certain parameter space arises, allowing estimates of the number of vortices and a description of a natural coordinate system for the vortices at the intersections of a family of hyperbolas. We then see how the theory, which has been derived for spherical point sources, may be mapped onto the case of a Young's interferometer in which the illuminated screen contains three rather than two pinholes. The 3D nodal line structure is examined for both the spherical point source and the pinhole interferometer cases and is shown to exhibit a rich geometry. The case of interfering Gaussian waves is shown to give rise to an infinitely extended vortex-antivortex lattice embedded in a Gaussian intensity envelope.

2.1 Young's interference experiment revisited

Figure 2.1 shows the interference pattern arising from the superposition of two spherical waves observed on a screen parallel to the plane in which the sources lie. Two point sources naturally give rise to surfaces of constant phase that are hyperboloids of two sheets having the sources as their foci. The condition for

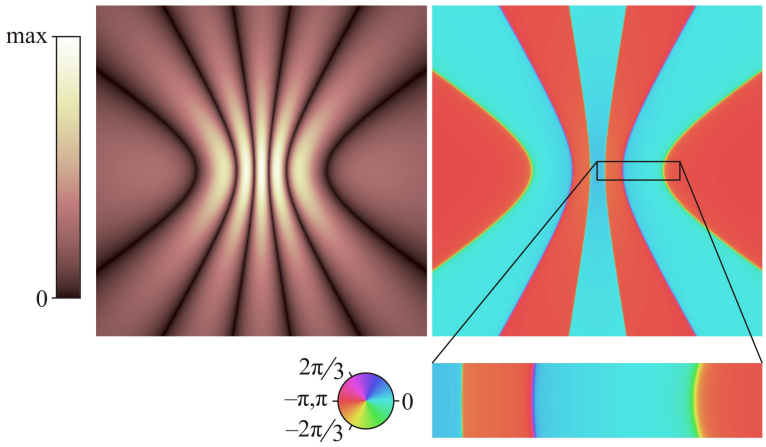

Figure 2.1: The interference pattern from Young's two-pinhole interferometer is a series of bright and dark hyperbola-shaped fringes. The outset region shows the phase changing rapidly but not instantaneously across regions separated by dark fringes. Colour legends here apply to all other figures.

constant phase is established by a constant difference in path length; this being equivalent to the well known geometric construction method for hyperboloids. Hyperbolas of two branches are formed when these hyperboloids intersect with a plane that is parallel to a line joining the sources.[1] Thus the peaks and troughs of intensity that arise due to constructive and destructive interference trace out hyperbolas. The phase pattern appears two-valued with a π phase discontinuity between regions whose boundaries coincide with the trough location. As we are concerned with identifying defects of wavefields, one might expect that the troughs are associated with nodal sheets or domain walls (Pismen, 1999). However, careful examination of the outset region in Fig. 2.1 shows that the phase changes rapidly but not discontinuously (Ruben and Paganin, 2007b). If a paraxial approximation is made to the diverging wave functions, nodal sheets are produced in the resulting wave field. However, in physical systems the amplitude of each interfering wave component must be equal along these surfaces if nodal sheets are to be produced. If the sources have equal amplitude, this can only happen in the rare case where their source phase differs by π and then only over the plane bisecting the two sources. In general, true nodal sheets are not produced.

We have reminded the reader of the geometry resulting from the interference of two spherical waves and explained that defects are not usually created. However, when a third source is included, the presence of defects becomes the norm and only

[1] Apollonius of Perga (c262 BC–c190 BC) first noted the two-branched nature of the hyperbola (Heath, 1896). The term *hyperbolas of two branches* describes the intersection of the hyperboloid with the plane along two open curves.

in rare cases are they not produced. We now proceed to describe this remarkable change of circumstance.

2.2 Previous work related to the three-pinhole interferometer

Gbur et al. (2004) studied the three-pinhole interferometer, paying particular regard to the conditions on source coherence required to produce zeros of intensity in the resulting field. They showed that the three sources need not be completely mutually coherent or monochromatic in order for the interference pattern to contain zeros of intensity. The approach taken was to consider the paraxial propagation of spherical expanding waves, which gives rise to an infinite regular extended lattice of intensity nodes. In contrast, our approach in this chapter avoids the paraxial approximation, and by so doing, finds that a finite number of vortices is produced.

Two other studies by Masajada et al. (2007) and Vyas and Senthilkumaran (2007), of the vortex lattice produced by three interfering spherical waves, were performed contemporaneously with the work we will present here (Ruben and Paganin, 2007a,b,c). Masajada et al. (2007) sought to describe the positions of the vortices from the three-pinhole interferometer, which coincide with the zeros of the field. Their results are qualitatively different to those we obtain, due to different assumptions being made; primarily that the pinholes are circular apertures giving rise to amplitudes described by interfering Bessel functions in the far field. There is also an implicit assumption that the wavelength λ of the radiation illuminating the pinholes is much shorter than the pinhole spacing r. In following the paraxial approach, the resulting predicted lattice is again infinitely extended, and differs in the predicted 3D nodal line structure. However, the authors have experimentally realized the three-pinhole interferometer and verified the observed vortex locations, so their results are valid for the limiting case $r \gg \lambda$.

Vortex generation has been demonstrated in two experiments related to the one described here. Lee et al. (2006) illuminated three (and more) micron-scale spheres with a laser and observed vortices in the resulting interference pattern. More recently, Scherer et al. (2007) observed vortices resulting from the merging of three non-rotating Bose-Einstein condensate (BEC) clouds. Disregarding nonlinear effects and reconsidering the 3D system described here in (2+1)D by replacement of the spatial dimension z with time t, the BEC vortex generation may be understood as arising from the linear interference of propagating, expanding waves. We explore this topic in detail in Chap. 4.

2.3 Phase vortices from the interference of three spherical waves

In this section we present and extend the findings in our papers on the three-pinhole interferometer, Ruben and Paganin (2007a,b,c). Given that the superposition of three complex plane-wave spatial wavefunctions may lead to phase vortices (Nicholls and Nye, 1987; Masajada and Dubik, 2001), it is natural to enquire whether the superposition of three outgoing spherical waves may not also lead to phase vortices. It is to this question that we now turn.

2.3.1 Extending the plane-wave case to spherical waves

The complex spatial wavefunction $\Psi_j(\mathbf{r})$, due to a point source at position $\mathbf{r}_j$ that is radiating outgoing spherical waves *in vacuo*, is given by

$$\Psi_j(\mathbf{r}) = \frac{A_j}{|\mathbf{r}-\mathbf{r}_j|} \exp\left[i\left(k_j|\mathbf{r}-\mathbf{r}_j| + \phi_j\right)\right], \tag{2.1}$$

where the source is characterised by the wave-number $k_j \equiv 2\pi/\lambda_0$, amplitude A_j and phase ϕ_j, defined relative to some phase reference. For all $\mathbf{r} \neq \mathbf{r}_j$, such spherical waves obey the free-space Helmholtz equation. This applies to monochromatic complex scalar electromagnetic waves in vacuum, to non-relativistic spinless particles in the form of the time-independent free-space Schrödinger equation, and to relativistic spinless particles in the form of the time-independent free-space Klein–Gordon equation. As such, the following discussions are applicable to all of these physical systems. For example, experimental application involving a high-energy transmission electron microscope might be envisaged, using the paraxial form

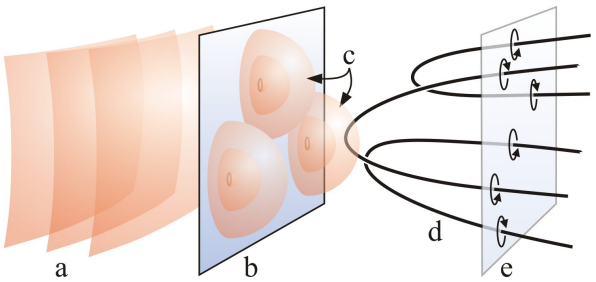

Figure 2.2: In this schematic of a Young's three-pinhole interferometer, incident illumination (a) impinges upon a punctured screen (b), producing three divergent waves (c), which interfere, giving rise to a network of nodal lines (d). These are observed as phase vortices over a plane (e).

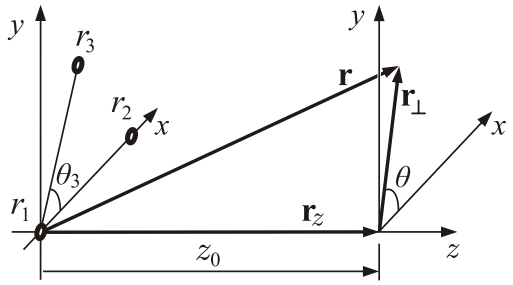

Figure 2.3: Coordinate system. The point sources r_1, r_2, and r_3 lie in the plane $z = 0$. The position vector $\mathbf{r}$ is to a point with cylindrical-polar coordinates $(r_\perp, \theta, z_0)$.

of the time-independent free-space Klein–Gordon equation, which ignores the typically-small effects of electron spin in this setting (De Graef, 2003).

The problem of three interfering spherical waves may be mapped onto a Young-type experiment, in which a black screen with three small pinholes is coherently illuminated by a propagating complex scalar field (see Fig. 2.2).[2] Note that this identification is only possible when one is both sufficiently far from the screen and sufficiently close to the optic axis, in which case the radiation transmitted by each of the pinholes is approximately spherical (cf. §2.3.9).

Let us consider an assembly of three point sources, all of which have the same wave-number k. Without loss of generality we may consider these sources to occupy the same plane $z = 0$, with source locations $\mathbf{r}_j \equiv (x_j, y_j, 0)$, where $j = 1, 2, 3$. The resulting spatial wavefunction $\Psi(\mathbf{r})$ may thus be written as

$$\Psi(\mathbf{r}) = \sum_{j=1}^{3} \frac{A_j}{|\mathbf{r} - \mathbf{r}_j|} \exp\left[i \left(k|\mathbf{r} - \mathbf{r}_j| + \phi_j \right) \right], \tag{2.2}$$

where $|\mathbf{r} - \mathbf{r}_j| \equiv \sqrt{(x - x_j)^2 + (y - y_j)^2 + {z_0}^2}$ is the distance from the jth source to a given observation point $\mathbf{r}$. Referring to Fig. 2.3, we label both the jth source and its distance from the coordinate origin by the same symbol r_j. The position vector $\mathbf{r}$ and its perpendicular component $\mathbf{r}_\perp$ have lengths $r \equiv |\mathbf{r}|$ and $r_\perp \equiv |\mathbf{r}_\perp|$, respectively.

To determine the locations of the vortices, which result from the superposition of the three spherical waves, we utilize the fact that vortex cores lie at points of zero amplitude. Given that the problem is restricted to two degrees of freedom, due to the complex wavefield representation, a geometric phasor diagram can be constructed with one phasor for each wave component in Eq. (2.2): see Fig. 1.4. We follow the phasor approach of Paganin (2006), which is based on

[2] Here the term *black* is meant in the technical sense that all portions of illuminating waves not passing through apertures are completely absorbed by the screen.

Masajada and Dubik (2001), and which was applied to the plane wave case in §1.5. At any point coinciding with a vortex core, the phasor components must sum to zero when placed tip to tail. Note that if the source amplitudes differ sufficiently, it is possible that no closed triangle of phasors may be formed, i.e., circles A and B in Fig. 1.4 cannot intersect if $|\mathbf{p}_1| > |\mathbf{p}_2| + |\mathbf{p}_3|$. In this case, no vortices will be produced.

We now restrict consideration to the special case of equal-amplitude sources where $A_1 = A_2 = A_3 = 1$. At a given point $\mathbf{r}$ in space, let $\mathbf{p}_1, \mathbf{p}_2, \mathbf{p}_3$ denote the three complex terms that are summed on the right side of Eq. (2.2). These three numbers are represented as phasors in Fig. 1.4. Here, we set $\phi_1 = 0$, which implies no loss of generality, since the invariance of the equations of motion under a shift in the origin of time implies global phase factors to have no physical meaning. The circle B' represents the possible orientations of $\mathbf{p}_3$, constrained by the tip of $\mathbf{p}_2$. The zero sum condition is easier to construct if $\mathbf{p}_3$ is notionally flipped to give circle B whose centre coincides with the tail of $\mathbf{p}_1$. The resulting vortex solutions correspond to the phasors $\mathbf{p}_2$ and $\mathbf{p}_3$ meeting at the intersections of the circles A and B. Note that there are two such "closed triangle" intersections and hence two solutions. However, there are restrictions on the association of the phasors with particular sources, as will be discussed below. In the case of equal amplitudes, where $|\mathbf{p}_1| = |\mathbf{p}_2| = |\mathbf{p}_3|$, an equilateral triangle of phasors is formed, dictating that there are only two unique solution angles η and γ [see Fig. 1.4(b)].

2.3.2 Vortices in the far-field regime

We evaluate Eq. (2.2) in the far-field regime, namely in the half-space $z > z_0$ in which z_0 is sufficiently large that (Messiah, 1961, p. 811)

$$|\mathbf{r} - \mathbf{r}_j| \sim r - \frac{\mathbf{r}_\perp \cdot \mathbf{r}_j}{r}, r \equiv |\mathbf{r}| \gg r_j. \tag{2.3}$$

This approximation is worthy of some discussion as the claim is made in Ruben and Paganin (2007a) that it is equivalent to a paraxial approximation, but with further insight we here make the weaker claim that it is a far-field approximation. This softening of language indicates that the approximation is valid even when far from the z-axis, provided evaluation is sufficiently far from the source. In an alternative approach, one might seek solutions of the paraxial wave equation, in restricting attention to the far field. However, we make the unexplored conjecture that this would probably reproduce the results of other authors in which an infinite, regular lattice results. Messiah (1961, p. 811) shows that this expression applies asymptotically as $z_0 \to \infty$. With reference to Fig. 2.3, expanding the LHS of

Eq. (2.3) gives

$$|\mathbf{r}-\mathbf{r}_j| \equiv r\left[1-2\frac{\mathbf{r}\cdot\mathbf{r}_j}{r^2}+\left(\frac{r_j}{r}\right)^2\right]^{\frac{1}{2}}. \tag{2.4a}$$

The last term inside the square brackets may be ignored when $r \gg r_j$, i.e., on length scales much larger than the source spacing, when the middle term almost always dominates. The exception is when $\mathbf{r}$ is near perpendicular to $\mathbf{r}_j$, i.e., close to the z-axis, in which case the last term may in fact dominate. The condition $r \gg r_j$ saves us from invalidating the approximation in this case, as both terms are still $\ll 1$. It is worth emphasising that, in this derivation, no direct restrictions have been placed on the size of $r_\perp$. Now we apply the binomial approximation $(1+\varepsilon)^{1/2} \sim 1+\varepsilon/2$, noting that $\mathbf{r} = \mathbf{r}_z + \mathbf{r}_\perp$ and $\mathbf{r}_z \cdot \mathbf{r}_j = 0$ to give Eq. (2.3). This approximation is applied to the phase term in the exponent of Eq. (2.2). One may perform a Maclaurin series expansion of any position-dependent term of the propagated field in terms of the source coordinates $\mathbf{r}_j$ of the unpropagated field. The Fraunhofer regime corresponds explicitly to that region of space in which quadratic and higher-order terms in the series may be neglected (Born and Wolf, 1999, §8.3.3). Expanding Eq. (2.4a) in $\mathbf{r}_j$ gives

$$|\mathbf{r}-\mathbf{r}_j| = r - \frac{\mathbf{r}\cdot\mathbf{r}_j}{r} + \frac{\mathbf{r}_j\cdot\mathbf{r}_j}{2r} - \frac{(\mathbf{r}\cdot\mathbf{r}_j)^2}{2r^3} - \cdots, \tag{2.4b}$$

from which we immediately see that Eq. (2.3) represents the Fraunhofer approximation of the position coordinate of the phase.

The wavefunction Ψ depends linearly on the amplitude term $A_j/|\mathbf{r}-\mathbf{r}_j|$, so for large r the divisor varies much more slowly with $|\mathbf{r}-\mathbf{r}_j|$ than the phase argument. Consequently, the stronger approximation $|\mathbf{r}-\mathbf{r}_j| \sim r$ is made to this term (Messiah, 1961, p. 811). Thus, Eq. (2.2) becomes

$$\begin{aligned}\Psi(\mathbf{r}) = \frac{1}{r}\exp(ikr) &+ \frac{1}{r}\exp\left\{i\left[k\left(r-\frac{r_\perp r_2}{r}\cos\theta\right)+\phi_2\right]\right\} \\ &+ \frac{1}{r}\exp\left\{i\left[k\left(r-\frac{r_\perp r_3}{r}\cos(\theta-\theta_3)\right)+\phi_3\right]\right\},\end{aligned} \tag{2.5}$$

where we have made use of the assumption that $A_1 = A_2 = A_3 = 1$. This expression vanishes when

$$1+\exp\left[i\left(-k\frac{r_\perp r_2}{r}\cos\theta+\phi_2\right)\right]+\exp\left[i\left(-k\frac{r_\perp r_3}{r}\cos(\theta-\theta_3)+\phi_3\right)\right]=0. \tag{2.6}$$

Geometrically, the above condition may be represented as the addition of three unit-length phasors in the complex plane, such that they form an equilateral triangle when placed tip-to-tail (Masajada and Dubik, 2001). This construction

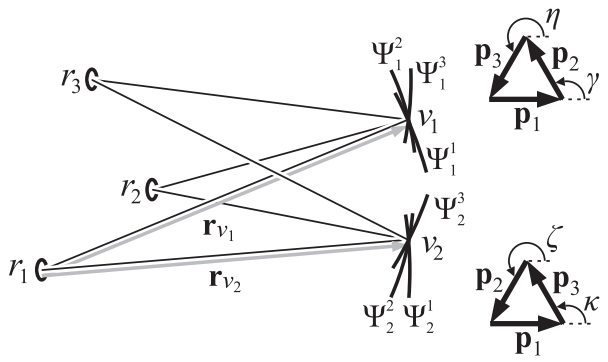

Figure 2.4: Schematic showing two vortices ν_1 and ν_2 from one (n,m) pair. Position vectors $\mathbf{r}_{\nu_1}$ and $\mathbf{r}_{\nu_2}$ (grey and vertically offset for clarity) indicate the locations of two vortices where $\Psi_1 = \Psi_1^1 + \Psi_1^2 + \Psi_1^3 = 0$ and $\Psi_2 = \Psi_2^1 + \Psi_2^2 + \Psi_2^3 = 0$, respectively. The phase winding senses of the two vortices are complementary. That is, if ν_1 is a vortex, ν_2 is an antivortex.

is shown in Fig. 1.4(b), with the arguments of the two exponentials in Eq. (2.6) being denoted by γ and η, respectively. These phase angles are uniquely defined to within an integer multiple of 2π, so that:

$$\gamma = -k\frac{r_\perp r_2}{r}\cos\theta + \phi_2 = \frac{2\pi}{3} + 2m\pi, \tag{2.7a}$$

and

$$\eta = -k\frac{r_\perp r_3}{r}\cos(\theta - \theta_3) + \phi_3 = \frac{4\pi}{3} + 2n\pi, \tag{2.7b}$$

where m and n are integers.

At a particular vortex location, say ν_1 in Fig. 2.4, the phasors are associated with particular, identifiable sources. This association is fixed for that particular vortex. However, another vortex ν_2 may exist at another location, where the phase values of the wave components are the same, but the association with the sources is swapped. As we are still free to rotate the phases of the three sources such that r_1 has a relative phase of 0, corresponding to phasor $\mathbf{p}_1$, the two remaining phasors at ν_2 are now associated with the complementary sources. The consequence of this freedom is that both phasor diagrams must be considered for each (m, n) pair. The association of the m and n indices with the vertices of the phasor triangle is arbitrary; the choice is made here to match m with r_2 and n with r_3. Thus we have two additional equations

$$\zeta = -k\frac{r_\perp r_2}{r}\cos\theta + \phi_2 = \frac{4\pi}{3} + 2m\pi, \tag{2.8a}$$

and

$$\kappa = -k\frac{r_\perp r_3}{r}\cos(\theta - \theta_3) + \phi_3 = \frac{2\pi}{3} + 2n\pi. \tag{2.8b}$$

2.3.3 Vortex locations

Here we show how the construction of §2.3.2 can be used to determine the polar coordinates, $r_{\perp mn}$ and θ_{mn}, of vortex ν_1 in the plane $z = z_0$, which is specified by the integer indices (m, n) (cf. Fig. 2.3).

Dividing Eq. (2.7b) by (2.7a) gives

$$\frac{r_3 \cos(\theta - \theta_3)}{r_2 \cos\theta} = \frac{N(n)}{M(m)}, \tag{2.9}$$

where

$$M(m) \equiv 2\pi\left[1 + 3\left(m - \phi_2/2\pi\right)\right], \tag{2.10a}$$

and

$$N(n) \equiv 2\pi\left[2 + 3\left(n - \phi_3/2\pi\right)\right]. \tag{2.10b}$$

Next, making the substitution

$$\begin{aligned}\frac{\cos(\theta - \theta_3)}{\cos\theta} &= \frac{\cos\theta\cos\theta_3 + \sin\theta\sin\theta_3}{\cos\theta} \\ &= \cos\theta_3 + \tan\theta\sin\theta_3\,,\end{aligned} \tag{2.11}$$

gives

$$\frac{r_3}{r_2}\left(\cos\theta_3 + \tan\theta\sin\theta_3\right) = \frac{N(n)}{M(m)}. \tag{2.12}$$

Finally, isolating θ and labelling it with an mn subscript, to identify it with the (m, n)th vortex core, gives the desired expression for the polar angle to the (m, n)th vortex core for ν_1:

$$\theta_{mn} = \arctan\left(\frac{r_2 N(n) - r_3 M(m)\cos\theta_3}{r_3 M(m)\sin\theta_3}\right). \tag{2.13}$$

When implementing Eq. (2.13) in a computer program, the $\arctan(y/x)$ function is replaced with the quadrant-preserving $\arctan2(y, x)$ function. This returns values in the range $(-\pi, \pi)$, in contrast with arctan which is restricted to the principal branch $(-\pi/2, \pi/2)$. Also, if one allows for $\theta_3 \in (\pi, 2\pi)$, i.e. reflex angles, the selection of the solution branch of the arctan function must be swapped $\theta \to \theta + \pi$ and all associations with vortices and antivortices must be exchanged.

With a view to obtaining the radial coordinate $r_{\perp mn}$ of the vortex core, we take Eq. (2.7a) and write the denominator r in terms of its components z_0 and $r_\perp$ (see Fig. 2.3):

$$-k\frac{r_\perp r_2}{\sqrt{{z_0}^2 + {r_\perp}^2}}\cos\theta_{mn} = \frac{1}{3}M(m). \tag{2.14}$$

Squaring, and then solving for $r_\perp$, we obtain

$$r_{\perp mn}{}^2 = \frac{z_0{}^2}{\left(\dfrac{3kr_2\cos\theta_{mn}}{M(m)}\right)^2 - 1}, \tag{2.15}$$

where an mn subscript has been added to $r_\perp$. Applying the identity

$$\cos^2\theta_{mn} = \frac{1}{1+\tan^2\theta_{mn}}, \tag{2.16}$$

and making use of Eq. (2.13), we obtain our final expression for the radial coordinate $r_{\perp mn}$ of the (m,n)th vortex core for v_1:

$$r_{\perp mn} = \frac{z_0}{\sqrt{\dfrac{\left(3kr_2r_3\sin\theta_3\right)^2}{\left[r_2N(n)\right]^2 - 2r_2r_3N(n)M(m)\cos\theta_3 + \left[r_3M(m)\right]^2} - 1}}. \tag{2.17}$$

Note that the terms of this expression have been rearranged from that in Ruben and Paganin (2007a) so as to avoid singularities during its evaluation which arose for zeros of $M(m)$. Note also that Eq. (2.17) is only valid for integers (m,n) that yield a real number for $r_{\perp mn}$ (cf. §2.3.4).

Repeating the above steps for v_2 gives expressions for $r_{\perp mn}$ and θ_{mn} in terms of the following equations $K(m)$ and $L(n)$

$$K(m) \equiv 2\pi\left[2 + 3\left(m - \phi_2/2\pi\right)\right], \tag{2.18a}$$

and

$$L(n) \equiv 2\pi\left[1 + 3\left(n - \phi_3/2\pi\right)\right], \tag{2.18b}$$

where we have made the substitutions $M(m) \to K(m)$ and $N(n) \to L(n)$ in Eqs (2.13) and (2.17).

The polar-coordinate equations (2.13) and (2.17) specify the vortex core locations for all allowed m and n parameter values, in the far-field regime. Note that $r_{\perp mn}$ is proportional to z_0, as one would expect in the far field. This corresponds to a 3D nodal line structure of asymptotically straight lines radiating from a single point in the source plane. This may be contrasted with the case of three superposed plane waves, where the nodal lines are mutually parallel (Nicholls and Nye, 1987; Masajada and Dubik, 2001).

2.3.4 Parameter Space

We first consider vortices corresponding to v_1. For real solutions, the argument of the square root in Eq. (2.17) must be positive, imposing a condition on the

allowable (m, n) values for a given source arrangement. The integers m and n must therefore satisfy the inequality

$$[r_2 N(n)]^2 - 2r_2 r_3 N(n) M(m) \cos\theta_3 + [r_3 M(m)]^2 < \left(3kr_2 r_3 \sin\theta_3\right)^2. \quad (2.19)$$

This equation describes the interior of an ellipse in the Cartesian (m, n) plane, for all non-collinear arrangements of the three sources. The equation of the corresponding boundary curve – obtained by replacing the inequality in Eq. (2.19) with an equality – is consistent with the form of a general conic section in the (m, n) plane, namely (see, e.g., Gibson, 2003):

$$Q(m, n) = am^2 + 2hmn + bn^2 + 2gm + 2fn + c = 0, \quad (2.20)$$

where a, h, b, g, f and c are real numbers. We set $\phi_j = 0$, corresponding to all three point sources radiating in phase with one another. In §2.3.5 we remove this restriction, imposed here only to clarify the exposition. The coefficients in Eq. (2.20) are then given by

$$\begin{aligned} a &= 9{r_3}^2, \qquad h = -9r_2 r_3 \cos\theta_3, \qquad b = 9{r_2}^2, \\ g &= 3{r_3}^2 - 6r_2 r_3 \cos\theta_3, \qquad f = 6{r_2}^2 - 3r_2 r_3 \cos\theta_3, \\ c &= 4{r_2}^2 + {r_3}^2 - 4r_2 r_3 \cos\theta_3 - \left(\frac{3kr_2 r_3 \sin\theta_3}{2\pi}\right)^2. \end{aligned} \quad (2.21)$$

We now introduce the invariants (Gibson, 2003) which, when suitably combined in the manner described below, categorise the type of conic:

$$\Delta = \begin{vmatrix} a & h & g \\ h & b & f \\ g & f & c \end{vmatrix}, \qquad \delta = \begin{vmatrix} a & h \\ h & b \end{vmatrix}, \qquad \tau = a + b. \quad (2.22)$$

Substituting Eqs (2.21) into Eqs (2.22) and evaluating gives

$$\Delta = -\left(\frac{27k}{2\pi}\left(r_2 r_3 \sin\theta_3\right)^2\right)^2, \quad \delta = \left(9r_2 r_3 \sin\theta_3\right)^2, \quad \tau = 9\left({r_2}^2 + {r_3}^2\right). \quad (2.23)$$

In order for Eq. (2.20) to correspond to an ellipse, the discriminant conditions $\Delta \neq 0$, $\delta > 0$ and $\Delta/\tau < 0$ must be satisfied. These three conditions are met when: (i) $r_2, r_3 \neq 0$, and (ii) $\theta_3 \neq p\pi$, $p \in \mathbb{Z}$. This will always be true for non-collinear arrangements of three distinct sources. Since the area of the corresponding ellipse is finite, for three non-collinear sources each of which are separated by a finite distance, we have a finite number of vortices labelled by the integer pairs (m, n) obeying Eq. (2.19).

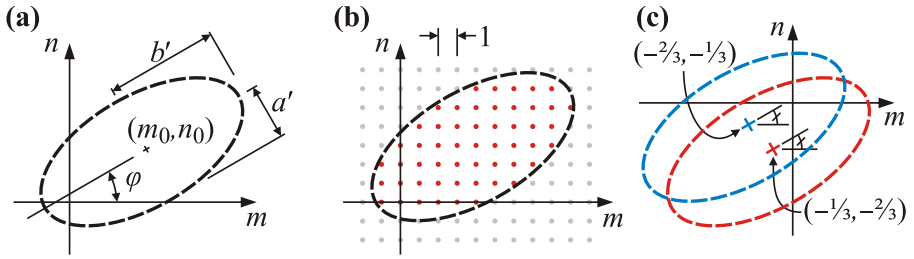

Figure 2.5: There are two parameter-space ellipses in the (m, n) plane. These set upper limits on the number of vortices that are created by the interfering radiation from three point sources. (a) Each bounding ellipse has centre (m_0, n_0), makes an angle φ to the positive m-axis and has semi-axis lengths a' and b'. (b) The enclosed (m, n) pairs lie on a discrete square lattice of unit spacing. Each of these interior (red) points maps to a vortex location. (c) The ellipses differ only by location. Vortices corresponding to the red ellipse are of complementary charge to those of the blue ellipse.

We now consider vortices v_2 corresponding to the substitutions $M(m) \to K(m)$ and $N(n) \to L(n)$ in Eq. (2.19). Upon making these substitutions, the coefficients in Eq. (2.21) become

$$\begin{aligned} a &= 9{r_3}^2, \qquad h = -9r_2r_3\cos\theta_3, \qquad b = 9{r_2}^2, \\ g &= 6{r_3}^2 - 3r_2r_3\cos\theta_3, \qquad f = 3{r_2}^2 - 6r_2r_3\cos\theta_3, \\ c &= {r_2}^2 + 4{r_3}^2 - 4r_2r_3\cos\theta_3 - \left(\frac{3kr_2r_3\sin\theta_3}{2\pi}\right)^2, \end{aligned} \tag{2.24}$$

thus remaining largely unchanged; the exceptions being that the factors in g and f have exchanged places and the factor 4 in c has moved from multiplying ${r_2}^2$ to ${r_3}^2$. The invariants Δ, δ and τ remain unchanged.

The parameter-space ellipse has centre (m_0, n_0), is rotated anti-clockwise at an angle φ, and has semi-axis lengths a' and b' (Fig. 2.5). These ellipse parameters are given by well known expressions in terms of the coefficients in Eq. (2.21) (Gibson, 2003). The centres are given by

$$(m_0, n_0) = \left(\frac{bg - hf}{h^2 - ab}, \frac{af - hg}{h^2 - ab}\right) = \begin{cases} \left(-\frac{1}{3}, -\frac{2}{3}\right), & \text{for vortices } v_1, \\ \left(-\frac{2}{3}, -\frac{1}{3}\right), & \text{for vortices } v_2, \end{cases} \tag{2.25}$$

and the rotation angle, which is shared by both ellipses, is

$$\varphi = \frac{1}{2}\operatorname{arccot}\left(\frac{b-a}{2h}\right) = \frac{1}{2}\operatorname{arccot}\left(\frac{{r_3}^2 - {r_2}^2}{2r_2r_3\cos\theta_3}\right). \tag{2.26}$$

In §2.3.2 we chose to match m with r_2 and n with r_3. This choice has led to a parameter space description of a single lattice of points but two similar ellipses

differing only in the location of their centres. The points enclosed in one ellipse map to vortices and the points in the other map to antivortices. Had the m and n indices been associated with a particular phasor triangle vertex, the parameter space representation would instead have contained two lattices and a single ellipse. From this point in the discussion, we will refer only to the ellipse centred at $(-\frac{1}{3}, -\frac{2}{3})$, with the implicit understanding that a second ellipse exists, centred at $(-\frac{2}{3}, -\frac{1}{3})$, associated with vortices of complementary charge.

The semi-axis lengths $a' \equiv s_+$ and $b' \equiv s_-$ are given by

$$s_\pm = \sqrt{\left|\frac{\Delta}{\lambda_\pm \delta}\right|}, \tag{2.27}$$

where $\lambda_\pm$ denotes the two solutions to the quadratic

$$\lambda^2 - \tau\lambda + \delta = 0. \tag{2.28}$$

Thus

$$\lambda_\pm = \frac{9}{2}\left(r_2{}^2 + r_3{}^2 \pm \sqrt{\left(2r_2r_3\cos\theta_3\right)^2 + \left(r_2{}^2 - r_3{}^2\right)^2}\right), \tag{2.29}$$

so that the semi-axis lengths are

$$s_\pm = \frac{|kr_2r_3\sin\theta_3|}{\pi\sqrt{2\left|\sqrt{\left(2r_2r_3\cos\theta_3\right)^2 + \left(r_2{}^2 - r_3{}^2\right)^2} \pm \left(r_2{}^2 + r_3{}^2\right)\right|}}. \tag{2.30}$$

For fixed k, r_2, and r_3, and variable θ_3, Eqs (2.25), (2.26) and (2.30) define a family of ellipses. A *bounding rectangle* may be constructed, as the envelope of this continuum of ellipses. Any one ellipse in this family, corresponding to a particular value of θ_3, touches each side of this bounding rectangle exactly once. The bounding rectangle is centred at (m_0, n_0), and has dimensions of kr_2/π and kr_3/π in the m and n directions, respectively. [Note that these dimensions are found by setting $\theta_3 = \pi/2$ in Eq. (2.30).] Thus the ellipses scale with r_2 along the m direction and with r_3 along the n direction. As θ_3 is varied from 0 to π, while keeping k, r_2, and r_3 fixed, the parameter-space ellipse transforms from: (i) a line identified with the positive-gradient diagonal to the bounding rectangle, to (ii) a series of non-degenerate ellipses, each of which touch each side of the bounding rectangle exactly once, to (iii) the negative-gradient diagonal to the bounding rectangle. Note that no vortices are produced in the limiting cases (i) and (iii) above, since the open region bounded by a straight line is an empty set [cf. Eq. (2.19)]. The change in shape of the ellipse with θ_3 is symmetric about $\theta_3 = \pi$ [corresponding to case (iii)], so that the ellipse for $\theta_3 = \pi - \xi$ is coincident with that for $\pi + \xi$, for any angle ξ.

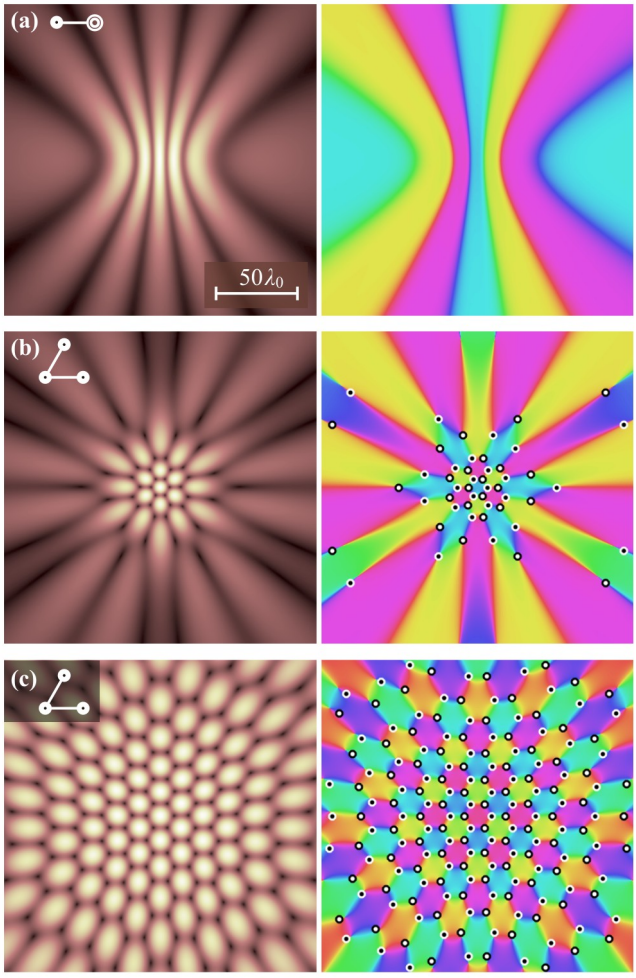

Figure 2.6: Amplitude $|\Psi|$ and associated phase χ from Eq. (2.2) at $z_0=25\lambda_0$ with different source arrangements, shown in insets alongside the figure labels. Small circles overlaid on numerical simulations show the vortex locations as approximated by Eqs (2.13) and (2.17). Amplitude is represented by linear levels from dark to light (0 to maximum). All sources are in phase (i.e. $\phi_2=\phi_3=0$), and the source arrangements are: (a) $\lambda_0=\pi$, $r_2=r_3=3\lambda_0$, $\theta_3=0°$, (b) $\lambda_0=\pi$, $r_2=r_3=3\lambda_0$, $\theta_3=60°$, (c) $\lambda_0=4\pi$, $r_2=r_3=8\lambda_0$, $\theta_3=60°$. Note that a spherical background has been subtracted from all phase maps, as described in the main text.

Figures 2.6 and 2.7 present simulations with various source geometries showing predicted vortex locations for the far-field case. The corresponding parameter space ellipses are shown in Fig. 2.8. The fields of view of the intensity and phase plots do not show the outermost vortex cores in some cases. This is evident from a count of the lattice points enclosed by the corresponding ellipse in Fig. 2.8. Figure 2.7(b) and 2.7(f) have vortices outside the visible region.

Note that, to aid visualisation in all of the phase plots in Figs 2.6 and 2.7, a

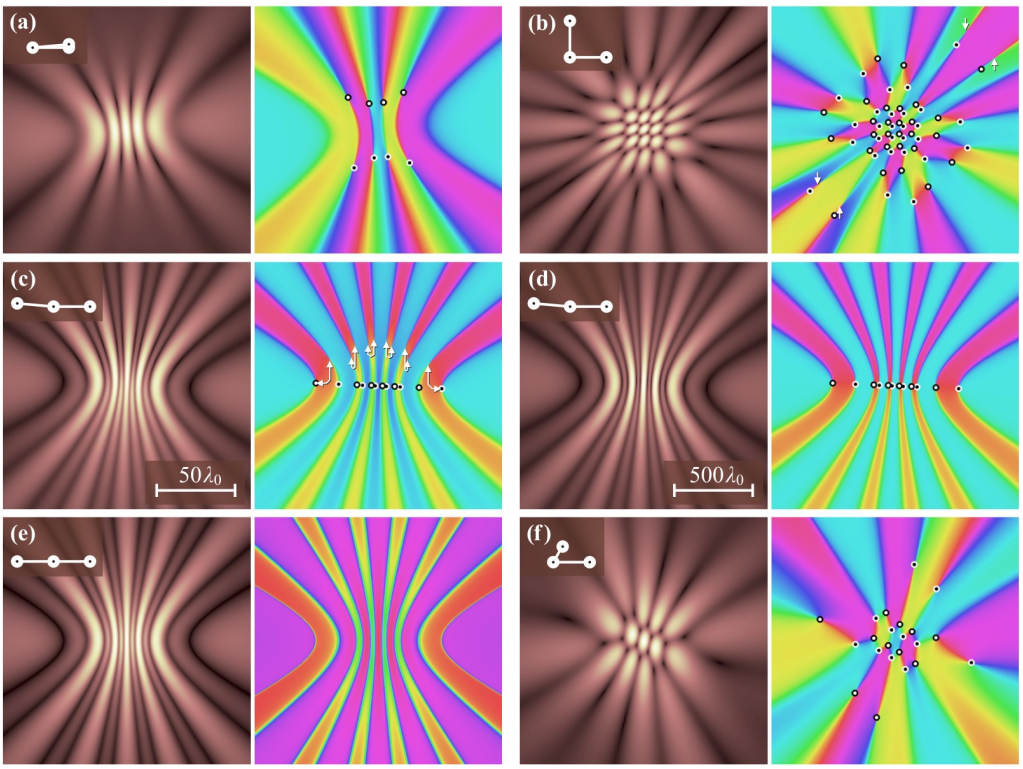

Figure 2.7: Amplitude $|\Psi|$ and phase χ from Eq. (2.2) and vortex-core locations approximated by Eqs (2.13) and (2.17), with variation in source arrangement. The representation and parameters are as described in Fig. 2.6. The scale-bar in (c) applies to all images and corresponds to z_0=25λ_0, except for (d) which corresponds to z_0=250λ_0. Small arrows in (b,c) point to the exact vortex locations, to indicate their deviation from the far-field predictions. λ_0=π and source arrangements are: (a) r_2=r_3=3λ_0, θ_3=10°, (b) r_2=r_3=3λ_0, θ_3=90°, (c) r_2=r_3=3λ_0, θ_3=175°, (d) r_2=r_3=3λ_0, θ_3=175°, z_0=250λ_0, (e) r_2=r_3=3λ_0, θ_3=180°, (f) r_2=3λ_0, r_3=1.5λ_0, θ_3=60°. A spherical background has been subtracted from all phase maps (see main text).

constant spherical background has been subtracted. Indeed, far from the three point sources, one may meaningfully write the wavefunction as a single expanding "background" spherical wave, multiplied by an envelope whose functional form depends on the particular local arrangement of the sources. The envelope will contain all the information about any vortical structure. By subtracting the phase of this spherical background from all of the displayed phase maps, the structure of the envelope alone may be examined, without the distraction of a large number of concentric phase contours from the background wave.[3] Such phase contours may generate moiré artefacts depending on the sampling resolution of the image screen.

[3]This idea is applied in Chap. 3 where a Gaussian envelope is subtracted from a Gaussian beam wavefront.

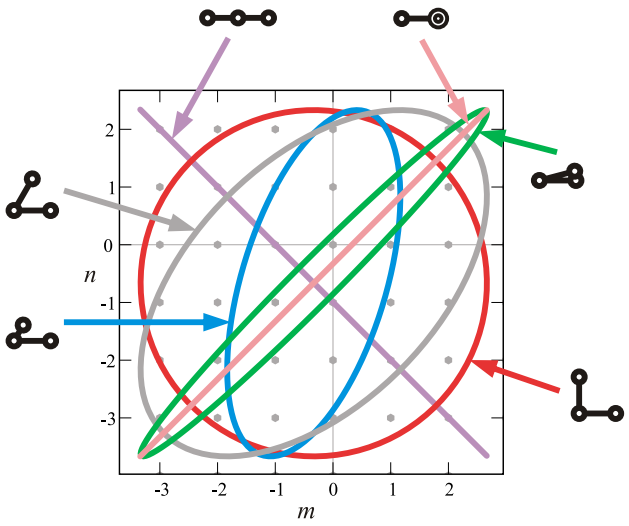

Figure 2.8: Parameter space ellipses corresponding to Figs 2.6 and 2.7 [not including 2.6(c) and 2.7(c,d)]. The enclosed lattice points and ellipses map to vortex locations. A second set of ellipses (not shown), obtained by translating the ellipse centres from $(-\frac{1}{3}, -\frac{2}{3})$ to $(-\frac{2}{3}, -\frac{1}{3})$, yields solutions for vortices of opposite charge (cf. Fig. 2.5). Here, the lattice is not translated (cf. §2.3.5), corresponding to relative phases $\phi_2 = \phi_3 = 0$.

Removing the background phase envelope continuously deforms the field, leaving the locations of topological defects unchanged, and allows the numerical detection of vortices from phase data to be performed more simply over the deformed 2D field, rather than in 3D. Note also that this background spherical wave corresponds to an effective source located at the geometric centroid of the real sources, with amplitude $A = A_1 + A_2 + A_3$ (see Appendix B).

Figure 2.6(a) exhibits a degenerate case in which two of the point sources are co-located, thereby reducing the system to two in-phase spherical sources with one having twice the amplitude of the other. As expected for only two sources, no vortices are generated. Rather, one has a series of Young-type fringes. As mentioned in the introduction to this chapter, only in the case where two sources have equal amplitude and their phase differs by π can a true domain wall be produced. This case can only arise if one allows the source amplitudes to vary. Then by setting the amplitude of one source equal to the sum of the other two (i.e., $A_1 = A_2 + A_3$), and setting the phase of the former such that it differs from the other two by π, so that $\phi_1 \pm \pi = \phi_2 = \phi_3$, we reproduce the two-pinhole Young's interferometer case which produces a single vortex sheet.

In Figs 2.6(b) and 2.6(c), the sources are arranged at the corners of an equilateral triangle. A radially distorted honeycomb vortex-antivortex lattice results. As the

wavelength is decreased compared to the source spacing, the lattice becomes more regular close to the axis through the source centroid. In the asymptotic limits of large spacing or small wavelength, corresponding to many practical optical systems, the regular lattice of the three plane wave case will result.

In Fig. 2.6(a), the phase is not left-right mirror symmetric, due to the positioning of the geometric centroid for three sources being to the right of centre. Thus, there is a global tilt to the phase, which is observed to cycle through two branch-cuts. For this example, the parameter-space ellipse in Fig. 2.8 is the limiting case of a line at 45°. The complementary limiting case is Fig. 2.7(e), where the three sources are collinear; the ellipse in Fig. 2.8 is the line at −45° and again no vortices are generated in the far field. We will see later (in §2.3.10) that vortices are generated in the near field. The phase in Figs 2.6(a–c) and Figs 2.7(a–e) is nevertheless mirror symmetric, since in each of these cases: (i) the initial field configuration is mirror symmetric, and (ii) the wavefield propagator is rotationally symmetric. The mirror symmetry plane is shared between the sources and the resulting phase map; it passes through source r_1 and bisects sources r_2 and r_3; in Fig. 2.6(a) it lies horizontally.

In Fig. 2.7(a), where $\theta_3 = 10°$, one of the sources has been moved just enough from coincidence with another so that the corresponding ellipse just encompasses some lattice points and vortices are created. There are four points clearly within the ellipse, giving rise to the vortices seen in the panel. If the additional two points near the boundary are just inside the ellipse, more vortices will be present at large $r_\perp$ and these will lie at the other ends of the branch-cut lines; otherwise the branch-cut lines will extend to infinity. Figure 2.7(b) shows the case for $\theta_3 = 90°$, giving a circle in parameter space. The number of vortices will therefore be close to the maximum for fixed values of r_2 and r_3.

The far-field solution is usually considered valid for a Fresnel number $N_F \equiv a^2/\lambda_0 z \ll 1$, where a is the largest transverse length scale present in the system (see, e.g., Paganin, 2006). We take this to be the maximum pinhole–pinhole spacing. The far-field condition corresponding to Fig. 2.6 is then $(3\lambda_0)^2/\lambda_0 z \ll 1$ or, including an extra order-of-magnitude factor to establish the condition with increased confidence, $z > 100\lambda_0$. The value of z_0 for numerical simulations in Fig. 2.7 was deliberately chosen as $25\lambda_0$ to show up visual disagreements between the vortices in the numerically determined phase map and their analytically determined locations. Small arrows illustrate the true locations of some vortices, which do not coincide with their predicted far-field positions. The discrepancy between numerical and analytical results is highlighted in Fig. 2.7(c), corresponding to all parameter space lattice points lying close to the ellipse boundary. In Fig. 2.7(d), the Fresnel number

is smaller and the correspondence is improved because the observation is being made further into the far field, where nodal lines have asymptotically approached closer to the straight lines predicted in §2.3.3. Note that, for any finite z_0, there will be some angle θ_3, close to π, at which the numerical and analytical prediction disagree by an arbitrarily large amount. Predictions are more reliable for (m, n) lattice points closer to the ellipse centre. In contrast with the far-field prediction that vortices may abruptly appear and disappear with infinitesimal changes in source arrangement as lattice points cross the ellipse boundary, we observe through simulations at finite z_0, that the vortex location becomes highly sensitive to source arrangement, with vortices arriving from and escaping transversely to an infinite $r_\perp$ distance.

2.3.5 Source phase variation

We now consider the effects of source phase variation on the geometric parameter space description. The functions $M(m)$, $N(n)$, $K(m)$, and $L(n)$ [Eqs (2.10) and (2.18)] contain the dependence of the vortex coordinates on source phase via Eqs (2.13) and (2.17), where ϕ_j is the relative phase of the jth source and $\phi_1 = 0$. We see that a 2π change in relative phases ϕ_2 or ϕ_3 may be absorbed as an integer change in an associated parameter-space coordinate m or n, respectively. By allowing the lattice point coordinates to correspond to discrete real values, spaced at intervals of 2π, the coordinates specified by m and n may then also absorb fractional parts of the relative phase. Variation of the phase ϕ_2 or ϕ_3 corresponds to subtraction of a value from m or n, respectively. This in turn corresponds geometrically to a translation of the (m, n) lattice points along the associated axis, with a relative phase change of 2π effecting a translation of one lattice unit.

In summary, parameters defining the source configuration or the wave-number map to the parameter space as different ellipse constructions, whereas source phase variations correspond to translations of the lattice itself.

2.3.6 Estimate of number of vortices

In contrast to the case of three interfering plane waves reviewed in §1.5, in which infinitely many nodal lines are produced, the analysis of the preceding sub-sections demonstrated that only a finite number of vortices are produced by three overlapping spherical waves, provided that there is a finite spacing between the three corresponding point sources. Here, a simple means is presented of estimating the number of vortices over a given plane in the far field, as a function of the geometry of the three point sources.

Because the m and n values have unit spacing [see Fig. 2.5(b)], the number of vortices n_v may be approximated by the sum of the two ellipse areas, or twice the area $\pi a' b'$ of one ellipse. Thus

$$n_v \approx 2\pi a' b', \tag{2.31}$$

or

$$n_v \approx \frac{k^2}{2\pi}\left|r_2 r_3 \sin\theta_3\right| = \frac{k^2\mathcal{A}}{\pi} = \frac{4\pi\mathcal{A}}{\lambda^2}, \tag{2.32}$$

where $\mathcal{A}$ is the area of a triangle whose vertices coincide with the locations of the three point sources, and $\lambda = 2\pi/k$.

Gabor's measure for the information capacity of a beam

Remarkably, the result for the vortex number [Eq. (2.32)] is exactly the expression $N = \mathcal{A}\Omega/\lambda^2$ found by Gabor (1969), and attributed (though left uncited) by him as a re-statement of an earlier result of Max von Laue, for the degrees of freedom N (a measure of the information carrying capacity) of a light beam of area $\mathcal{A}$. Here Ω is the solid angle of any beamlet, equal to 2π, corresponding to a forward propagating spherical wavefront. If we assume that $\phi_2 = \phi_3 = 0$, our system has a zero net topological charge, and the number of vortices and antivortices must be equal. In this case, the two similar ellipses, corresponding to vortices and antivortices, contain equal numbers of lattice points. Because the number of vortices and antivortices is forced to be equal, the degrees of freedom correspond to the number of vortices or antivortices, not to both; hence $N = n_v/2$. Correspondingly, $\mathcal{A}$ is found to be the area of the triangle whose vertices coincide with the pinholes. Although it is unlikely to be a coincidence, the connection to Gabor's measure remains unclear, particularly as it refers to transmissible beam modes through an aperture and not to defects.

Relation to circle-lattice problems in number theory

One may ask whether it is possible to develop an exact expression for the number of lattice points enclosed by our parameter-space ellipse, thereby improving on the approximation for n_v given in Eq. (2.32). Indeed, this question is a generalisation of a famous problem in number theory known as *Gauss's circle problem*. With $\phi_2 = 2\pi/3$, $\phi_3 = -2\pi/3$ and $\theta_3 = \pi/2$, the conditions corresponding to the common form of Gauss's circle problem are established; the circle is a degenerate ellipse and is centred on a lattice point. The resulting solution for this case is both involved and well known, and so will not be given here (see, e.g., Andrews, 1994). It incorporates

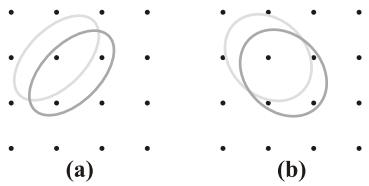

Figure 2.9: Illustration of ellipses for source configurations corresponding to the generation of (a) one central antivortex surrounded symmetrically by three vortices, and (b) one central antivortex surrounded by four vortices.

a function which has no simple solution and remains a topic of research in number theory. Furthermore, Gauss's circle problem has been studied for certain ellipses, particularly where the ellipse remains centred on a lattice point and its axes are aligned with the lattice. The degree to which the approximate expression Eq. (2.32) is an estimate of both the information capacity and the number of vortices is also addressed in studies of Gauss's circle problem which concentrate on its asymptotic behaviour with increasing circle radius.

Steinhaus proved that a circle may always be constructed that contains exactly $p \in \mathbb{Z}$ points of an integer lattice (Schumer, 2004, Chap. 12). Since we have control over the circle centre by varying the source phases, and control over the circle size by varying the source spacing or wavenumber, we may interpret this as saying that it is in theory always possible to produce a specified number of vortices (or antivortices) for pinhole sources at three corners of a square, by judicious choice of source spacing $r_2 = r_3$ or wavenumber k, and relative source phases ϕ_2, ϕ_3.

A natural question then arises of what constraints exist between the number of vortices and antivortices in general. To answer this question is difficult, requiring generalisation to arbitrary ellipses of both Steinhaus's theorem and of the asymptotic behaviour of Gauss's circle problem, and furthermore to the constraints that exist between two ellipses with given relative positions. As shown in the examples in Fig. 2.9, it is possible to construct parameter space configurations where, for an ellipse containing p points (producing p vortices) the corresponding second ellipse contains $p + j$, $j \in \{-3, -1, \cdots, +3\}$ points, corresponding to $p + j$ antivortices. Whether the number of vortices and antivortices may differ by $|j| > 3$ remains an open question requiring further research.

2.3.7 Vortex trajectories from phase variation

In most of the preceding discussion, the relative source phases ϕ_2 and ϕ_3 were set to zero. Here, we consider how vortices move along certain curves in response to varying these phases one at a time.

The equations of these curves are found by eliminating the phase ϕ_j corresponding to the source r_j in Eqs (2.13) and (2.17). For example, the vortex trajectories for variation of source r_2 are found by solving Eq. (2.13) for ϕ_2 and substituting this into Eq. (2.17).[4] Repeating this for ϕ_3 gives a second set of trajectories along which the vortices move with ϕ_3 variation. This analysis was performed with the aid of a computer algebra system, resulting in the equations

$$r_{\perp m} = \frac{M(m)\, z_0}{\sqrt{(3kr_2 \cos\theta_m)^2 - M(m)^2}}, \tag{2.33a}$$

and

$$r_{\perp n} = \frac{N(n)\, z_0}{\sqrt{[3kr_3 \cos(\theta_n - \theta_3)]^2 - N(n)^2}}, \tag{2.33b}$$

with associated forms containing $K(m)$ and $L(n)$, where the subscripts mn have been changed to m or n to highlight the independence of the equations with respect to the complementary parameter space coordinate.

We have seen (§2.3.5) that variation of ϕ_2 (or ϕ_3) corresponds to a translation of the m (or n) lattice alone. Thus, our choice to eliminate the respective phase has led to the separation of the m and n dependence. The equations describe hyperbolas, where the polar coordinate system origin is centred between the two hyperbola branches.[5] Note that this polar form is less common than that typically seen in the study of conics, in which the origin is placed at the focus of one branch. Equations (2.33) may be thought of as a (one-to-many) mapping from lines of constant m or n in parameter space to hyperbolas in real space. Figure 2.10 shows an example of the trajectories overlaying the results from a numerical simulation for the source arrangement seen in Fig. 2.7(f).

Fixing the source phases defines particular hyperbolas corresponding to the parameter space coordinates m and n, respectively, with vortices located at the intersections of an m and an n curve. Vortices are observed to lie at the intersection of $M(m)$ and $N(n)$ curves, and antivortices at the intersection of $K(m)$ and $L(n)$ curves for $\theta_3 \in (0, \pi)$, or antivortices and vortices respectively for $\theta_3 \in (\pi, 2\pi)$.

[4] The term "vortex trajectory" has sometimes been applied in the singular optics literature as a synonym for "nodal line geometry" [see, e.g., Freund (2000), and Soskin and Vasnetsov (2001)]. This usage is contentious because the term "trajectory" is not being used to describe any spatiotemporal variation (motion) of an object, which is the usual implication. Our use of the term "vortex trajectory" refers to the motion of a vortex and its associated nodal line structure in response to a continuous change in source phase, which is assumed to occur over some unspecified timescale. In particular, we consider the motion of vortices across a 2D image plane in response to the continuous variation of phase of one of the spherical sources. As time does not explicitly arise in our description, we should arguably speak of vortex paths here, rather than trajectories.

[5] Menaechmus (380 BC–320 BC) is believed to be the original discoverer of the conics. We use the later description in terms of a focus (point) and directrix (line), believed to be due to Aristaeus the Elder (c370 BC–c300 BC). (Heath, 1896).

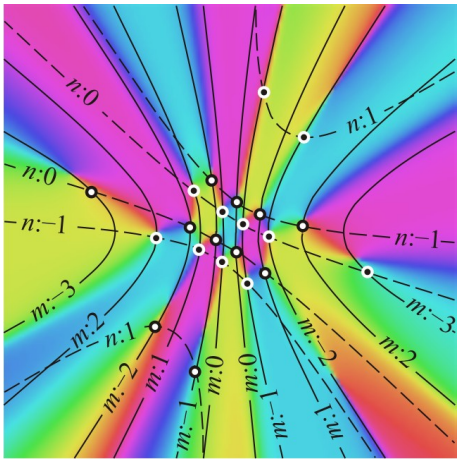

Figure 2.10: Vortices lie at the intersections of the negative branches of two independent sets of hyperbolas and travel along these curves as source phase is varied. Two independent phases give rise to two sets of hyperbolas indexed by m (solid lines) and n (dashed lines). The trajectories shown correspond to varying the phase of one source with the others set to 0. The hyperbolas are shown overlaying the phase χ from Eq. (2.5) with source parameters the same as in Fig. 2.7(f).

The angle θ_3 in Eq. (2.33b) corresponds to the rotation of the n-indexed hyperbola axes with respect to the coordinate system axes. The square-root-operation limits the range of real solutions, hence the number of hyperbolas and the number of vortices. The domain of the parameter-space variable m (or n) is restricted to match that determined by the corresponding ellipse. Thus these equations may be applied to determine the valid domains of m or n independently, without recourse to the ellipse solution.

It turns out that physical solutions only lie at the intersection of negative hyperbola branches. The negative branch may be parameterised in Cartesian coordinates (x, y), via the parameter $t \in (-\pi, \pi)$, as (Gibson, 2003)

$$\begin{aligned} x &= -a \cosh t, \\ y &= b \sinh t. \end{aligned} \tag{2.34}$$

The parameters a and b are found by first squaring Eq. (2.33a) and identifying this with the canonical polar form of the hyperbola:

$$r^2 = \frac{a^2 b^2}{b^2 \cos^2\theta - a^2 \sin^2\theta} \equiv \frac{a^2 b^2}{(a^2 + b^2)\cos^2\theta - a^2}. \tag{2.35}$$

Doing so we find that $b \equiv z_0$. Vortices lie at the intersection of an m and an n

curve, i.e. either curves for which

$$a \equiv \begin{cases} \dfrac{M(m)z_0}{\sqrt{(3kr_2)^2 - M(m)^2}} & \text{nonrotated branch,} \\ \dfrac{N(n)z_0}{\sqrt{(3kr_3)^2 - N(n)^2}} & \text{rotated branch,} \end{cases} \tag{2.36a}$$

or

$$a \equiv \begin{cases} \dfrac{L(m)z_0}{\sqrt{(3kr_2)^2 - L(m)^2}} & \text{nonrotated branch,} \\ \dfrac{K(n)z_0}{\sqrt{(3kr_3)^2 - K(n)^2}} & \text{rotated branch.} \end{cases} \tag{2.36b}$$

Because the parameterisation is given in Cartesian coordinates, the branch solutions involving n are finally obtained by rotating the coordinates through angle θ_3 with the transform $\mathbf{R}(\theta_3)\,\binom{x}{y} \to \binom{x'}{y'}$, or

$$\begin{pmatrix} x' \\ y' \end{pmatrix} = \begin{pmatrix} \cos\theta_3 & -\sin\theta_3 \\ \sin\theta_3 & \cos\theta_3 \end{pmatrix} \begin{pmatrix} x \\ y \end{pmatrix}. \tag{2.37}$$

The hyperbola equations also describe an intersecting curvilinear coordinate system. The location of a vortex on the phase map may be thought of as addressable by selection of a particular patch having coordinates (m, n) and then finely addressable within that patch by variation of the source phases. Variation of the phases from 0 to 2π shifts the vortices along one of the two families of curvilinear trajectories within the patch (see Fig. 2.11). When there are a large number of vortices present, the patches in the central region of the phase map are correspondingly small. In this case, the vortices shift a small distance with changing phase. In the outer, sparsely populated regions, small changes in phase lead to arbitrarily large distance changes since the outermost patches have boundaries at infinity.

It is not surprising that vortices should lie along intersecting hyperbolas. Two point sources naturally give rise to surfaces of constant phase that are hyperboloids of two sheets having the sources as their foci. The difference in path length being constant establishes the condition for constant phase and is equivalent to the well known geometric construction method for hyperboloids. The intersections of hyperboloids of two sheets with the $z = z_0$ plane will be hyperbolas of two branches. Note that this is merely a plausibility argument as it is the field value and not the phase that must sum to zero at the vortex locations. Most generally, conics describe lines in systems where a relationship exists between a plane and a point. Symmetry planes arise in the three-pinhole interferometer bisecting the source locations, when taken in pairs. The points are the sources themselves. Numerical simulations

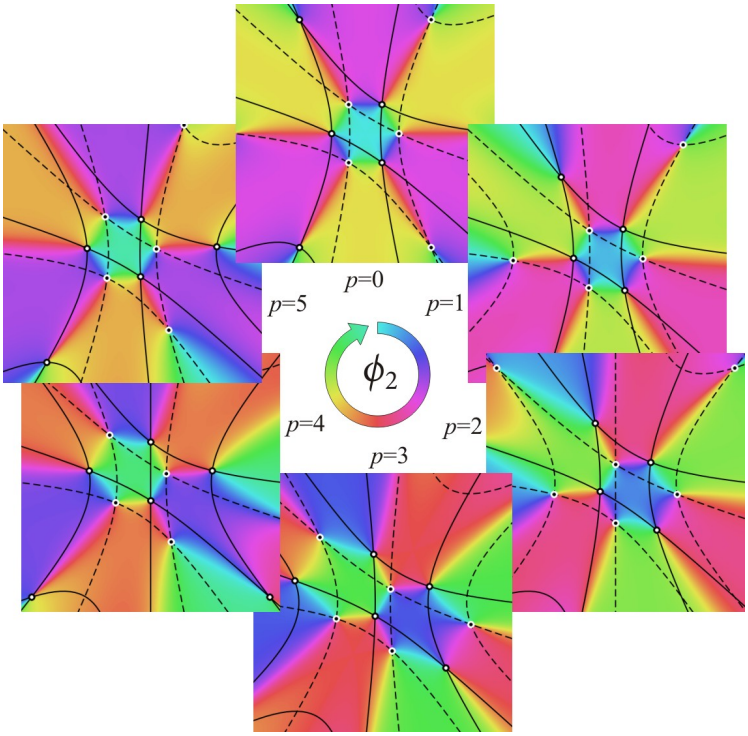

Figure 2.11: Vortex motion along hyperbola trajectories with phase ϕ_2 swept through 2π with snapshots at $p\pi/6, p = 0,1\ldots5$. Here, $r_2 = r_3 = 1.5\lambda_0, \theta_3 = 60°, \phi_3 = 0$. Solid lines correspond to $K(m)$ and $L(n)$ and dashed lines to $M(m)$ and $N(n)$.

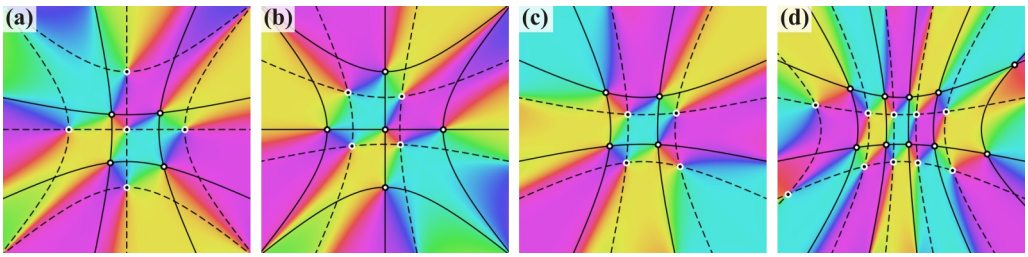

Figure 2.12: Hyperbolas for $\theta_3 = 90°$. (a) $r_2 = r_3 = 1.5\lambda_0, \phi_2 = 2\pi/3, \phi_3 = 4\pi/3$, (b) $r_2{=}r_3{=}1.5\lambda_0, \phi_2{=}4\pi/3, \phi_3{=}2\pi/3$, (c) $r_2{=}r_3{=}1.5\lambda_0, \phi_2{=}\phi_3{=}0$, (d) $r_2{=}3\lambda_0, r_3 = 1.5\lambda_0, \phi_2{=}\phi_3{=}0$. Solid lines correspond to $K(m)$ and $L(n)$ and dashed lines to $M(m)$ and $N(n)$.

of the two-pinhole interferometer show that, even if the source amplitudes are allowed to vary, a bisecting plane of constant phase still arises.

Figure 2.12 shows some typical examples of trajectories for the case of $\theta_3 = 90°$. In Figs 2.12(a) and 2.12(b), the source phases have been chosen such that a vortex and antivortex, respectively, is centrally placed, with the constituent hyperbolas being straight lines. This corresponds to the parameter-space lattice being centred

on each of the parameter-space ellipses in turn. In Figs 2.12(c) and 2.12(d) the phases are all zero, with Fig. 2.12(c) showing the symmetric case where $r_2 = r_3$. In Fig. 2.12(d), r_2 has been doubled, with a corresponding compression by one half in the m-indexed coordinate system and associated doubling along the m axis of the parameter-space ellipse.

2.3.8 The parameter space near collinearity

Here we examine the behaviour of the nodal lines in the far field as θ_3 approaches π (three collinear sources) when $\phi_2 = \phi_3 = 0$, since we observe a marked deviation between numerical simulation and analytical results in this regime [see Fig. 2.7(c), which clearly illustrates this discrepancy].

An analysis around $\theta_3 = \pi$ may be performed by substituting $\theta_3 = \pi + \varepsilon$ into Eq. (2.12), where ε is small:

$$\frac{r_3}{r_2}\Big(\cos(\pi+\varepsilon) + \tan\theta\sin(\pi+\varepsilon)\Big) = \frac{N(n)}{M(m)}. \tag{2.38}$$

Applying the small-angle approximations $\cos\varepsilon \sim 1$, $\sin\varepsilon \sim \varepsilon$, Eq. (2.38) yields

$$\tan\theta_{mn} = \frac{1}{\varepsilon}\left(\frac{r_2}{r_3}\frac{N(n)}{M(m)} + 1\right) \tag{2.39}$$

for the θ_{mn} coordinate of the vortex core. Substituting into Eq. (2.15) and applying Eq. (2.16) gives $r_{\perp mn}$ for our special case

$${r_{\perp mn}}^2 = \frac{{z_0}^2}{\left(\dfrac{3kr_2}{M(m)}\right)^2 \dfrac{1}{1+\tan^2\theta_{mn}} - 1}. \tag{2.40}$$

Finally, substituting Eq. (2.39), we get

$$r_{\perp mn} = \pm\frac{z_0}{\sqrt{\dfrac{\left(3kr_2/M(m)\right)^2}{1+\dfrac{1}{\varepsilon^2}\left(\dfrac{r_2}{r_3}\dfrac{N(n)}{M(m)}+1\right)^2} - 1}}. \tag{2.41}$$

In the limit $\varepsilon \to 0$, we now see that $\theta_{mn} \to \pi/2$ and $r_{\perp mn} \to \mp i z_0$. Regarding the latter limit, $r_{\perp mn}$ first approaches infinity and then becomes imaginary.

We may widen the context of this result by realizing that it is but one example of a lattice point crossing an ellipse boundary. Whenever this occurs, the far-field prediction is that associated vortices will be created or destroyed instantaneously. In contrast, in numerical simulations, which are at some finite distance from the source, vortices rapidly enter from or escape to infinity.

2.3.9 Relation to the Young's three-pinhole interferometer

Here we show how to map the far-field results for three spherical point sources onto a three-pinhole Young's interferometer. In this interferometer, coherent radiation illuminates a black screen that is punctured with three small pinholes, with the resulting transmitted radiation being observed at a distance that is large compared to the spacing between the pinholes (see Fig. 2.2). Note that the assumptions of equal amplitude and a single wave-number, applied in Eq. (2.5), correspond to uniform coherent illumination of the screen. The following argument is based on the Rayleigh–Sommerfeld diffraction theory (see, e.g., Born and Wolf, 1999).

The Rayleigh–Sommerfeld diffraction integral of the first kind yields a rigorous solution to the Helmholtz equation (time-independent free-space Schrödinger equation) in a vacuum-filled half-space, for a field that obeys the Sommerfeld radiation condition. For a field $U^{(i)}$ incident on an aperture $\mathcal{A}$ centred on the plane $z = 0$, the wavefunction U may be determined at an arbitrary point (x, y, z) in the half-space $z \geq 0$. With the boundary conditions that $U(x, y, z = 0) \approx U^{(i)}(x, y, z = 0)$ when $(x, y, z = 0)$ is in $\mathcal{A}$, and $U(x, y, z = 0) \approx 0$ when $(x, y, z = 0)$ is not in $\mathcal{A}$, the diffraction integral is:

$$U(x, y, z) = \iint_{\mathcal{A}} U^{(i)}(x', y', 0)\, K(x, y, x', y')\, dx'dy', \tag{2.42}$$

where

$$K \equiv \frac{1}{2\pi}\frac{\partial}{\partial z}\left(\frac{\exp(ikr)}{r}\right) \tag{2.43}$$

is the corresponding propagator and $r = \sqrt{(x - x')^2 + (y - y')^2 + z^2}$. Evaluation of the derivative gives

$$K = \frac{1}{2\pi}\frac{z}{r}\left(\frac{ik}{r} - \frac{1}{r^2}\right)\exp(ikr)\,. \tag{2.44}$$

For a pinhole aperture, $U^{(i)} \approx \delta(x - x', y - y', z)$, and the wavefield $U(x, y, z)$ takes the form of the propagator, Eq. (2.44). In general, the pinhole aperture does not produce spherical waves. However, when the observation point is such that $r \gg \lambda_0$, the first term inside the parentheses dominates the second, giving

$$K \approx \frac{ikz}{2\pi r^2}\exp(ikr)\,. \tag{2.45}$$

It can now be seen that Eq. (2.6), which resulted from factoring out a common term of $\exp(ikr)/r$ from the simplified three-spherical-source wavefield, Eq. (2.5), also results if a common term of $ikz\exp(ikr)/2\pi r^2$ is instead factored out from a superposition of three "illuminated pinhole" waves of the form in Eq. (2.45).

Similarly, when one is both in the far field and sufficiently close to the z-axis that the approximation $z \approx r$ holds, Eq. (2.45) reduces to a spherical wavefunction with a constant multiplier, as asserted.

The conclusion is that the analysis of the preceding sections may be mapped onto the case of a Young's three-pinhole interferometer, in the far field.

2.3.10 The three dimensional nodal line structure

As previously mentioned, our far-field analysis implies that the nodal lines, produced by either the superposition of three spherical waves or by coherent illumination of a Young's three-pinhole interferometer, are asymptotically straight [see Eqs (2.13) and (2.17), noting the proportionality of the latter to z_0]. When one is not in the far field the nodal lines are curved. Here, we examine this point in more detail by presenting near-field simulations of the 3D structure of nodal lines in fields produced from the interference of spherical-waves or pinhole-waves, which are described by Eqs (2.1) and (2.44), respectively.

With reference to Fig. 2.13, the nodal line structures are shown within a volume close to the sources and not corresponding to the far field. Here, the relative phases of the three sources have been set to zero. These results are generated by numerically summing the spherical wave or pinhole propagator expressions explicitly and then applying a vortex detection algorithm, as described in Appendix A. The contrast between the simulations, resulting from the differing forms of the source waves, is strikingly apparent. Comparing the positions of the nodal lines between Figs 2.13(c) and (f) as they intersect the volume face at $z_0 = 5.2\lambda_0$, both are asymptotically approaching the same set of straight lines predicted for the far field (§2.3.3). The projection in Fig. 2.13(c) is shown again in (f) within a dashed border to aid visual comparison. In the case of spherical sources, the simulation is over the positive z half-space, on the implicit understanding that the nodal structure is mirror symmetric about the virtual plane in which the sources lie. Figure 2.14 is provided as an example to demonstrate this point. It shows the complete near-field volume $z_0 \in [-5.2\lambda_0, 5.2\lambda_0]$ and is otherwise identical to Fig. 2.13(c). The geometry of the nodal lines is mirror symmetric about the source plane. In contrast, the phase is antisymmetric about this plane so that the sense of the nodal lines does not reverse. To be precise, the phase value at a location $\phi_0^+(x_0, y_0, z_0)$ is related to the phase $\phi_0^-(x_0, y_0, -z_0)$ by symmetry relative to the value $\phi_p(x_p, y_p, 0)$ at a point p in the source plane, since $\phi_0^+ = \phi_p(x_p, y_p, 0) + \Delta\phi$ and $\phi_0^- = \phi_p(x_p, y_p, 0) - \Delta\phi$, hence $\phi_0^+ - \phi_0^- = 2\Delta\phi$. Three general types of nodal lines can be identified; those that pass through the source plane having approached from the far-field, those that

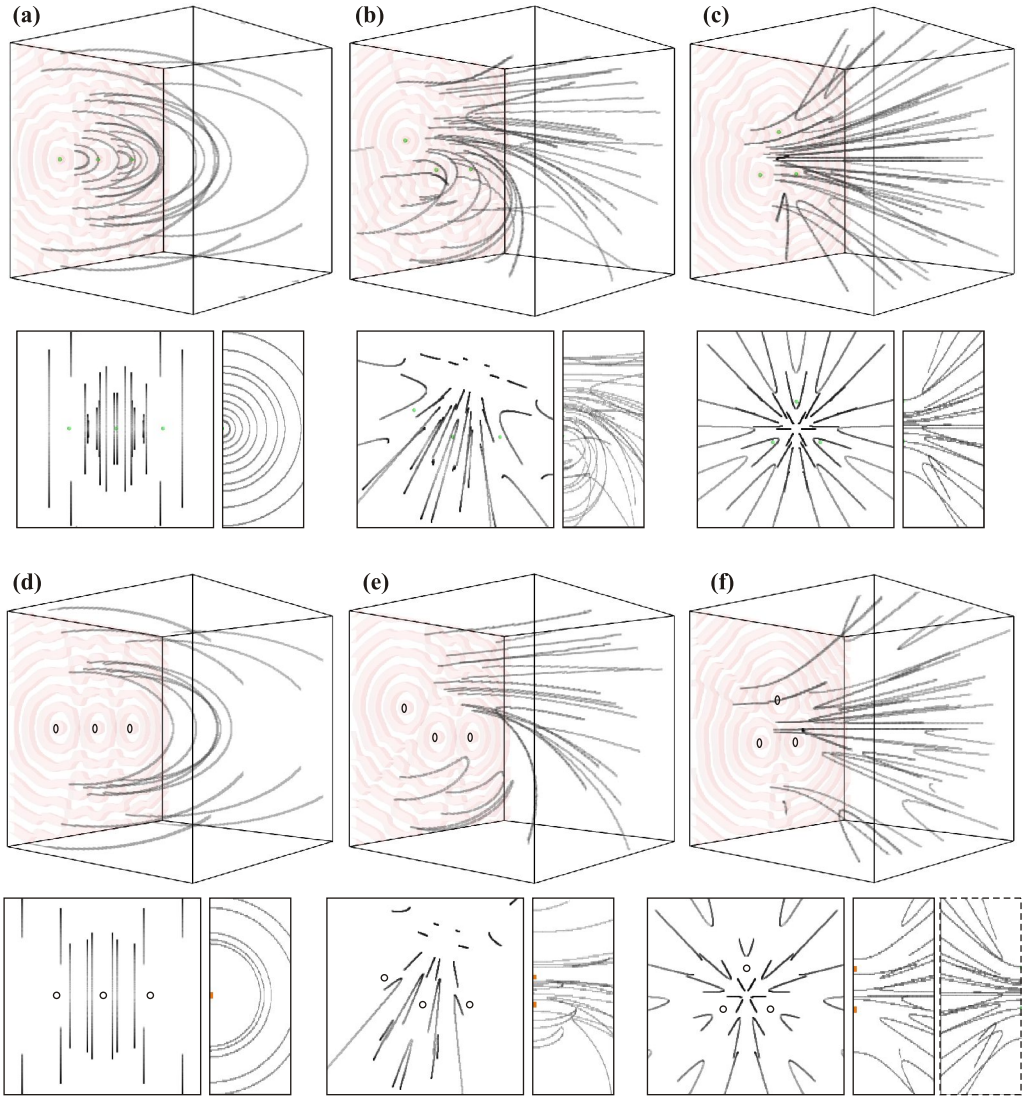

Figure 2.13: Numerically determined nodal line structures arising from different arrangements of three sources in the near-field region, where $z = 0 - 5.2\lambda_0$ for source wavelength $\lambda_0 = \pi$. Note that the scaling in the perspective views is non-uniform $z : xy \approx 3$. The upper series (a–c) are for spherical wave sources, for which the sources define a mirror-symmetry plane that is shown explicitly in Fig. 2.14. The lower series (d–f) are for pinhole sources, for which the waves interfere within a semi-infinite volume. (a,d) Three collinear sources generate circular nodal lines (semicircular for pinholes) centred on the line defined by the sources. (b,e) Three sources with $r_2 = r_3 = 3\lambda_0$, $\theta_3 = 145°$ generate loops, curves extending through the source plane, and hairpins. (c,f) Three sources arranged symmetrically at the corners of an equilateral triangle of side length $r_2 = r_3 = 3\lambda_0$ [cf. Fig. 2.6(b)] generate no loops. In (f) the side projection from (c) is flipped and shown within a dashed border adjacent to the pinhole version to aid visual comparison of the asymptotic nodal line positions, which differ in the near-field structure but converge to the same far-field solution.

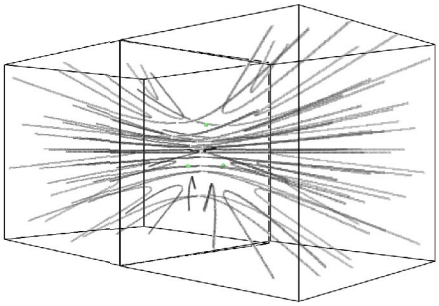

Figure 2.14: Nodal line structures developed by three spherical wave sources in the near-field region $z \in [-5.2\lambda_0, 5.2\lambda_0]$ corresponding to Fig. 2.13(c) showing symmetry of the nodal line structure about the plane defined by the sources.

form loops and pass through the source plane, and those that approach the source plane and without reaching it, retreat again. The latter features, commonly known as *hairpins*, correspond to annihilating vortex/anti-vortex pairs when observed in any plane which is a tangent to the associated nodal line (Berry, 1998); hairpins are well known to exist in fields near focal points (Berry et al., 1979). For the pinhole cases, nodal lines either attach to the source plane or contain a hairpin structure.

As highlighted by the z-projection in Fig. 2.13(b), in all these cases the nodal line structure shares the mirror symmetry of the sources for a symmetry plane that bisects the sources r_2 and r_3. This is related to the phase symmetry that was observed in Fig. 2.7, since $r_2 = r_3$.

Regions devoid of nodal structure arise close to the source plane and near a source, where the intensity from that source dominates the contributions from the others. This may be understood in terms of the phasor diagram in Fig. 1.4(a) as an inability to form a closed triangle. Nodal lines approaching these regions join in hairpins.

Although we have seen that three sources do not form loops in the far field, loops for which the source plane is a mirror plane do form. A special case arises when the sources are collinear and a unique source plane can no longer be identified [Figs 2.13(a, d)]. With an infinite number of equivalent planes intersecting along the line of sources, the field must be cylindrically symmetric. The resulting nodal loops are therefore circles (for spherical sources) or semicircles (for pinholes) centred on the line defined by the sources. The lack of nodal-line loops whose extent lies completely within the open half space $z_0 > 0$ is an indicator that there are three sources. If a fourth source of sufficient intensity was provided, loops could be formed in this region. The condition for the existence of loops depends on the allowed combinations of four phasors arranged tip-to-tail in a closed quadrilateral (O'Holleran et al., 2006). If four plane waves are labelled in order of decreasing

amplitude a_j, such that $a_1 \geq a_2 \geq a_3 \geq a_4$, loops will form iff $a_1 + a_4 > a_2 + a_3$. In contrast to plane waves, the amplitude of spherical and pinhole waves varies with distance from the source; hence the requirement that the phasor amplitudes are labelled in decreasing order means that the phasors must be locally evaluated before being ordered according to the labelling scheme requirements if the condition for the existence of loops is to be valid.

In summary, the 3D nodal line simulations reveal asymptotic behaviour commensurate with the analytically described far-field structure. In regions close to the sources, the simulations display a structure of nodal lines distinguished by the different source descriptions of spherical sources and pinholes.

2.4 Linear interference of Gaussian waves

Having described the vortex structure that arises from the interference of spherical and pinhole waves, we now proceed to the study of the interference of three Gaussian waves. Such a model may be applied to the interference of monochromatic Gaussian beams propagating parallel to a common z-axis or to the superposition of three localised (2+1)D Gaussian matter-wavepackets, that are evolving in time. The exposition here begins by describing and presenting experimental results corresponding to the former case, before proceeding to the latter case, for which an analysis of the vortex structure is provided.

2.4.1 Experimental results

Here we present an analysis of experimental data obtained within the Optics group at The University of Glasgow, showing the interference of three Gaussian beams.[6] For a full description of the experimental setup, see O'Holleran (2008, Chap. 3).

The *Gaussian beam* is commonly used as the simplest model for a laser beam propagating in free space (Guenther, 1990, pp. 336–342). It is a paraxial model in that it satisfies the paraxial wave equation. The model has a Gaussian intensity profile that is mirror-symmetric about the xy-plane, and spreads under propagation along z, thus forming a minimal waist radius at $z = 0$.[7] The wavefunction $\Psi(\mathbf{r}, z)$ in cylindrical coordinates is fully specified at the beam waist by the peak amplitude Ψ_0, wavelength λ (or wavenumber k), and beam waist radius w_0, defined as the radial distance at which the amplitude has fallen to Ψ_0/e. These parameters are combined into the following useful expressions. The *Rayleigh range* $z_R = {w_0}^2 k/2 \equiv \pi {w_0}^2/\lambda$ is

[6] Raw data from experiments by Kevin O'Holleran are used here with his kind permission.
[7] Note that the phase is not mirror symmetric about $z = 0$ due to the Gouy phase term.

the distance at which the beam cross-section is double that at the waist. The *spot size* $w(z) = w_0\sqrt{1 + z^2/{z_R}^2}$ describes the spreading with propagation. The *radius of curvature* of the wavefront is $R(z) = z\,(1 + {z_R}^2/z^2) \equiv z^2 + {z_R}^2/z$. The Gaussian beam is then defined as

$$\Psi(\mathbf{r}, z) = \Psi_0 \frac{w_0}{w(z)} \exp\left(\frac{-|\mathbf{r}|^2}{w^2(z)}\right) \exp\left(\frac{-ik|\mathbf{r}|^2}{2R(z)}\right) \exp\left[i\zeta(z)\right], \tag{2.46}$$

where $\zeta(z) = \arctan(z/z_R)$ is the Gouy phase.

Experimentally, three Gaussian beams $\Psi(\mathbf{r}-\mathbf{r}_j, z)$, $j = 1, 2, 3$, offset from one another but propagating parallel to a common axis, were generated by a holographic technique, using a monochromatically illuminated spatial light modulator (SLM) (O'Holleran, 2008). The beams share a common waist plane and waist radius, hence they have the same Rayleigh range. Servo-controlled mirrors and translation stages allow the measurement of intensity and phase via interference with a reference beam of variable phase. A CCD camera takes the place of a screen over which the intensity and phase are measured. Figure 2.15 shows the measured intensity and phase of the resulting interference pattern $\sum_{j=1,2,3} \Psi(\mathbf{r} - \mathbf{r}_j, z = z_0)$ over a representative plane close to the source end of the z-axis. Also shown is the 3D nodal line structure over a range of z where, to improve clarity, the z-scaling has been compressed. No data were provided of the beam parameters, so these results serve only as qualitative descriptors of the honeycomb vortex-antivortex lattice, which is clearly visible in Fig. 2.15(c). It it also clear in 2.15(d), where the winding sense is identified for an observer facing the source, along with evidence of a radial phase gradient centred toward the top-centre. This may be evidence of the expected gradient due to the Gaussian envelope, which will be discussed in the next section, or of a phase gradient introduced by the phase reference. The usable data corresponds to a range over which the beams had substantially overlapped and interfered. However, hairpin structures facing to the left are visible in the lower part of the 3D data as expected of the growing lattice, which forms as the individual beams expand and interfere. Some looped and random structures are also visible towards the left, indicating that the amplitude of the Gaussians has decreased to the point where contributions from interfering waves, due to experimental imperfections, are of sufficient amplitude to perturb the honeycomb structure.

2.4.2 Gaussian wavepackets

As previously mentioned, the Gaussian interference model applies equally well to the superposition of three localised (2+1)D Gaussian matter-wavepackets, that are

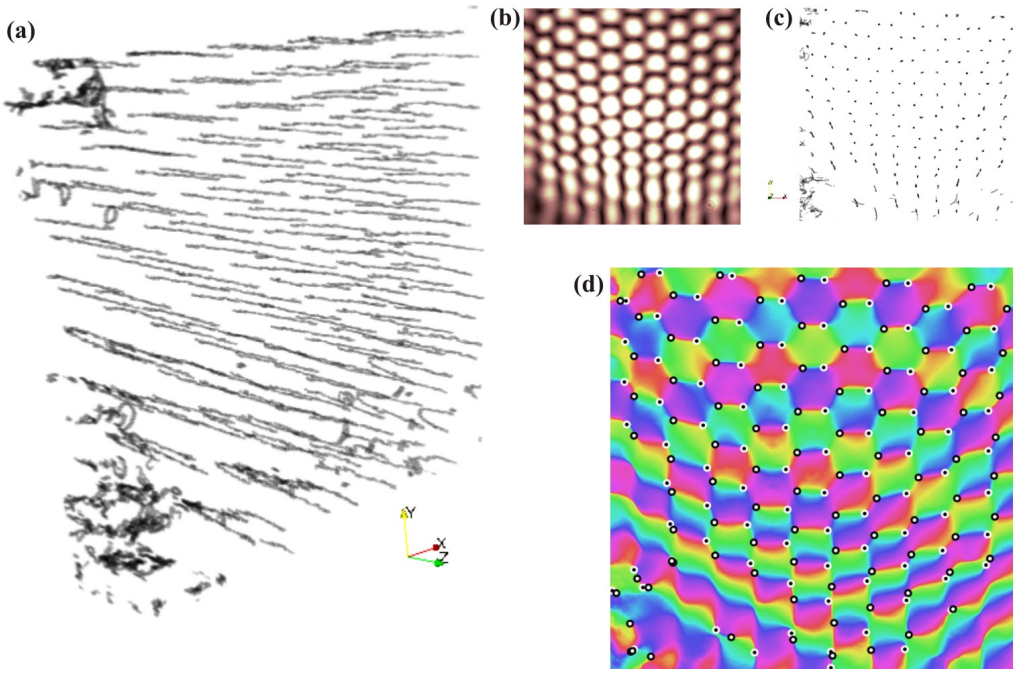

Figure 2.15: Experimental nodal line structure from three interfering Gaussians. (a) 3D nodal line structure. (b) Intensity. (c) 3D nodal line structure projected along z. (d) Phase with overlaid detected vortices and antivortices. The raw experimental data on which these figures are based was provided by Kevin O'Holleran and is used with permission.

evolving in time. The exposition here follows a similar approach to that reported in §2.3 which studied vortices in the interference pattern from the Young's three-pinhole interferometer.

Consider three (2+1)D Gaussian wavepackets, each of unit mass, whose position expectation values are stationary and centred about coordinates $\mathbf{r}_1 \equiv \mathbf{0}, \mathbf{r}_2, \mathbf{r}_3$. This is shown in the polar coordinate system schematic, Fig. 2.3, where we here replace the z-axis with a time t-axis.

The normalized probability amplitude for a Gaussian centred at the origin, as a function of position $\mathbf{r}$ and time t is given by (Bransden and Joachain, 2000, p. 65)

$$\Psi(\mathbf{r}, t) = \left(\frac{\pi^{-1/2} \Delta p/\hbar}{1 + i(\Delta p)^2 t/(m_a \hbar)} \right)^{1/2} \exp\left(\frac{-(\Delta p/\hbar)^2 |\mathbf{r}|^2}{2[1 + i(\Delta p)^2 t/(m_a \hbar)]} \right), \qquad (2.47)$$

where m_a is the mass of an atom of the atomic species, Δp is the momentum uncertainty that defines the wavepacket width, and $\mathbf{r}_t = (\mathbf{r}, t)$ is a (2+1)D position vector covering the xy-plane, whose origin lies at $(\mathbf{r}, t) = (\mathbf{0}, 0)$. The total probability

amplitude arising from the three superposed Gaussians is then

$$\Psi(\mathbf{r},t)=\sum_{j=1}^{3}\left(\frac{\pi^{-1/2}\Delta p/\hbar}{1+i(\Delta p)^2t/(m_a\hbar)}\right)^{1/2}\exp\left(\frac{-(\Delta p/\hbar)^2|\mathbf{r}-\mathbf{r}_j|^2}{2[1+i(\Delta p)^2t/(m_a\hbar)]}+i\phi_j\right), \tag{2.48}$$

where $|\mathbf{r}-\mathbf{r}_j|\equiv\sqrt{(x-x_j)^2+(y-y_j)^2}$ is the distance from the centre of the jth Gaussian to a given observation point $(\mathbf{r},t)$ and ϕ_j is the relative phase of the jth Gaussian. Separating the amplitude and phase terms of the wave field components $\Psi_j(\mathbf{r},t)=A_j(\mathbf{r},t)\exp[i\chi_j(\mathbf{r},t)]$, we get

$$A_j(\mathbf{r},t)=\left(\frac{\pi^{-1/2}\Delta p/\hbar}{1+i(\Delta p)^2t/(m_a\hbar)}\right)^{1/2}\exp\left(\frac{-(\Delta p)^2{m_a}^2|\mathbf{r}-\mathbf{r}_j|^2}{2[(\Delta p)^4t^2+{m_a}^2\hbar^2]}\right), \tag{2.49}$$

and

$$\chi_j(\mathbf{r},t)=\frac{(\Delta p)^4m_at|\mathbf{r}-\mathbf{r}_j|^2}{2[(\Delta p)^4t^2\hbar+{m_a}^2\hbar^3]}+\phi_j. \tag{2.50}$$

Vortices lie at points of the phase $\chi(\mathbf{r},t)$, at which a line integral of $\nabla_\perp\chi$ along a closed path Γ about such a point evaluates to a nonzero value [see Eq. (1.3)]. At any point coinciding with a vortex core, the phasors $\mathbf{p_1},\mathbf{p_2},\mathbf{p_3}$ corresponding to the three wavepackets, must sum to zero. Equivalently, Eq. (2.48) is equated to zero. With reference to Fig. 1.4, if the phasors are of equal length (corresponding to equal amplitude contributions from the three Gaussians) an equilateral triangle is formed, allowing the angles at the vertices to be specified simply.

As the amplitude contributions from the Gaussians are not unconditionally equal we must make an appropriate approximation to the amplitude term. By restricting consideration to some finite region of the xy-plane defined by $|\mathbf{r}-\mathbf{r}_j|\leq|\mathbf{r}_{\max}-\mathbf{r}_j|$, the exponential term in Eq. (2.49) will be approximately unity provided its argument is small, or $(\Delta p)^4t^2+{m_a}^2\hbar^2\gg(\Delta p)^2{m_a}^2|\mathbf{r}_{\max}-\mathbf{r}_j|^2/2$. For a given $\mathbf{r}_{\max}$, this is always true after sufficient time has elapsed. The amplitude term may now be factored out of the probability amplitude expression. Expanding the term $|\mathbf{r}-\mathbf{r}_j|^2=r^2-2\mathbf{r}\cdot\mathbf{r}_j+\mathbf{r}_j\cdot\mathbf{r}_j$ and remembering that $\mathbf{r}_1=\mathbf{0}$, the probability amplitude $\Psi(\mathbf{r},t)$ from Eq. (2.48) vanishes when

$$\begin{aligned}&1+\exp\left\{i\left[\alpha\left(r_2^2-2r_2r\cos\theta\right)+\phi_2\right]\right\}\\&\quad+\exp\left\{i\left[\alpha\left(r_3^2-2r_3r\cos(\theta-\theta_3)\right)+\phi_3\right]\right\}=0,\end{aligned} \tag{2.51}$$

where $\alpha=m_a\hbar t/[2(\hbar t)^2+2{m_a}^2(\hbar/\Delta p)^4]$. The three summands are associated with the three phasors in Fig. 2.4. Whereas the first summand, 1, is uniquely identified with the horizontal phasor $\mathbf{p_1}$, the association of the sources with the other two phasors allows two permutations, corresponding to the two phasor

diagrams; one for each vortex, ν_1 and ν_2. In fact one will be a vortex and the other an antivortex.

The arguments of the two exponentials in Eq. (2.51) are denoted γ and η, respectively. As we have seen, these phase angles are uniquely defined to within an integer multiple of 2π, so that:

$$\gamma = \alpha\left(r_2^2 - 2r_2 r\cos\theta\right) + \phi_2 = \frac{2\pi}{3} + 2m\pi, \tag{2.52a}$$

$$\eta = \alpha\left(r_3^2 - 2r_3 r\cos(\theta - \theta_3)\right) + \phi_3 = \frac{4\pi}{3} + 2n\pi, \tag{2.52b}$$

where m and n are integers. The association of the m and n indices with the vertices is arbitrary. Following the convention in §2.3, the choice is made here to match m with r_2 and n with r_3. The alternative phasor association is thus

$$\zeta = \alpha\left(r_2^2 - 2r_2 r\cos\theta\right) + \phi_2 = \frac{4\pi}{3} + 2m\pi, \tag{2.53a}$$

$$\kappa = \alpha\left(r_3^2 - 2r_3 r\cos(\theta - \theta_3)\right) + \phi_3 = \frac{2\pi}{3} + 2n\pi. \tag{2.53b}$$

Forming the fraction γ/η or ζ/κ yields

$$\frac{r_3}{r_2}\left(\cos\theta_3 + \tan\theta\sin\theta_3\right) = \frac{r_3^2 - \beta N(n)}{r_2^2 - \beta M(m)}, \tag{2.54}$$

where $\beta = 1/(3\alpha) = 2[(\hbar t)^2 + {m_a}^2(\hbar/\Delta p)^4]/(3m_a\hbar t)$. For the fraction γ/η, we get

$$\begin{aligned} M(m) &= 2\pi\left[1 + 3\left(m - \phi_2/2\pi\right)\right], \\ N(n) &= 2\pi\left[2 + 3\left(n - \phi_3/2\pi\right)\right], \end{aligned} \tag{2.55a}$$

and for the fraction ζ/κ, we instead have

$$\begin{aligned} M(m) &= 2\pi\left[2 + 3\left(m - \phi_2/2\pi\right)\right], \\ N(n) &= 2\pi\left[1 + 3\left(n - \phi_3/2\pi\right)\right]. \end{aligned} \tag{2.55b}$$

Examination of these expressions reveals that a 2π change in relative phases ϕ_2 or ϕ_3 may be absorbed as an integer change in the associated parameter-space coordinate m or n, respectively. By allowing m and n to correspond to discrete real values instead of integer values, they may then also absorb fractional parts of the relative phase. Consequently, the vortex lattice may be continuously translated by a single lattice cell for each 2π change in the source phase. Isolating θ in Eq. (2.54) yields

$$\theta_{mn} = \arctan\left[\frac{1}{\sin\theta_3}\left(\frac{N_3(n)}{M_2(m)} - \cos\theta_3\right)\right], \tag{2.56}$$

where the mn-subscript associates the coordinate with the (m, n)th vortex. We have compacted the notation further by defining the expressions

$$\begin{aligned} M_2(m) &\equiv r_2 - \beta M(m)/r_2, \\ N_3(n) &\equiv r_3 - \beta N(n)/r_3. \end{aligned} \tag{2.57}$$

Finally, the expression for the radial coordinate r_{mn} of the (m, n)th vortex core is obtained from Eq. (2.52a) or Eq. (2.53a) by applying the identity $\cos^2\theta = 1/(1+\tan^2\theta)$ and making use of Eq. (2.56):

$$r_{mn} = \frac{1}{2}\sqrt{M_2(m)^2 - 2M_2(m)N_3(n)\cos\theta_3 + N_3(n)^2}. \tag{2.58}$$

Together with Eq. (2.56), we have the vortex coordinates (r_{mn}, θ_{mn}, t), with the sign of the vortex charge, i.e. whether they describe the positions of vortices or antivortices, depending on the choice of Eqs (2.55a) or (2.55b) and the value of θ_3.[8] If $\theta_3 \in (0, \pi)$, vortices are indicated by Eq. (2.55a) and antivortices by Eq. (2.55b). If $\theta_3 \in (\pi, 2\pi)$, the association is reversed, with vortices indicated by Eq. (2.55b) and antivortices by Eq. (2.55a).

In contrast with the case described in §2.3, in which the allowed range of integers (m, n) was restricted, here there are no restrictions and an infinite, uniform vortex–antivortex lattice is generated. Although there is no ellipse construction in the mn-parameter space, the lattice origin retains the property of depending on the source phases as in the three-spherical-wave case. However, the amplitude term Eq. (2.49) applies a Gaussian envelope to the probability density $|\Psi|^2 = \left|\sum_{j=1}^{3} A_j(\mathbf{r})\right|^2$, effectively limiting the lattice. For sources arranged at the three corners of an equilateral triangle, the lattice has a honeycomb symmetry, with regular hexagonal cells. Changing the angle θ_3, or the side lengths r_2 or r_3, distorts the cells and the lattice.

Results from this model are presented in §4.4, where it is applied to the lattice that forms in numerical simulations of three wavepackets that interfere according to a nonlinear Schrödinger equation (NLSE).

[8] Note that there are some errors in the published versions in Ruben et al. (2008) of the above equations; Eqs (A1–3), (A10), and (A11) all contain errors. The amplitude terms in Eqs (A1–3) are missing the surrounding exponents of ½. In Eq. (A10) the closing parenthesis is erroneously placed and in Eq. (A11) the first parenthesised term is omitted and the first θ_3 is missing its subscript. Despite these errors, the expressions were correctly applied to the computation of the vortex and antivortex locations in the relevant figure in that paper.

2.5 Summary

A network of phase vortices was seen to be generated by the superposition of three stationary-state sources of outgoing complex spherical waves. We presented an analysis of the structure of the associated vortex cores (nodal lines), in the far-field regime. A finite number of vortices was seen to be generated. Determination of the number of such vortices was mapped onto the problem of determining how many points, on a two-dimensional square lattice, lie within a given ellipse. The equation of the ellipse depends in a known way on the geometry of the sources. The parameter space description also gives some insight into the effects of varying both the arrangement of the three sources, and their relative phase. Indeed, phase variation of two of the sources provides a means for precisely positioning one or several vortex cores. We showed how to map all of the preceding analyses onto the problem of determining the far-field disturbance that results when a three-pinhole Young's interferometer is coherently illuminated. We relaxed the far-field approximation, to study numerically the curved nodal lines which arise when one is not in the far field. In contrast to the classical two-pinhole Young's interferometer, in which the resulting diffracted field vanishes over a series of nodal planes, the three-pinhole interferometer yields a quite different phase topology, permeated with a rich structure of nodal lines that thread vortex cores.

Lastly, we studied the related case of the superposition of three sources of expanding complex Gaussian wavepackets, which evolve in (2+1)D, rather than 3D. We found that an infinite uniform lattice of vortices and antivortices is produced, albeit with a Gaussian amplitude envelope that expands with time.

3 Propagation of a vortical beam through a ground glass plate

> Donuts. Is there anything they can't do?
>
> — Homer Simpson

This chapter describes a computational model of a laser beam bearing an axial vortex as it diffracts upon passing through a ground glass plate (GGP), generating a speckled field in the process. Preliminary results from the model will be presented, which show that the field vorticity achieves a maximum at a characteristic distance from the plate and that this distance depends on the vortex charge. We aim to develop a physical model that explains this distance in terms of surface properties of the plate and the beam properties. The model may find application in surface property measurement, to which speckle field metrology has been applied (Erf, 1978; Sirohi, 1993; Goodman, 2007). In contrast with related studies of Laguerre-Gauss (LG) beams propagating through continuously diffracting turbulent media, such as the atmosphere (Paterson, 2005; Gbur and Tyson, 2008; Tyler and Boyd, 2009), the beam in our model interacts once with the GGP, and propagation then occurs *in vacuo*.

3.1 Laguerre-Gauss beams

If a laser passes through a forked diffraction grating or a spiral phase plate, a beam carrying a central vortex is produced. Vaughan and Willetts (1979) first noted that vortical beams are created as natural modes of some laser cavities. Later Bazenhov et al. (1990) engineered vortical beams in the nonzero-diffracted orders of a laser-illuminated forked grating. These gratings may be produced using spatial light modulators (SLMs), allowing dynamic control of the resulting fields for applications such as optical tweezers and communications (Curtis and Grier, 2003). If the laser has a Gaussian profile, the resulting diffracted orders are LG beams.

The field surrounding the LG beam's axial charge ℓ vortex carries orbital angular momentum (OAM) [or "optical orbital angular momentum" (O'Holleran, 2008)] of $\ell\hbar$ per photon (Allen et al., 1992). Dennis et al. (2009) provide a useful review of vortex beams. Other vortex-carrying beam models have been applied to various laser cavity designs and aberrations, such as Bessel-Gauss and Hypergeometric-Gauss models. We do not consider these models here, except to note that LG beams may be produced by passing a Hypergeometric-Gauss beam through a *mode-converter* composed of two spaced cylindrical lenses.

The LG beam model obeys the paraxial wave equation and is closely related to the Gaussian model introduced in Eq. (2.46) in the previous chapter. We summarise the Gaussian beam properties again here, as they are of direct relevance to the LG beam model. For clarification of any properties, we refer the reader to the definitions in §2.4.1. The Gaussian beam wavefunction $\Psi(r,z)$ in cylindrical coordinates is fully specified by the peak amplitude Ψ_0, wavelength λ (or wavenumber $k = 2\pi/\lambda$), and beam waist radius w_0. It has Rayleigh range $z_R = {w_0}^2 k/2 \equiv \pi {w_0}^2/\lambda$, spot size $w(z) = w_0\sqrt{1+z^2/{z_R}^2}$ and radius of curvature $R(z) = z\,(1+{z_R}^2/z^2) \equiv z^2 + {z_R}^2/z$. In terms of these parameters, the Gaussian beam wavefunction is

$$\Psi(r,z) = \Psi_0 \frac{w_0}{w(z)} \exp\left(\frac{-r^2}{w^2(z)}\right) \exp\left(\frac{-ikr^2}{2R(z)}\right) \exp\left[i\zeta(z)\right], \tag{3.1}$$

where $\zeta(z) = \arctan(z/z_R)$ is the Gouy phase.

In contrast, the LG beam wavefunction $\mathrm{LG}_p^\ell(r,\phi,z)$ in cylindrical-polar coordinates, with mode indices ℓ and p is

$$\begin{aligned}\mathrm{LG}_p^\ell(r,\phi,z) = \Psi_0 \frac{w_0}{w(z)} \left(\frac{r\sqrt{2}}{w(z)}\right)^{|\ell|} \mathrm{L}_p^{|\ell|}\left(\frac{2r^2}{w^2(z)}\right) \exp\left(\frac{-r^2}{w^2(z)}\right) \exp\left(\frac{-ikr^2}{2R(z)}\right) \\ \times \exp\left[i\zeta(z)\right] \exp(-i\ell\phi),\end{aligned} \tag{3.2}$$

where L_p^ℓ is the associated Laguerre polynomial (Kogelnik and Li, 1966; Allen et al., 1992; Soskin and Vasnetsov, 2001).[1] The beam contains an axial vortex with integer charge $\ell \in \mathbb{Z}$, and p is a non-negative integer $p \in \{0,1,2,\ldots\}$. These combine in the Gouy phase shift $\zeta(z) = (2p + |\ell| + 1)\arctan(z/z_R)$ via the *mode order* term $(2p + \ell + 1)$. The simplest vortical beam is produced for $p = 0$ and $\ell = 1$ (i.e. LG_0^1), producing a charge 1 vortex along the beam axis. The LG_0^0 mode recovers the

[1] Only non-negative ℓ values of this polynomial are evaluated for the LG beam. L_p^ℓ is also called the *generalised Laguerre polynomial* (see, e.g., Riley et al., 2006).

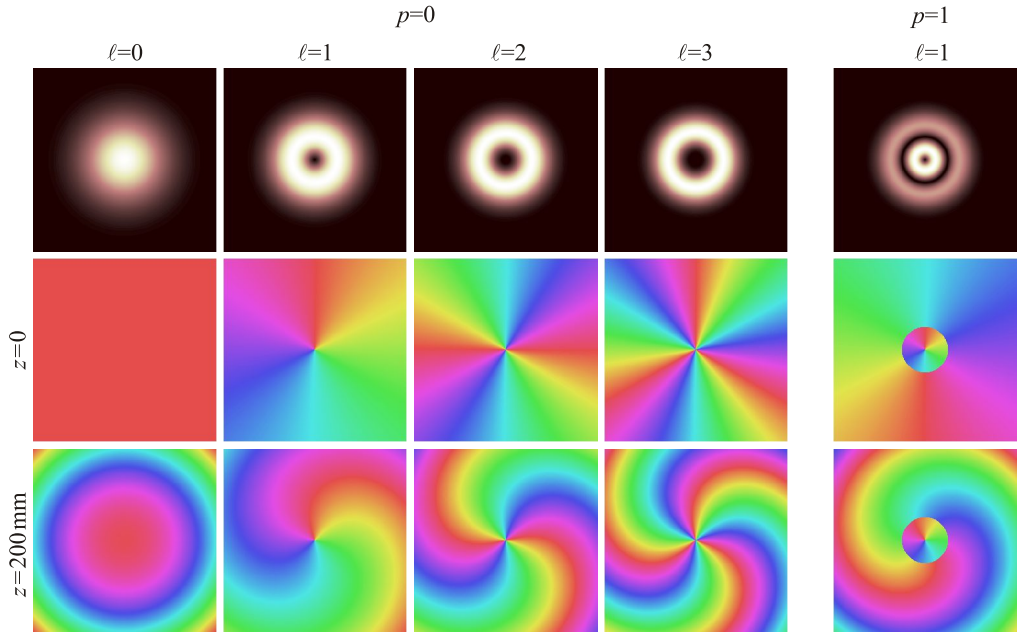

Figure 3.1: The intensity and phase of some LG_p^ℓ modes shown at the beam waist $z_{w_0} = 0$ and at $z_{200} = 200\,\mathrm{mm}$ for $w_0 = 0.5\,\mathrm{mm}$. The areas shown have half-side length given by Eq. (3.3). The spiralling phase is due to a propagation-acquired curvature, visible in LG_0^0. Cylindrical nodal sheet defects arise as concentric π-discontinuities for $p \neq 0$ modes.

Gaussian beam, and the beam parameters reintroduced above apply directly to this case.

The Gaussian beam parameter definitions do not necessarily apply to the more general LG beam. For example, the Rayleigh range is no longer the distance at which the beam cross-section is double that at the waist. The definitions are in terms of purely Gaussian beam properties. The spot size defined above ceases to have a simple interpretation for a beam intensity without a simple radially decreasing functional form. To address this, the LG beam spot size was defined by Phillips and Andrews (1983) in terms of a standard deviation of intensity as

$$w_0\sqrt{2p + |\ell| + 1}\sqrt{1 + \frac{z^2}{{z_R}^2}}. \tag{3.3}$$

For the remainder of this chapter, we consider only the case where $p = 0$.

Figure 3.1 shows the intensity and phase of several LG_p^ℓ modes. As the beam propagates, the peak intensity decreases and the transverse scale increases. The areas shown have a half-side length given by Eq. (3.3), accounting for this scaling. Therefore the normalised intensity plot applies to both phase profiles at z_{w_0} and z_{200}. The phase cycles ℓ times around the central charge-ℓ vortex. A circularly

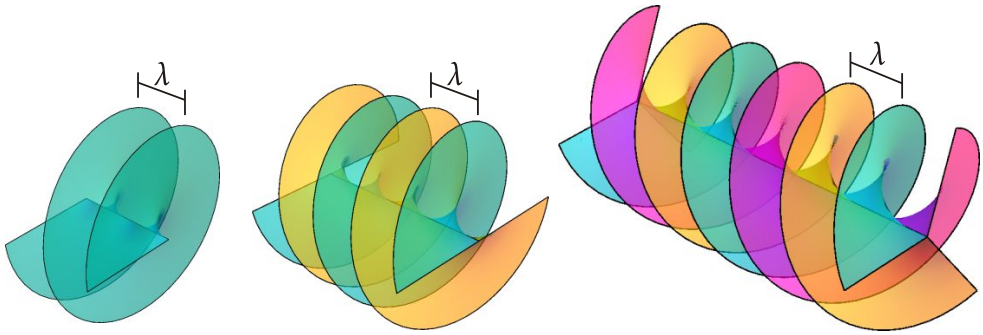

Figure 3.2: The constant-phase wavefronts of charge-ℓ beams are shown in left-to-right order for $\ell = 1, 2, 3$. They are locally helicoidal about the nodal line, which lies parallel to the field propagation direction z.

symmetric phase gradient associated with the propagated LG_0^0 Gaussian mode is visible in the bottom leftmost plot, due to the $\exp\{-ikr^2/[2R(z)]\}$ term in Eq. (3.2). This is responsible for the spiralling of phase visible in the propagated phases of other modes. After removal of this gradient and the uniform Gouy phase term from the spiral phase profiles, just the topological phase component $\exp(-i\ell\phi)$ remains, corresponding to the phase profile at $z = 0$. For the LG_1^1 mode, a topologically-cylindrical nodal sheet defect is visible as a radial π phase discontinuity, where the cylinder scales with spot size $w(z)$.

The wavefronts are roughly helicoidal in the neighbourhood of the LG beam axis, as Fig. 3.2 illustrates. Propagation-induced distortion of the pure helicoidal form shown will occur due to the Gaussian $\exp\{-ikr^2/[2R(z)]\}$ and Gouy phase terms.

3.2 Laguerre-Gauss beam and ground glass plate model

To study the interaction of an LG beam with a ground glass plate (GGP), a numerical model was developed. The intention is to perform experiments to confirm the findings from the modelling. Figure 3.3 is a schematic of the modelled system. In Fig. 3.3(a) an LG laser is shown passing through a GGP and striking a screen. The corresponding experimental system will implement both the LG laser beam and the GGP with one or more SLMs, in order to allow exploration of the system parameters. The $\mathrm{LG}_{p=0}^{\ell}$ beam strikes the GGP at the beam waist $z = 0$ and the resulting field is calculated at some plane z_0.

A GGP is a slab of uniform thickness glass on which mechanical grinding

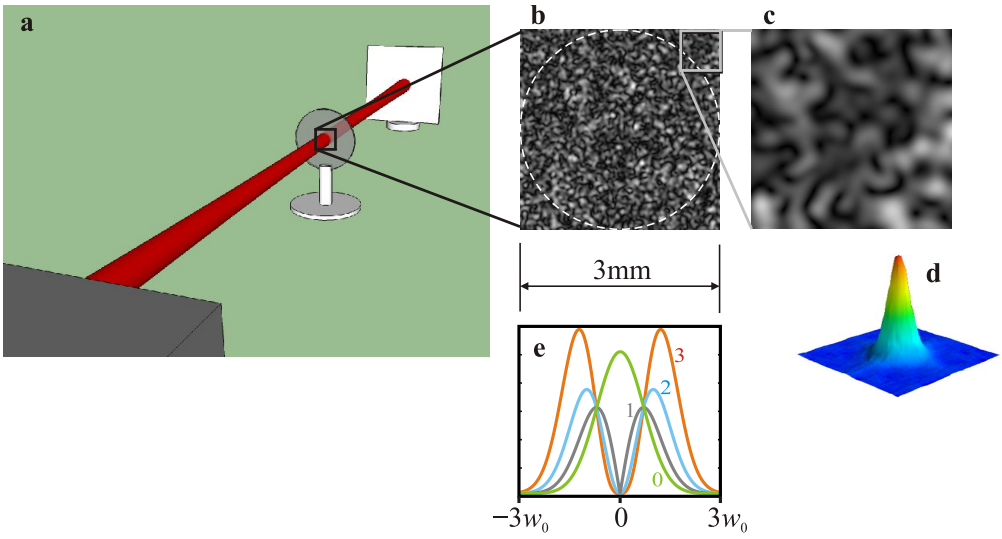

Figure 3.3: (a) An LG beam passes through a (circular) GGP at its beam waist and the resulting field is observed on a screen. (b) The GGP is treated as a height map that acts as a phase object, with surface feature detail shown in (c) generated from a Gaussian autocorrelation function shown in (d). In (e), the circularly symmetric intensity profiles of LG_0^ℓ, $\ell = 0, 1, 2, 3$ with beam waist $w_0 = 0.5\,\mathrm{mm}$ are fitted within the $3\,\mathrm{mm} \times 3\,\mathrm{mm}$ sampled interaction region.

or chemical etching creates a roughened surface. Cheng et al. (2002) presented surface profiles of GGPs obtained using atomic force microscopy and characterised the surface with the Gaussian autocorrelation function

$$R(\mathbf{r}, \mathbf{r}') = w^2 \exp(-|\mathbf{r} - \mathbf{r}'|^2 / {L_c}^2) \tag{3.4}$$

where w is the *rms deviation roughness* that characterises the feature height, L_c is the correlation length that characterises the transverse length over which features are related, and $\mathbf{r}$ and $\mathbf{r}'$ are both general position 2-vectors. For our model, setting $w = 1$, taking the square root of the Fourier transform of R, applying a random phase to the result, and inverse Fourier transforming generates a realisation of such a surface. The resulting surfaces [e.g., Fig. 3.3(b–c)] look qualitatively like those presented in Cheng et al. (2002). We used a correlation length $L_c \approx 30\,\mu\mathrm{m}$ in all simulations in this chapter. The height (hence w) of the surface heightmap was obtained iteratively by repeatedly modelling a plane wave passing through this surface to get a Gaussian intensity profile and adjusting the height until the intensity full width at half maximum (FWHM) roughly matched that of the profiles from available data (FWHM $\approx 7°$) (ThorLabs, 2009). As shown in Fig. 3.3(e), sampling a beam of waist radius w_0 out to the intensity tails at $\pm 3w_0$ captures most of the beam intensity and ensures that the effect of convolution with the aperture function is

negligible.

According to Eq. (3.3), a beam with a small waist radius has a correspondingly short Rayleigh range and spreads faster than a beam with a large waist. Numerical Fourier propagation methods impose restrictions on the allowed degree of beam spreading and the propagation distance over which propagation is valid. In order to model beam propagation without restriction, the field is modelled at the exit surface of the GGP using an arrangement of spherical point sources. The number of these sources is chosen according to the Nyquist limit imposed by the beam waist w_0 and wavelength λ.

Each source, indexed by j, lies at a particular coordinate (x_j, y_j). The amplitude A_j of each individual source is determined from the LG beam model and the phase from the LG beam model propagated through the small extra distance of the GGP height field at that location $\phi_j = \phi_{\mathrm{LG}}(x_j, y_j) + \phi_{\mathrm{hf}}(x_j, y_j)$. The complete field due to these sources is then evaluated over a rectangular region of the plane at z_0 according to:

$$\Psi(\mathbf{r}) = \sum_{j=1}^{n} \frac{A_j}{|\mathbf{r} - \mathbf{r}_j|} \exp\left[i\left(k|\mathbf{r} - \mathbf{r}_j| + \phi_j\right)\right], \tag{3.5}$$

where $|\mathbf{r} - \mathbf{r}_j| \equiv \sqrt{(x - x_j)^2 + (y - y_j)^2 + z^2}$ is the distance from the jth source to a given observation point $\mathbf{r}$ on the observation screen. This is a direct-space computation of the Kirchhoff diffraction integral, which is a mathematical re-statement of the Huygens-Fresnel construction, which models diffraction by placing spherical wave secondary sources at each point on a wavefront of the field (Born and Wolf, 1999, §8.2–§8.3).

The phase of a simple Gaussian beam LG_0^0 evaluated at the plane z_0 is then subtracted from the calculated phase in order to remove any radial phase gradient. As we explained in §2.3.4, this allows the use of a 2D vortex detection algorithm, which would otherwise fail due to the radial moiré phase artefacts.

3.3 Results from the model

In this section we present preliminary results from the numerical model. These indicate the type of results we can obtain from the simulations and might expect from experiments, and reveal that the field vorticity displays an unexpected dependence on the beam properties.

The modelled GGP surface was 3 mm × 3 mm in extent, to allow a typical physical beam waist radius $w_0 = 0.5$ mm of a HeNe laser with wavelength $\lambda = 633$ nm. The correlation length L_c was fixed at approximately 30 µm. The parameter space

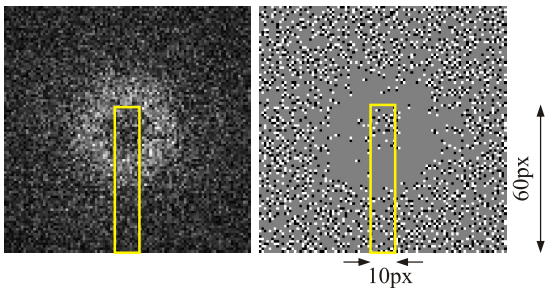

Figure 3.4: Intensity and detected vortices overlaid with a yellow region indicating the area of results computed in subsequent figures.

was explored by adjusting the height h (hence rms deviation roughness w) of the GGP, and the beam vortex charge ℓ, waist radius w_0, and screen locations z_0.

The Nyquist criterion ensures correct sampling of the source. For a beam waist radius w_0, which requires a source sample area of side length $s = 6w_0$ and area $A = (6w_0)^2$, $N > (2s/\lambda)^2$ sources are required. This corresponds to $N \approx 10^7$ sources. To compute the resulting field over a $100 \times 100 = 10,000$ pixel screen would require about 15 days of computation time on a contemporary 4 GHz processor, so the model allows specification of a rectangular windowed region of the screen with pixel locations mapped to known physical (x, y) coordinates. The $60 \times 10 = 600$ pixel window, corresponding to the yellow region indicated in Fig. 3.4, allows each result to be computed in about 24 hours, which allows the parameter space to be explored, albeit slowly.

Two sampling schemes were tried. The source was sampled both uniformly and randomly within the circle that touches the four sides of the source square, indicated by the dashed circle in Fig. 3.3(b). The simulation results using randomly positioned samples produced spurious vortices and are not presented here.

We define the vorticity here to be the total number of vortices detected over the field Ψ at z. An interesting behaviour was discovered. As the beam propagates, the speckle and associated vorticity increase and than decrease again, after peaking at a characteristic distance z_p. We speculate that this occurs because the concave regions of the GGP surface focus incident plane waves at a distance z_f characteristic of the surface's mean curvature and wavelength of radiation. As vortices are associated with focal regions of fields, the vorticity achieves a maximum at this distance (Boivin et al., 1967). Instead of plane waves, our illumination source is an LG beam. We observe that z_p depends on the beam vortex charge ℓ and the beam waist w_0; decreasing with ℓ and increasing with w_0. We have not yet established the precise dependence but will present the evidence to date, which we hope to

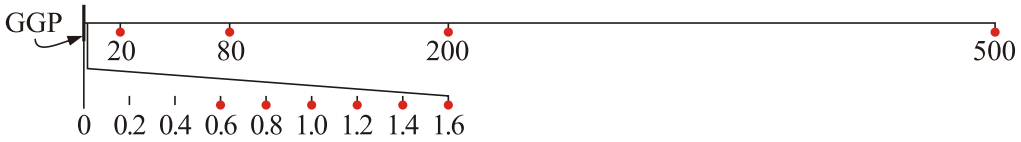

Figure 3.5: Key indicating locations (z_0) at which results in Figs 3.6–3.8, are computed. Values are in millimetres, relative to the GGP and beam waist at $z = 0$.

supplement with experiments and further simulations (see Chap. 6).

To counter the movement of z_p, we found it necessary to modify the height h in response to changes to beam charge ℓ. Figure 3.5 indicates the z locations at which the results presented in Figs 3.6, 3.7, and 3.8, were computed. In each series of results, the field was computed at the ten positions indicated, which are presented in increasing order from left to right. Each row of results shows the intensity, phase, and vortices detected using the 2D phase unwrapping algorithm described in Appendix A. To draw conclusions from the simulation results, we focus on the speckle and associated vortices in the vicinity of the LG beam axis. There is also a visible change in behaviour in the intensity tail, near the bottom of the simulated rectangular field regions. However, numerical artefacts are particularly likely in this region given the large number of source contributions.

Exploration of the parameter space showed that the effect of varying ℓ on z_p could be countered by varying h. This suggests a relationship between λ, h, and ℓ. A few examples of this dependence are presented here. Figures 3.6 and 3.7 straddle the height $h = \lambda/\ell$ and show the results for $\ell = 1, 2, 3$. In Fig. 3.8 the beam waist w_0 has been halved. It appears that peak vorticity is reached at $z_p = 80$ mm for $h = \lambda/\ell$ when $w_0 = 0.5$ mm and at $z_0 = 20$ mm when $w_0 = 0.25$ mm. Thus, it appears that z_p changes in proportion to the square of the beam waist w_0. Further simulations may be required to clarify whether z_p reduces to one quarter, or possibly one half of the previous value.

By straddling $h = \lambda/\ell$ in Figs 3.6 and 3.7, we see that the amount of speckle and vorticity increase significantly at z_p, but the beam profile still recovers at large distances. The same effect is visible between the upper and lower series of Fig. 3.8. We found that for $h \gg \lambda/\ell$ the beam profile was lost completely, although results may not have been obtained at sufficiently large z_0 to observe the recovery. It is possible that there is a peaked statistical distribution of vorticity centred on z_p whose width depends on the ratio $h\ell/\lambda$.

In summary, it seems that both the distance z_p and the distribution centred at z_p depend on the dimensionless ratio $h\ell/\lambda$ and $z_p \propto {w_0}^d$, where d appears to be 2. Whether the distribution width also depends on w_0 is unknown. We fixed

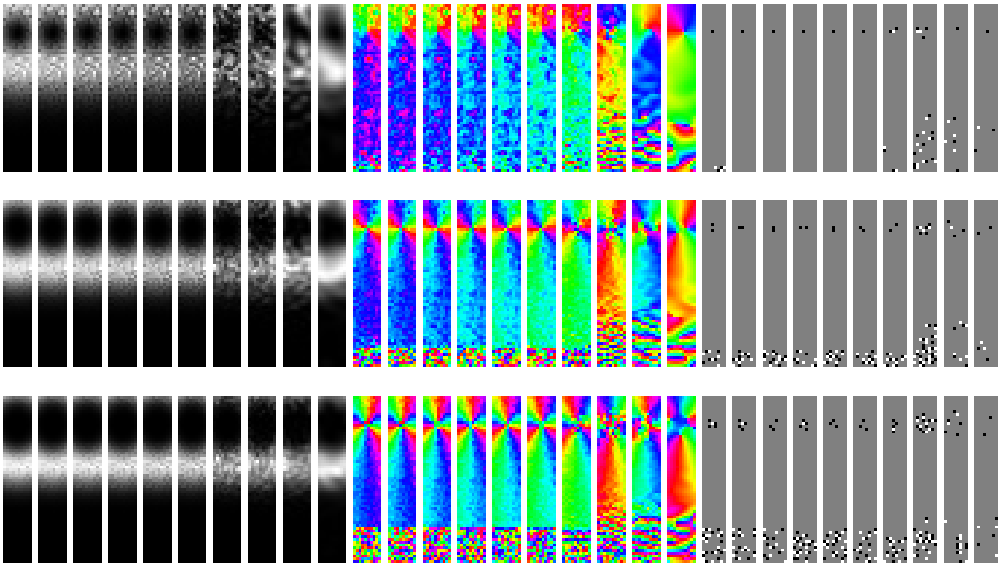

Figure 3.6: Simulation results for GGP height $h = \lambda/\ell - 50\%$. 1st row: $\ell = 1$; 2nd row: $\ell = 2$; 3rd row: $\ell = 3$.

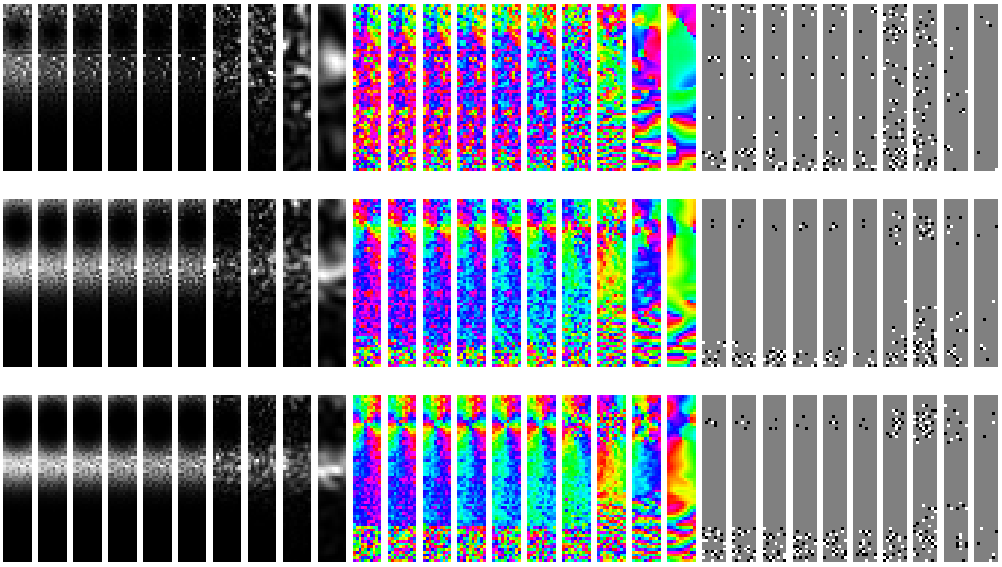

Figure 3.7: Simulation results for GGP height $h = \lambda/\ell + 50\%$. 1st row: $\ell = 1$; 2nd row: $\ell = 2$; 3rd row: $\ell = 3$.

the correlation length L_c in our modelling, but z_p must also depend on this. We do not have an explanation for the observed behaviour; it is possible that we may be studying just one regime of model parameters, in which many physical effects, operating over different characteristic length scales, contribute to the behaviour. For example, the observations may change for higher numerical aperture beams

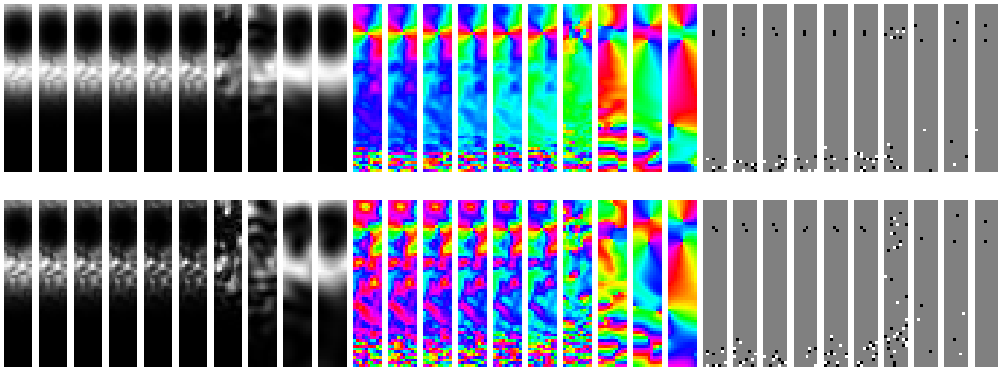

Figure 3.8: Simulation results for $\ell = 2$ with beam waist w_0 halved. 1st row: $h = \lambda/\ell - 50\%$; 2nd row: $h = \lambda/\ell + 50\%$.

(with small waist and Rayleigh range) and low mean curvature surfaces, since the surface properties may characterise speckle behaviour, whereas the Rayleigh range characterises beam behaviour. Further simulations or experiments will help to clarify the situation and provide insight into the underlying physics.

The axial vortices in an LG beam of charge $|\ell| \geq 2$ naturally separate due to perturbation as the beam propagates. This separation is visible in the phase and detected vortex maps at distances $z_0 > z_p$ due either to perturbation by the GGP or due to numerical artefacts. The vortices may explode into charge-1 vortices with spacings greater than the coherence length at the point they intersect the GGP. If this occurs, we would expect the results to be affected since s independent charge-1 beams should behave differently to a single charge-s beam, according to the preliminary results from the model. By choosing to interact the beam and GGP at the beam waist, this effect should be minimised. However, care must be taken in experiments to ensure that this effect is controlled.

Although we argued for the use of direct-space evaluation over Fourier-based methods, certain schemes employing the fast Fourier transform may be appropriate for the parameter regime studied to date. Evaluation using multislice or finite difference codes may permit quicker exploration of the parameter space, with verification by experimental or direct-space-numerical modelling (Nascov and Logofătu, 2009; Liu et al., 2009).[2]

[2]The major features we found using direct-space evaluation have also been observed by Miles Padgett using a Fourier-based method, private communication.

3.4 Summary

A GGP illuminated by a non-vortical light source generates a speckle field whose features depend only on the wavelength of the incident light. When the illumination source is changed to a vortical LG beam, numerical simulations show that the field speckle and associated vorticity achieve a maximum at a characteristic distance, beyond which the beam is recovered. The distance appears to depend on all the parameters of the model; the beam wavelength, waist radius, and topological charge, and the GGP surface feature height and correlation length.

4 Vortices from interference in nonlinear fields

> If you give people nothingness, they can ponder what can be achieved from that nothingness.
>
> — Tadao Ando, architect

In this chapter we apply our knowledge of the three-pinhole Young's interferometer to the case of three initially localised, nonlinear interfering wavepackets evolving in time. The specific nonlinear system is that of a Bose-Einstein condensate (BEC), which is a quantum system that has been observed to contain quantised vortices. The production of vortices has attracted great interest in the study of BECs, yet the mechanism of generation as a result of direct interference remains largely unrecognised amongst BEC researchers (see, e.g., Pismen, 1999; Dalfovo et al., 1999; Fetter and Svidzinsky, 2001; Minguzzi et al., 2004).

4.1 Bose-Einstein condensates

When a gas of atoms, each of mass m, is cooled to a temperature T where the de Broglie wavelength $\lambda_{dB} = \hbar/(2mk_BT)^{1/2}$ is much smaller than the mean atomic spacing, a state is produced called a BEC in which the wavefunctions of the atoms overlap and become indistinguishable (Leggett, 2006; Pethick and Smith, 2008). In order for the atoms to persist in this state over experimentally useful time-scales (seconds to minutes), three-body collisions must be minimised, requiring the gas to be of low density (Leggett, 2001).

A significant literature exists discussing the nature of vortices in superfluid ^{3}He and ^{4}He, which were the earliest experimentally realised systems capable of supporting quantised vortices (Tilley and Tilley, 1990). The first experimental creation of BECs of atomic alkali gases in 1995 made it possible to directly image vortices, albeit after a period of *ballistic expansion* of the Bose-condensed cloud;

this is required in order to increase the feature size above the limits of current optics. Proposals for imaging vortices using in-situ diffraction-based imaging may permit their direct observation (Turner et al., 2005). For reviews of BECs, see Dalfovo et al. (1999); Leggett (2001); Ketterle (2002); Minguzzi et al. (2004); Leggett (2006); Pethick and Smith (2008). Although the creation of the first BEC was a significant achievement, involving a combination of magnetic and optical trapping to cool the atoms, the description of the physics of cooling and trapping is beyond the scope of this thesis.

Illuminating the Bose-condensed atoms with a laser tuned to a suitable energy can excite atoms from the ground state. By detuning the laser frequency, an effective potential is experienced by the atoms (Pethick and Smith, 2008, §4.2). An increased frequency or *blue* detuning is experienced as an increased potential and a decreased frequency or *red* detuning corresponds to a decreased potential. Thus atoms are repelled from regions illuminated by blue detuned lasers and attracted to regions illuminated by red detuned lasers. Similarly, detuned lasers with varying phase can act as phase-dependent potentials, conferring phase gradients on the condensate.

A typical BEC experiment involving the creation of vortices might follow the following sequence. The atoms are cooled to form the condensate cloud within a magnetic or optical trap. Some sequence of experimental operations (e.g., involving rotating the trap potential) would then be performed on the BEC, resulting in the creation of vortices, which would then be imaged to observe their structure. BEC imaging typically employs a ballistic expansion stage in which the confining magnetic trap is removed immediately prior to destructive imaging (Mewes et al., 1996). As a result, the structure of the condensate cloud becomes effectively frozen and simultaneously magnified. This occurs because the local number density decreases, reducing the nonlinear self-interaction. The size of features in the BEC is related to the local density, so vortex core diameters increase and become resolvable by the experiment's optics during this stage. In fact the structure is not frozen, but, since the density decreases during expansion, the time evolution becomes progressively dominated by linear dynamics. The expansion stage is typically of the order of 10 ms, which is a relatively short interval on the scale of the condensate evolution. If the dynamics are deterministic, a time sequence can be produced by repetition of the above sequence with precise modification of the timing of the experimental operation to vary the final state immediately prior to ballistic expansion. Chaotic vortex dynamics, related to turbulence, cannot be imaged this way as they are non-repeatable.

4.1.1 Vortex creation mechanisms in BECs

As we did for optical vortices, we find the circulation about a vortex $\oint_\Gamma \mathbf{v} \cdot \mathbf{t}\, dl$ as the integral of the velocity field $\mathbf{v}$ over the closed contour Γ having tangent vector $\mathbf{t}$. Because the probability current or velocity field is irrotational in a BEC, the circulation is quantised in amounts sh/m, where s is the integer vortex charge, h is the Planck constant, and m is the mass of an atom of the condensate species. High charge vortices are typically unstable to perturbation and decay into vortices with unit charge.

Experimental vortex production in BECs is usually a result of bulk rotation of the condensate cloud. This is performed by either rotating the confining trap, stirring with a focused *laser spoon*, or by laser phase imprinting. The angular momentum of the cloud is quantised in amounts of $s\hbar$ per atom. The vortices in these rotating systems form an *Abrikosov lattice* with hexagonal symmetry (Abrikosov, 1957). Because each vortex carries quantised angular momentum in the surrounding field, the number of vortices in the rotating BEC is governed by the net angular momentum of the system. In contrast, in any mechanism that produces vortices in a nonrotating BEC, equal numbers of vortices and antivortices are produced, since the net angular momentum is zero.

Perhaps the two most commonly attributed mechanisms for vortex generation in nonrotating BECs are the Kibble-Zurek (KZ) mechanism, and the *snake instability* of dark stripe solitons (Feder et al., 2000). The KZ mechanism describes the production of vortices as a result of phase windings introduced from the reconciliation of initial random phases in the BEC (Kibble, 1976; Zurek, 1985; Anglin and Zurek, 1999). Recent experiments have demonstrated the production of vortices in BECs undergoing rapid cooling through the condensation temperature (Weiler et al., 2008). Here, rapid cooling leads to a series of domains whose phases are uncorrelated; the reconciliation of these phases then seeds vortices via the KZ mechanism.

Dark stripe solitons are the nonlinear analogue of vortex sheet defects or two-source Young's interference fringes. The snake instability of dark stripe solitons describes the development from perturbations of a stripe-soliton or interference fringe to a snake-like shape, which eventually breaks up into a series of alternating vortices and antivortices. Figure 4.1 shows a (2+1)D numerical simulation of the development of vortices resulting from this process.[1] Nonlinear self-interactions cause the resulting dark interference fringes to form a series of dark-stripe solitons. The phase varies by π across each stripe, associated with a zero probability density

[1] We will describe the computational method used to produce this simulation in §4.3.

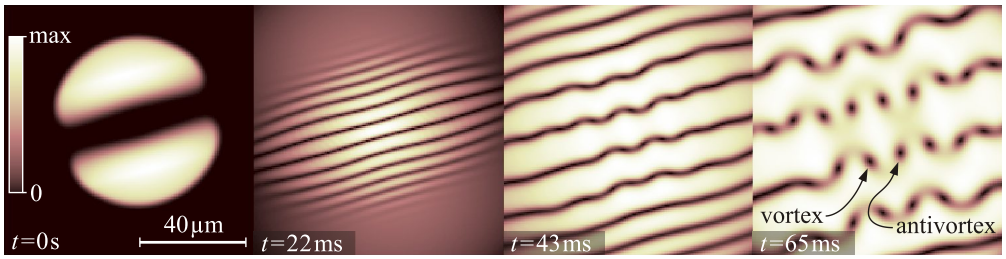

Figure 4.1: A pancake-geometry BEC is formed in a harmonic trap divided in two by a laser light sheet. Upon removal of the trap and laser, the pieces interfere, forming a series of dark-stripe solitons that are nonlinear versions of Young's interference fringes. Each dark-stripe soliton decays via the snake instability into a row of alternating vortices and antivortices.

or visible absence of matter along its length. Each stripe then decays via the snake instability into a necklace of alternating vortices and antivortices. Dark stripe solitons need not be straight lines; they need only be of low curvature compared to the snaking pattern to decay into vortices by this mechanism. For example, ring dark solitons (RDSs) are circular defects analogous to the cylindrical nodal sheets mentioned in Chap. 1, which also decay via the snake instability (Theocharis et al., 2003).

Other mechanisms have been described for vortex production in nonrotating BECs. Vortex production was observed in the wake of a focused laser swept through a condensate cloud, producing vortices analogous to the *vortex streets* seen in classical fluids passing obstacles (Jackson et al., 1998; Inouye et al., 2001). Ruostekoski et al. (2001) observed vortex production due to self-interference of a trapped BEC in which structures resembling RDSs were first promoted and then allowed to expand and reflect within a hard-walled trap.

4.2 Interference of a three-way segmented BEC

Recently Scherer et al. (2007) (see also Scherer, 2007) performed an experiment in which vortices were observed as a result of the interference of a three-way segmented BEC. An oblate spheroidal BEC was formed in an asymmetric trap partitioned into three regions by shining a laser light sheet on the condensate (see Fig. 4.2). The partition walls were then removed at varying rates and vortices were sought after different elapsed times, during which the three pieces were allowed to expand and interfere. Both 2D and 3D numerical simulations of this experiment have also been performed by Carretero-González et al. (2008a).

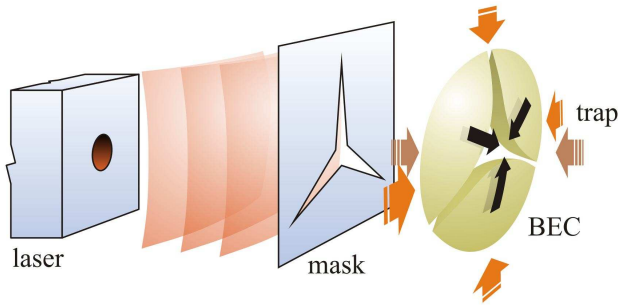

Figure 4.2: A laser-illuminated mask separates a pancake-shaped BEC, formed in an asymmetric trap, into three pieces. Upon removal of the illumination – and optionally the trap – the pieces interfere (black arrows), forming a lattice of vortices and antivortices.

There were several motivations for embarking on the study of a similar system. First, by replacing the z-dimension, in the theory developed for the three interfering spherical waves, with time t, the formation of vortices may be understood as arising from the same mechanism, albeit now in a highly nonlinear system. The generation of vortices by this mechanism was (and remains largely) unknown to the BEC community. Assuming the existence of effects predicted by the Young's interferometer carry over to the nonlinear case, it should be experimentally feasible to search for these effects, making the work immediately relevant. Because the experiment had been performed and the expected honeycomb lattice was not reported, investigation of the potential for lattice formation spurred us to show that it should be formed.

The system must be quasi-2D (i.e. pancake shaped), in order to support vortices that behave analogously to the three-pinhole interferometer system. The analogy requires swapping the spatial z-dimension for time t, forcing a change of viewpoint from nodal lines in 3D to vortices in (2+1)D. Although we were motivated to describe the evolution in (2+1)D to maintain the analogy with our previous work, there is also a computational benefit to doing so. Simulation of BECs can be slow, even for today's computers. It is thus common to choose the dimensionality of the simulation to be as low as possible in order to maximise the simulation speed and accuracy.

Figure 4.3 visually summarises the dynamics of the (2+1)D case, which links to the previous work on the Young's interferometer. Following this image from left-to-right, we see the initial BEC state formed in a harmonic trap divided into three parts by a laser light-sheet. Upon removal of the laser, the three wavepackets interfere within the trap, progressing from the initial state, to the production of

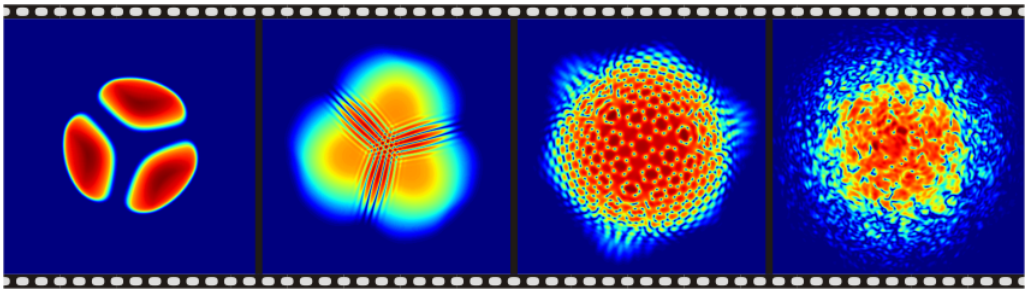

Figure 4.3: Selected frames from a temporal simulation sequence of a three-way segmented BEC showing (left to right) the ground state, interference fringes, vortex lattice, and the chaotic aftermath following melting of the lattice.

Young-like two-piece interference fringes between pairs of pieces, to the formation of a honeycomb vortex-antivortex (VA) lattice which is the signature of three-source interference. Finally, following melting of the lattice due to harmonic trap confinement, the late stage is characterised by turbulent vortex-antivortex-sound dynamics.

The numerical simulation of the (2+1)D case, resulting in Fig. 4.3, is described in §4.3 and §4.4, which are based on our paper Ruben et al. (2008). In §4.3 we describe the numerical BEC model, concentrating on the time-dependent and ground state models, the reduction from 3D to 2D, and a vorticity metric for the order parameter field. The description of vortex production via the phasor approach is applied to the nonlinear system in §4.4.2. We present the simulation results in §4.4.3, highlighting the effects of light-sheet intensity, different light sheet geometries and phase variation between the condensate pieces in the trapped and untrapped cases, whilst making connections to the linear theory. We provide a visualisation of the lattice formation and melting, and in §4.4.5, describe the rich VA dynamics that arise after the lattice has melted. Finally, we summarize our findings in §4.4.7. After considering this analogous system and investigating the degree to which our previous knowledge of the linear interference may be applied, we model a fully (3+1)D system in §4.5. We examine the evolution of the string-like objects that are formed and show that the (2+1)D results are valid, even for thick condensates.

4.3 Numerical modelling of nonlinear BEC dynamics

In this section we describe the derivation and parameters of the numerical model for the interference of the three-way segmented nonrotating BEC. We are not interested in the BEC formation per se but rather its dynamics once formed. The mean-field approach applied here has been shown to be valid for this task for weakly interacting atomic gases containing moderate to large numbers of Bose-condensed atoms where the condensate fraction is high.

The governing dynamical equation is the Gross-Pitaevskii equation (GPE), which describes the BEC state via a complex scalar order parameter field (Leggett, 2006). The GPE takes the form of the familiar Schrödinger equation with an additional cubic nonlinear term and the wavefunction replaced by the order parameter field. It is a particular example of the nonlinear Schrödinger equation (NLSE), which in general also admits non-cubic nonlinearities. As with most nonlinear partial differential equations (PDEs), the GPE must be solved numerically, where solving involves integration with respect to the time variable.

We modelled an experiment similar to that conducted by Scherer et al. (2007) in which a BEC is initially formed within a harmonic trapping potential modified by an illuminating laser so as to produce three dividing walls within the trap. In all simulations the laser light sheet walls are removed instantaneously at $t = 0$, allowing the ground state and time evolution simulations to be separated. The separated simulations may then use different numerical schemes as appropriate.

To simulate the system, we need the time-dependent version of the GPE, and an estimate of the initial field distribution and chemical potential of the ground state, which is provided by the Thomas-Fermi (TF) limit of the time-independent solution (Pethick and Smith, 2008, §6.2.2). The simulation procedure was as follows: Beginning with the TF condensate profile as an initial condition, a Wick-rotated version of the GPE is evolved with the full trap potential, including the laser light sheet, until a steady solution is found, which corresponds to the ground state. In the Wick-rotation scheme the GPE is converted to a diffusion equation, which is evolved *through imaginary time* (Chiofalo et al., 2000). The ground state is then used as the initial state to the time-dependent equation, which is solved with appropriately chosen trapping potentials that were varied for different simulations.

4.3.1 The Gross-Pitaevskii equation

To model this experiment, because we are not concerned with the physics of establishing the BEC state, a conventional mean-field approach to modelling the condensate dynamics is used. In this approach, as mentioned earlier, the evolution of the macroscopic wavefunction or order parameter field Ψ of the BEC is governed by the Gross-Pitaevskii equation (GPE)

$$i\hbar\partial_t\Psi(\mathbf{r},t) = \left(-\frac{\hbar^2}{2m}\nabla^2 + V(\mathbf{r}) + NU_0\left|\Psi(\mathbf{r},t)\right|^2\right)\Psi(\mathbf{r},t), \tag{4.1}$$

where t denotes time and we will use either cylindrical-polar $\mathbf{r} \equiv (r,\theta,z)$, or Cartesian $\mathbf{r} \equiv (x,y,z)$ coordinates depending on circumstance (Leggett, 2006). When the result of interest is the TF limit of the GPE, to be used as an input to the initial condensate (ground state) profile computation, cylindrical polar coordinates are appropriate for the harmonically-trapped condensate. However, the actual potential V, applied numerically to find the initial condensate profile, includes the laser light sheet, breaking the cylindrical symmetry. Thus, the calculation of the full potential, and the application of the numerical scheme are more appropriately described in Cartesian coordinates.

The derivation that follows is well explained by Lee et al. (2002) and Leggett (2006), using the same convention for writing the GPE as Eq. (4.1). The GPE takes the form of the time-dependent Schrödinger equation with an additional nonlinear self-interaction term $NU_0\left|\Psi\right|^2\Psi$ for a condensate containing N atoms. Here $U_0 = 4\pi\hbar^2 a/m$ depends on the mass m of the atomic species (^{87}Rb and ^{23}Na were examined in this work) and the s-wave scattering length a, which we require to be positive in order to permit the BEC pieces to expand and interfere, and to support dark solitons, particularly vortices.[2] The BEC contains N atoms and evolves within a trapping potential which, for the moment, assumes that any light sheet is instantaneously removed at $t = 0$. Thus $V(\mathbf{r}) = m(\omega^2 r^2 + \omega_z^2 z^2)/2$ describes the trapping potential as an asymmetric harmonic trap, with radial angular frequency ω and axial angular frequency ω_z. The establishment of the ground state with the light sheet present, where $V(\mathbf{r}) = m(\omega^2 r^2 + \omega_z^2 z^2)/2 + L(x,y)$ for $t < 0$, is discussed in §4.3.4. If the initial condition is known, the time evolution of the system can now be computed from a numerical implementation of Eq. (4.1).

[2] The controllable parameters of a condensate of a given atomic species are contained in the self-interaction term and the trapping potential. For a harmonically trapped condensate, the dynamics may be experimentally controlled by varying the trap frequency ω, the number of atoms N, or the scattering length a; the last of these being tuned via Feshbach resonances by altering an external magnetic field (Pethick and Smith, 2008).

However, it is usually considered prudent to transform to a dimensionless form for the numerical implementation; we discuss this in §4.3.3.

In the form of the GPE used in Eq. (4.1), the normalisation condition is

$$\int |\Psi|^2 \, dV = 1, \tag{4.2}$$

where $dV \equiv dx\, dy\, dz$ is a volume element (see, e.g., Holland and Cooper, 1996; Lee et al., 2002; Bao et al., 2003). However, there is a second convention for representing the GPE that is commonly seen in the BEC literature. This differs due to the order parameter field Ψ being normalised, not to 1, but to the number of atoms in the condensate N. One may swap between these two conventions by simply substituting $\psi = \sqrt{N}\Psi$ into Eqs (4.1) and (4.2) to give

$$i\hbar\partial_t\psi = \left(-\frac{\hbar^2}{2m}\nabla^2 + V + U_0\left|\psi\right|^2\right)\psi \tag{4.3}$$

and

$$\int |\psi|^2 \, dV = N, \tag{4.4}$$

We follow the convention shown in Eqs (4.1) and (4.2), which leads to N appearing explicitly in the GPE. A specific limitation of this choice arises when one tries to describe multicomponent BECs through coupled PDEs, since N_j, where the index j represents the condensate component, is no longer constant in this case. Instead the constant quantity is $\sum_j N_j$. Thus, when we proceed to discuss multicomponent condensates, a change will be made to use the form in Eqs (4.3) and (4.4). For the moment, we proceed from Eqs (4.1) and (4.2).

4.3.2 The Gross-Pitaevskii equation in 2D

Different degrees of flattening of trapped BECs are modelled by different physical approximations (Tanatar et al., 2002). For compactness of notation in the proceeding discussion we will drop the "+1" notation when referring to the dimensionality; the time dependence is implied. The production of vortices in pancake-shaped condensates may be numerically modelled in two rather than three spatial dimensions. The approach to reducing the simulation from 3D to 2D in this highly-flattened pancake regime is to make a simplifying assumption that the transverse xy and axial z solution components may be considered independently. The z-dimension of the BEC is then independently treatable as a simple 1D harmonic oscillator problem, giving a Gaussian distribution for the ground state z-profile. This distribution is then used to obtain the expectation value of the 2D transverse governing equation.

Separating the axial and transverse spatial components of Eq. (4.1) gives

$$i\hbar\partial_t\Psi = \left(-\frac{\hbar^2}{2m}\nabla_\perp^2 - \frac{\hbar^2}{2m}\partial_z^2 + \frac{m}{2}\left(\omega^2 r^2 + \omega_z^2 z^2\right) + NU_0\left|\Psi\right|^2\right)\Psi, \tag{4.5}$$

where the 2D Laplacian operator arises from separation of the full 3D Laplacian into its transverse and axial components, $\nabla^2 \equiv \nabla_\perp^2 + \partial_z^2$.

The axial dimension of the BEC is determined by the axial trap component $m\omega_z^2 z^2/2$, whose angular frequency ω_z relates to the characteristic length $a_z = [\hbar/(m\omega_z)]^{1/2}$.[3] When a_z is much greater than the scattering length a, the 3D order parameter may be separated into a product of independent axial and transverse components according to $\Psi_{3D}(r,\theta,z) \approx \Theta(z)\ \Psi_{2D}(r,\theta)$, where the axial condensate profile $\Theta(z)$ is assumed to be the well-known ground-state solution $\Theta_0(z) = (\pi a_z^2)^{-1/4}\exp[-z^2/(2a_z^2)]$ to the 1D linear time independent Schrödinger equation. This is a solution for a Schrödinger equation normalised to 1, so the 2D normalisation condition Eq. (4.2) in polar coordinates is now $2\pi\int_0^\infty |\Psi(r,\theta)|^2\, r\, dr = 1$. Appendix C contains a Mathematica notebook showing the following GPE derivation in detail. Evaluating the expectation value of Ψ_{3D} along the axial direction z (Tanatar et al., 2002; Lee et al., 2002)

$$\mathrm{GPE}(\Psi_{2D}) = \int_{-\infty}^{\infty} {\Theta_0}^*(z)\ \mathrm{GPE}(\Psi_{3D})\ dz, \tag{4.6}$$

results finally in a (2+1)D GPE that can be written in the conventional GPE form, with an additional nonlinear multiplication factor $\Gamma = [m\omega_z/(2\pi\hbar)]^{1/2}$ that represents the averaged value of the 3D nonlinear factor over all z:

$$i\hbar\partial_t\Psi_{2D} - \frac{\hbar\omega_z}{2}\Psi_{2D} = \left(-\frac{\hbar^2}{2m}\nabla_\perp^2 + m\omega^2 r^2/2 + \Gamma NU_0\left|\Psi_{2D}\right|^2\right)\Psi_{2D}. \tag{4.7}$$

An additional energy offset $\hbar\omega_z/2$ has also arisen. Because the observable quantity is $|\Psi_{2D}|^2$, it turns out that this may be *gauged away*, i.e. it is a constant factor that cancels in any evaluation of $|\Psi_{2D}|^2$. Therefore, for convenience, it is set to zero in the simulation.

The method just described is perhaps the most common for modelling a 3D system in 2D. An alternative method is to directly evaluate the nonlinearity occurring at $z = 0$, corresponding to the location of the peak density of the axial profile, and assign this value to Γ. In this case $\Gamma = |\Theta_0(0)|^2 = [m\omega_z/(\pi\hbar)]^{1/2}$. Since the nonlinearity achieves a maximum in the $z = 0$ plane, this method is arguably well suited to modelling the vortex dynamics. This latter approach was applied in

[3] Caveat lector: Here again, different conventions are followed in the literature with some authors choosing a similar but different length scale $a_z = [\hbar/(2m\omega_z)]^{1/2}$.

the simulations in this section, except where explicitly noted. Simulations were performed with both approaches and no qualitative difference was observed with any of the effects reported here. The reader preferring the former approach may note that the factor of $\sqrt{2}$ by which the Γ factors differ may be absorbed as a change in the number of condensate atoms N.

4.3.3 Dimensionless representation

It is common, when numerically solving physical problems, to deal with equations in terms of dimensionless variables, both in order to reduce the likelihood of numerical underflow or overflow errors, and also so that generated results are able to be mapped to a wide variety of physical systems by simply changing the dimension-scaling factors. The choice of physical variables to rescale is somewhat arbitrary and often a matter of convenience. Sometimes not all of the available variables are rescaled. As a result, several representations are found in the literature, which can be a source of confusion.

Conversion between the dimensionless and the fully-dimensioned physical system is conceptually not difficult, involving choosing some natural length and time scale of the system; in our case and that of most investigators this is based on the harmonic trap. Any physical properties of the system are then rescaled by these quantities. However, in the BEC literature some investigators choose different natural lengths or choose not to normalise all lengths or times in their systems. For example, in 3D it is common to base the natural length scale on the geometric mean of the harmonic trapping frequencies. However, as we are primarily interested in pancake-shaped condensates, it is natural to rescale the length and time variables in terms of the radial trap frequency ω and provide some consistency between our 2D and 3D representations. The length scale is then $l = [\hbar/(2m\omega)]^{1/2}$, hence the energy scale is $[\mathrm{M}][\mathrm{L}]^2[\mathrm{T}]^{-2} = ml^2\omega^2 \equiv \hbar\omega/2$.[4] The complete set of coordinate transforms is

$$t \mapsto \tau/\omega,\ r \mapsto \rho l,\ z \mapsto \zeta l,\ a \mapsto \alpha l, \tag{4.8}$$

which transform the dimensioned quantities time t, radial distance r, axial distance z, and scattering length a, to the dimensionless parameters τ, ρ, ζ, and α, respectively. The differentiation operators consequently transform according to $\nabla^2(r) \mapsto l^{-2}\nabla^2(\rho)$ and $\partial_t \mapsto \omega\partial_\tau$. Noting that the order parameter field Ψ is a probability density and hence has dimensions of $[\mathrm{L}]^{-3/2}$, it transforms according to $\Psi(r,\theta,t) \mapsto l^{-3/2}\varphi(\rho,\theta,\tau)$. Applying all these substitutions to Eq. (4.7), as

[4] This expression for the length scale l is common in the BEC literature, but so is $[\hbar/(m\omega)]^{1/2}$.

shown in the Mathematica notebook in Appendix C, results in the dimensionless equation

$$i\partial_\tau\varphi - \frac{\omega_z}{2\omega}\varphi = \left(-\nabla_\perp^2 + \frac{\rho^2}{4} + 4N\sqrt{\pi}\alpha\sqrt{\frac{\omega_z}{\omega}}\,|\varphi|^2\right)\varphi, \tag{4.9}$$

where $\varphi \equiv \varphi(\rho, \theta, \zeta, \tau)$ and $\rho^2/4$ is the radial harmonic trap term. Again, we can simply gauge away the $-\omega_z\varphi/(2\omega)$ term by deleting it. For the 2D simulation, this is the governing equation to use. For completeness, note that the normalisation condition Eq. (4.2) for a circularly-symmetric condensate in 2D polar coordinates, $2\pi\int_0^\infty |\Psi(r)|^2\, r\, dr = 1$, becomes $2\pi\int_0^\infty |\varphi(\rho)|^2\,\rho\, d\rho = 1$.

An alternative to transforming the 2D equation to dimensionless form is to start from the dimensioned 3D equation (4.5), apply the substitutions to obtain a dimensionless 3D equation, then reduce this to 2D. This approach is shown in the Mathematica notebook in Appendix C. Applying the transforms, remembering that we can gauge away the energy term, results in

$$i\partial_\tau\varphi = \left(-\nabla^2 + \frac{\rho^2}{4} + \frac{\zeta^2}{4}\left(\frac{\omega_z}{\omega}\right)^2 + 8N\pi\alpha\,|\varphi|^2\right)\varphi. \tag{4.10}$$

For a full 3D simulation, this would be the governing equation to use. Of course, reducing this to 2D, as shown in the Mathematica notebook in Appendix C, results in Eq. (4.9) as expected, which can equivalently be rewritten as

$$i\partial_\tau\varphi = \left(-\nabla_\perp^2 + \frac{\rho^2}{4} + 8\gamma N\pi\alpha\,|\varphi|^2\right)\varphi. \tag{4.11}$$

The dimensionless multiplication factor is $\gamma = [\omega_z/(4\pi\omega)]^{1/2}$, corresponding to $\Gamma = [m\omega_z/(2\pi\hbar)]^{1/2}$ or, if the peak axial density of the z-profile $\Gamma = [m\omega_z/(\pi\hbar)]^{1/2}$ is used, $\gamma = \varphi_0(\zeta = 0) = [\omega_z/(2\pi\omega)]^{1/2}$.

4.3.4 Establishing the ground state

To model the system numerically, the ground state order parameter must first be found for use as the initial condition of the time-dependent GPE.

The ground state is the eigenfunction solution of the time-independent GPE, including the light-sheet. This is obtained by time evolving a modified version of the time dependent GPE, obtained by Wick rotating the time variable t in the energy operator to a new time variable t', according to $t \mapsto it'$ [See, e.g., Chiofalo et al. (2000)]. We subsequently drop the prime from t'. The resulting equation is

$$\hbar\partial_t\Psi = \left(\frac{\hbar^2}{2m}\nabla^2 - \frac{m}{2}\left(\omega^2 r^2 + \omega_z^2 z^2\right) - NU_0\,|\Psi|^2 + \mu\right)\Psi. \tag{4.12}$$

The real-valued parameter μ has been added because the system acquires a constant energy associated with the number of atoms in the condensate, where this number converges to N as the iteration proceeds toward the ground state. In the limit $t \to \infty$, μ is identified as the chemical potential, which has dimensions of energy, rescaled by dividing by $\hbar\omega/2$ for the dimensionless case. In this limit, $\partial_t \Psi \to 0$ and Eq. (4.12) approaches the time-independent GPE, obtained by setting $\Psi(r,t) = \Psi(r)\exp(-i\mu t)$. Pethick and Smith (2008) note that μ adopts the role of a Lagrange multiplier (see also Minguzzi et al., 2004).

This technique is often termed *evolution through imaginary time*. The time evolution is performed by repeatedly stepping according to the chosen numerical scheme (e.g. fourth-order Runge-Kutta) and renormalising the order parameter at each iteration. Note that the Wick rotation is performed only on any time-dependent operators, not on the order parameter. This converts the wave equation into a diffusion equation, making it unconditionally stable. The appropriate initial condition to the ground state computation is the TF limit of Eq. (4.12) with the light-sheet $L(x,y)$ absent, which has a simple analytical form (see, e.g., Holland and Cooper, 1996; Bao et al., 2003). Starting with this limit should allow faster establishment of the ground state than starting from a Gaussian function or constant value, which are other commonly chosen initial profiles. The ground state computation then evolves the full expression

$$\hbar\partial_t\Psi = \left(\frac{\hbar^2}{2m}\nabla^2 - \frac{m}{2}\left(\omega^2 r^2 + \omega_z^2 z^2\right) + L(x,y) - NU_0\left|\Psi\right|^2 + \mu\right)\Psi, \tag{4.13}$$

to determine the true ground state.

4.3.5 Thomas-Fermi limit

The Thomas-Fermi (TF) limit of Eq. (4.1), which neglects the kinetic energy term $-\hbar^2\nabla^2\Psi/(2m)$, holds when the number of atoms is large (Pethick and Smith, 2008). It is found by substituting $\Psi(r,t) = \Psi(r)\exp(-i\mu t)$ into Eq. (4.1) with the kinetic energy term removed to give

$$\mu\Psi = \left(V + NU_0\left|\Psi\right|^2\right)\Psi. \tag{4.14}$$

Assuming a purely real order parameter field, as required of any steady-state solution, the cubic term $\left|\Psi\right|^2\Psi$ simplifies to Ψ^3 giving a simple polynomial equation in Ψ with the solution

$$\Psi(\mathbf{r}) = \sqrt{\frac{\mu - V(\mathbf{r})}{NU_0}}, \tag{4.15}$$

where we have selected the positive root. This is the steady-state profile for a condensate with chemical potential μ. In 1D, for a harmonic trapping potential, the profile $\Psi(r)$ is a parabola that reaches a maximum at $r = 0$ and is defined over the range $r \in [0, r_{\max}]$, where $r_{\max}$ is found by solving Eq. (4.15) for $\Psi = 0$.

In 3D, the approximate ground-state chemical potential μ corresponding to the TF limit is then found by applying the normalisation condition

$$\int |\Psi_{3D}|^2 \, dV = 1, \tag{4.16}$$

where $dV \equiv dx\,dy\,dz$ is a volume element. The resulting expression is (Pethick and Smith, 2008)

$$\mu = \left(\frac{15Na}{\bar{a}}\right)^{2/5} \frac{\hbar\bar{\omega}}{2}, \tag{4.17}$$

where $\bar{\omega} = (\omega_x\omega_y\omega_z)^{1/3}$ is the geometric mean trap frequency and $\bar{a} = [\hbar/(m\bar{\omega})]^{1/2}$ is the mean trap length scale. The dimensionless chemical potential is found by dividing by the energy scale $\hbar\omega/2$ to give

$$\mu = \left(\frac{15Na}{\bar{a}}\right)^{2/5} \frac{\bar{\omega}}{\omega}. \tag{4.18}$$

Substituting this into Eq. (4.15) gives the expression used as the initial profile for the numerical true-ground-state computation in 3D.

In 2D, Ψ is now the radially symmetric order parameter field Ψ_{2D}, and the appropriate normalisation condition is

$$\int |\Psi_{2D}|^2 \, dA = 1, \tag{4.19}$$

where $dA \equiv r\,dr\,d\theta$ is now an areal element, so $2\pi \int_0^{r_{\max}} |\Psi_{2D}|^2 \, r\,dr = 1$. The final dimensionless solution is

$$\mu = 2\sqrt{\gamma N\alpha}, \tag{4.20}$$

which is substituted into Eq. (4.15) [in which, for 2D, $\mathbf{r} \equiv (r, \theta)$] to give the correct expression used as the initial profile for the numerical true-ground-state computation in 2D.

4.3.6 Numerical method and implementation details

We have discussed the representation of the governing dynamical and ground state equations in the earlier parts of §4.3. Here we discuss some other computational issues, such as the determination of the grid size and associated domain, how and why to break the symmetry of the system, selection of the numerical methods, and the inclusion of a damping function.

Grid geometry

In the simulation, the continuous order parameter field Ψ is represented as complex scalar values in a discretised numerical grid. The physical geometry of an experiment may guide selection between Cartesian, polar, cylindrical-polar, or linear grid geometries. We used an underlying Cartesian grid geometry because the physical geometry has no rotational or translational symmetry which could be exploited to reduce computation time, and the pre-existing numerical codes supported this choice directly. A Cartesian grid also permits the application of Fourier operator methods, which can be much faster than direct-space methods.

A potential problem with matching the geometry of the numerical scheme to that underlying the physical system is that the symmetry is usually not precisely maintained in real experiments. The breaking of that symmetry may be necessary to give a true physical measure of certain time-dependent stability or coherence effects. By imposing a symmetry in the computational modelling, such physical effects may be partially or completely suppressed. In the three-piece BEC system, rotational symmetry is broken due to the presence of the light-sheet. However, one of the radial light-sheet walls may align with the underlying numerical grid. In order to minimise the effects of any such alignment, the light-sheet was rotated by $\pi/12$ to maximise the departure of the angle of any wall to that of one of the grid axes. In the 3D simulations, the axial dimension of the condensate is mirror symmetric about the xy-plane. A minimal attempt to break this symmetry was made by offsetting the centres of the grid voxels (the volumes whose vertices are grid points) from those of the grid along the z-direction. A more rigorous approach might be to rotate the whole condensate away from lying parallel to the xy-plane, or to perturb the axial harmonic component of the trap slightly, perhaps by adding a small cubic term to the quadratic trap potential.

Simulation domain and grid resolution

To map the simulation order parameter field to the numerical grid, both the grid resolution and the spatial limits of the simulation domain must be specified. These then determine the mapping from numerical array locations to physical coordinates. Increasing the resolution carries computational costs of both increased time and memory requirements, so we want to minimise the resolution whilst providing sufficient resolution for correct representation of the dynamics.

We must provide sufficient unoccupied space around the simulated BEC to correctly represent the condensate tails and allow for expansion due to dynamics beyond the initial profile. We also require additional unoccupied space in the

outer region of the grid to support inclusion of a damping function, which is described below. The BEC therefore occupies some initial fraction of the available simulation volume. A rule-of-thumb is to scale the simulation such that the condensate boundary, as determined by the TF limit (which does assume a hard boundary), occupies 50% to 75% of the simulation volume. Choosing a small fraction requires that we increase the overall resolution to adequately sample over the region of interest, whereas choosing a large fraction may lead to edge effects in the condensate tails.

The vortex cores in the condensate have a diameter approximately equal to the natural condensate length scale, called the healing length $\xi(\mathbf{r}) = 1/[8\pi n(\mathbf{r})a]^{1/2}$, which depends on the local density of condensed atoms $n(\mathbf{r}) = |\Psi(\mathbf{r})|^2$, and the scattering length a (Pethick and Smith, 2008). The Nyquist criterion suggests that we require two grid squares over this length scale ξ. However, to study effects that depend on the density profile near a vortex core, a higher resolution may be required. Conversely, as the phase winding is topological and hence its effect extends throughout the whole of the condensate, the healing length may represent a conservative length scale on which to base the resolution.

Clearly, there are many considerations in the choice of resolution and specification of the simulation domain. It is important to verify that the resolution is adequate; usually by doubling the resolution and testing that the dynamics do not change qualitatively, or preferably quantitatively if metrics are available. In practice, a numerical grid was chosen that, when doubled in resolution, gave identical results for the locations of vortices in the honeycomb lattice that forms as the BEC evolves. Subsequent to the lattice being destroyed, we observed chaotic vortex motion that was sensitive to initial conditions and the choice of numerical grid. For this evolution phase, we ensured that the dynamics did not change qualitatively as the grid resolution was changed.

The temporal resolution and evolution time must likewise be specified. The evolution time was chosen to permit dynamics to be observed over timescales of interest, which varied between different simulations. By analogy with the spatial criteria, the temporal resolution was chosen, such that when doubled, results were unchanged.

Numerical method

Many numerical schemes have been described for modelling the evolution of the GPE, which often requires care in its evaluation. PDEs are typically solved using finite-difference, finite-element, or finite-volume methods. The finite-element

and finite-volume approaches are often considered superior to finite-difference solvers for smoothly-varying fields, but do not lend themselves to representing fields containing topological defects. For this reason, we applied a finite-difference scheme.

The XmdS (2007) software package was adopted because it makes changing the particular finite-difference method easy and contains high speed, mature code that has been used for BEC simulations in several publications. It also supports parallelised execution on computer clusters and was therefore seen as more future-proof than other alternatives. From the available numerical algorithms, the fourth-order Runge-Kutta in the interaction picture (RK4IP) scheme was chosen, as this is a proven algorithm that executes with acceptable speed.

Because the Laplacian operator in the GPE has no spatial dependence, although the field on which it operates is clearly spatially dependent, it can be evaluated using a Fourier-operator method because the operator itself is applied uniformly. This means that the Laplacian operator is applied in the Fourier domain, which is more efficient for this purpose. Fourier-operator methods, based on the fast Fourier transform, operate most efficiently on grid sizes that are expressible in the form 2^n, $n = 1, 2, \ldots$ (Press et al., 1992).

Light sheet walls

The combined potential of the harmonic trap and light sheet was calculated as a real-valued 2D or 3D array, depending on the dimensionality of the simulation, in dimensionless units. Diffraction effects from the mask and additional optics place limits on the sharpness of the light sheets. To simulate these effects, the light sheet pattern was first calculated in 2D before being convolved with an optical point spread function in Fourier space by multiplication by a second order, low-pass Butterworth filter, whose spatial cutoff frequency was found by trial and error. The resulting blurred light-sheet pattern was then optionally extended to 3D and scaled to the correct relative amplitude before being added to the harmonic trap potential, which was itself calculated in either 2D or 3D.

Damping function

The time-dependent solution of the GPE requires careful choice of the simulation domain to avoid propagation of effects to the edges. Depending on the implementation of the numerical method, this can either cause reflections or wrapping at the boundaries of the simulation region, which can propagate back into the region of interest. The way to determine whether this is occurring is to add a purely

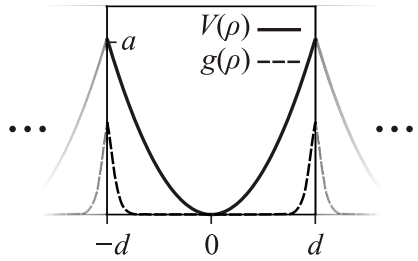

Figure 4.4: Harmonic trap $V(\rho)$ and damping function $g(\rho)$ in 1D showing the aliasing effect arising from the Fourier operator method. $V(\rho)$ achieves a maximum a at the limits $-d$ and d of the numerical lattice.

imaginary damping function $ig(\mathbf{r})$ to the Hamiltonian in the simulation that has no effect within the region of interest but damps the matter near the edges. By monitoring the total number density $\int |\Psi|^2 \, dV$ of the simulation over time, one can check that the simulation region is sufficiently large, since, the damping function absorbs matter near the edges, reducing the number density. The trade-off is that the damping function occupies part of the numerical grid requiring the simulation domain to be slightly larger.

A suitable shape for the damping function is a *super-Gaussian*, which has the basic form $g(\rho) = g_{\max}\{1 - \exp[-(\rho/\rho_0)^M]\}$, where M is the order ($M = 2$ recovers the standard Gaussian form), $\rho = \sqrt{x^2 + y^2}$, ρ_0 is a factor related to the standard deviation, and $g_{\max}$ is a scaling factor. Figure 4.4 shows an example of the desired functional form, showing the effect of aliasing (spatial wrapping) due to the application of the Fourier operator scheme. Some typical values used in the simulations were $M = 20$ and $g_{\max} = 100$, where this maximum value was determined to be of the same order as the maximum value a of the harmonic trap potential $V(\rho) \equiv \rho^2/4$ at the domain limit. These values, with $\rho = 26$ and $\rho_0 = 25$ are illustrated in Fig. 4.4. In fact, different forms of the super-Gaussian with different symmetries were used for the 2D simulations (i) with, and (ii) without the transverse trap, and (iii) for the 3D simulations in which both trap components were present:

$$\begin{aligned}
&\text{(i)} && g_{\max}\left\{1 - \exp\left[-\left(\frac{\rho}{\rho_0}\right)^{20}\right]\right\}, \\
&\text{(ii)} && g_{\max}\left\{1 - \exp\left[-\left(\frac{x}{x_0}\right)^{20} - \left(\frac{y}{y_0}\right)^{20}\right]\right\}, \\
&\text{(iii)} && g_{\max}\left\{1 - \exp\left[-\left(\frac{\rho}{\rho_0}\right)^{20} - \left(\frac{z}{z_0}\right)^{20}\right]\right\}.
\end{aligned} \tag{4.21}$$

4.3.7 Vorticity metric

Independently of the above mean field model, which allows us to simulate the time evolution of the condensate, we define a vorticity metric for the order parameter field Ψ. This provides a quantitative measure of the degree of vorticity over time and relates to the number of vortices and antivortices produced due to any dynamical processes. The metric is

$$\text{vorticity} = \frac{1}{V} \iint \left| \nabla \times \mathbf{j} \right| \, dx \, dy, \tag{4.22}$$

where the integral is over the numerical field of volume V, and $\mathbf{j}$ is the probability current density $\mathbf{j} = i\hbar(\Psi \nabla \Psi^* - \Psi^* \nabla \Psi)/(2m) \equiv (\hbar/m)\mathrm{Im}(\Psi^* \nabla \Psi)$.[5]

This metric is similar to the usual vorticity measure in fluids $\boldsymbol{\omega} = \nabla \times \mathbf{v}$, of the velocity field $\mathbf{v} = \mathbf{j}/\rho$, where $\rho = |\Psi|^2$ is the local probability density (Acheson, 1990, p. 10). By not dividing the probability current by ρ, extra weighting is conferred upon vortices located within a locally increased density over vortices in regions of lower density. This modification of the usual expression provides a degree of robustness to the metric, because low density regions are more prone to acquiring random phase windings due to numerical errors. The metric sums the modulus of the local vorticity measure over the whole field.

The argument of the modulus operator in Eq. (4.22) is a function that is peaked at any vortex cores. These peaks provide a means of detecting and visualising vortices and antivortices, prior to integration to obtain the global vorticity measure. Computing this argument involves evaluating grad and curl operators numerically. Numerical differentiation algorithms are prone to introducing noise artefacts and must therefore be carefully chosen. Our results might be improved by taking further care in the evaluation of these differential operators, for which Fourier-based methods are currently employed.

4.4 Results from the three-way segmented pancake-BEC

In this section, we demonstrate with numerical simulations that vortices are produced by a three-segment pancake-shaped BEC devoid of initial phase variations and show that this mechanism is, in contrast with the two-piece case, predicted by the linear theory that was developed in §2.4.2. In contrast with Carretero-González

[5] The version of this expression in Ruben et al. (2008) erroneously omitted an overall factor $-i$, although all computations correctly apply the form shown here.

et al. (2008a), we have not sought to replicate the Scherer et al. (2007) experiment exactly. By instead focusing attention on those initial states characterized by a constant phase, we aim to demonstrate that initial phase variations are unnecessary for vortex formation. In addition, we demonstrate interference and vortex production in the absence of a confining transverse trap, thereby reducing the degree of influence of any nonlinear processes at play (namely, the snake instability) in two-fragment condensate interference, and providing deeper insight into the assertion that the vortex generation mechanism for three symmetrically arranged, well-separated pieces is, by contrast, primarily a linear process.

By increasing the intensity of the light sheet, we have also been able to generate a lattice comprised of significant numbers of vortices and antivortices. In the trapped system, the regular VA lattice subsequently melts, exhibiting a diversity of interactions, for example, self-propelled vortex-antivortex dipoles (VDs) (Nozières and Pines, 1990; Crasovan et al., 2003; Möttönen et al., 2005; Sakaguchi and Higashiuchi, 2006; Higashiuchi and Sakaguchi, 2007; Pietilä et al., 2006; Klein et al., 2007; Carretero-González et al., 2008a), rotating vortex tripoles, and quadrupoles (Möttönen et al., 2005; Pietilä et al., 2006). These interactions between vortices and vortex clusters in the condensate include dipole scattering and annihilation events. The large vortex population produced in the trapped system makes it an excellent environment for the study of vortex dynamics, VDs, and vortex-sound interactions (Pismen, 1999).

4.4.1 Modelling the experiment

We model an experiment similar to that conducted by Scherer et al. (2007) (see also Scherer, 2007) but note the following features that distinguish our simulation from the experiment and its modelling by Carretero-González et al. (2008a). First, in order to demonstrate vortex production as predicted by the linear theory, we establish an initial condition prior to time evolution that is a ground state with a uniform global phase, so that no initial phase variation is allowed within or between the three pieces. In contrast, phase variations were present in the initial model conditions of Carretero-González et al. (2008a). Although we subsequently also apply an example of different relative phases to the three pieces following establishment of the ground state, this is presented to demonstrate how the linear theory applies to this case. The second distinguishing feature is the instantaneous removal of the light sheet at $t = 0$. In contrast, Scherer et al. (2007) removed the light sheet at varying finite rates, but reported a maximum efficiency of vortex generation for the maximum observable rate of removal. A final difference is

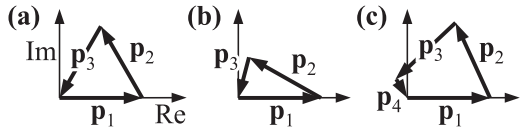

Figure 4.5: Representing the sources with a phasor diagram, vortices lie at locations corresponding to a closed loop of phasors. (a) Three sources linearly superposed. (b) Two sources and a nonlinear interaction term. (c) Four sources linearly superposed or three sources plus a nonlinear interaction term.

that we present simulations with and without the transverse trap to demonstrate that lack of transverse confinement is not an impediment to vortex production, consistent with predictions from the linear theory.

In this section we model the system in 2D and address our conclusions to the case of pancake-shaped condensate clouds, in which the ratio of the axial to transverse trap frequencies is large in the sense outlined below. Later, in §4.5, we present fully 3D results and compare these with the pancake-condensate.

4.4.2 Phasor description for nonlinear interference

In weakly nonlinear systems, typical of experimentally realistic BEC systems, we expect to observe phenomena approximately predicted by the linear theory. The creation of a VA lattice is one such observation, whose geometry was described in §2.4.2. In this section we explain the extension of the model of production of vortices by linear interference, from which the lattice is formed, to nonlinear systems.

In order to form vortices by a linear interference process, we have explained that at least three source waves are required (Braunbek, 1951; Masajada and Dubik, 2001). Figure 4.5(a) illustrates this minimal requirement for three complex scalar wave sources of equal amplitude whose sum $\Psi_1 + \Psi_2 + \Psi_3$, evaluated at the vortex location, is represented graphically as a sum of phasors $\mathbf{p}_1 + \mathbf{p}_2 + \mathbf{p}_3$.

Alternatively, Fig. 4.5(b) represents a nonlinear system in which the third, weaker contribution is now associated with the interaction term in the sum $\Psi_1 + \Psi_2 + f(\Psi_1, \Psi_2)$. The production of vortices by the snake instability might be represented by such a picture. Thus, a loop of n phasors may correspond either to the interference of n sources in a linear system, or to $n-1$ sources plus a nonlinear interaction term. Although both (a) and (b) are illustrations of vortex production, the physical source of the phasor contributions determines whether the production is or is not a primarily linear process. In (a) no interaction term is operating yet the phasors form a closed loop, so we say that the interaction is

linear. In (b), if we remove the contribution of $\mathbf{p}_3$ due to the interaction, we are left with two phasors, which cannot form a closed loop, so any vortices must arise from nonlinear processes.

As a further example, Fig. 4.5(c) may represent either four sources $\Psi_1 + \Psi_2 + \Psi_3 + \Psi_4$ in the case of a linear system, or three sources plus a nonlinear interaction term $\Psi_1 + \Psi_2 + \Psi_3 + f(\Psi_1, \Psi_2, \Psi_3)$ in the case of a nonlinear system. In the latter case we would still claim vortex production is due to a primarily linear process, since removing $\mathbf{p}_4$ results in an *almost* closed loop of phasors.

The results of the interference of 2D condensates sliced into two and four pieces have been studied (Carretero-González et al., 2008b). Examination of these results for the case of four pieces suggest that sufficient contributions from at least three of the four source pieces have combined in a primarily linear process. Further evidence for the role of the linear interference mechanism is presented in §4.4.3.

4.4.3 Results

In Fig. 4.6 we present simulations, showing the probability density and phase, of the evolution of a BEC initially segmented into three pieces. The global ground state in Fig. 4.6(a) is established within a harmonic trap with a superposed three-way light sheet. Two cases of subsequent evolution are shown, following instantaneous removal of the light sheet. In both cases, the pieces expand and interfere to form a VA lattice. In the first case [Fig. 4.6(b)], evolution proceeds within the confining harmonic trap and we observe a turbulent condensate in which the vortices have migrated from their initial locations following melting of the lattice.

In the second case [Fig. 4.6(c)], the transverse trap is removed along with the light sheet, and the lattice expands over time whilst maintaining its form. For this latter case, the outer parts of the condensate expand beyond the finite simulation domain. To allow for this in the numerical model, the damping term Eq. (4.21)(ii) is added to the GPE to absorb the outward propagating matter; the images have been cropped to remove the visible effect of this term. For all simulations prior to §4.4.6 in which the transverse trap is removed, the probability density images are independently normalised to the peak value within each image. This compensates for any overall decrease in the visibility of matter removed by the damping term. The normalisation, combined with the choice of colour-map, allows us to present the lattice evolution and other structures clearly, but it is likely to give a false sense of their visibility in real experiments. We discuss this point further in §4.4.6.

The parameter values used in our simulations were $a = 5.77 \times 10^{-9}$ m for ^{87}Rb (Dalfovo et al., 1999), $N = 2.6 \times 10^5$, $\omega = 46.5\,\text{rad s}^{-1}$ and $\omega_z = 88.6\,\text{rad s}^{-1}$.

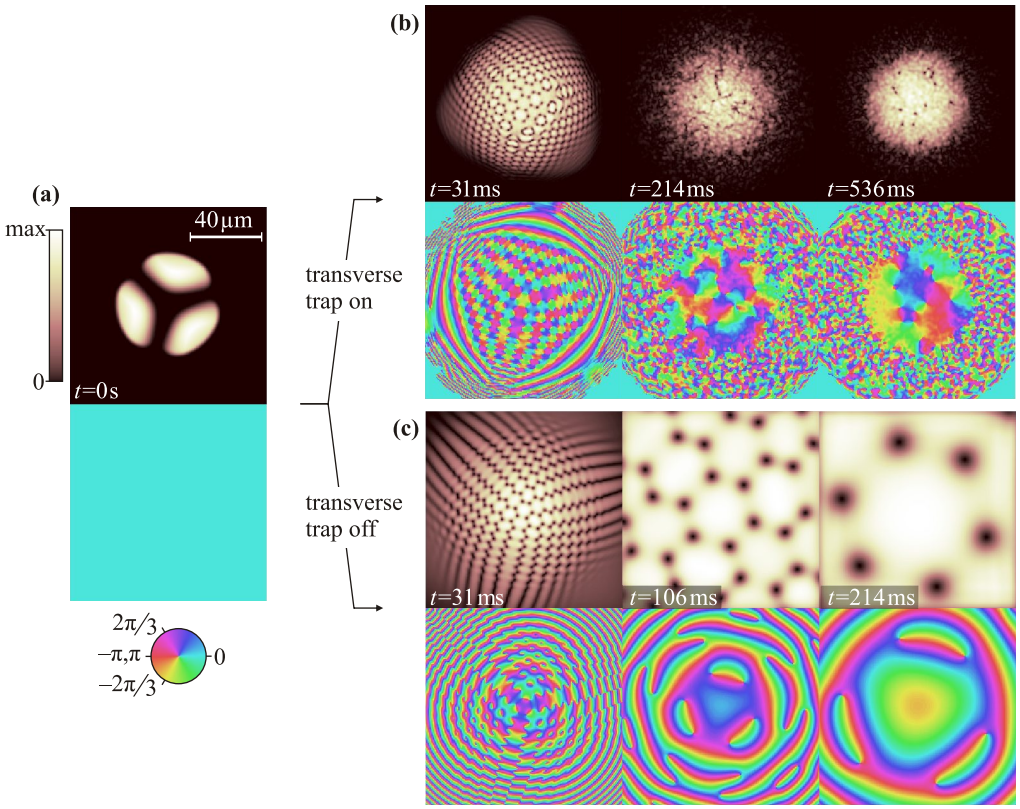

Figure 4.6: Probability density (upper) and associated phase plots (lower) for a three-segment BEC formed in a 2D harmonic trap with a superposed three-way light sheet of dimensionless amplitude $I_0 = 0.8$. All panels are of equal area. (a) Initial state with the lower constant-colour panel showing identically-equal phase. (b) Interference in the presence of a transverse confining trap showing progression through lattice formation to a late-stage characterized by turbulent vortex-antivortex (VA) dynamics. (c) Free expansion and interference with the transverse trap component removed showing honeycomb lattice formation.

The intensity of the laser light sheet is represented by a dimensionless quantity I_0. Figure 4.7 is a contour plot of the combined harmonic trap and light sheet potentials, which relates their scales. We have chosen to present results for $I_0 = 0.3$ and $I_0 = 0.8$, as these values allow exposition of the different behaviours of poorly and well separated BEC pieces, respectively. As shown in the trap profile plots, the walls are characterized by wall height h_0, expressed in units of energy, and full width at half maximum width w_0. $I_0 = 0.3$ and 0.8 correspond to $h_0 \approx k_B \times 70$ nK and $k_B \times 180$ nK, respectively; both higher than the $k_B \times 26$ nK barrier produced by Scherer et al. (2007). Our wall width $w_0 \approx 9$ μm may be challenging to produce experimentally. A comparison value is not given in Scherer et al. (2007), although the condensate profiles are indicative of wider walls.

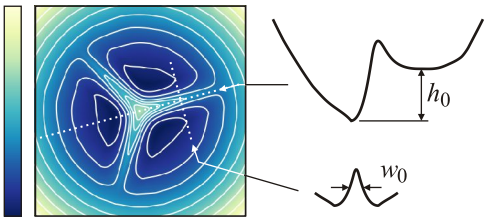

Figure 4.7: The 2D harmonic trap with a superposed three-way light sheet of dimensionless amplitude $I_0 = 0.8$ shown with contours of constant potential. The trap profiles identifying wall height h_0 and width w_0 are taken along the dotted paths.

Since these are 2D simulations, and as such are applicable to pancake-shaped condensates, to maximise the validity of the results when compared to experiment would require maintenance of the axial trap component in both cases, not just to allow for establishment of the lattice, but also for any free-expansion stage prior to imaging. The consequence of removing the axial trap at $t = 0$ is that experiment will no longer correspond to these simulations, as the axial condensate density will immediately begin to reduce. In Ruben et al. (2008) we provided an argument in favour of maintaining the axial trap. In light of the regularity of the interference pattern in Henderson et al. (2009), our opinion has changed, for the case where one is aiming to produce a regular honeycomb lattice, in favour of simultaneously removing both the axial and transverse traps. This has no adverse effect on the ability to image the condensate as imaging typically integrates the density along the z-direction. Thus, in cases where we attribute deviation from the predictions of the linear interference model to nonlinear effects, these effects will play a much less significant role compared to the simulations. The effect of removing the axial trap at $t = 0$ is explored further in §5.3.1.

In Chap. 2, we demonstrated the production of a distorted honeycomb VA lattice from the linear interference of three expanding monochromatic spherical waves. In §2.4.2, we presented a related linear theory for the case of three Gaussian wavepackets, evolving in (2+1)D, and clarified the effect of source phase variation on the predicted vortex locations. In this case, it was stated without evidence that an infinite, regular honeycomb VA lattice is formed, with a Gaussian probability density envelope. Figure 4.8 presents the results of that model for the equal [Figs 4.8(a–b)] and rotated [Fig. 4.8(c)] phase cases, demonstrating the honeycomb symmetry. The formation of vortices by a three-piece BEC may be understood as arising from the same mechanism, albeit now in a nonlinear system.

For these examples, the source spacings r_2 and r_3 [see Fig. 2.3], and the momentum uncertainty Δp were determined by fitting Gaussian profiles to the leading

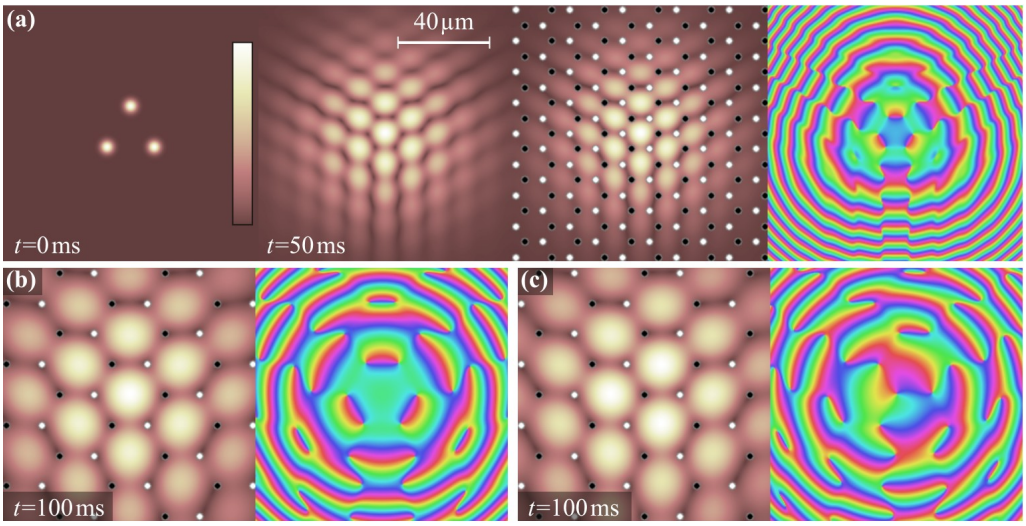

Figure 4.8: Three linearly superposed Gaussian wavepackets lying at the corners of an equilateral triangle [cf. Figs 4.6(c) and 4.9(c)]. The amplitude and phase of Eq. (2.48) are shown, with vortices (dark) and antivortices (light) analytically determined from Eqs (2.56) and (2.58). (a) Equal-phase wavepackets shown at 0 ms, after interference at 50 ms (with and without the overlaid lattice), and (b) after 100 ms. (c) Phases 0, $2\pi/3$ and $-2\pi/3$ cause a lattice translation.

(innermost) edges of the probability density of the three BEC pieces at $t = 0$ for the $I_0 = 0.8$ case, i.e. from Fig. 4.6(a). Because the model assumes that the BEC pieces are well described by circularly-symmetric Gaussian pieces, which is not the case here, this approach was found to be better than fitting to the whole BEC-pieces. Applying this method, the honeycomb lattice parameters of the nonlinear simulation and linear model match to within $\approx 20\%$ near $t = 100$ ms. Note that, in Ruben et al. (2008), we erroneously stated that the linear model cannot be usefully applied to the nonlinear simulations as the lattice parameters match poorly, and as such "the linear model is best applied qualitatively." This statement was made based on incorrectly calculated simulation frame times. In fact, in light of the uncertainties arising from the Gaussian fitting approach, the linear model can be applied to provide a useful quantitative prediction of the lattice parameter and its evolution.

The linear theory applies most directly to the untrapped system. For observing interaction dynamics, the presence of the trap must be maintained. However, if the interference is instead performed with the transverse trap switched off, experimental measurement of the lattice parameter, and the position of any central vortex with respect to the centre of mass of the BEC cloud, should allow determination of the relative phases of the initial BEC pieces. Figure 4.6(c) shows the formation

of an extremely regular lattice, which compares favourably with that formed by linear superposition in Fig. 4.8. The locations of vortices and antivortices coincide, as revealed by the similarity of the phase maps in Fig. 4.8(b) and Fig. 4.6(c) at $t = 106$ ms.

Scherer et al. (2007) observed vortices consistent with production by the KZ mechanism. They reported that 10% of nonsegmented condensates contain vortices. In our simulations, by starting from a state in which the phases of the initially separated pieces are equal, no vortices may be produced by this mechanism. The KZ mechanism is primarily concerned with the symmetry-breaking phase transition that occurs when a number of domains of different local phases, created by non-causally-connected randomly seeded phase values, are reconciled to either generate or fail to generate vortices at the vertices of neighbouring domain boundaries (Anglin and Zurek, 1999). The method of reconciliation is a side issue in this description, although the formation of the individual vortices that comprise the honeycomb lattice could be considered to arise in this way. However, the KZ mechanism confers no overall symmetry that relates the locations of multiple vortices. The lattice's honeycomb symmetry is therefore not explained by this picture and must arise from longer-range phase coherence due to the propagation of the initial piece phases over length scales greater than the lattice parameter, or any domain size used in the KZ description.

A laser beam illuminating a ground glass plate (GGP) may also serve as a model of the KZ mechanism. As we saw in Chap. 3, the optical field acquires random phases due to GGP height variations, and the propagated field generates vortices as a result of interference. In the near-field region, where secondary spherical wavelets have not propagated beyond their local neighbourhood, they will interfere with neighbouring wavelets to produce a speckle field with vortices produced by interference. This is the KZ mechanism. Furthermore, the Laguerre-Gauss (LG)-beam in Chap. 3 can be interpreted as conferring long-range order on the wavefield exiting the GGP; in this way the LG beam is analogous to a source exhibiting long-range phase coherence. Whereas in the BEC case, this long-range coherence is exhibited as the formation of the honeycomb lattice, in the model of an LG-beam illuminating a GGP, it manifests as the background helical phase present in the speckle field which subsequently leads to recovery of the LG beam profile. In the optical model, the analogy is tested beyond the region close to the GGP surface, since the wavelets continue to expand beyond the local neighbourhood, albeit with decreasing influence as their amplitude A decreases as A/r with distance r.

Returning to BECs, if the three pieces are sufficiently isolated from each other, they may acquire random relative phases (Röhrl et al., 1997). Scherer et al. (2007)

describe the presence or absence of a central vortex according to reconciliation of these phases. The linear theory instead describes an equivalent effect, which predicts the central vortex as resulting from translation of the lattice as a whole. Röhrl et al. (1997) state that the pieces are "virtually degenerate," allowing them to be treated as coherent pieces whose relative phases may vary randomly. For a lower intensity light sheet, BEC tunnelling through the light-sheet walls ensures that the phases of the separate pieces remain coupled. The interference pattern is said to become "locked." In our case, the lattice translation becomes locked in an equivalent sense to give the result in Fig. 4.6. To simulate the effect of decoupling between the pieces, we apply global phase factors by rotating the phase of the BEC pieces, following establishment of the ground state but prior to time evolution.

In Fig. 4.9, the relative phases of two of the regions have been rotated from 0 to $2\pi/3$ and $-2\pi/3$, as shown in the $t = 0$ s phase plot. The $t = 106$ ms and $t = 214$ ms cases without a transverse trap show a vortex at the centre. This may be understood by evaluating the predicted vortex locations using the linear theory. As shown in Fig. 4.8(c), the linear theory predicts the generation of the central vortex as resulting from an overall lattice translation.

If the initial phases are close to these values, a vortex will be created close to the centre of the trap. If the wall height is also low, few other vortices will be produced and the near-central vortex will be free to migrate and take up residence in the centre of the trap. The central vortex in the final frame of Fig. 4.10(c) exemplifies this behaviour. Since flows associated with phase gradients cancel in the centre, any resident vortex occupies a privileged position and remains there until perturbed by a local change, such as might be caused by a passing vortex set in motion following melting of the lattice.

Figure 4.10 presents further examples of trapped and untrapped BECs, which are included to illustrate several predictions of the linear theory, such as the effect of changes in light-sheet intensity and geometry. These predictions are measured by the vorticity metric Eq. (4.22), which is plotted against time for four different initial conditions in Fig. 4.11(a). Figures 4.11(b–c) are time-series plots of the vortices in the side-on condensate slices. These are plots of the thresholded argument of the modulus operator in Eq. (4.22). In these figures, period (i) denotes the initial formation of the regular VA lattice. In the subsequent period (ii), the regular lattice melts, as the condensate matter washes back towards the centre due to confinement by the harmonic trap. During this subsequent period, the high population of vortices and antivortices promotes a high interaction rate characterized by a rich variety of vortex interaction dynamics. VA annihilation reduces the vortex population to a level where this rate slows and dynamics involving VDs begin

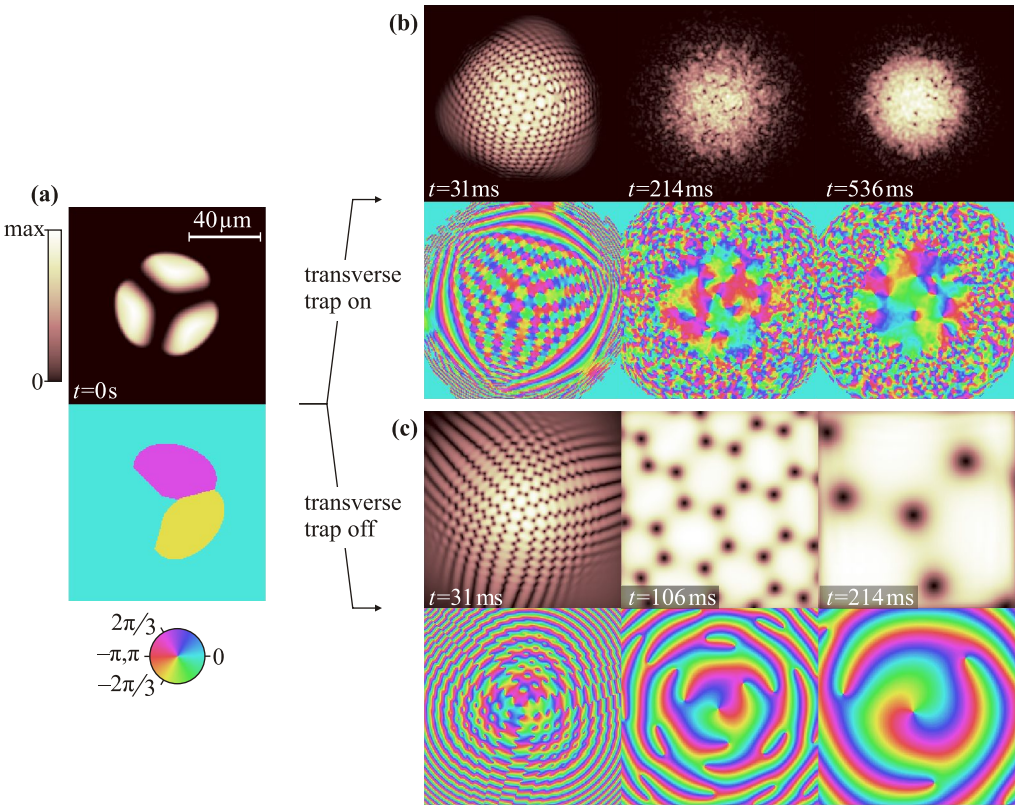

Figure 4.9: Probability density (upper) and associated phase plots (lower) for the three-segment BEC with the initial piece phases rotated to 0, $2\pi/3$ and $-2\pi/3$. (a) Initial state with the lower panel showing the phases assigned at $t = 0$ prior to time evolution. (b) Interference in the presence of a transverse confining trap showing a similar time evolution to Fig. 4.6. (c) Free expansion and interference in the absence of the transverse trap showing a honeycomb lattice similar to Fig. 4.6(c) but with the effect of the initial phase winding clearly visible as a change of phase symmetry and an associated lattice shift so that an antivortex coincides with the trap centre.

to dominate in the final period (iii). The inward and outward motion is roughly circularly symmetric, cyclically increasing and decreasing the probability density in the centre. These global oscillations are visible in Fig. 4.11(a) due to the vorticity measure giving extra weight to vortices embedded in a locally increased condensate probability density. The predicted frequency of the radial breathing mode of a harmonically trapped 2D condensate is twice the trap frequency ω (Pitaevskii, 1996) (in our simulations $\omega = 46.5$ rad s^{-1}). The measured frequency from the lower three plot series, whose condensates have centroids coinciding with the trap centre, is 93.6 ± 0.6 rad s^{-1}, in agreement with theory. From Figs 4.11(b) and (c) we see that the vortices themselves are carried in and out by the bulk motion of

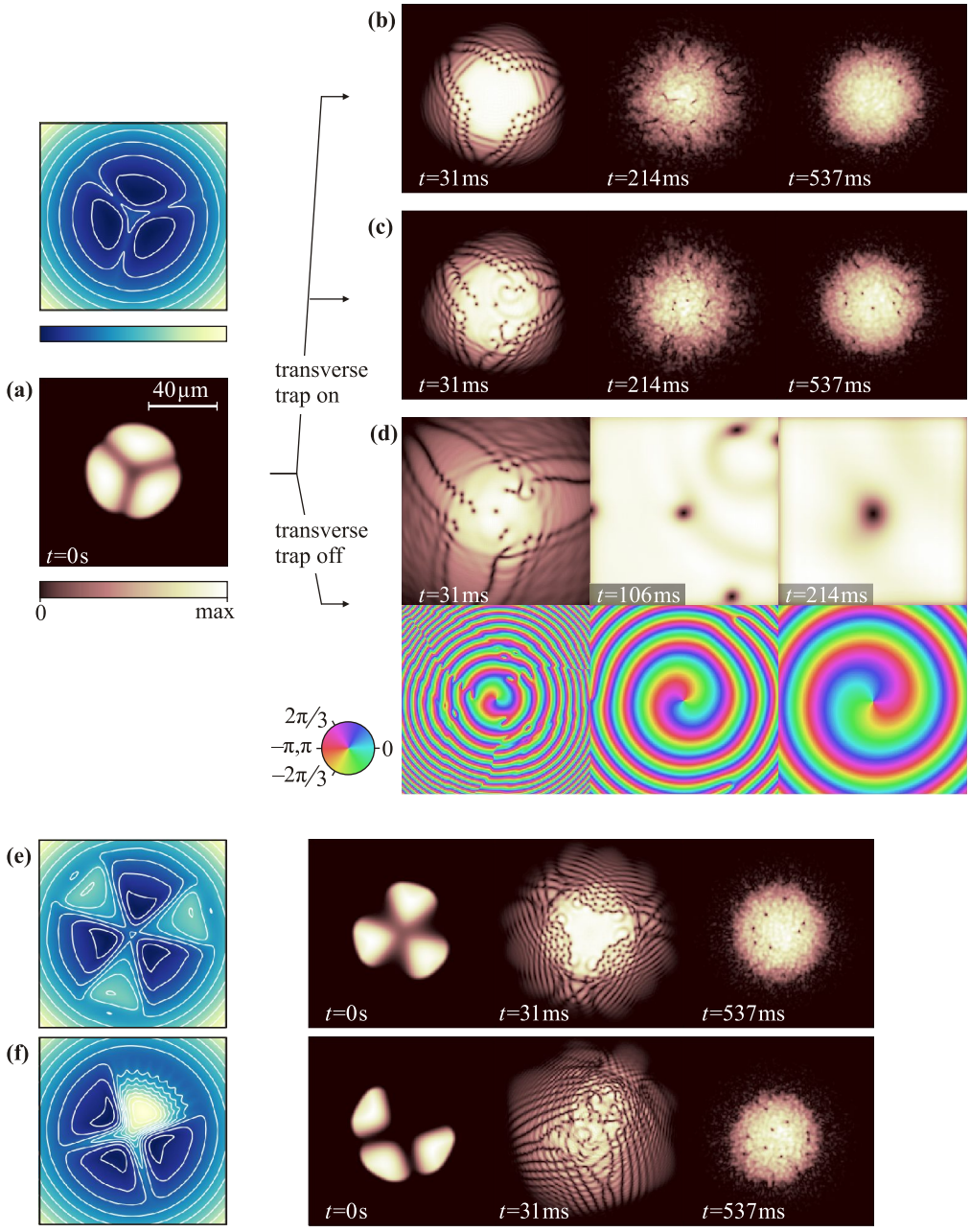

Figure 4.10: Probability density [and associated phase plots for (d)] for light sheets characterized by the trapping potentials shown as adjacent contour plots. (a–d) When compared with Fig. 4.6, the lower intensity light sheet ($I_0 = 0.3$) allows vortices to propagate outwards with the condensate matter. In (b), the central region of the lattice is left devoid of vortices. In the trapped (c) and untrapped (d) cases, in which the relative phases of the initial pieces are set to 0, $2\pi/3$ and $-2\pi/3$, the central vortex is clearly visible. (e–f) Two alternative arrangements with (e) propeller-shaped pieces, and (f) pieces at three corners of a square are discussed in the main text.

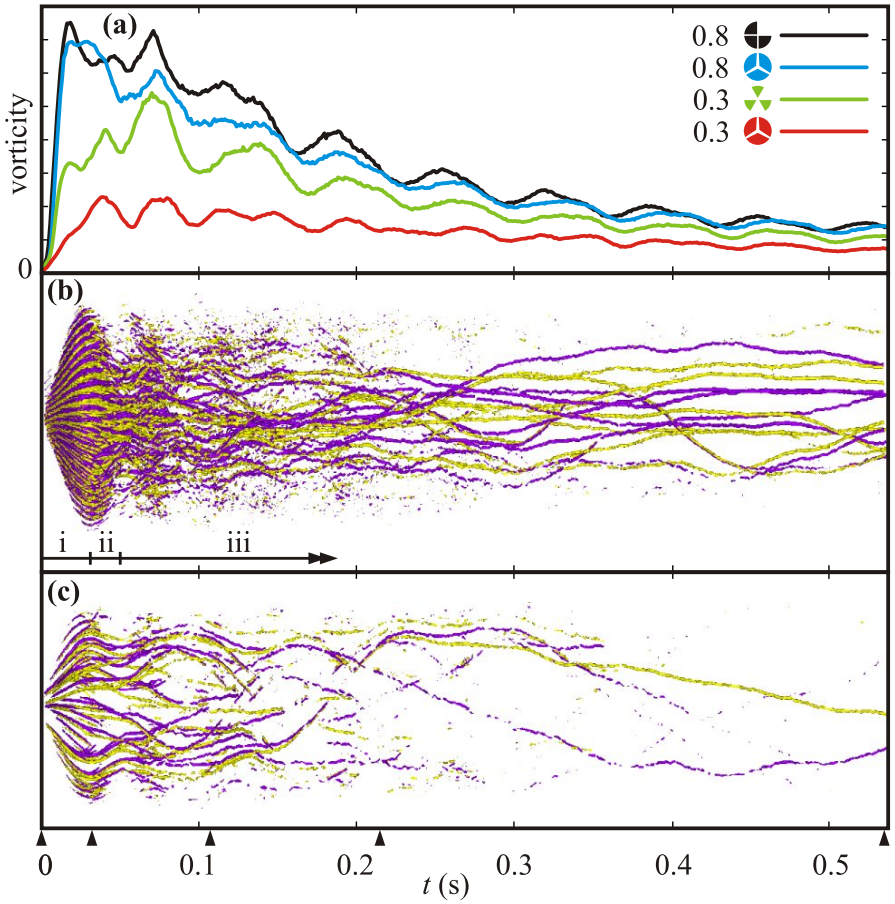

Figure 4.11: Vorticity plots for selected BEC segmentation schemes with a harmonic trap. Small arrows along the time axis correspond to the times selected in Figs 4.6 and 4.10. (a) Vorticity measure [Eq. (4.22)] for $I_0 = 0.3$ and 0.8 and for sources at three corners of an equilateral triangle, a square and propeller shaped schemes (see main text). (b) Vortices (dark) and antivortices (light) generated from the equilateral triangle scheme with $I_0 = 0.8$. Regions (i), (ii) and (iii) are described in the main text. (c) Fewer vortices are produced with a lower intensity $I_0 = 0.3$ light sheet.

the condensate matter, presumably changing the vortex interaction rate in turn. The interaction dynamics are discussed in more detail in §4.4.5.

A lower wall height results in the pieces starting closer together. In the linear theory describing the three-pinhole interferometer (see §2.3), correspondingly smaller r values generate smaller numbers of vortices. This is clearly illustrated by the smaller vorticity values in Fig. 4.11(a) and the reduced population of vortices in Fig. 4.11(c) over Fig. 4.11(b). In Figs 4.10(b–c), we see that the matter expanding from the centre carries most of the vortices to the outer parts of the trap as the lattice is forming, where they may be lost altogether, further reducing the vortex

population.

The propeller shape in Fig. 4.10(e) is included to show an alternative mask, which also produces BEC pieces at 120° angles to each other, but which pushes the centres of the condensate pieces further apart. Accordingly, higher numbers of vortices are predicted by the BEC created from this mask. Indeed, this is the case, as can be seen by comparing the bottom two results in Fig. 4.11(a), which plot vorticity for the same light sheet intensity $I_0 = 0.3$ for the two 120° alternatives.

The linear theory in §2.3 predicts the production of a maximum number of vortices for a source arrangement in which the pieces are initially arranged at three corners of a square. This prediction guided investigation of the source configuration shown in Fig. 4.10(f), which may be realized by a cross-shaped light sheet mask with one quadrant open to the passage of light from the illuminating laser. Confirmation of the prediction is apparent by comparing the top two results in Fig. 4.11(a), which are for the same light-sheet intensity. In fact, the spacing of the condensate centroids for the 90° arrangement is smaller than for the 120° case. Thus the increase in vorticity due to the angular arrangement more than offsets the decrease in vorticity-generating capacity caused by reducing the piece spacing. Whilst we have shown a geometry with an increased capacity to generate vortices, it is possible that nonlinearity causes the absolute maximum to be achieved for another angle close to 90°. Evidence of nonlinear effects is visible in this case; the snake instability (Kivshar and Luther-Davies, 1998; Brand and Reinhardt, 2002) is visible as a curvature of some fringes of the second frame in Fig. 4.10(f). On closer inspection we see that the linear vortex generation mechanism dominates in this region, as disturbances from the third BEC piece propagate through and interfere with these fringes prior to the snake instability evolving to form vortices directly. The initial displacement of the condensate centroid from the centre of the trap results in the merged condensate oscillating back and forth along the initial mirror symmetry plane, in addition to the radial oscillation mode. In a previous investigation the ability to suppress the snake instability was reported in a system containing an RDS – a dark stripe soliton formed into a closed loop – that shared the circular symmetry of the confining harmonic trap (Theocharis et al., 2003). Depending on the RDS parameters, this structure could preferentially decay by emission of phonon radiation instead of the snake instability. In the three-segment BEC system, the intervention of linear interference can be seen as another means for suppressing the onset of the snake instability in dark stripe solitons.

A possible explanation for Scherer et al. (2007) not observing the production of large numbers of vortices along with a regular lattice in experiments may be their application of light-sheet intensities below our lower intensity results. Blur-

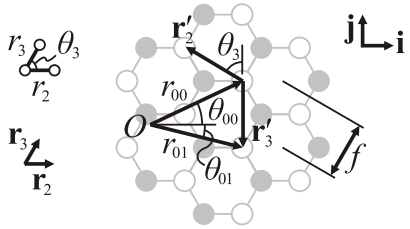

Figure 4.12: The lattice formed from the interference of three Gaussian wavepackets has a description in terms of crystallographic basis vectors $\mathbf{r}'_2$ and $\mathbf{r}'_3$, which relate to the source position vectors $\mathbf{r}_2$ and $\mathbf{r}_3$. Here, $\mathbf{i}$ and $\mathbf{j}$ are the usual Cartesian unit basis vectors.

ring and possible nonuniformity of the light-sheet walls is related to the size and manufacturing process used for the mask; attention to the design of the mask optics and optical path may permit the creation of more uniform, sharper walls, leading to the lattice structures we see in our simulations. Also, real experimental initial conditions with a non-zero-temperature chemical potential introduce some phase randomness which would disrupt the lattice. Finally, as noted by Carretero-González et al. (2008a), if the condensate is more spheroidal than pancake-like, the probability of observing vortices in the projected 2D image is reduced due to the extra freedom of possible vortex line geometries.

4.4.4 Crystallographic lattice description

Henderson et al. (2009) performed an experiment in which three Bose condensed "spots" of ^{87}Rb, arranged at the corners of an equilateral triangle of side length 14 μm, were formed in a pancake trap. A measurement was made of the "fringe spacing" f of the resulting interference pattern 19 ms after removal of both the spot-forming trap and light sheet.[6] The quoted measurement was $f = 6.7\,\mu$m. Using the vortex coordinate expressions, Eqs (2.56) and (2.58), it is possible to derive an expression for the lattice parameter and associated fringe spacing f, which may be compared with experiment.

By describing the initial positions of the three wavepackets using the source position vectors $\mathbf{r}_2$ and $\mathbf{r}_3$ as shown in Fig. 4.12, corresponding lattice vectors $\mathbf{r}'_2$ and $\mathbf{r}'_3$ may be found that describe the basis vectors of the vortex or antivortex lattice. The lattices are interleaved and share the same basis vectors, only differing in their origins. For the case of the wavepackets lying at the three corners of an equilateral triangle, interleaved triangular lattices are formed. The source position vectors and

[6] Additional information about the light sheet removal was provided by Chang Ryu, private communication.

lattice vectors are determined by the usual crystallographic relationship between real- and reciprocal-lattice vectors (Kittel, 1996):

$$\mathbf{r}_i \cdot \mathbf{r}'_j = v\delta_{ij}, \;\; i, j \in \{2, 3\}, \tag{4.23}$$

where v is a real number that will depend on time, in accord with the lattice growth.

The source position vectors may be described in terms of the usual Cartesian unit vectors $\mathbf{i}$ and $\mathbf{j}$:

$$\begin{aligned} \mathbf{r}_2 &= r_2\,\mathbf{i}, \\ \mathbf{r}_3 &= r_3 \cos\theta_3\,\mathbf{i} + r_2 \sin\theta_3\,\mathbf{j}. \end{aligned} \tag{4.24}$$

Evaluating the four orthogonality conditions given by Eq. (4.23) gives

$$\begin{aligned} \mathbf{r}'_2 &= \frac{v}{r_3}\left(\mathbf{i} - \cot\theta_3\,\mathbf{j}\right), \\ \mathbf{r}'_3 &= \frac{v}{r_2 \sin\theta_3}\,\mathbf{j}. \end{aligned} \tag{4.25}$$

This gives $\angle\,\mathbf{r}'_2 = \arctan(-\cot\theta_3) = \pi - \theta_3$.

In order to evaluate the number v, two neighbouring vortex positions in the lattice are evaluated explicitly. Figure 4.12 shows the example for determining the length of $\mathbf{r}'_3$ by finding the polar coordinates (r_{mn}, θ_{mn}), defined by Eqs (2.56) and (2.58), of the vortices with coordinates $(x_{00}, y_{00}) \equiv (r_{00}, \theta_{00})$ and $(x_{01}, y_{01}) \equiv (r_{01}, \theta_{01})$. As source phase variation results only in lattice translation, the phases ϕ_2 and ϕ_3 may take arbitrary values. These were set to $2\pi/3$ and $4\pi/3$, respectively, in order to simplify the $M(m)$ and $N(n)$ expressions in Eqs (2.56) and (2.58), although any choice should give the same result. The length is then $|\mathbf{r}'_3| = \sqrt{(x_{01} - x_{00})^2 + (y_{01} - y_{00})^2}$. Evaluating this expression by hand would be rather messy. Using a computer algebra system results in

$$|\mathbf{r}'_3| = \frac{\pi}{r_2 \alpha \sin\theta_3}, \tag{4.26}$$

where $\alpha = m_a\hbar t/[2(\hbar t)^2 + 2{m_a}^2(\hbar/\Delta p)^4]$ was defined earlier in §2.4.2 in terms of the mass m_a of the atomic species, the reduced Planck constant $\hbar$, the time t, and the initial wavepacket momentum uncertainty Δp, which is assumed equal for all three wavepackets.

We have found that $v = \pi/\alpha$, so Eqs (4.25) become

$$\begin{aligned} \mathbf{r}'_2 &= \frac{\pi}{r_3 \alpha}\left(\mathbf{i} - \cot\theta_3\,\mathbf{j}\right), \\ \mathbf{r}'_3 &= \frac{\pi}{r_2 \alpha \sin\theta_3}\,\mathbf{j}. \end{aligned} \tag{4.27}$$

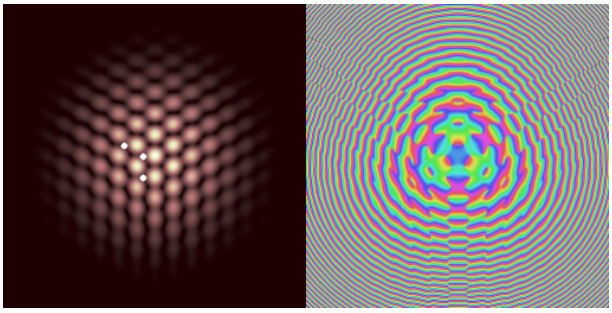

Figure 4.13: Simulation of the Henderson et al. (2009) experiment, which shows the probability density (left) and phase (right) resulting from the interference of three Gaussian wavepackets with initial spacing $r_2 = r_3 = 13.3\,\mu\text{m}$ and momentum uncertainty $\Delta p = 1.4 \times 10^{-28}\,\text{kg}\,\text{ms}^{-1}$ at $t = 19\,\text{ms}$ after their release. Three vortices are marked as white dots, corresponding to the positions in Fig. 4.12.

The length of $\mathbf{r}_2'$ may be found either by direct evaluation, by repeating the above steps for vortices with neighbouring m indices whose coordinates are (x_{00}, y_{00}) and $(x_{10}, y_{10}) \equiv (r_{10}, \theta_{10})$, or most simply with a symmetry argument applied to Eq. (4.26), to give

$$|\mathbf{r}_2'| = \frac{\pi}{r_3 \alpha \sin\theta_3}. \tag{4.28}$$

Although we now have the lattice basis vectors, it remains to find an expression for the fringe spacing. In fact, an infinitely extended regular lattice has an infinite number of sets of parallel lines on which the lattice points lie. Therefore, the particular choice of set of parallel lines joining intensity peaks identified as fringes is somewhat arbitrary. Assuming that Henderson et al. (2009) chose the lines indicated in Fig. 4.12 with spacing f in their reference to fringes, we see that, for the particular case of three spots at the vertices of an equilateral triangle, $\theta_3 = \pi/3$, so

$$f = |\mathbf{r}_3'|\frac{\sqrt{3}}{2} = \frac{\pi}{r_2\alpha\sqrt{3}/2}\frac{\sqrt{3}}{2} = \frac{\pi}{r_2\alpha}. \tag{4.29}$$

Both r_2 and Δp can be varied to give the predicted spacing $f \approx 6.7\,\mu\text{m}$ at $t = 19\,\text{ms}$ that was observed by Henderson et al. (2009). Although they quote $r_2 = 14\,\mu\text{m}$, the resulting pattern that most closely matches the published image is produced when $r_2 = r_3 = 13.3\,\mu\text{m}$ and $\Delta p = 1.4 \times 10^{-28}\,\text{kg}\,\text{ms}^{-1}$. The resulting pattern is shown in Fig. 4.13.

We can also find the offset-distance between the vortex lattice and the antivortex lattice as the distance between the respective 00-indexed vortex and antivortex.

Following the above method for finding the length $|\mathbf{r}'_3|$,

$$\begin{aligned}|\mathbf{r}^{\mathrm{v}\prime}{}_{00} - \mathbf{r}^{\mathrm{av}\prime}{}_{00}| &= \sqrt{(x^{\mathrm{v}}_{00} - x^{\mathrm{av}}_{00})^2 + (y^{\mathrm{v}}_{00} - y^{\mathrm{av}}_{00})^2} \\ &= \frac{\pi}{3r_2 r_3 \alpha \sin\theta_3}\sqrt{{r_2}^2 + 2r_2 r_3 \cos\theta_3 + {r_3}^2}. \end{aligned} \tag{4.30}$$

For $r = r_2 \equiv r_3$, this reduces to

$$|\mathbf{r}^{\mathrm{v}\prime}{}_{00} - \mathbf{r}^{\mathrm{av}\prime}{}_{00}| = \frac{\pi}{3r\alpha \sin(\theta_3/2)}. \tag{4.31}$$

The ratio of this distance to one of the source distances given by Eq. (4.26) or Eq. (4.28) with $r = r_2 \equiv r_3$ is

$$\frac{|\mathbf{r}^{\mathrm{v}\prime}{}_{00} - \mathbf{r}^{\mathrm{av}\prime}{}_{00}|}{r} = \frac{3\sin(\theta_3/2)}{\sin\theta_3}. \tag{4.32}$$

As we explain in the following section, the dynamics of a VD depend on the vortex-antivortex spacing. Thus Eq. (4.32) demonstrates that changing the source angle θ_3 with r_2 and r_3 fixed may provide a means of controlling the formation and/or subsequent dynamics of VDs in the BEC honeycomb lattice.

4.4.5 Vortex dynamics

In this section we focus attention on the striking interactions seen to occur between those vortices and antivortices remaining in the condensate following the melting of the lattice. The vortices and antivortices are propelled and evolve within a seething background sea of sound waves (phonons). Due to the complexity of these interactions, we provide a phenomenological description of just some of the rich dynamics, making observations of structures previously described by other investigators.

The chaotic dynamics described in this section will be exhibited primarily in 2D pancake-shaped condensates. In 3D, vortices are string-like objects, either forming closed loops (e.g., ring solitons) or terminating at two points on the condensate surface (Minguzzi et al., 2004; Carr and Clark, 2006).[7] In this case, the interaction dynamics are instead characterized by string intercommutation or formation of smaller loops. We investigate the 3D case in §4.5.

Most of the BEC vortex literature has concentrated on vortices (or antivortices) in rotating traps, in which antivortices (vortices) are expelled from the condensate. The complex interactions described here instead rely on the presence of a population of vortices and antivortices and hence are best observed in a nonrotating

[7] Ring solitons, also called *vortex loops*, are not to be confused with RDSs, which are defects in two spatial dimensions rather than three. Smoke rings are familiar examples of ring solitons.

system. Interfering condensates comprised of two, three, or more pieces can all generate the required conditions, provided they are nonrotating; whether the vortices are produced by direct interference, the snake instability, or the KZ mechanism is unimportant in this context. Experimentally, diffraction-based imaging with detuned light may leave the BEC sufficiently undisturbed to allow observation of these dynamics (Turner et al., 2005).

A vortex generates a local circulating velocity field and an associated phase gradient, which falls off rapidly with distance. Another vortex or antivortex in this field experiences a force in the direction of flow (Nozières and Pines, 1990). As a result, an adjacent vortex and antivortex will combine to form a vortex-antivortex dipole (VD), which travels at a velocity determined by the spacing of these partners. This is illustrated in Fig. 4.14(a) where the paths of several VDs are traced over a 106 ms period. The more widely spaced the dipole partners, the shorter the distance covered in the given interval.

In contrast, rotating vortex-vortex (or antivortex-antivortex) molecules are rarely and only fleetingly seen. Two equal-charge vortices can circulate around a common midpoint, like a pair of facing figure skaters. In a linear optical system, this is observed as the two forming a pair of intertwined or braided helical nodal lines (Berry and Dennis, 2001). However, these structures have been shown to be unstable in nonlinear radiative media, where they radiate energy in the form of outgoing spiral waves (Pismen, 1999; Proukakis et al., 2004). They would also be disturbed by the more mobile VDs, or prevented from rotating by (countering) field gradients due to the presence of nearby antivortices (vortices).

In Fig. 4.14(b), a VD approaches a lone, near-stationary antivortex, with which it couples to form the tripole shown in Fig. 4.14(c). The net angular momentum of the tripole subsequently causes it to rotate through approximately 90° before it interacts again (Möttönen et al., 2005; Pietilä et al., 2006). In Fig. 4.14(d), a rare event is shown, in which two counter-propagating VDs approach and momentarily meet, forming a quadrupole, before exchanging partners and retreating along paths orthogonal to the original directions. In Fig. 4.14(e), a VD approaches a stationary vortex, which is swapped for the partnered vortex. The new VD continues on a new trajectory. This case may be contrasted with the formation of the tripole. In both cases, a VD approached a stationary (anti)vortex. However, the different interaction geometries resulted in the two different examples of dynamics shown.

The spacing of VDs changes in response to local field gradient perturbations, causing them to slow, speed up, separate completely, or annihilate. An example of annihilation, promoted by the proximity of another vortex, is shown in Fig. 4.14(f). Following the annihilation, scattered remnant waves travel ahead of the event

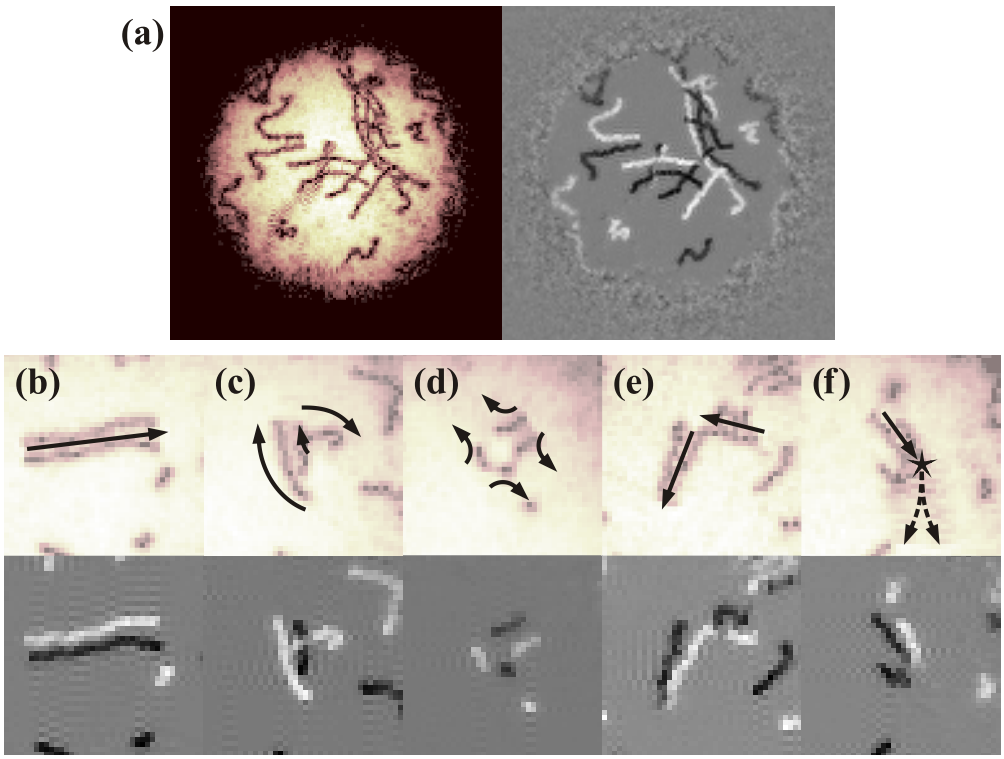

Figure 4.14: Vortex interaction dynamics for the 120°, $I_0 = 0.8$ arrangement. In the grey-scaled frames vortices (dark) and antivortices (light) are shown. (a) Vortex trails corresponding to the range $t = 323$–429 ms. (b) A propagating vortex-antivortex dipole (VD). $t = 430$–471 ms. (c) Vortex-vortex-antivortex tripole rotating through $\approx 90°$. $t = 471$–517 ms. (d) Two VDs meet to form a quadrupole. VA partners are exchanged and the new VDs move off orthogonally to the original directions. $t = 526$–537 ms. (e) A VD meets a lone vortex. The antivortex exchanges its vortex partner and the new VD moves off on a new trajectory. $t = 285$–328 ms. (f) VA annihilation resulting from passing by a lone vortex. $t = 342$–366 ms.

location, dissipating the residual VD kinetic energy. Such interactions of the vortex with field perturbations and radiation of energy as waves are examples of vortex-sound interactions (Pismen, 1999). As already mentioned, vortex-vortex molecules are unstable, emitting spiral waves as they travel apart. Indeed, the sound waves emitted by all dynamical vortex interactions travel outwards and are reflected by the trap, recombining to form a chaotic fluctuating background that affects the ongoing condensate evolution.

Parker et al. (2004) analysed a BEC containing a lone vortex within a harmonic trap that was carefully modified to control the emission of spiral waves from a confinement region near the trap centre. When spiral wave radiation was permitted to escape confinement and prevented from reinteracting with the vortex, the local

energy was thus reduced, manifesting as a migration of the vortex away from the condensate centre and its precession around the trap. Although our system is complex in comparison, we nevertheless observe sound emission from isolated vortices in the form of spiral waves. As our system evolves, a reduction in the number and associated energy of the vortices also occurs, consistent with the conversion of this energy to sound.

Vortices residing in the outer parts of the trap spiral helically about the centre in a right-hand screw sense, where the axis of the helix is time. Antivortices spiral in the opposite sense and are therefore likely to meet the aforementioned vortices. These often form VDs, which appear, as if created from nowhere in the diffuse condensate limits, then move inward toward the trap centre.

4.4.6 Simulations of Sodium BECs

To this point we have presented models of BECs composed of ^{87}Rb, as this atomic species is commonly used in experiments and was the system used by Scherer et al. (2007). Motivated by the possibility of experimentally confirming the production of a honeycomb lattice, simulations were also performed on a ^{23}Na BEC system to try to find optimal parameters for experiment. The ^{23}Na experiment in the NIST Laser Cooling and Trapping Group employs a red-detuned laser light sheet as the axial trap component along with a magnetic trap for transverse trapping to produce pancake condensates.[8] This provides independent control of the trap components since the axial trap can be maintained whilst the magnetic trap is removed.

Two methods are available to produce separation of the BEC into three pieces. Three red-detuned Gaussian lasers could form three wells within the harmonic trap. Alternatively, a spatial light modulator (SLM) illuminated by a blue-detuned laser could be employed to produce the light sheet walls, and possibly a tighter transverse harmonic trap than the magnetic trap used during trapping and cooling. It is hoped that the simulations will aid selection of the preferred method for separating the pieces.

As in previous sections, we advocate removing the transverse trap in order to observe the honeycomb lattice; any explicit ballistic expansion stage is therefore eliminated by being incorporated with the source interference. The optimal timing for any ballistic expansion period depends on the desired final size of the condensate cloud by the imaging system; this being a trade-off between wanting a

[8] Details of the NIST experiment were provided by Kristian Helmerson, private communication.

large cloud to maximise the resolving power of the imaging system and wanting a small cloud to maximise contrast in the projected line density image.

Because the phase cannot be directly measured, we assume an absorption image will be obtained. In order to better assess the visibility of any resulting lattice, the simulation visualisation method was changed. All previous images, and in particular Figs 4.6(c) and 4.9(c), were automatically normalised to the peak density within that image alone. A better assessment of visibility may be made by instead establishing a reference image intensity based on the local peak density of the *initial state* condensate profile and scaling images at later times relative to this reference value. We also apply a neutral grey-scale colour-map to these results. However, the presentation of the BEC probability density results in this section may still give a false sense of the feature visibility as we have not explicitly modelled the behaviour of the experimental imaging system.

In an experiment designed to demonstrate the creation of a honeycomb VA lattice, we would aim for the lattice to be as regular as possible and to maximise the visibility of the vortices. The vortex cores should be well-formed dark circular spots against a smooth bright background, as in Fig. 4.6(c). We have independent control over the initial sizes of the pieces and their spacing, so the aim here is to explore the effects of varying these parameters on the lattice quality. The lattice parameter must be larger than the vortex core size in order to best observe vortex cores against a uniform background density, suggesting that the piece spacing should be small. As evolution proceeds, the lattice parameter increases but so does the vortex core size, since the density and healing length decrease. The background density and associated visibility therefore decrease, so the spacing cannot be too large. Thus, there should be an optimum spacing for the sources to achieve the best visibility, but this spacing may not produce the most regular lattice.

Figure 4.15 shows the evolution of a ^{23}Na condensate, characterised by a scattering length $a = 2.75 \times 10^{-9}$ m, and containing $N = 50,000$ atoms [except for case (g)], each of mass 3.8175×10^{-26} kg. The trap frequencies for the transverse and axial components of Figs 4.15(a–d) were $\omega = 20$ rad s^{-1} and $\omega_z = 500$ rad s^{-1}, respectively. These were later changed to $\omega = 2\pi \times 20$ rad s^{-1} and $\omega_z = 2\pi \times 500$ rad s^{-1}, to match the NIST experiment, when it was realised that the trap frequency units had been misinterpreted. The length scale in Figs 4.15(e–g) is consequently reduced by a factor 2π. Apart from changing the evolution rate and condensate size, restoring the missing 2π increases the condensate density with a consequent slight improvement in the vortex visibility due to reduction of the healing length and vortex core size. The resulting lattice is not very visible. However, the imaging system gain is unknown. Therefore, although the relative visibility across the frames is likely to

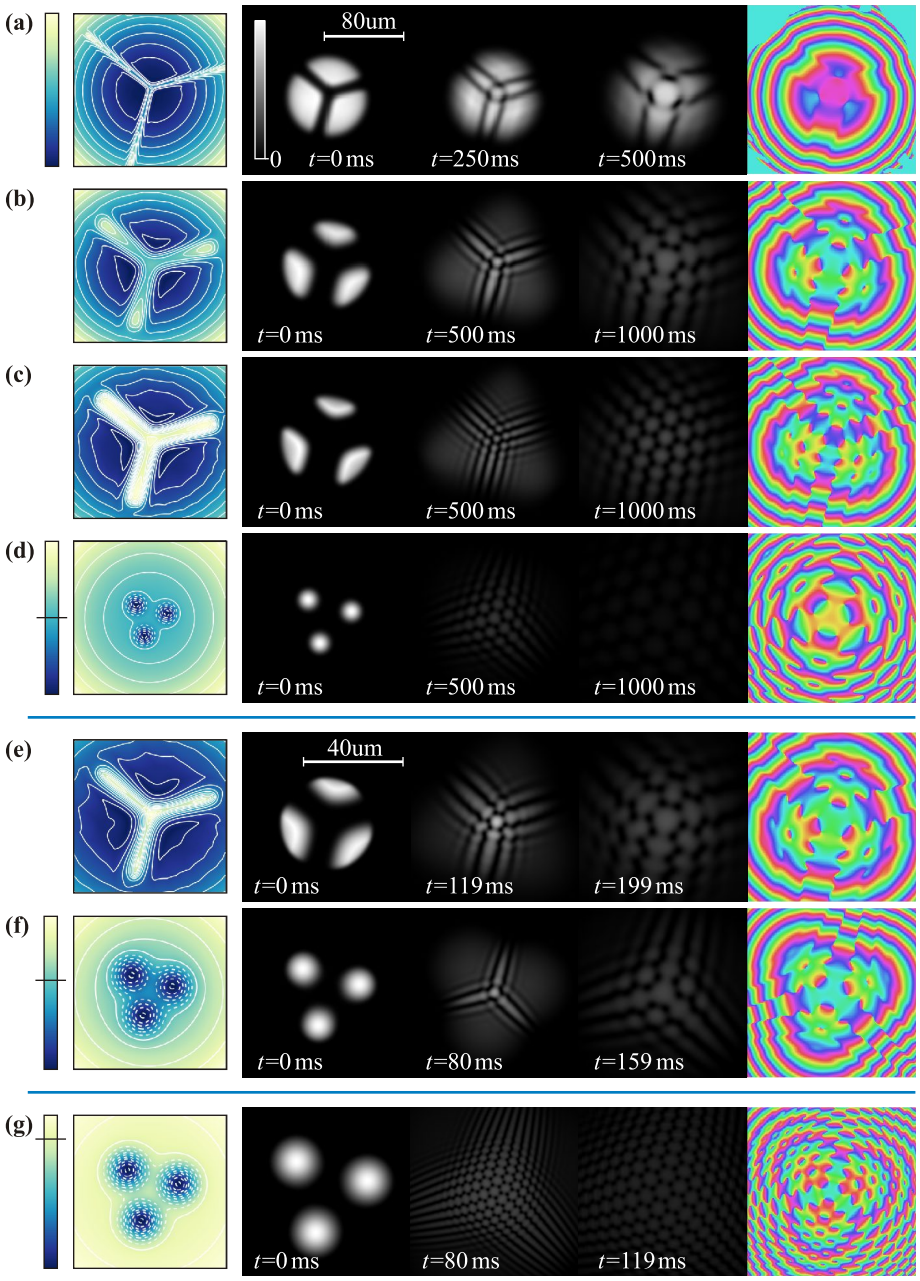

Figure 4.15: Lattice evolution of ^{23}Na BECs showing probability density and phase (corresponding to the final frame). Trap potentials shown at left (not to scale) indicate harmonic trap modification by light sheets (a–c,e) or with wells (d,f,g) formed by red-detuned lasers. For the latter cases, horizontal lines on the colourbars indicate the lowest potential due to the harmonic component (i.e. in the absence of the wells). The length-scale bar in (a) refers to sequences (a–d), for which angular trap frequencies were $\omega = 20\,\text{rad s}^{-1}$ and $\omega_z = 500\,\text{rad s}^{-1}$. The scale bar in (e) refers to (e–g), which uses trap frequencies $\omega = 2\pi \times 20\,\text{rad s}^{-1}$ and $\omega_z = 2\pi \times 500\,\text{rad s}^{-1}$. The condensates contain (a–f) $N = 50,000$ atoms, and (g) $N = 500,000$ atoms.

be indicative of the actual imaging system, the absolute visibility would have to be determined experimentally and may be improved over the simulation frames.

Because of the increased density of atoms in Fig. 4.15(e), the light sheet intensity is increased for this case to adequately separate the condensate into its initial pieces. Similarly the intensity of the red-detuned Gaussian lasers is increased to form the wells in Figs 4.15(f–g). The lasers employed to form the wells in Fig. 4.15(d) have beam waist radii of 8.4 μm and lie on a circle of radius 25 μm, whereas in Fig. 4.15(f) the beam waist radii are 6.8 μm and these lie a circle of radius 14 μm. Because of the small number of simulations performed, the results here are inconclusive but point the way to further simulations, should a ^{23}Na experiment be pursued.

The best result, indicating a starting point for exploration of the experimental parameter space was produced using the laser light-sheets [Fig. 4.15(e)] and shows a reasonably regular lattice and distinct vortex cores. The ability to see these features will depend heavily on the imaging system. Although there is not much difference between it and the result produced with red-detuned laser wells, Fig. 4.15(f) shows a better defined lattice, albeit with the less desirable presence of three-fold symmetry in place of the honeycomb symmetry.

Returning attention to the upper figure series [Figs 4.15(a–d)], some useful observations may nevertheless be made. Figures 4.15(a–c) show results from light sheets of different intensities and sizes, and are representative of the behaviours seen in simulations when parameters were varied. In (a), vortices are not formed within the simulation period shown. Six vortices do subsequently form at the vertices of the central hexagon, at later times than shown. Here, the pieces are closely spaced relative to their size, resulting in an obvious three-fold symmetry with vortices forming at late times, far from the trap centre. In (b), the piece spacing and sizes are similar, resulting in a compromise between lattice regularity and vortex core visibility. In (c), although the vortex cores are indistinct, the lattice is highly regular. If a phase imaging technique is able to be employed, perhaps by interference with a plane-wave source (Bolda and Walls, 1998), or using phase reconstruction from a series of absorption images (Tan et al., 2003; Martin and Allen, 2007), it may be desirable to opt for more widely-spaced initial pieces, giving rise to a more regular lattice at the expense of vortex visibility in absorption images.

The dual aims of a highly regular lattice along with distinct vortex cores were not met for any parameter combinations shown in Figs 4.15(a–f), in contrast with the observations for ^{87}Rb condensates. Further optimisation may be possible by delaying removal of the transverse trap. Increasing the number of atoms should increase the density, in turn decreasing the healing length and vortex core radii. Vortex cores and a regular lattice are indeed observed in Fig. 4.15(g), for which the

number of atoms was increased by a factor of 10 to $N = 500,000$. In this example, the beam waist radii are 6.8 μm and these lie on a circle of radius 17.2 μm.

In conclusion, the simulations do not provide a clear answer to the question of whether it is better to begin with Gaussian-shaped pieces or light-sheet walls. Compared to the previous results for ^{87}Rb, the reduced visibility of cores in these ^{23}Na BEC simulations may be substantially due to the different approaches of normalising the overall intensity, and the use of different colour-maps. In any case, if an experiment is pursued, it will be desirable to maximise the number of condensed atoms. Given the difficulty of finding an optimal set of experimental parameters, we defer further optimisation to future work, which could take the form of simulations or experimental investigations.

4.4.7 Concluding remarks for the 2D model

A nonrotating pancake-shaped Bose-Einstein condensate (BEC) fragmented into three pieces, with a repulsive nonlinearity, forms significant numbers of vortices and antivortices after merging. We have demonstrated, with numerical 2D simulations of this system, that the vortex creation mechanism may be explained in terms of a linear theory of the interference of expanding wavepackets. This was contrasted with the vortex creation mechanism from a two-fragment BEC, in which dark stripe solitons decay into necklaces of vortices and antivortices; an intrinsically nonlinear physical process. With the three pieces separated sufficiently and arranged symmetrically, the formation of a distorted honeycomb lattice containing equal numbers of vortices and antivortices was demonstrated and explained using the linear theory. Moreover, this theory shows that phase differences between the initially separated pieces manifest as a global lattice translation. If allowed to expand in the absence of a trapping potential, the honeycomb lattice maintains its form as it expands. If instead the BEC evolves within a trap, the lattice melts, exhibiting a diversity of vortex interactions, including the formation of VDs and other vortex clusters.

4.5 3D simulations of the trapped BEC

In the previous section we studied the trapped three-piece pancake condensate of ^{87}Rb in (2+1)D. Here we extend the investigation of this system to (3+1)D enabling us to explore the effects of relaxing the requirement of tight axial-confinement; we can thereby test the validity of the previous 2D results on less tightly confined BEC clouds. We will demonstrate that relaxing the restriction still allows for the

formation of a honeycomb VA lattice, now with a fully-3D nodal line structure. An important motivation for investigating the 2D condensate was to enable application of the three-pinhole interferometer results to that system. In this section, we probe the limitations of the analogy. Experimental imaging of BECs is inherently a 2D exercise typically involving imaging from a fixed camera. Because investigation of 3D structure requires tomographic reconstruction from multiple projections, some of the results in this section are unable to be easily verified with existing experimental systems. In the next chapter we present simulations of a 3D multi-component BEC system. The modelling of that system entailed several changes to the computational realisation – to compactly represent the numerical data, to allow the simulations to operate on a computing cluster, and to visualise the results. The 3D simulations here provided a way to assess these changes at intermediate stages of development. We again chose the parameters of the BEC system based on those used by Scherer et al. (2007), hoping to obtain further insight into the reasons that a vortex lattice was not observed in their experiment.

In the results we will present, we observe only nodal lines formed into loops. We will discuss their shape, stability, and dynamics. Increasing the number of spatial dimensions to three allows for the existence of codimension-1 nodal sheets (domain walls). Because such defects are unstable, none were observed. In order to see evidence of their formation, we would have to take great care to create them. Like vortex sheets, knotted loops would also have to be formed through careful contrivance, as they would rapidly reconnect to form multiple unknotted loops.[9] In the process of reconnection, the four ends of two adjacent nodal lines of opposite winding sense have two possible associations with the line ends. This association may change if the nodal lines are allowed to reconnect after crossing. The phenomena of a vortex loop breaking into two smaller loops or of a loop attaching to or splitting from a nodal line may be related to this picture, since the local senses of the near and far sides of a continuous loop are opposites when viewed from the location of a particular observer. We will also see an example of this process in reverse, where two small loops join to form a larger loop.

If not in the form of loops, nodal lines may exist as infinitely long lines extending through the condensate. However, in the sense that we normally think of the BEC cloud as localised – this corresponding to setting a threshold at some probability density value – we will speak of a nodal line as being of finite length if it is truncated by the surface of constant threshold value. We will see the consequences of this when visualising the probability density and nodal lines. The previous 2D simulations implicitly assume that nodal lines are straight and extend from the

[9] cf. the recent paper by Dennis et al. (2010) reporting a means to construct knotted loops.

upper to the lower surface of the cloud. The question of whether the nodal lines extended beyond the condensate surface does not arise in 2D. Also, by assuming that the BEC had a pancake geometry, we avoided any possibility that nodal lines might reconnect.

As previously discussed, three-source interference gives rise to straight nodal lines, whereas a fourth source perturbs these into helices, or ultimately into loops as its influence increases. The helical excitations of otherwise straight nodal lines are known as Kelvin-mode excitations or Kelvin-wave excitations. These excitations have been shown to propagate throughout the structure of Abrikosov vortex lattices produced in rotating BECs, thereby disrupting the lattice and leading ultimately to turbulence (Tsubota et al., 2003, 2004; Simula et al., 2008; Klawunn et al., 2008; Takeuchi et al., 2009). The honeycomb lattice can be thought of as two interleaved hexagonal Abrikosov lattices; one containing only vortices and the other only antivortices. It is interesting to ask whether the presence of interleaved nodal lines of one of these lattices might counteract the propagation of phonons produced by excitations of the other lattice. Even if the honeycomb lattice is not stabilised by any such shielding effect, the more general question might be asked of whether turbulence arises in a different manner to that in the rotating BEC.

4.5.1 Simulation description

Three simulations are presented here of a ^{87}Rb three-piece condensate, with only the trap frequencies, light-sheet intensity, and number of atoms changed to observe the effects. The BEC evolves within the confining trap in all cases, with only the light sheet being removed at $t = 0$. We observe the turbulent phenomena that arise within such a trapped system, but also note the surprising robustness of the honeycomb lattice, despite its production in the presence of nonlinear interactions and within an environment with additional axial freedom.

For these full 3D simulations, the time dependent GPE [Eq. (4.1)], with its associated unit normalisation condition [Eq. (4.2)], was evolved from the ground state using the damping function described by Eq. (4.21)(iii). The ground state was in turn established by evolving the Wick rotated GPE [Eq. (4.13)] starting from the circularly symmetric TF limit [Eqs (4.15) and (4.17)]. An example of the trap potential including the light sheet used in establishing the ground state is shown in Fig. 4.16.

In all cases, the x and y numerical grid was 256×256. For the cases presented here, the resolution was reduced along z to 128 or 64, which reduced the computation time whilst still allowing us to observe the resulting structures. Where

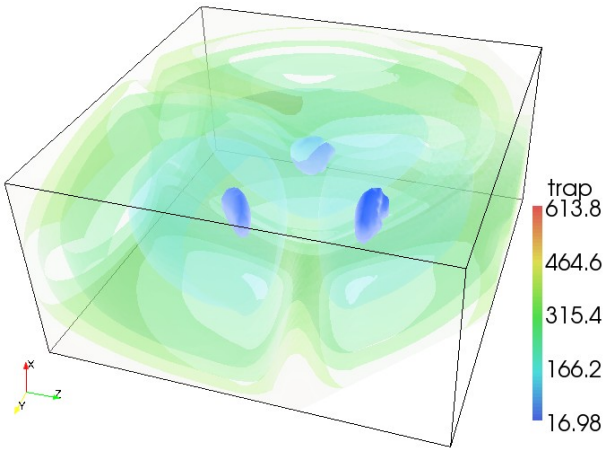

Figure 4.16: The trap potential (green) shown using equispaced isosurfaces. An isosurface of the ground-state condensate probability density (blue) is revealed in-situ within the trap. The angular frequencies are $\omega = 46.5\,\mathrm{rad\,s^{-1}}$ and $\omega_z = 88.6\,\mathrm{rad\,s^{-1}}$, with a superposed light-sheet of dimensionless intensity $I_0 = 0.6$ and width $w_0 \approx 6\,\mu\mathrm{m}$ (See Fig. 4.7). Note that the legend refers to the trap and not the condensate.

the scaling along z differs, this was corrected for in the visualisations in all 2D projections, but remains uncorrected in some 3D cases, these being pointed out in the text.

The visualisation approaches taken here were to use surfaces of constant value (isosurfaces) of the probability density. When applied over the whole field, a single-value isocontour reveals many separated isosurfaced objects. The local phase can optionally be shown on this surface. Volumetric visualisation, in which rays traced through the volume acquire colour and opacity as they propagate through the field, gives a good sense of the probability distribution throughout the volume. The field may be integrated or projected, typically along x, y, or z to produce 2D images, whose degree of similarity to those seen in the 2D simulations gives a sense of whether 2D simulations are likely to be valid. These projections also correspond to the absorption images that might be obtained from cameras in an experiment.

Three methods of visualising the nodal lines were used. The most common way seen in the literature of visualising nodal lines is to view isosurfaces of some large value of the integrand $|\nabla\times\mathbf{j}|$ of Eq. (4.22). This way of visualising the local vorticity metric is somewhat prone to errors produced by numerical differentiation artefacts. A more direct method is to directly detect phase windings at each voxel location as described in Appendix A. In practice this worked well. The resulting array of Boolean values is then mapped via True $\mapsto$ 1 and False $\mapsto$ 0, and visualised using a volumetric method. Finally, the detected voxels can be clustered and ordered in

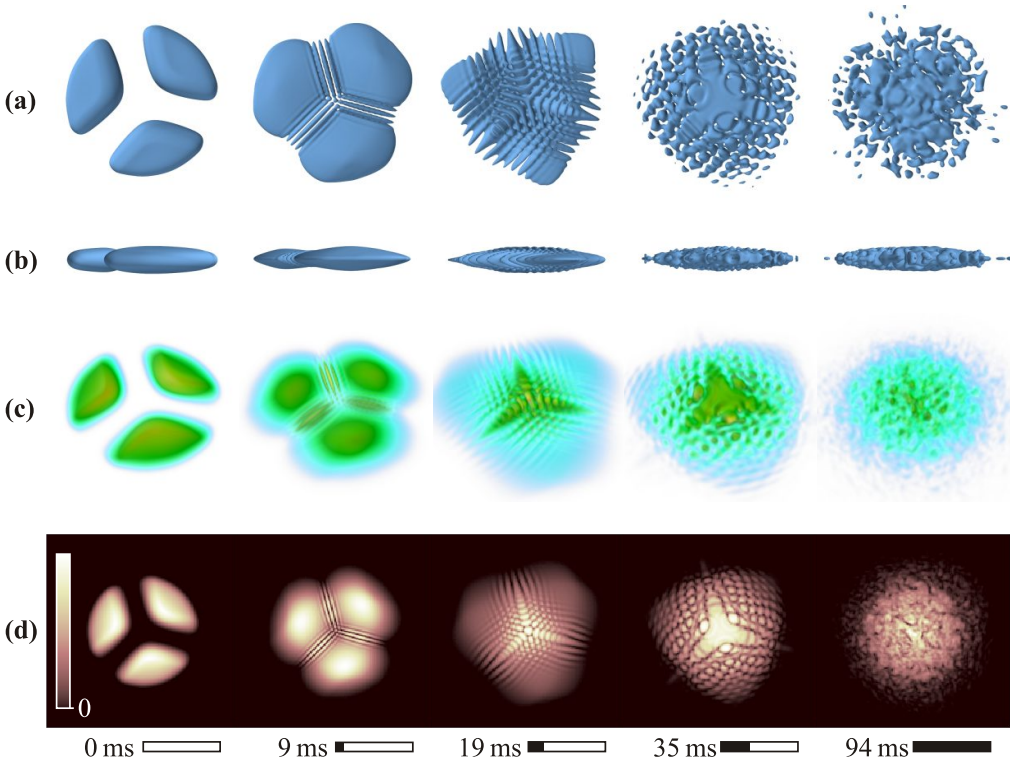

Figure 4.17: Different visualisations of 3D simulations showing the probability density of a condensate of $N = 260,000$ ^{87}Rb atoms within a trap having angular frequencies $\omega = 46.5\,\text{rad}\,\text{s}^{-1}$ and $\omega_z = 300\,\text{rad}\,\text{s}^{-1}$ and initially divided by a light-sheet of dimensionless intensity $I_0 = 0.6$. (a) Top and (b) side views of an isocontour of the probability density, (c) volumetric view, and (d) z-integrated projection.

space to allow curves to be fitted through them. These curves may be visualised using coloured lines or tubes to aid in distinguishing a large number of nodal lines from one another. The difficulty here is that detecting distinct loops or lines that are touching or crossing requires heuristic methods to form or break the clusters. A simple heuristic was applied here, which resulted in a useful visualisation. This was based on forming the minimum spanning tree of a graph whose nodes coincided with the clustered voxel locations then traversing the branches of this tree.

4.5.2 Results

In Fig. 4.17 we show the evolution of a segmented BEC of $N = 260,000$ ^{87}Rb atoms. The same scattering length $a = 5.77 \times 10^{-9}$ m as in the 2D studies characterises the condensate. For this case, the transverse trap frequency is kept at $\omega = 46.5\,\text{rad}\,\text{s}^{-1}$ and a relatively high axial trap frequency $\omega_z = 300\,\text{rad}\,\text{s}^{-1}$ is selected in order

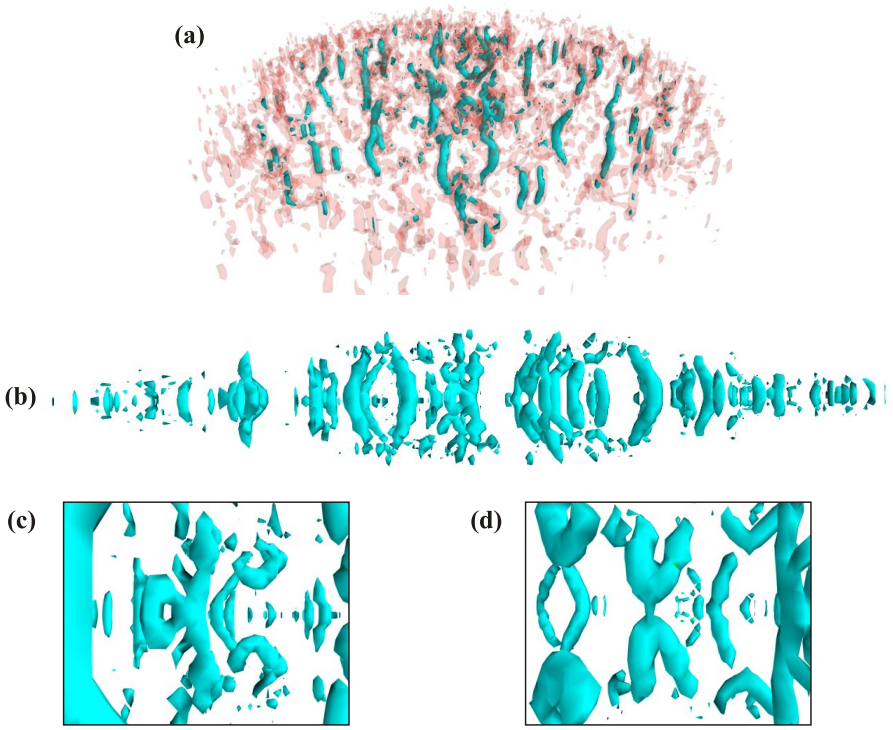

Figure 4.18: 3D nodal line structure of the system described in Fig. 4.17, corresponding to the final frame $t = 94$ ms. (a) Two isocontours of $|\nabla \times \mathbf{j}|$. (b) The aqua isosurface value from (a) shown side-on. (c) A view of the nodal lines seen side-on showing a loop attaching-to/detaching-from a nodal line that extends through the condensate. (d) Another side-on view showing two neighbouring nodal lines of opposite sense that have undergone reconnection to form two horseshoes truncating on the condensate surface.

to produce a pancaked condensate for comparison with the 2D simulations. For this case, the light sheet intensity is $I_0 = 0.6$. In this figure, we show the (a) top and (b) side isocontoured views, (c) a volumetric view seen from 60° above the xy-plane, and (d) the z-projected density. From left to right, we see the initial state, two-piece interference fringes, the formation and partial expansion of a honeycomb lattice, and finally a turbulent state at a time following melting of the lattice. The vortex structures existing in this final state are presented in Fig. 4.18 as isocontours of $|\nabla \times \mathbf{j}|$.

The red semi-transparent objects in Fig. 4.18(a) are for an isocontour of smaller value than the opaque aqua objects. Conventionally, a vorticity measure divides the probability current $\mathbf{j}$ by the local probability density ρ to obtain the velocity field $\mathbf{v}$ and then takes the curl of this [see §4.3.7 and Carretero-González et al. (2008a)]. Our vorticity measure explicitly avoids the weighting, to avoid detection of vorticity

where the condensate cloud becomes tenuous (cf. §4.3.7). We believe that this simplifies matters when calculating an integrated vorticity metric. However, it means that we cannot choose an isocontour that will be guaranteed to only detect true nodal lines, based on a single value of this local measure. Thus the aqua objects may correspond to values of field vorticity which have not achieved the requisite quantised value to be considered true nodal lines. In this case, a more conventional vorticity metric, which divides the probability current by the local probability density and applies a carefully calculated value of the isocontour value, might provide a more correct visualisation.[10] However, this conventional approach shares the problem with the phase unwrapping method of requiring selection of a probability density threshold to avoid vortices *outside* the condensate cloud. The vorticity measure is then zeroed when the probability density falls below this threshold value.

Assuming the isocontour value is showing objects corresponding to nodal lines, we observe the reconnection examples mentioned above in Fig. 4.18(c) and Fig. 4.18(d) and described in the figure caption. This pancake geometry is dominated by nodal lines truncating at a threshold defining the condensate boundary. A few loops are also visible.

Figure 4.19 shows the probability density and nodal lines of a ^{87}Rb BEC evolving within a spherical trap and initially divided by a light-sheet of dimensionless intensity $I_0 = 0.6$. The nodal lines in these images are produced by phase unwrapping, according to the method described in Appendix A, which required a condensate boundary threshold to be applied. As most of the nodal lines are visible as closed loops, this approach appeared to work reasonably well. The corresponding projected probability density images are shown separately in Fig. 4.20. Note the comments in the captions; namely, the z-scaling is compressed in Fig. 4.19 but shown correctly in Fig. 4.20. The first and most obvious observation, revealed in Fig. 4.20 for $t = 18$–42 ms and visible in the central loop structures in Fig. 4.19 for $t = 18$–25 ms, is that although this condensate is not pancake-shaped, nodal lines with winding senses corresponding to the honeycomb lattice are nevertheless produced near the centre of this system, albeit without the regularity seen in the 2D examples with higher light sheet intensities. It would be interesting to repeat these simulations with higher intensity light-sheets to see whether a more regular lattice could be formed. Instead of investigating this, we chose to develop the multicomponent BEC simulations presented in Chap. 5.

In Fig. 4.19 loops are visible at the outer parts of the condensate, where the density is low, at times $t = 18$–25 ms. Three pairs form and neighbouring pairs

[10] The metric would be $\left|\nabla \times [(\hbar/m)\mathrm{Im}(\Psi\nabla\Psi^*)/|\Psi|^2]\right| = (\hbar/m)\left|\nabla \times \mathbf{v}\right| \equiv (\hbar/m)\left|\boldsymbol{\omega}\right|$.

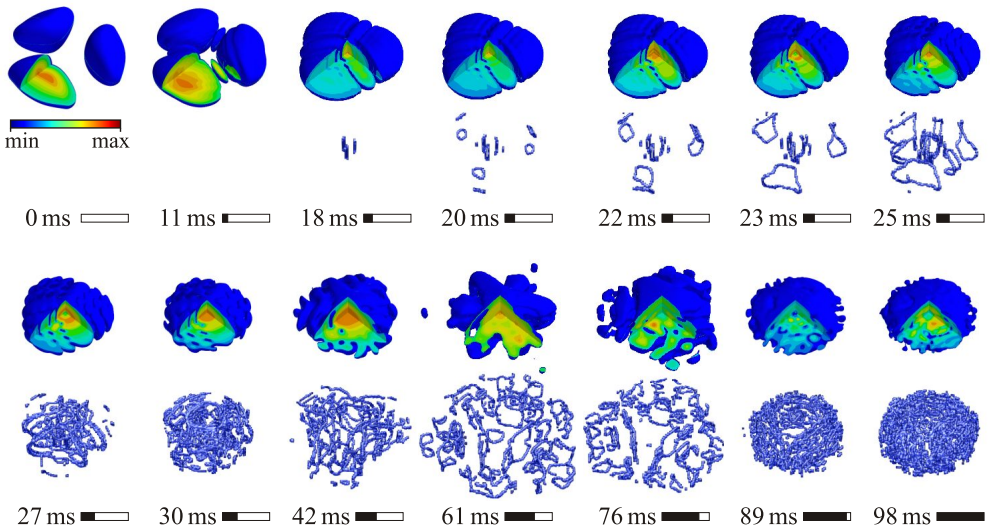

Figure 4.19: In this evolution sequence of a condensate of $N = 260,000$ ^{87}Rb atoms, interference occurs within a spherical harmonic trap, in which $\omega_x = \omega_y = \omega_z = 46.5\,\mathrm{rad\,s^{-1}}$, initially divided by a light-sheet of dimensionless intensity $I_0 = 0.6$. The z-scale in this figure is half the xy-scale, so the modelled condensate is double the thickness shown; the envelope in the last frame being roughly spherical. The upper images in the two rows show the probability density. An octant is removed from the isocontoured surface. The lower images show the vortex structure, where the honeycomb lattice appears around $t = 18\,\mathrm{ms}$. Note that these are slightly rotated about the z-axis compared to the upper images.

coalesce into three larger loops at $t = 23\,\mathrm{ms}$. The only essentially straight nodal line structures are those in the central region, which are identified with the honeycomb lattice formed from three sources (see §2.4.2). All other loops are curved and convoluted and can be thought of as forming from four or more interfering waves. As confinement by the harmonic trap becomes important at $t = 76\,\mathrm{ms}$ and later, turbulence dominates and the loops, having already undergone many reconnections, become highly entangled. Note that a few nodal lines near the outer parts of the condensate visibly end without connecting into loops. This is due to the application of the probability density threshold mentioned above.

For the remainder of this section, we match the geometry used by Scherer et al. (2007), to assess the validity of our earlier 2D results and extend them to 3D. The modified system is identical to that above, but with the z-trap angular frequency now changed to $\omega_z = 88.6\,\mathrm{rad\,s^{-1}}$. Figure 4.21 shows the noteworthy times in the evolution of this system visualised using a variety of methods described in the figure caption. Figure 4.22 shows the corresponding z- and x-projected views, with two additional times shown. A direct quantitative comparison was not performed

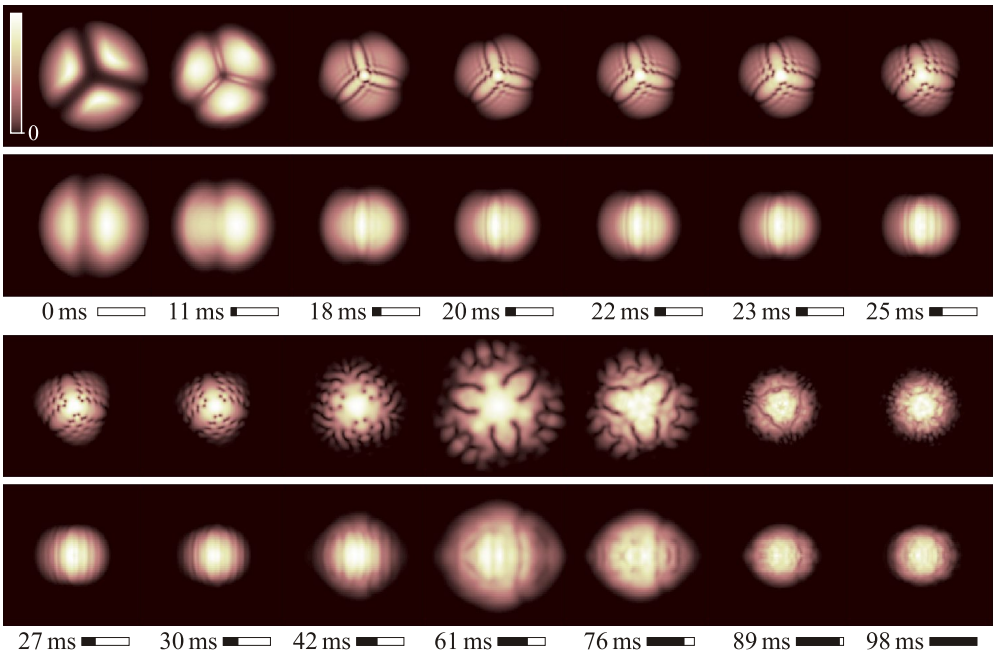

Figure 4.20: Projected probability density for a BEC in a divided, spherical trap, corresponding to the system shown and described in Fig. 4.19. The upper and lower images in the series show the z and x-projections respectively, where the length scaling is equal in both (unlike the case in Fig. 4.19).

with the 2D case. The light sheet intensity here is kept at $I_0 = 0.6$ following from the above simulations, whereas a higher intensity $I_0 = 0.8$ was used in the 2D simulations. In hindsight, it may have been better to perform the 3D simulation with $I_0 = 0.8$. However, with reference to the z-projected initial state, shown in Fig. 4.20, a concentration of mass near the trap centre is visible, which is related to the deviation from pancake geometry. Thus, even with $I_0 = 0.8$ the mass centroids of the pieces would likely differ from the 2D case.

At $t = 15$ ms, a honeycomb lattice is beginning to form in the centre along with some loops in the low density regions associated with outward flows from the initial concentrations of matter. This is visible as a slight increase in density on the cut-plane in Fig. 4.21(a) compared to the surrounding density and also with reference to the direction of the phase gradient in Fig. 4.21(b) indicating the direction of flow. The nodal lines embedded within the condensate are shown in further detail for this frame in Fig. 4.23(a), which reveals that the lattice structure resides within a high density region and the outer loops are in a low density region. In Fig. 4.23(c) the honeycomb lattice length scale is close to the numerical lattice scale so structures are not yet well distinguished.

A well-developed honeycomb lattice has formed at $t = 24$ ms, obscured in

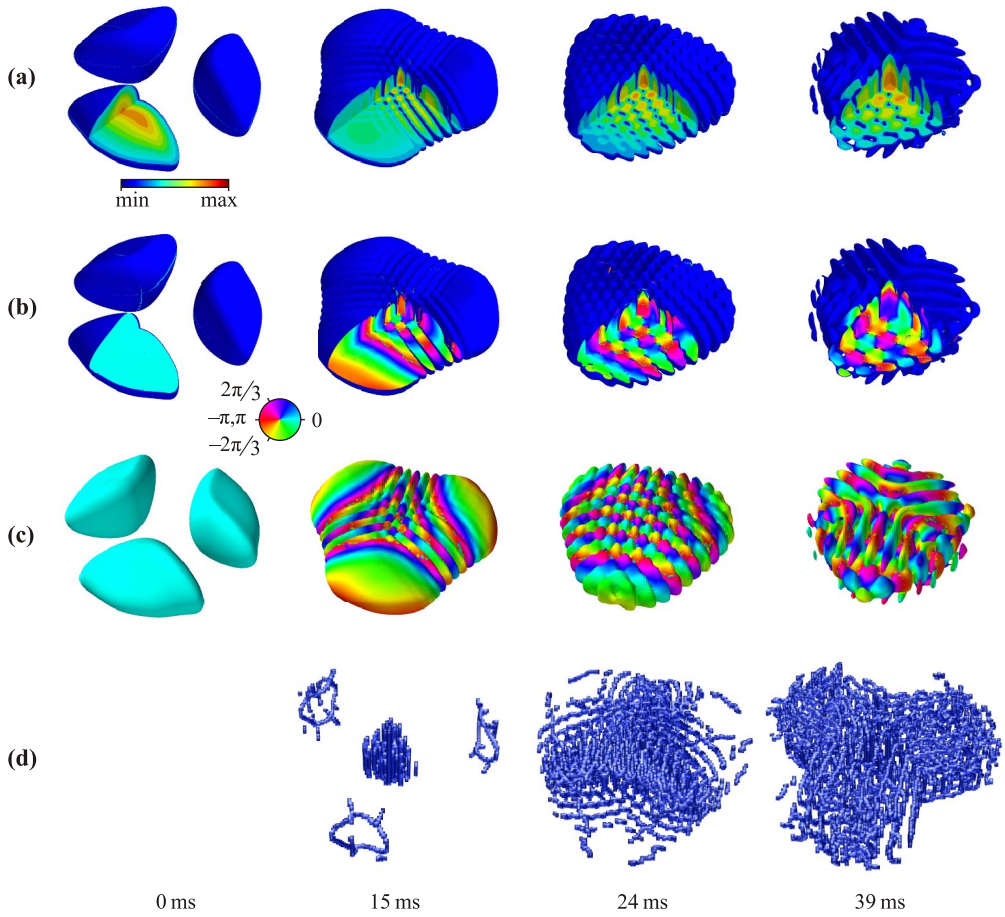

Figure 4.21: Probability density (a), phase (b,c), and nodal line structure (d) within a volume bounded by a contour of the probability density in an oblate spheroidal trap. The views from 60° above the xy-plane show the probability density (a) and phase (b) on the faces created when an octant is removed. In (c), the phase values are shown on the isocontour.

Fig. 4.22(d) by structures forming above and below the cloud. We can see the lattice in the projected image in Fig. 4.22 and infer it by noting the regular phase structure in Fig. 4.21(c), which tiles the isocontour resembling a close-packing of spheres with three equispaced phase values (≈ 0, $2\pi/3$ and $-2\pi/3$). The lattice persists and expands throughout the condensate (see Fig. 4.22) with the nodal lines extending through the condensate cloud thickness. These have begun to reconnect into loops resulting in a stratified structure where three layers have formed, divided by two low density layers visible in Fig. 4.22 in the x-projection at $t = 39$ ms. The honeycomb lattice structure is preserved in its z-projection

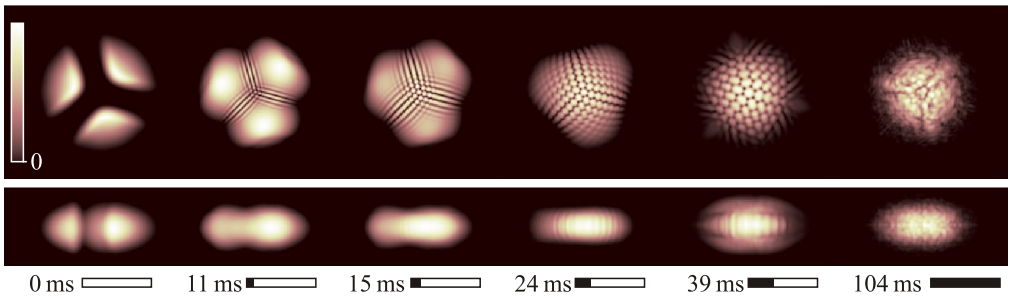

Figure 4.22: Projected probability density for a BEC in a divided trap, corresponding to the system shown and described in Fig. 4.21. The upper and lower images in the series show the z and x-projections respectively, where the length scaling is equal in both.

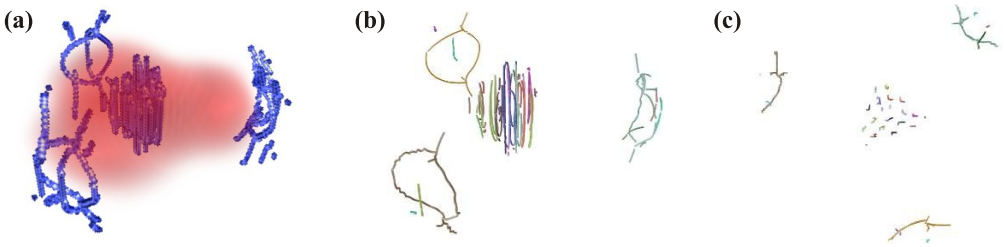

Figure 4.23: Vortex structure detail at $t = 15\,\text{ms}$ in the oblate-spheroidally trapped system. (a) Nodal lines embedded within the condensate. A visualisation as randomly coloured nodal lines is shown in (b) and again viewed along the z-axis to reveal the loops whose two straight sides are seen in 2D as a vortex and antivortex in (c).

in the same figure with the details of the nodal lines being difficult to display in static images. An attempt is made to display the structure in Fig. 4.24 by partially screening some of the structure to reveal loops surrounded above and below by snaking nodal lines. These are also visible in the side view in the same figure. The same structure is shown in Fig. 4.25 using the phase unwrapping and clustering technique, with colour used to separate connected nodal line structures. Careful inspection shows large loops assembled with more-or-less regular spacing around non-vortical regions. The nodal lines, whilst exhibiting snaking excitations, tend to be composed of sections aligned along the z-axis and parallel to the xy-plane. Smaller loops, lying mostly within the middle stratified layer and extending to its boundary, are also visible.

We see that straight nodal lines, created as a result of three-wave interference, are surprisingly stable and robust against bending, but are subject to reconnections. The z-projected density reveals these, even in the extreme example of a spherical

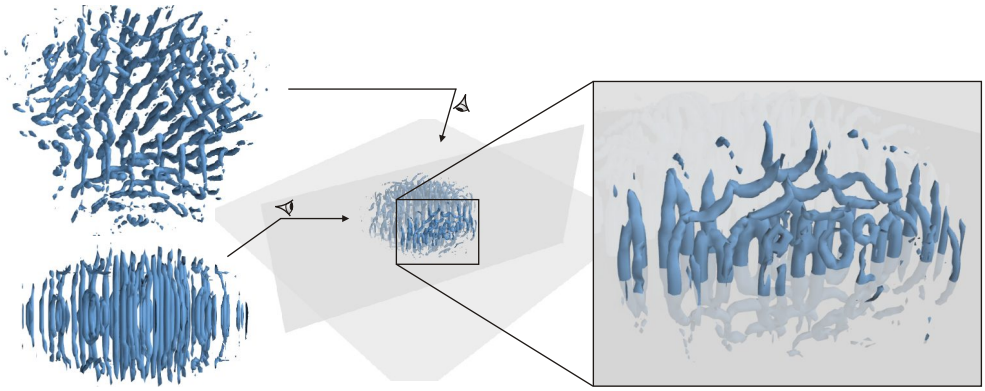

Figure 4.24: Nodal lines in the interfered oblate-spheroidally trapped system, at t = 39 ms. The regular honeycomb lattice is clearly visible from above (upper left image). Nodal lines extend through the condensate (lower left image). Two screens are placed to aid visualisation. The magnified region (right) reveals loops extending through the mid-plane, some loops above and mirrored below this plane, and horseshoes that truncate on the condensate surface.

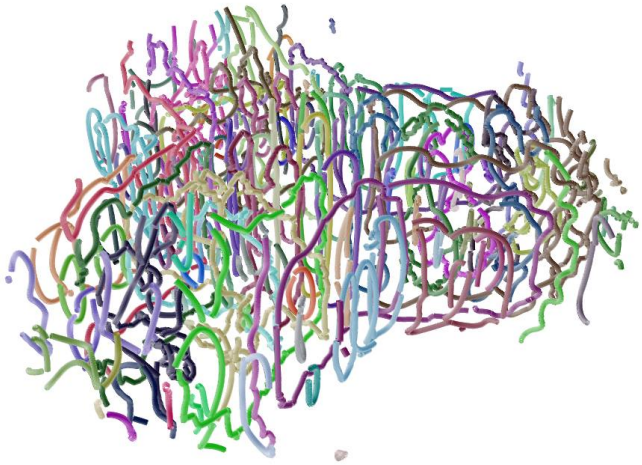

Figure 4.25: Nodal lines in the interfered three-piece BEC at t = 39 ms, when a regular honeycomb lattice has formed. These have been found using a phase-unwrapping algorithm and are randomly colourised to help distinguish them from each other.

harmonic trap. The lack of observation of the honeycomb lattice, or at least a three-fold symmetric arrangement of vortices and antivortices, by Scherer et al. (2007) seems not to be due to the thickness of their system allowing for the bending of nodal lines, but is likely to be due to the other factors discussed in §4.4.3. This robustness contrasts with the propensity for nodal lines to bend in non-pancaked rotating BECs (Takeuchi et al., 2009).

In the introduction of this section we commented that the honeycomb lattice can be thought of as two interleaved hexagonal Abrikosov lattices; one containing only vortices and the other only antivortices. We speculated that Kelvin-mode excitations, which normally lead to instability and turbulence in rotating BECs, might be shielded by the interleaving. This is one possible explanation for the robustness of the nodal lines forming the lattice.

The honeycomb lattice observed in the condensate evolving within a spherical trap exhibited a three-fold symmetric distortion of the type seen in 2D simulations when the light-sheet intensity was low. Further simulations with higher intensity may produce a more regular lattice. Despite this, even in this extreme case, the nodal lines were straight enough that their projected density should create experimentally visible vortices with the predicted symmetric arrangement. The 3D simulations make it clear that the 2D simulations provided good predictions of the visibility of the lattice. The dynamics of vortex-antivortex dipoles (VDs) in the trapped pancake condensate are a 2D phenomenon that was not investigated in 3D. These are replaced by the dynamics of formation and reconnection of loops observed as a prominent feature in all the 3D simulations.

4.6 Summary

Motivated by our earlier work on the three-pinhole Young's interferometer, a honeycomb lattice composed of equal numbers of vortices and antivortices was predicted to form as a result of the interference of three initially separated pieces of a trapped BEC. We demonstrated, with numerical 2D simulations of this system, that the predicted lattice is formed by a sufficiently well divided BEC. The vortex creation mechanism was explained in terms of a linear theory of the interference of expanding Gaussian wavepackets. The direct interferometric creation of vortices was placed in context with other mechanisms for vortex creation in BECs that are well-known to BEC researchers.

If the trapping potential was removed, the honeycomb lattice maintained its form as it expanded. We took parameters for our simulations from those reported by Scherer et al. (2007) of the first experiment to study the interference of a three-way divided BEC, in which no honeycomb lattice was reported, and suggested reasons for the lack of observation. A more recent three-piece interference experiment by Henderson et al. (2009), which did not search for vortices, nevertheless produced an interference pattern consistent with the regular honeycomb lattice. We developed a crystallographic model of the vortex locations in this lattice, which compared favourably with the experimental results.

If the magnetic confining trap was maintained after the pieces are allowed to interfere, the honeycomb lattice melted, leading to a diversity of chaotic vortex interactions, including the formation of VDs and other vortex clusters that migrated and scattered throughout the cloud.

Although we were careful to say that the validity of the 2D model depends on the BEC having a pancake-geometry, we demonstrated with 3D simulations, that the honeycomb lattice was produced, even for thick condensates. We also observed the formation of nodal line loops and dynamics involving loop reconnections and the merging of smaller loops into larger ones.

5 Texture defects from interference in multicomponent fields

> By nature we have no defect that could not become a strength, no strength that could not become a defect.
>
> — Goethe

We have described the production of quantised vortices from linear interference and explored this in the linear optics case and in the nonlinear Bose-Einstein condensate (BEC). In this chapter we will see that three-piece interference can also be applied to the generation of defects whose topology is revealed in higher-dimensional order parameter spaces; namely the creation of *texture defects*, or simply *textures*. More degrees of freedom are required for these textures than are available in the complex scalar fields previously examined, so we must introduce multicomponent fields composed of the simpler fields. A strong connection exists between textures and vortices in the individual field components. This connection allows us to build on our knowledge of the creation of vortex lattices to create a texture lattice.

We begin this chapter by introducing texture defects – specifically skyrmions, and their study in multicomponent BECs. Exploiting the connection between skyrmions and vortices, we then describe a physical system that interferometrically generates a texture lattice. The creation of this system builds on results developed in earlier chapters; the interferometric creation of the honeycomb vortex-antivortex (VA) lattice from three wavepackets, and the effect of the relative phases of these pieces on the lattice translation. We employ a Laguerre-Gauss (LG) beam to engineer the required phases.

In the remainder of the chapter, we examine textures in the turbulent trapped two-component BEC into which vortices have been seeded by some interference process. Using a model of a 2D pancake BEC with two coupled field components,

we see that, by virtue of the strong connection between vortices and certain texture defects, such a system naturally generates textures.

5.1 Introduction

Despite ongoing interest in defects in multicomponent BECs, there appears to be only one review on the subject by Kasamatsu et al. (2005). Specific aspects related to topology are discussed by Volovik (2003) and Mueller (2004).

Tony Skyrme originally posited a nonlinear field theory model that supported topological soliton solutions that he associated with baryons (Skyrme, 1961; Manton and Sutcliffe, 2004). Such solitons, called skyrmions, are examples of texture defects that correspond to arrangements of 3-vectors defined over a 3D region of space (Volovik, 2003; Kasamatsu et al., 2005). A second type of skyrmion called a *baby skyrmion*, corresponds to arrangements of 3-vectors defined over a 2D plane (Hen and Karliner, 2008b). The dimensionality of the associated order parameter space differs for the two types. For 3D fields of 3-vectors, the order parameter space is the 3-sphere S^3, and for 2D fields the order parameter space is the 2-sphere S^2. Skyrme's original model dealt with the former type.

Baby skyrmions arise as texture defects of the magnetisation field of certain ferromagnetic materials in planes perpendicular to an applied magnetic field (Timm, 2009). Their connection with the 3D skyrmions provides a way to test some of the physics that these defect types have in common. The initial motivation for moving to 3D simulations was that our understanding of skyrmions at the time required a two-component 3D system. With greater understanding, we see that this is not the case provided we restrict ourselves to the study of baby skyrmions.

We will present both 2D and 3D numerical models. For the 3D case, we restrict attention to a 2D plane of a system that does not contain defects. The study of 3D systems containing defects in a 2D plane allows for the possibility of baby skyrmions. We study a 2D model of such a system composed of a two-component pancake BEC. Due to time constraints, the modelling of fully-3D models containing defects was left for future study. Such a system could support both skyrmions and baby skyrmions.

5.1.1 The two-component Bose-Einstein condensate

Two coupled complex scalar fields are sufficient to support the texture defects in our models. To emphasise the connection to our previous work, these could be the separate polarization states of a linear wavefield. Alternatively, the two

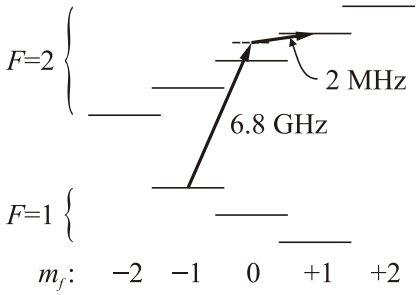

Figure 5.1: The two groundstate $\left|F = 1, m_f = -1\right\rangle \equiv |1\rangle$ and $\left|F = 2, m_f = +1\right\rangle \equiv |2\rangle$ hyperfine levels of ^{87}Rb are connected using a *two-photon pulse* (arrows) via an intermediate level. Whilst connected, populations oscillate between the two hyperfine levels.

components may be different atomic species or two long-lived internal states of the same species. Here, we consider the latter case. Matthews et al. (1998) used the $\left|F = 1, m_f = -1\right\rangle \equiv |1\rangle$ and $\left|F = 2, m_f = +1\right\rangle \equiv |2\rangle$ hyperfine levels of the groundstate ^{87}Rb system as the levels of a two-component system (see Fig. 5.1). Some advantages they cited for using this system are that the two states experience approximately the same harmonic trapping frequency when confined, and that the states may be conveniently coupled by the combination of a 6.8 GHz microwave pulse along with a 2 MHz radio frequency (RF) field, called a *two-photon pulse*. This is shown connecting the states in Fig. 5.1. Because the $m_f = -1$ and $m_f = +1$ states differ by two spin quanta, the coupling is performed by such a two-stage process via some intermediate state. In this case, the photons come from a microwave pulse and an RF field, but they could equally well be provided by the coupling of two lasers via some higher energy level. The occupation population of the levels oscillates in a controlled manner when the states are connected, so that applying a pulse of known duration can drive atoms into a controlled superposition of states. Specifically, application of a 0.930 ms duration pulse corresponds to a "$\pi/2$ pulse," which drives the atoms from the ground state $|1\rangle$ to a state in which the levels are equally populated, creating a *Bell state* $\frac{\rho}{\sqrt{2}}(|1\rangle + |2\rangle)$, where ρ is a probability density. In the remainder of this chapter, we will use the two-level ^{87}Rb system with $\left|F = 1, m_f = -1\right\rangle \equiv |1\rangle$ and $\left|F = 2, m_f = +1\right\rangle \equiv |2\rangle$ as the basis for our modelling as it has been well studied by the BEC community.

The dynamical evolution of the two components is governed by two coupled Gross-Pitaevskii equations (GPEs):

$$i\hbar\partial_t\Psi_i(\mathbf{r},t) = \left(-\frac{\hbar^2}{2m}\nabla^2 + V_i(\mathbf{r}) + \sum_{j=1,2} U_{ij}\left|\Psi_j(\mathbf{r},t)\right|^2\right)\Psi_i(\mathbf{r},t),\ i = 1,2, \quad (5.1)$$

where $U_{ij} = 4\pi\hbar^2 a_{ij}/m$ now depends on the intra- and inter-component s-wave scattering lengths a_{ij}. There are three independent scattering lengths, since $a_{12} = a_{21}$. The trapping potentials $V_i(\mathbf{r})$ may differ for the two components. As we are modelling two internal states of one atomic species, only one mass m appears in the nonlinear coupling term; if we were modelling different atomic species, separate masses m_i would appear. The corresponding normalisation condition is

$$\int \sum_i |\Psi_i|^2 \, dV = N, \tag{5.2}$$

where dV is a volume element and the total number of atoms N is preserved independently of their internal state. For the single component model, there was no compulsion to prefer either of the two equivalent representations of the GPE, which normalised the order parameter field to either 1 or N (cf. §4.3.1), so it was normalised to 1. However, for the multicomponent model, choosing to normalise the order parameters according to Eq. (5.2) makes numerical implementation much simpler.[1]

Establishing the ground state of the condensate can involve both components, increasing the complexity of both the Thomas-Fermi (TF) limit expression and the numerical solution. For the experiments modelled here, the system is prepared in a single internal state, so we need only consider one of the GPEs. The numerical solution of the ground state is thus exactly the same as before for the single component BEC. Following establishment of this initial state, half the atoms are then excited into the other internal state from which time evolution proceeds according to the above coupled equations.

The scattering lengths in the two-component system may be combined to form a determinant $D = a_{11}a_{22} - {a_{12}}^2$ on which the miscibility and hence dynamics of both components is strongly dependent (Ho and Shenoy, 1996; Kasamatsu et al., 2005). When $D \gg 0$ the components are miscible in the ground state; their wavefunctions will overlap significantly. When $D \ll 0$ they are immiscible and they spatially separate. The scattering lengths are all similar in magnitude, hence small changes in their value can have a large impact on the predicted ground state of the system. In the dynamical cases that we study here, small differences in experimentally determined scattering length values quoted in the literature can have large effects on the simulation results. Control of these scattering length values via Feshbach resonances can be used to control the system dynamics (Zhang et al., 2009). We have not attempted to explore the effects of changes caused by

[1] Although Leggett (2006) does not explicitly state a reason, he suggests that this representation is less problematic.

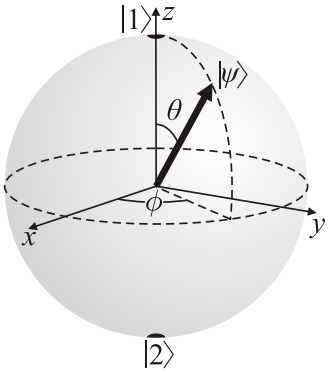

Figure 5.2: The state $|\Psi\rangle$ represented on the Bloch sphere in terms of the basis states $|1\rangle$ and $|2\rangle$.

varying the scattering lengths, but note that their experimental control provides a powerful method of exploring the system. Varying these values could lead to significant changes in the observations made in this section. We use the values determined by Mertes et al. (2007), which were found with a combination of careful modelling and comparison with experiment.

5.1.2 Pseudo-spinor representation in terms of order parameter components

The two individual order-parameter fields Ψ_1 and Ψ_2 may be combined into a single entity or complex-valued vector, called a *pseudo-spinor*,

$$|\Psi\rangle \equiv \begin{pmatrix} \Psi_1 \\ \Psi_2 \end{pmatrix}. \tag{5.3}$$

The pseudo spinor is a position- and time-dependent state vector $|\Psi(\mathbf{r},t)\rangle = \Psi_1(\mathbf{r},t)\,|1\rangle + \Psi_2(\mathbf{r},t)\,|2\rangle$, with basis vectors $|1\rangle \equiv \binom{1}{0}$ and $|2\rangle \equiv \binom{0}{1}$. The state at a given position $\mathbf{r}$ and time t may be represented graphically as a vector within a *Bloch sphere*, which represents the Hilbert space of a two-state system, as shown in Fig. 5.2 (Nielsen and Chuang, 2000). The Bloch vector is naturally expressed using spherical-polar coordinates (θ,ϕ) as

$$|\Psi\rangle = \sqrt{\rho}e^{i\chi}\begin{pmatrix} \cos\frac{\theta}{2}\,e^{-i\phi/2} \\ \sin\frac{\theta}{2}\,e^{i\phi/2} \end{pmatrix} \equiv \sqrt{\rho}e^{i\chi}\left(\cos\frac{\theta}{2}\,e^{-i\phi/2}\,|1\rangle + \sin\frac{\theta}{2}\,e^{i\phi/2}\,|2\rangle\right). \tag{5.4}$$

Often the Bloch sphere has unit radius and represents states normalised to 1, e.g., when it is applied to the description of quantum bits (qubits). The time-dependence of the unitary-transformed state is observed as a motion of the vector around the

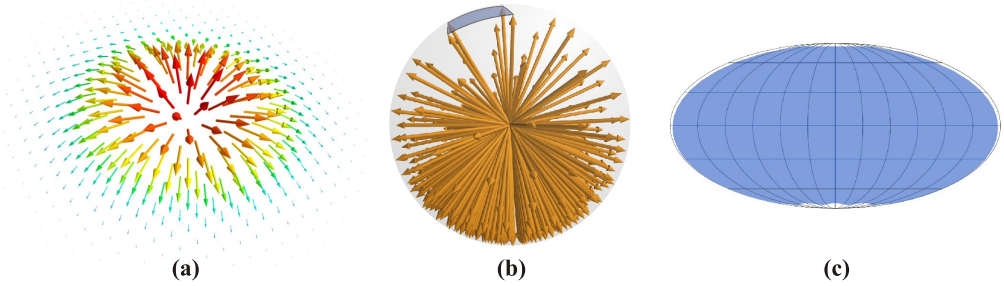

Figure 5.3: (a) The prototypical baby skyrmion Eq. (5.5) evaluated over a region centred at $(x, y) = (0, 0)$. (b) Neighbouring normalised Bloch vectors in (a) define adjacent areas that cover part of the order parameter space S^2. (c) Mollweide projection of the coverage of the order parameter space.

sphere. In our case, the local density is position- and time-dependent and is normalised to $|\Psi(\mathbf{r}, t)|^2 \equiv \rho(\mathbf{r}, t) = |\Psi_1(\mathbf{r}, t)|^2 + |\Psi_2(\mathbf{r}, t)|^2$, so we have a series of Bloch spheres whose radii depend on position and time.

The field may be usefully visualised by a Bloch vector positioned at each point, whose length and orientation change with time. As the phase $\chi(\mathbf{r})$ is not an observable of the system, to find $\theta(\mathbf{r})$ and $\phi(\mathbf{r})$ given $\Psi_1(\mathbf{r})$ and $\Psi_2(\mathbf{r})$ at a particular time t, one can apply the following algorithm, where the index $j = 1, 2$ and all values are locally parameterised by the position vector $\mathbf{r}$:

1. $\rho \leftarrow \sqrt{|\Psi_1|^2 + |\Psi_2|^2}$
2. $\psi_j \leftarrow \Psi_j / \rho$
3. $\chi \leftarrow \arg(\psi_1)$
4. $\psi_j' \leftarrow e^{-i\chi}\, \psi_j$
5. $\theta \leftarrow 2 \arccos[\mathrm{Re}(\psi_1')]$
6. $\phi \leftarrow \begin{cases} 0, & \theta \in \{0, \pi\} \\ \arg\left[\psi_2' / (\sin\theta/2)\right], & \text{otherwise} \end{cases}$
7. Finally, the vector components are transformed to Cartesian coordinates for visualisation purposes $(x, y, z) \equiv (\rho \sin\theta \cos\phi, \rho \sin\theta \sin\phi, \rho \cos\theta)$.

5.1.3 Skyrmion and meron defects

Recently, Leslie et al. (2009) demonstrated the experimental creation of a baby skyrmion in a three-component spin-2 BEC. In this experiment, a texture structure resembling that in Fig. 5.3(a) was generated, where a position-dependent spin vector is associated with the three hyperfine states $\left|F = 2, m_f = -2, 0, +2\right\rangle$ of ^{87}Rb.

Figure 5.3(a) is an image of the spatially varying Bloch vectors of the two-

component pseudo-spinor system (Mueller, 2004):

$$|\Psi\rangle \equiv \begin{pmatrix} \Psi_1 \\ \Psi_2 \end{pmatrix} = \begin{pmatrix} 1 \\ z/d \end{pmatrix} e^{-|z|^2/2d^2}, \tag{5.5}$$

where $z = x + iy$ and $d = \sqrt{\hbar/m\omega}$, evaluated at regular lattice points over the 2D xy plane. This two-component pseudo-spin-half system is commensurate to the three-component system created by Leslie et al. (2009). That is, there are additional degrees of freedom in the three-component system which may be neglected for our purposes, at the cost of losing a direct physical interpretation of the spin vector. In this pseudo-spin-half example, a radial harmonic trap of angular frequency ω confines both components of a two-component condensate, in which only the Ψ_2 component contains a vortex. This describes a skyrmion by virtue of the following properties:

1. We take the order parameter to be the unit, normalised Bloch vector. The order-parameter space is thus a unit two-sphere S^2.
2. The field defined by the continuous function $|\Psi\rangle$ is measured over some region Γ of a plane enclosed by a boundary. This boundary is mapped to a single point in the order-parameter space.
3. The Bloch vector projections of $|\Psi(\mathbf{r})\rangle$ for $\mathbf{r} \in \Gamma$ completely cover the order-parameter space at least once.

To visualise this from the sampled field, we first note that Fig. 5.3(a) shows the Bloch vectors including the amplitude ρ. The order parameter is the corresponding unit vector. Next, we note that the outermost vectors all point downwards, so these represent the texture boundary Γ. In the limit $|z| \to \infty$, all vectors point towards $|2\rangle$, which is the single reference point in the order parameter space relative to which the number of sphere coverings is measured. Next, the vectors in the interior of the texture boundary (in this case, all the visible vectors) are mapped into the order parameter space. The tails of four adjacent vectors, lying at the corners of the 2D lattice square, are placed at a point. When projected onto the interior of a sphere, these vectors form a four-sided polygon whose sides are segments of great circles [Fig. 5.3(b)]. This procedure is repeated for all lattice squares in the plane and the resulting polygons are shown on a Mollweide plot in Fig. 5.3(c), which is an equal-area map projection that shows the full surface of the sphere within a 2D ellipse (Snyder, 1987). Two types of numerical artefact prevent a perfect coverage of this flattened sphere. The uncovered area at the bottom (south pole or state $|2\rangle$) arises because the Bloch vectors corresponding to Eq. (5.5) only approach $|2\rangle$ in the limit of large $|z|$ and we have sampled a finite region. The second artefact is visible as a failure to cover the map at the sides and top. This arises because the

corresponding polygons crossed the constant-azimuth longitude corresponding to the sides and were discarded as a simple strategy to avoid having to deal with plotting these as a special case. Despite these artefacts, it is clear that the texture defect covers the sphere and describes a skyrmion.

If, instead of asymptotically approaching $|2\rangle$ for vectors corresponding to the defect boundary, the Bloch vectors asymptote towards covering the equator of the Bloch sphere – that is, they tend towards pointing radially outward – a *meron* defect is formed (Mueller, 2004; Kasamatsu et al., 2005). Such a defect can be said to be *topological* if the order parameter space is a hemisphere corresponding to the upper or lower half of the Bloch sphere, and the defect boundary is defined by vectors that map to the equator. We will call merons whose Bloch vectors cover the upper hemisphere *up merons*, and their antipodean counterparts *down merons*.

5.2 Modelling a known two-component 3D system

As mentioned in §5.1.1, the relationship between the scattering lengths in a multicomponent system determines the miscibility of its components. The natural scattering lengths in the $|F = 1, m_f = -1\rangle$ and $|F = 2, m_f = +1\rangle$ ^{87}Rb system correspond to the two components being immiscible. When an equal mixture of these components is prepared, they therefore separate spatially. In this section, we reproduce the results of Mertes et al. (2007), in which this equal mixture of states was studied, but we visualise the resulting two-component condensate evolution using Bloch vectors. This provides a test case of the numerical code that will be reused in the next section.

In establishing the ground state, the simulation method in §4.5.1 was applied to Ψ_1, with the second component Ψ_2 set to zero everywhere. The normalisation condition was changed to Eq. (5.2) as described in §5.1.1, where we now normalise the order parameter field to N rather than 1.

The details of finding the TF limit as an initial condition to computing the ground state are the same as described in §4.5.1. Once the ground state was found, a $\pi/2$ pulse was applied to shift half the population of atoms to the second internal state.

The $\pi/2$ pulse can be represented by the unitary transform $\mathbf{P} = \frac{1}{\sqrt{2}}\left(\begin{smallmatrix} 1 & -i \\ -i & 1 \end{smallmatrix}\right)$. This can be applied directly to the ground state calculation above according to $\mathbf{P}|\Psi\rangle \to |\Psi\rangle$. Alternatively, the coupled GPEs may be modified slightly with the addition of a linear coupling term. The appropriately modified form of the

dimensionless GPEs with a harmonic trapping potential is

$$i\partial_\tau \varphi_i = \left(-\nabla^2 + \frac{\rho^2}{4}\left(\frac{\omega_i}{\omega}\right)^2 + \frac{\zeta^2}{4}\left(\frac{\omega_{iz}}{\omega}\right)^2 + 8\pi \sum_{j=1,2} \alpha_{ij} \left|\varphi_j\right|^2 \right) \varphi_i + \frac{\pi\omega}{4T}\varphi_k, \;\; i = 1, 2, \tag{5.6}$$

where the transverse and axial angular trap frequencies for component $|i\rangle$ are $\omega_i \equiv \left\{ {\omega, \atop \omega_2,} {\; i=1 \atop \; i=2} \right.$ and $\omega_{iz} \equiv \left\{ {\omega_{1z}, i=1 \atop \omega_{2z}, i=2} \right.$ respectively, $T = 0.930\,\text{ms}$, $k \equiv 3 - i \equiv \left\{ {2, i=1 \atop 1, i=2} \right.$, and all other variables are as previously defined in §4.3.3. Evolving these equations for 0.930 ms corresponds to a $\pi/2$ pulse. A final alternative is to simply divide Ψ_1 by $\sqrt{2}$ and copy it to Ψ_2 which is equivalent to applying $\mathbf{P}$ to within a phase factor. This phase factor is not observable in any physically-based observations.

Our modelling differs in some details from that performed by Mertes et al. (2007). In addition to the above discussion on the $\pi/2$ pulse, Mertes et al. (2007) modelled condensate losses from the internal states with additional state-specific damping terms. They also directly modelled the ballistic expansion that was experimentally performed prior to imaging. Finally, their numerical modelling was implemented using a cylindrically symmetric grid. In contrast, in our model, no loss terms were incorporated as these would only have effects on time scales longer than the simulations. We did not include the 20 ms ballistic expansion stage, which may explain the increased visibility of overall size oscillations due to the trap breathing mode in our results. Finally, we used a 3D Cartesian numerical grid because we intended to reapply the numerical code to a non-cylindrically-symmetric case.

The physical values used in the model were taken from Mertes et al. (2007). There were $N = 350,000$ atoms of ^{87}Rb, each of mass $m = 1.4188 \times 10^{-25}\,\text{kg}$. The state-dependent scattering lengths were $a_{11} = 100.40\,a_0 \equiv 5.3132 \times 10^{-9}\,\text{m}$, corresponding to the $\left|F = 1, m_f = -1\right\rangle \equiv |1\rangle$ state, where a_0 is the Bohr radius, $a_{22} = 95.00\,a_0 \equiv 5.027 \times 10^{-9}\,\text{m}$, for the $\left|F = 2, m_f = +1\right\rangle \equiv |2\rangle$ state, and $a_{21} \equiv a_{12} = 97.66\,a_0 \equiv 5.168 \times 10^{-9}\,\text{m}$ for the coupling between the two states. The transverse and axial trap frequencies for the two states differed slightly. For state $|1\rangle$ these were $\omega_1 = 193.72\,\text{rad s}^{-1} \equiv 30.83\,\text{Hz}$ and $\omega_{1z} = 539.7\,\text{rad s}^{-1} \equiv 85.90\,\text{Hz}$, respectively, which differ slightly from those affecting state $|2\rangle$; $\omega_2 = 195.26\,\text{rad s}^{-1} \equiv 31.08\,\text{Hz}$ and $\omega_{2z} = 541.7\,\text{rad s}^{-1} \equiv 86.21\,\text{Hz}$.

The simulated, projected probability densities are shown in Fig. 5.4. The component probability densities are equal at $t = 1\,\text{ms}$, immediately following the $\pi/2$ pulse. The components then evolve under the combined influence of the various scattering lengths and trap frequencies. At $t = 41\,\text{ms}$, component $|2\rangle$ is enclosed by a ring of component $|1\rangle$. The difference in spatial distributions achieves a maximum around this time.

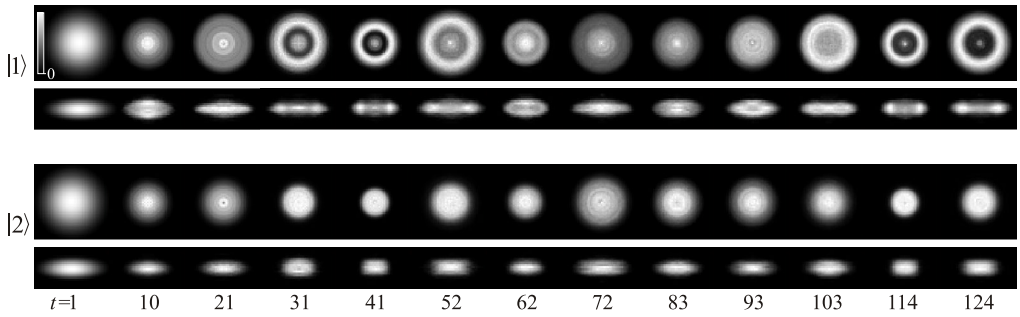

Figure 5.4: Probability densities of our simulation of the Mertes et al. (2007) experiment. Both z- (upper) and x-projections (lower) of both components $|1\rangle$ and $|2\rangle$ are shown for times in milliseconds.

Figure 5.5 shows the evolution with the Bloch vector visualisation. The order parameter space coverage is shown in blue on the Mollweide plots. Since the cosine of the polar angle of the Bloch vector is the normalised population difference, the polar angles covered within the order parameter space grow up to $t = 41$ ms, when Bloch vectors cover all polar angles. This is evident from the Bloch vectors, which point up toward $|1\rangle$ at large radius and down toward $|2\rangle$ in the centre.

Figure 5.6 is an illustrative slice through the two component condensate at $t = 41$ ms. The Bloch vectors have been normalised to make all their projections visible and correspond to the order parameter. The Mollweide plot projections [Fig. 5.6(c)] are grouped within a tight band of azimuthal angles and so do not describe a topological defect. This is not surprising, as we saw in §5.1.3 that the skyrmion corresponds to a vortex in one field component and Fig. 5.4 shows that the densities of both components are cylindrically symmetric and do not contain a vortex. This prompts us to ask whether the vortices created in the honeycomb lattice by the interference of three wavepackets could be associated with the existence of skyrmions. This is the subject of the remainder of this chapter.

5.3 Texture defect lattice formation in the untrapped two-component BEC

In this section we discuss the production of a hexagonal lattice of texture defects in the two-component BEC. We present the results of GPE-based simulations that demonstrate the production of this lattice in an experimentally-feasible system. We first develop a linear model of the defect lattice by extending our earlier model from §2.4.2 (see also Fig. 4.8), of the VA lattice produced by three interfering wavepackets, to a two-component wavefield. Such a system might be realised

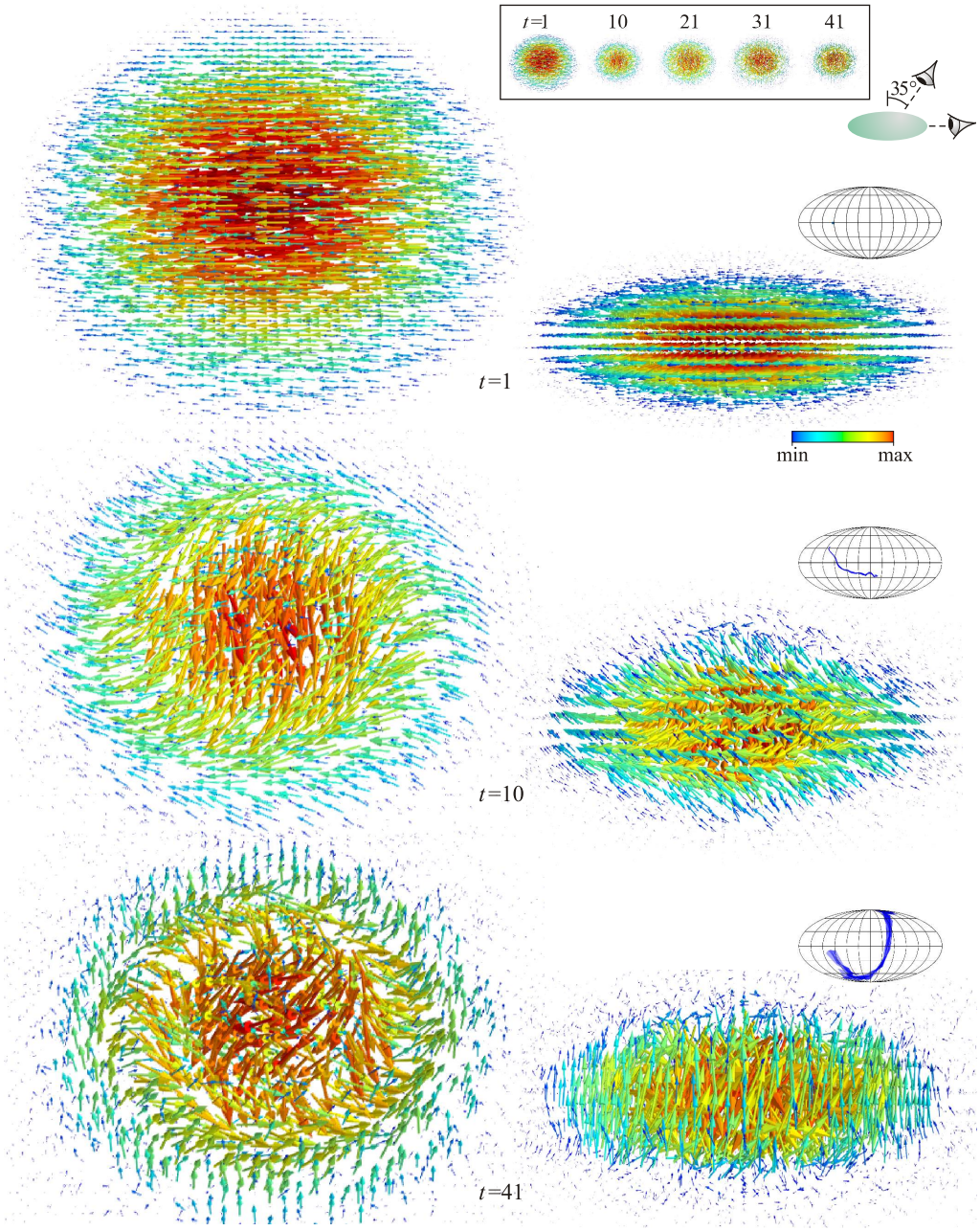

Figure 5.5: Bloch vector visualisation of our simulation of the Mertes et al. (2007) experiment for two viewpoints: a polar angle of 35° (left column) and side on (right column). The scales vary between the large plots, indicated by the fixed-scale smaller versions in the framed inset (with t in ms), which oscillate due to the trap breathing mode. Immediately following the $\pi/2$ pulse at $t = 1$ ms, the vectors point to a single location on the equator of the Mollweide projection of the Bloch sphere. At $t = 10$ ms the vectors begin to precess mostly within the equatorial plane, as shown by the Mollweide projection coverage near the equator. At $t = 41$ ms Bloch vectors cover all polar angles, evident from vectors pointing up toward $|1\rangle$ at large radius and down toward $|2\rangle$ in the centre.

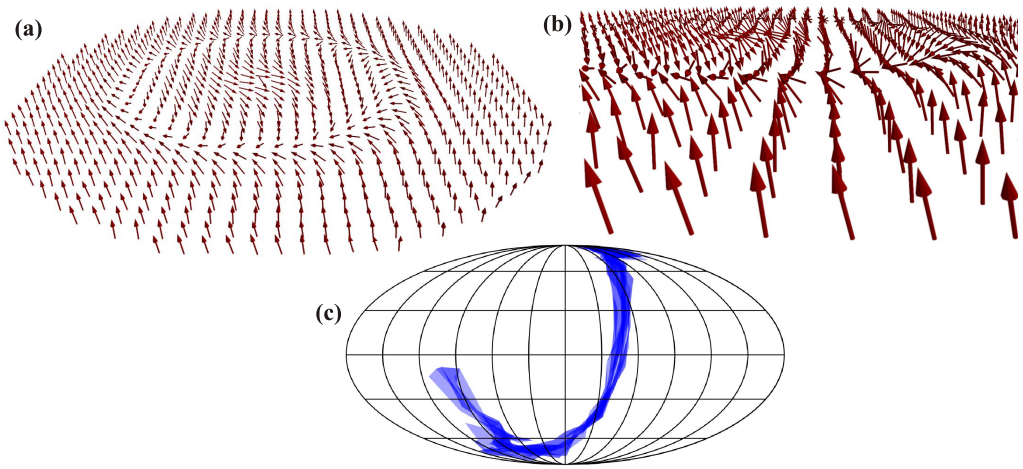

Figure 5.6: A slice through our simulation results of the Mertes et al. (2007) experiment at $t = 41$ ms showing (a) the order parameter, and (b) a view highlighting z-projection variation. (c) The Mollweide projection of the Bloch sphere shows that only a tight band of azimuthal angles is covered, so no topological defect has formed.

physically with two orthogonal polarization states of an optical wavefield.[2] In this case, we note that the Bloch sphere is isomorphic to the Poincaré sphere, on which polarization is usually represented. Following this introduction, the results of numerical simulations that include nonlinear effects are presented.

Just as the rapidly rotating BEC generates an Abrikosov lattice of vortices, when a two-component BEC is rotated rapidly, vortices are produced in both components, giving rise to associated texture defects (Mueller and Ho, 2002). Kasamatsu et al. (2005) also performed numerical studies of this system, varying the interaction between the two components and the rotation frequency, and found interlaced Abrikosov vortex lattices with both hexagonal and square geometries. Reijnders et al. (2004) made a comprehensive study of the texture defect structures in the ground state or *lowest Landau level* of the rapidly rotating spin-1 system. Hen and Karliner (2008b) studied the stability of baby skyrmion lattices by considering various crystallographic arrangements of unit cells with periodic boundary conditions and found that an hexagonal arrangement was most energetically favourable.

When we interfere three pieces of a two-component BEC, we expect two honeycomb lattices to form; one in each component. Because the lattice geometry is dictated mostly by the geometry of the pieces, we might expect the lattices to exactly coincide initially. For a skyrmion to be created, such as that locally described by Eq. (5.5), we would like a vortex in one component to spatially

[2] This was suggested by Lincoln Turner, private communication.

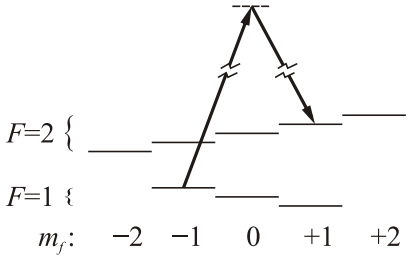

Figure 5.7: Coupling the two groundstate $|F = 1, m_f = -1\rangle$ and $|F = 2, m_f = +1\rangle$ hyperfine levels of ^{87}Rb with two lasers allows for transfer of orbital angular momentum to the excited atoms if either of the lasers (arrows) is an LG beam.

coincide with either a vortex-free region or a vortex of different charge in the other component. To allow the vortices in one component to spatially separate from those of the other, two possibilities will be explored. The first possibility relies on the deliberate misalignment of two honeycomb VA lattices and their subsequent expansion in the untrapped condensate. The second possibility relies instead on the natural separation of initially coincident vortex lines in the trapped condensate. We explore the latter case in the final section of this chapter.

First, we begin by creating a three-piece BEC in state $|1\rangle$ as before. The two-photon coupling of this state to state $|2\rangle$ is now performed by two lasers coupled via a higher virtual energy level, as illustrated in Fig. 5.7. By using an $\mathrm{LG}_{p=0}^{\ell=\pm1}$ beam (see §3.1) for one of these lasers such that the vortical beam axis is aligned with the vertex of the three-way light sheet and parallel to the axial direction z, orbital angular momentum is transferred to the atoms as they are excited to state $|2\rangle$. The excited atoms acquire average phases of $0, 2\pi/3$, and $4\pi/3$, when measured within each of the three pieces relative to the phase of the corresponding piece in state $|1\rangle$. Thus, regardless of the phases of the three pieces in state $|1\rangle$, the phases conferred during the excitation conspire to generate two honeycomb lattices aligned as shown in Fig. 5.8, in which one third of the vortices in one lattice are aligned with corresponding antivortices in the other lattice.

Because we are now using two lasers instead of a combined microwave and RF field, the $\pi/2$ pulse duration is much shorter, so that the piece centroids will not have an opportunity to begin rotating significantly and the lattices should remain aligned.[3] Immediately following the $\pi/2$ pulse, at $t = 0$, all trapping potentials are removed, although the $\pi/2$ pulse could perhaps be applied following removal of the light sheet but prior to interaction of the three pieces with each other. There is probably also further flexibility in the ordering of removal of the light sheet and harmonic trap components. The condensate components expand and

[3]The transition timescale is μs according to Kristian Helmerson, private communication.

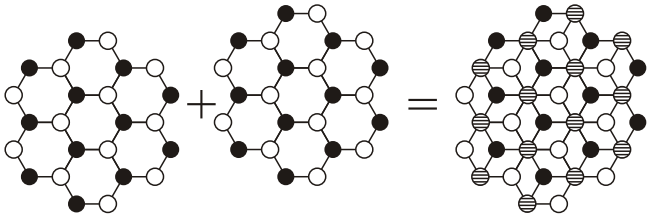

Figure 5.8: The result of combining two honeycomb lattices with the same lattice parameter, each created from three sources with different relative phases. Combining a lattice whose pieces are created with equal phases with one whose pieces are created with relative phases $0, 2\pi/3$ and $4\pi/3$ results in a lattice in which one third of the resulting sites have a relative winding number of 2. In the diagram of the resulting lattice, interpretation of the differently filled circles depends on whether one is interested in the absolute sense of the vortices or the relative sense between the two condensates, each containing one lattice.

interfere, each producing a honeycomb VA lattice, aligned such that three cases occur, indicated by the different markers in Fig. 5.8:

1. A vortex in $|1\rangle$ coincides with a vortex-free region in $|2\rangle$,
2. A vortex-free region in $|1\rangle$ coincides with a vortex in $|2\rangle$.
3. A vortex in $|1\rangle$ coincides with an antivortex in $|2\rangle$.

Naïvely, it might be possible to describe pseudo-spinor behaviours of these three cases with Eq. (5.5), which describes baby skyrmions, and two additional related equations for the two other cases:

$$|\Psi\rangle = \begin{pmatrix} z/d \\ 1 \end{pmatrix} e^{-|z|^2/2d^2}, \tag{5.7}$$

and

$$|\Psi\rangle = \begin{pmatrix} z/d \\ z^*/d \end{pmatrix} e^{-|z|^2/2d^2}, \tag{5.8}$$

which respectively describe baby skyrmions of opposite charge, and a *planar defect*, shown in Fig. 5.9, whose Bloch vectors all lie parallel to the *xy* plane (Mermin, 1979). For the sake of brevity, we drop the qualifier *baby* in the following discussion and refer to them as *skyrmions*.

5.3.1 Numerical model

Here, we describe the numerical model of the two-component BEC and present simulation results for two different lattice translations.

Because the texture defects exist in two component, 2D complex scalar fields, mapped to a representation of a 2D plane of 3-vectors, we numerically model the

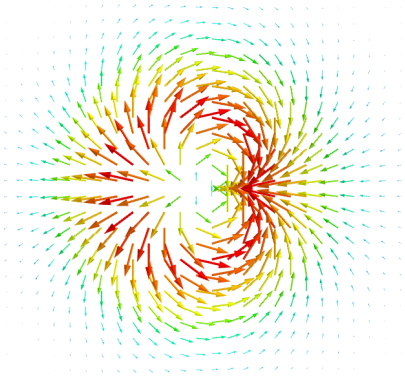

Figure 5.9: The planar defect described by Eq. (5.8), all of whose Bloch vectors lie in a plane and cover the equator of the Bloch sphere twice.

system using a reduced-dimensional model of two coupled 2D GPEs. Inspired by the regular lattices that were observed by Henderson et al. (2009), we modelled Gaussian wavepackets rather than model a condensate divided using laser light-sheets. Furthermore, the discussion in §4.4.3 argued in favour of removal of the axial trap when the aim is to generate a regular honeycomb lattice. This was incorporated into the 2D model explicitly as follows.

To reduce the 3D model to 2D in §4.3.2, the spatial wavefunction was separated into axial and transverse components and the axial component was taken to be the Gaussian ground state solution to a non-interacting 1D fixed harmonic oscillator. This amounts to the assumptions that the condensate is tightly trapped in the z direction and self interactions between adjacent parallel xy planes can be neglected. To model the removal of the axial trap at $t = 0$ and the associated ballistic expansion, we replace the fixed harmonic oscillator solution with the expanding wavepacket introduced in Eq. (2.47), but reduced to (1+1)D. By matching the Gaussian profiles of the fixed and expanding solutions at $t = 0$, the initial momentum uncertainty is found to be $\Delta p = \sqrt{m\omega_z\hbar}$, which, when substituted into Eq. (2.47), gives the expression for the time varying axial component

$$\Theta(z,t) = \left(\frac{m\omega_z}{\pi\hbar}\right)^{1/4}\left(\frac{1}{1+i\omega_z t}\right)^{1/2}\exp\left(\frac{-m\omega_z}{2\hbar(1+i\omega_z t)}z^2\right), \tag{5.9}$$

where z is length, t is time, m is the mass of an atom of the atomic species, and ω_z is the axial trap angular frequency. As shown in Appendix C, evaluating Eq. (4.6), with $\Theta(z,t)$ in place of $\Theta_0(z)$, results in the coupled GPEs

$$i\hbar\partial_t\Psi_i(\mathbf{r},t) = \left(-\frac{\hbar^2}{2m}\nabla_\perp^2 + V_i(\mathbf{r}) + \Gamma_i(t)\sum_{j=1,2}U_{ij}\left|\Psi_j(\mathbf{r},t)\right|^2\right)\Psi_i(\mathbf{r},t),\ \ i=1,2, \tag{5.10}$$

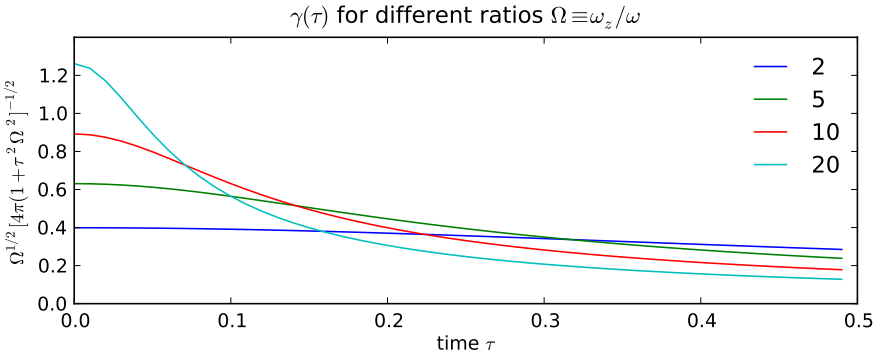

Figure 5.10: Ballistic expansion behaviour of the nonlinear coupling term $\gamma(\tau)$ for some typical ratios of axial to radial trap frequencies for dimensionless time τ.

where Ψ_i is now the 2D order parameter of component $|i\rangle$. The 3D-to-2D factor $\Gamma_i(t) = [m\omega_{zi}/(2\pi\hbar)]^{1/2}\,(1+t^2{\omega_{zi}}^2)^{-1/2}$, which matches the previously derived fixed factor at $t = 0$, may be different for the two components as they may experience different z-trapping frequencies. Thus ω_{zi} is the z-trapping frequency for component $|i\rangle$. Similarly, the transverse trap may influence the components differently, so $V_i(\mathbf{r}) \equiv m{\omega_i}^2|\mathbf{r}|^2/2$ contains a component-dependent trap frequency ω_i. Because we are considering Gaussian wavepackets initially trapped over short length scales by red-detuned lasers or a spatial light modulator (SLM)-based optical trap, the simulations neglect the harmonic trap term, or set it to a low frequency. As argued above for the 3D case, the normalisation condition here was changed to Eq. (5.2) for a volume element $dV \equiv dx\,dy\,dz$.

The related dimensionless forms of the above equations are

$$i\partial_\tau\varphi_i = \left(-\nabla_\perp^2 + \frac{\rho^2}{4}\left(\frac{\omega_i}{\omega}\right)^2 + 8\pi\,\gamma_i(\tau)\sum_{j=1,2}\alpha_{ij}\left|\varphi_j\right|^2\right)\varphi_i,\ \ i = 1,2, \tag{5.11}$$

where $\gamma_i(\tau) = [\omega_{zi}/(4\pi\omega)]^{1/2}\,[1+\tau^2(\omega_{zi}/\omega)^2]^{-1/2}$, $\omega \equiv \omega_1$ and the harmonic trap has been included directly. The behaviour of the factor $\gamma(\tau)$ is shown in Fig. 5.10 for some representative trap ratios.

The numerical model is the same as reported in §4.3.6, except for the following differences. The mass and scattering lengths used here were the same as reported by Mertes et al. (2007) (see §5.2). A radial trap of angular frequency $\omega = 46.5\,\mathrm{rad\,s^{-1}}$ was incorporated into the ground state computation. However, this has minimal physical significance as the superposed Gaussian wells trap the atoms over much shorter length scales. The axial traps $\omega_{zi} \equiv \omega_z = 500\,\mathrm{rad\,s^{-1}}$ were set equal for both components. These were incorporated via the fixed factor $\gamma(0)$ for the ground state computation and replaced by the time-dependent factor $\gamma(\tau)$ in the time evolution

code. The condensate contains a total of $N = 50,000$ atoms. This relatively small population size was found to be necessary to minimise nonlinear perturbative effects and maximise the regularity of the lattice. Higher populations still result in the production of texture defects, but the dynamics are more chaotic.

In order to observe the planar defect, it is most convenient in simulations and perhaps experimentally to form it in the centre of the lattice with respect to the initial pieces, where it remains as the lattice expands. To centre the lattice on the planar defect, a half lattice-spacing translation must be applied equally to both components by manipulation of the initial phases. This translation is effected by first applying a phase winding to $|1\rangle$ immediately following establishment of the ground state. Experimentally, such control of the initial relative phases of the pieces is only now becoming feasible. If the pieces can be created with equal phases, an appropriate phase winding could be established by the following method. By swapping the arbitrarily-assigned labels $|1\rangle$ and $|2\rangle$ of the component states, such that the system is prepared in state $|2\rangle$, a condensate whose three pieces have the appropriate phases in state $|1\rangle$ may be created using a π pulse with an $\mathrm{LG}_{p=0}^{\ell=-1}$ beam. Subsequent application of a $\pi/2$ pulse with an $\mathrm{LG}_{p=0}^{\ell=1}$ beam, as before, should then apply a further winding to those atoms transferred back to $|2\rangle$. The second set of results corresponds to this case.

5.3.2 Simulation results

The simulation results are presented in a series of figures showing both the individual BEC components and the corresponding Bloch vector visualisations. The individual components in Fig. 5.11(a) show the formation of the honeycomb VA lattices from the three approximately Gaussian wavepackets initially arranged at the corners of an equilateral triangle. The formation may be related back to that presented in Chap. 4.

The initial configuration at $t = 0$ s was formed from the trap potential shown in Fig. 5.11(d) corresponding to three wells in a shallow harmonic trap. This potential was removed at $t = 0$ s, immediately following the transfer of half the atoms from $|1\rangle$ to $|2\rangle$ with the $\pi/2$ pulse. Figure 5.11(b) shows the phases corresponding to this time, enveloped by the probability density of these pieces. Component $|1\rangle$ is created with uniform phase. A smoothly varying angular phase, such as would be conferred by an $\mathrm{LG}_{p=0}^{\ell=-1}$ beam, is applied to $|2\rangle$ along with the fixed phase rotation due to the $\pi/2$ pulse.

Note that the LG beam's radial intensity variation was not modelled. The location of the radial intensity peak is a controllable experimental parameter that

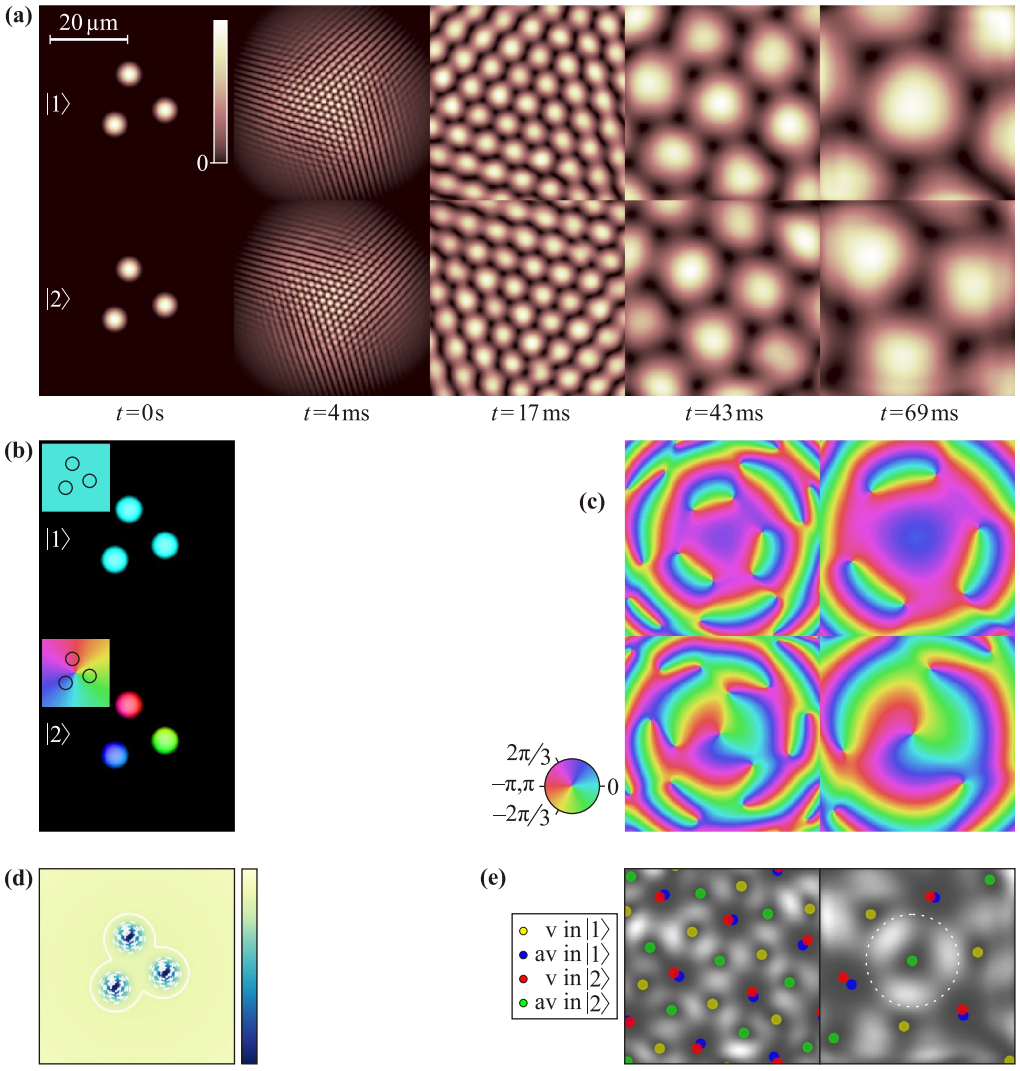

Figure 5.11: (a) Probability density, (b,c) phase, and (e) detected vortices in the two level ^{87}Rb system. As all traps are removed at $t = 0$, the approximately Gaussian wavepackets expand and interfere. The initial piece phases serve to align the resulting lattices so that vortices and antivortices combine in three different ways, associated with different texture defects. (d) A contour plot of the trap potential. The circular dashed region in (e) at $t = 69$ ms corresponds to Fig. 5.14(a).

can be chosen to coincide with the wavepacket centroids, but shifting the peak inwards or outwards from this radius may be desirable.

The initial phase coherence of the component $|2\rangle$ wavepackets is evident in the uniformity of the phase in Fig. 5.11(b), and is indirectly evident from the observation that the resulting lattices in the two components both have qualitatively similar visibility and uniformity. This coherence and associated behaviour was a

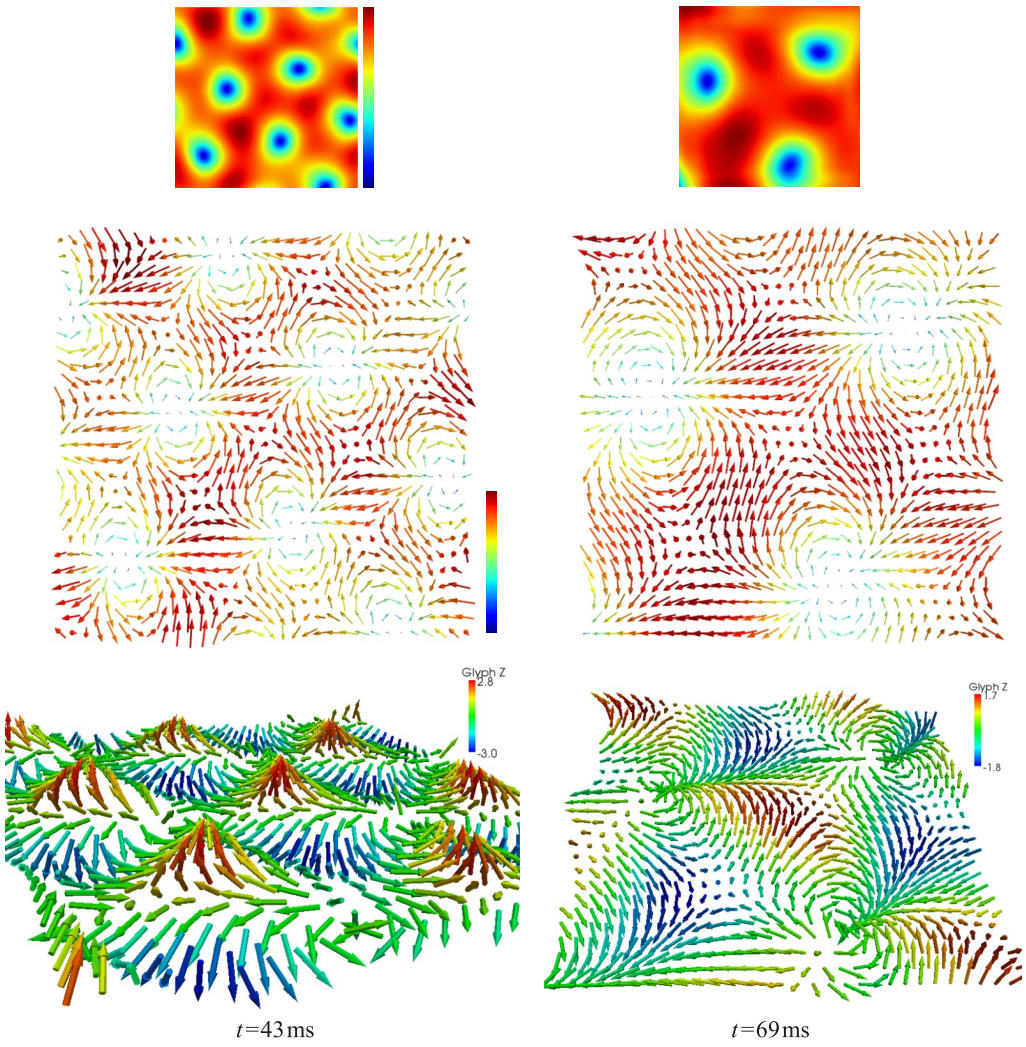

Figure 5.12: Texture defects in the two level ^{87}Rb system corresponding to the last two frames in Fig. 5.11. (Top row) Plots of the norm $\rho = \sqrt{|\Psi_1|^2 + |\Psi_2|^2}$. (Middle row) Bloch vectors scaled and coloured by ρ. (Bottom row) Normalised Bloch vectors coloured by their z component. Thus red vectors point toward $|1\rangle$, blue point toward $|2\rangle$, and green point toward the equator of the Bloch sphere.

primary motivation for choosing to model spatially localised Gaussian wavepackets instead of extended pieces created with laser light sheets. The phase at t = 43 ms and t = 69 ms is shown in Fig. 5.11(c), with the vortices and antivortices detected using phase unwrapping (see Appendix A) shown in Fig. 5.11(e) overlaid on the combined probability density $\Psi_1\Psi_1^*\Psi_2\Psi_2^*$.

Figure 5.12 shows the texture lattice corresponding to the final two frames of Fig. 5.11. Note that the images in the later figure have been reoriented. From top to bottom we see the norm $\rho = \sqrt{|\Psi_1|^2 + |\Psi_2|^2}$, the lattice viewed from above

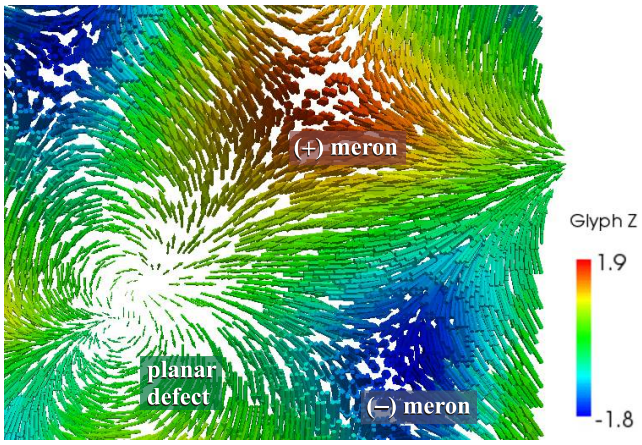

Figure 5.13: A section of lattice showing the triumvirate of texture defect types corresponding to a central region of Fig. 5.15(d) at $t = 69$ ms.

using Bloch vectors scaled and coloured by ρ, and an oblique view of the Bloch vectors, normalised and coloured by their z component. Thus red vectors point toward $|1\rangle$, blue point toward $|2\rangle$, and green point toward the equator of the Bloch sphere, enabling straightforward identification of the three defect types, which are explicitly labelled in Fig. 5.13.

Three lattices can be identified in Fig. 5.12, with reference to Fig. 5.8; a lattice of planar defects, and two lattices associated with a vortex in one component. When all information about the Bloch vector orientation is discarded, the norm forms a hexagonal lattice, as shown in the top-row images. The planar defects are identifiable in these images, as the Bloch vectors shrink only at the planar defect locations. Restoring the orientation information results in the middle row of subfigures, where the planar defect structure in Fig. 5.9 is now clear. We claim that the red and blue texture regions are merons, which we now proceed to justify.

In order to classify the texture defects that form the lattice, we must choose the defect boundaries carefully. Taken in isolation, we identified three cases in §5.3 by Eqs (5.5), (5.7), and (5.8). These describe the two signs of baby skyrmions and the planar defect. However, the lattice defects are not isolated from one another and the boundary is restricted by the presence of neighbouring lattice defects. We have some freedom in this choice of boundary location. One choice is midway between any pair of defects. This means that regions with a vortex in only one component might have natural boundaries along lines joining two planar defect centres. Examining the Bloch vector directions, no natural closed path exists, along which all Bloch vectors point in a single direction, which could be mapped to a single point in the order parameter space. Thus, none of the texture defects is

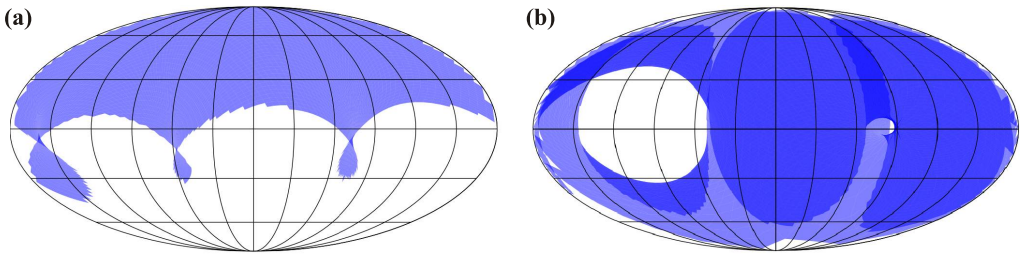

Figure 5.14: Mollweide plots of the order parameter space coverage for meron and planar defects. (a) Coverage for an up meron corresponding to the dashed region in Fig. 5.11(e). (b) Coverage for the planar defect delimited by the dashed region in Fig. 5.15(d); the covering colour is semi-transparent, with multiply-covered regions appearing as deeper shades.

actually a skyrmion. However, as Fig. 5.14(a) shows, mapping the vectors within the circular dashed boundary in Fig. 5.11(e) to the order parameter space results in coverage of the upper half of the Bloch sphere. As the vectors near the boundary cross through the equatorial plane, a boundary should exist that coincides exactly with the equator, so we identify the enclosed defect as a meron. Examination of the early lattice, when it is tens of milliseconds old, showed that certain directions on the equator seemed not be covered. However, at later times, as the influence of neighbouring defects on one another diminishes, these directions are filled in. The two meron lattices can be differentiated as one comprised of up merons and one of down merons. The spacings of the defects within each of the three interleaved lattices are equal and share the crystallographic description given in §4.4.4.

We now consider a lattice that has been translated so that the planar defect is formed centrally by addition of a phase winding to component $|1\rangle$ prior to the $\pi/2$ pulse. The results are presented in Fig. 5.15. Although we can begin to see variation in phase across the initial wavepackets in Fig. 5.15(b), particularly in component $|2\rangle$, the resulting lattices remain uniform; the reduction of initial phase coherence has not affected the lattice quality.

Figure 5.16 shows the associated Bloch vector visualisations. The planar defect is formed centrally in the simulation grid. Figure 5.13 focuses on this central region at $t = 69$ ms, revealing that the planar defect is skewed, when compared to the idealised case shown in Fig. 5.9. This is due to misalignment of the corresponding vortex and antivortex, visible at the centre of Fig. 5.15(d) at $t = 69$ ms. We did not study the influences affecting this alignment; further study of these influences might be worthwhile, in order to minimise them in any experiment that might be performed.

The choice of boundary defining the planar defect is less straightforward than

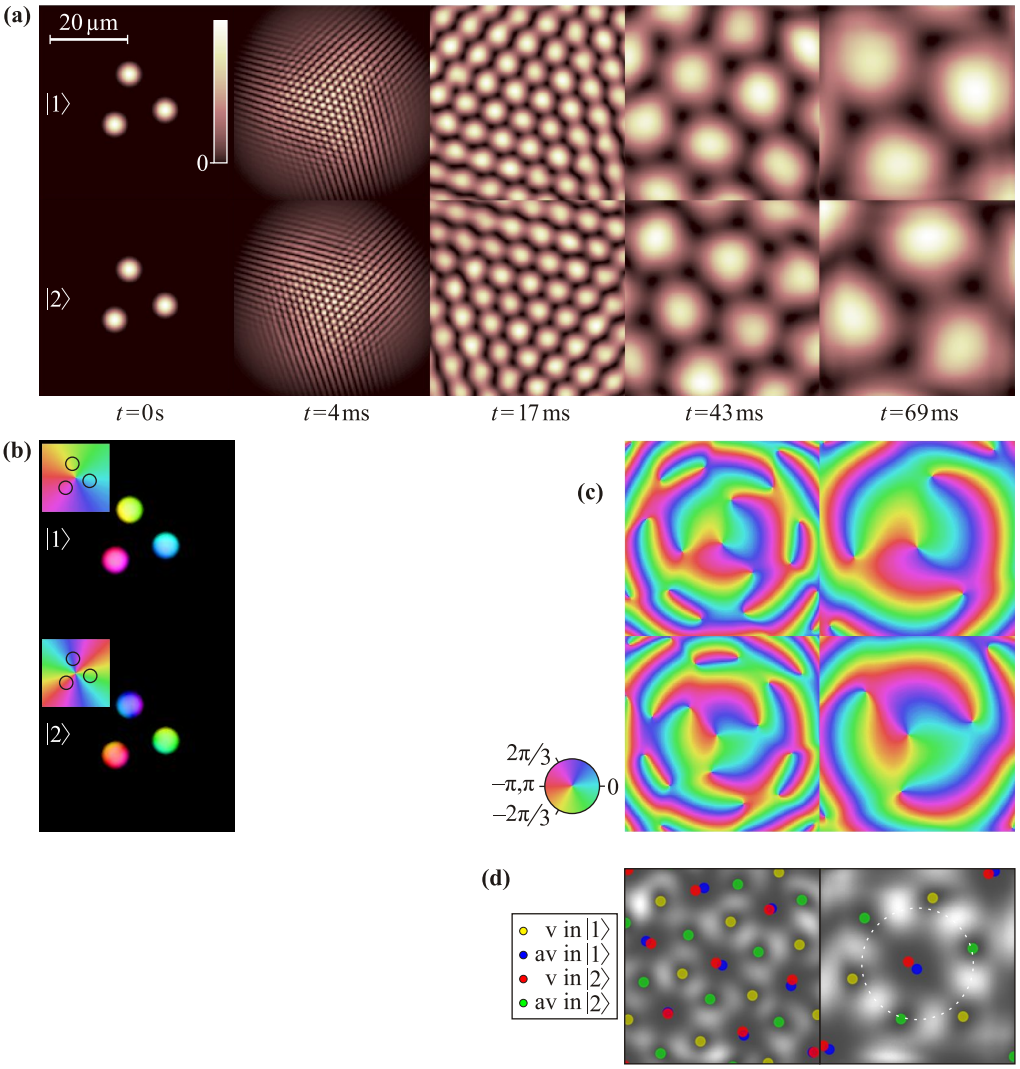

Figure 5.15: (a) Probability density, (b,c) phase, and (d) detected vortices in the two level ^{87}Rb system. Compared to the case shown in Fig. 5.11, both lattices here are translated by first applying a phase winding to the pieces in $|1\rangle$. The circular dashed region in (d) at t = 69 ms corresponds to Fig. 5.14(b).

with the merons. A circular boundary is plotted in Fig. 5.15(d) that extends almost out to the ring of vortices that are identified with merons. Figure 5.14(b) shows the order parameter space corresponding to the bounded region to be almost covered twice, except for a large hole which appears to be due to the misalignment of the associated vortex and antivortex causing the exclusion of certain projection directions. Holes are also observed along the equator at earlier times, when the defects of the expanding lattice are closer to one another and their neighbouring influence leads to the elimination of certain directions. As the lattice evolves, this

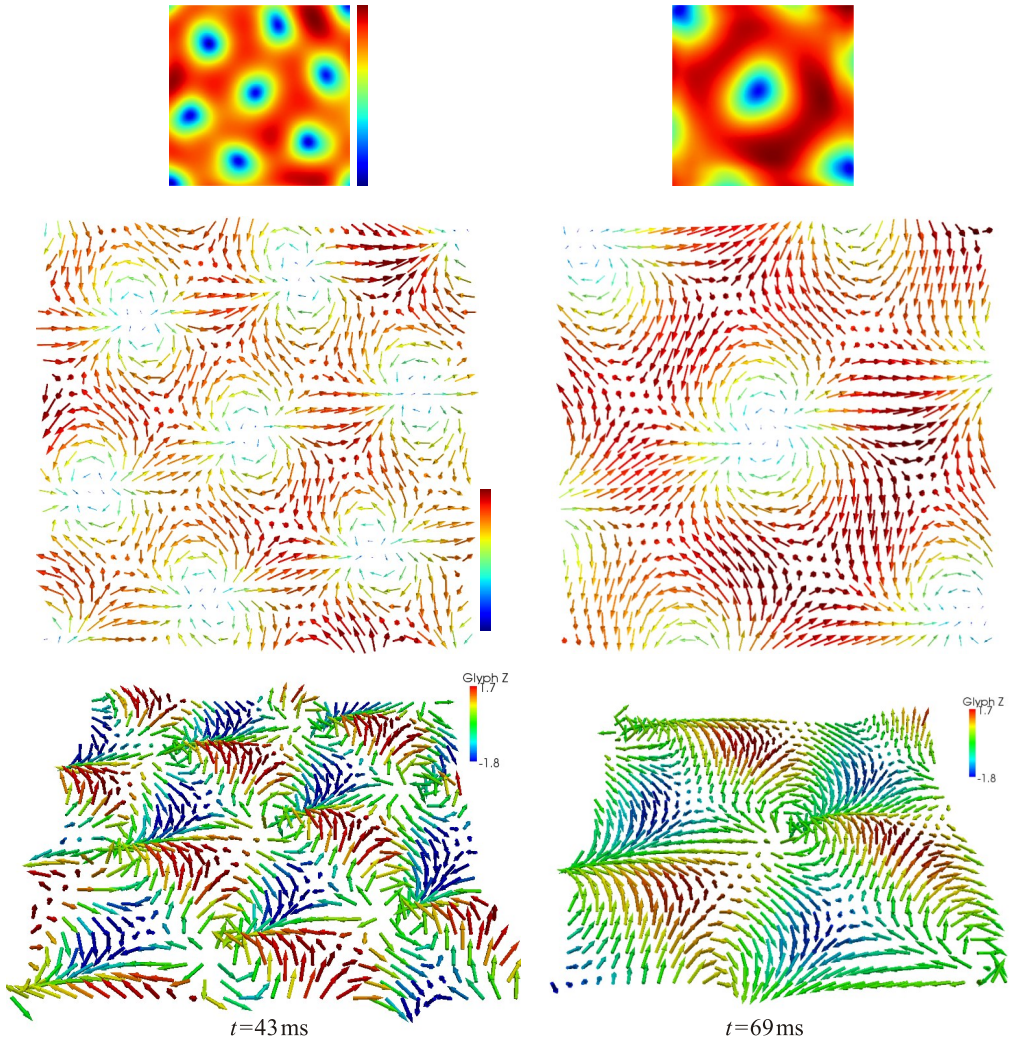

Figure 5.16: Texture defects in the translated two-level ^{87}Rb system corresponding to the last two frames in Fig. 5.15. (Top row) Plots of the norm ρ. (Middle row) Bloch vectors scaled and coloured by ρ. (Bottom row) Normalised Bloch vectors coloured by their z component.

influence is reduced and the corresponding holes close.

Consider any convex path enclosing both of the planar defect's component vortices, and extending out to the circular boundary shown in Fig. 5.15(d). In circling the planar defect once along such a path, the z component of the vectors repeatedly cycles three times through positive and negative values. If we had chosen the boundary to be the hexagon whose vertices are the six vortices associated with the encircling merons, the order parameter space would be covered approximately twice. If we relax the requirement that the boundary map to a single point in order parameter space we could then claim that the planar defect, with its boundary

defined by its neighbouring meron-forming vortices, is a topological texture defect. Even so, in order to cover the order parameter space fully, the projections must follow paths roughly along lines of longitude 120° apart, reaching the two poles. The projection directions of vectors on the boundary are visible in the Mollweide plot of Fig. 5.14(b) as clamshell-like edges, cycling from the upper to the lower hemisphere, but not reaching all the way to the poles. It should be possible to find such a boundary at late evolution times.

The charge of the defect and the number of times it covers the order parameter space relates to the relative charge of the vortices in its components. A 4π-skyrmion covers the S^2 order parameter space once, subtending a 4π solid angle; an 8π-skyrmion covers it twice. Since the relative charge of the associated vortex and antivortex is two, we might call the planar defect an 8π-skyrmion; although this is not strictly the case, as we have discussed.

We have presented an experimentally feasible scheme for the production of three interleaved hexagonal lattices of texture defects. The lattices were formed interferometrically as VA lattices within each of the two components of a pseudo-spin-half system of two coupled BECs. Each lattice evolved from a three-piece BEC initially formed with pancake geometry, where half of the atoms are excited into a second long-lived state using an LG beam immediately prior to removal of all traps. When the components were combined into the pseudo-spinor representation, one of the resulting texture defect lattices was seen to be composed of planar defects that cover the associated order parameter space twice. A second lattice was composed of merons, and the remaining lattice comprised merons of opposite charge.

5.4 Texture defects in the trapped two-component BEC

In trying to create skyrmions as a result of the interference of three BEC pieces, we have managed to create a lattice of texture defects by combining two suitably aligned honeycomb vortex lattices. Taking inspiration from the developments in the previous chapter, in which we studied the vortex dynamics in a trapped condensate following melting of the honeycomb lattice, we now investigate the creation of texture defects associated with the constituent vortices and antivortices in the trapped multicomponent condensate. In the single-component BEC, the dynamics of the vortex clusters were briefly investigated. In the multicomponent condensate the influence of vortices in both components will drive the associated

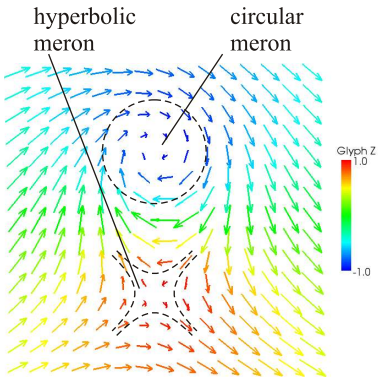

Figure 5.17: A vortex-skyrmion composed of a circular and a hyperbolic meron associated with an antivortex $z = x - i(y + y_0)$ in $|1\rangle$ and an antivortex $z = x - i(y - y_0)$ in $|2\rangle$, respectively. Image after Volovik (2003, p.204).

texture dynamics. We will not get as far as studying these dynamics but note that they are an interesting subject of future study. We will restrict attention to the trapped pancake geometry, both to make connections with the previous chapter, and also because we are concerned with textures on a 2D stage of 3-vectors, with our actors being the baby skyrmion, meron, and planar defects.

5.4.1 The vortex-skyrmion

Figure 5.17 shows an example of a textural object known as a vortex-skyrmion (Volovik, 2003, p.204). The vortex-skyrmion is composed of one circular meron and one hyperbolic meron; these names being associated with the orientations of the vectors surrounding the meron cores. When found in this paired configuration, these merons are often called *Mermin-Ho vortices* (Mermin and Ho, 1976). The vortex-skyrmion meets our previously identified requirements for being considered a skyrmion. First, a boundary exists around the pair of merons along which all vectors map to a single point on the Bloch sphere. Second, the circular and hyperbolic merons, enclosed within this boundary, cover the upper and lower hemispheres of the Bloch sphere, respectively; so that the order parameter space is completely covered once.

If a contour is traced around the core of the circular meron, the vector projections in the corresponding order parameter space wind in the same sense as the contour is traversed. Traversing a similar contour around the hyperbolic meron, the projections wind in the opposite sense. Surprisingly, as we will see below, this behaviour, and whether a particular meron is circular or hyperbolic, is not associated with the charge of the constituent vortex in an obvious way, but depends

on the defect neighbourhood.

The vortex-skyrmion and the skyrmion described by Eq. (5.5) are distinguished by the number of vortices of which they are composed. In the vortex-skyrmion each meron is associated with a separate vortex, whereas the skyrmion of Eq. (5.5) has only a single vortex. Associated with these skyrmions are vorticity quanta; the vortex-skyrmion carrying two quanta and the skyrmion carrying a single quantum of vorticity.

5.4.2 Simulation results

We modelled the ^{87}Rb $\left|F = 1, m_f = -1\right\rangle$ and $\left|F = 2, m_f = +1\right\rangle$ condensate as described above in §5.3.1, except that both the transverse radial and axial trap components were maintained to tightly confine both condensate components throughout the simulation. For all simulations in this section, the axial trap frequencies were set equal for both components, to $\omega_{zi} \equiv \omega_z = 1000\,\text{rad s}^{-1}$. These are incorporated via the fixed factor $\Gamma = [m\omega_z/(2\pi\hbar)]^{1/2}$. In contrast, the transverse trap frequencies were chosen with slightly differing values. This both reflects the physics and, as this is the only parameter that differs between the two components, also serves to break a symmetry in the numerical simulation, thus avoiding the exhibition of identical dynamics in the two components. The transverse trap frequencies were $\omega \equiv \omega_1 = 193.72\,\text{rad s}^{-1} \equiv 30.83\,\text{Hz}$ and $\omega_2 = 195.26\,\text{rad s}^{-1} \equiv 31.08\,\text{Hz}$, after those in Mertes et al. (2007). Since we are no longer concerned with trying to minimise nonlinear effects, the number of atoms was increased over the untrapped case above to $N = 300,000$ atoms.

The Gaussian trap wells that initially separated the three pieces were slightly shallower and wider than considered earlier. The motivation for this change was simply to reduce the extent to which the condensate expands upon removal of the trapping wells, and consequently to reduce the required size of the numerical lattice. In contrast with our previous studies, no particular care was taken to find an initial geometry aimed at producing a high quality lattice. We were not interested in the lattice here, nor with the details of the number of vortices produced; we simply wanted a mechanism to produce a number of vortices in the trapped condensate. Therefore, we could equally well have begun with a two-piece BEC and relied on the snake instability to create free vortices and antivortices.

Figure 5.18 shows the individual probability densities of the trapped two component condensate as it evolves from three Gaussian wavepackets, formed initially in state $|1\rangle$, and subsequently transferred by a $\pi/2$ pulse, into an equal population in states $|1\rangle$ and $|2\rangle$. In contrast with the untrapped case, no LG beam is included

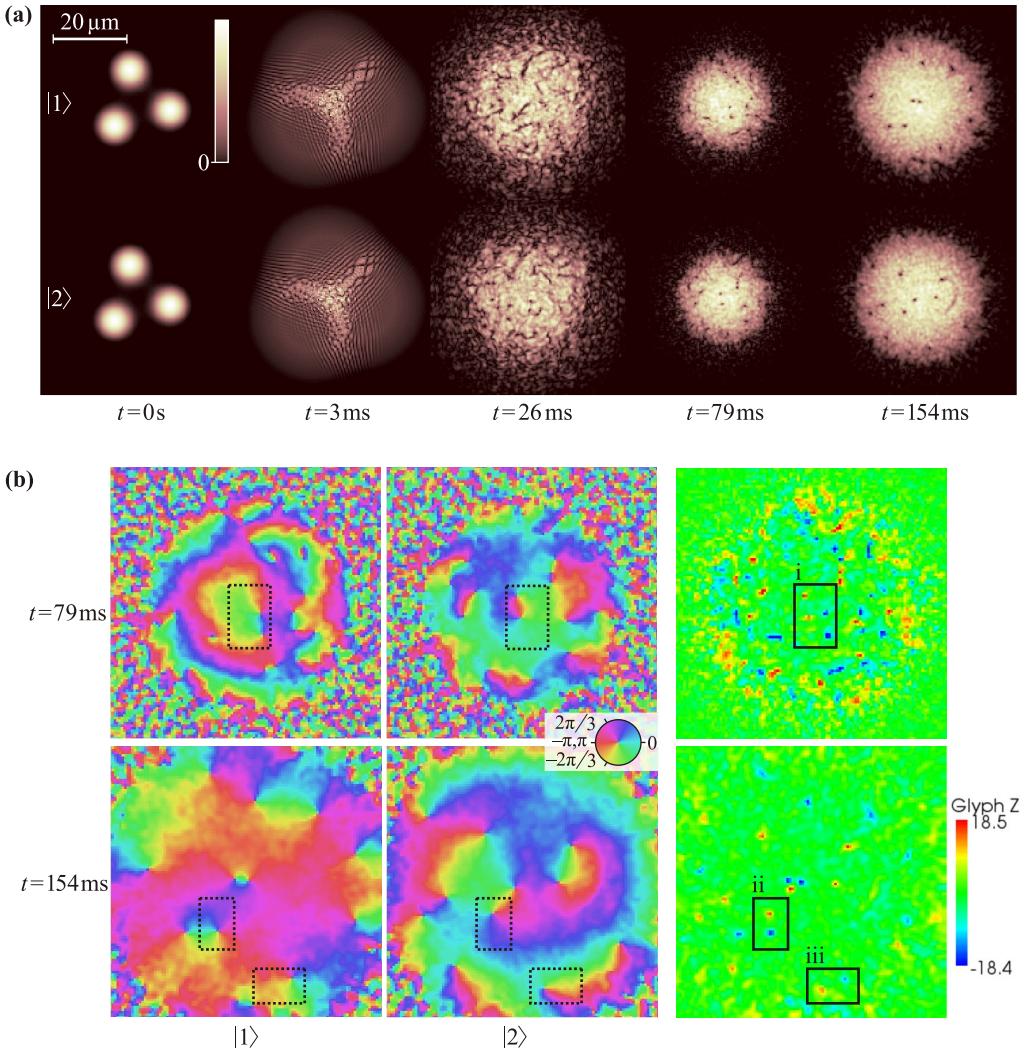

Figure 5.18: Evolution of the trapped two-component condensate. (a) Probability density. (b) The associated component phases (magnified) at $t = 79$ ms (upper) and $t = 154$ ms (lower) reveal the vortices and their association with the z component of the Bloch vector directions, shown to the right. Regions (i), (ii), and (iii) are identified in Fig. 5.20 and corresponding regions are overlaid on the phase with dotted outlines.

in this model. We are relying on the vortex dynamics following lattice melting to move vortices into arrangements that can be identified with textures.

Careful comparison of the interference patterns of the components at $t = 3$ ms shows that they differ minutely. The effect of the small difference in transverse trap frequency is amplified in the presence of the coupling term α_{12} [see Eq. (5.11)] and observed as a rapid divergence of the component dynamics, which appear completely uncorrelated soon afterwards. It is possible that the chaotic behaviour

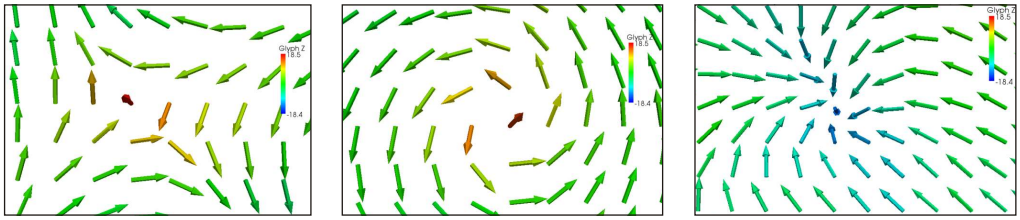

(a) (b) (c)

Figure 5.19: Meron defect types. (a) Hyperbolic up meron, (b) Circular up meron, and (c) Rotated circular down meron.

is due to numerical artefacts rather than an innate feature of the system; further investigation would be required to establish its source. Indeed, no clean honeycomb VA lattice is formed; the vortex production appears to be due to a combination of "linear" interference effects, the snake instability, and more general turbulence. We are not really concerned here with the vortex creation mechanism. The important aspect is that, given vortices are present, their dynamics in one component can be thought of as uncorrelated with those in the other component, as examination of the frames from $t = 26$ ms onwards suggests. Therefore, four possible permutations of vortices in one component with a vortex-free region in the other are likely to be observed; a vortex in $|1\rangle$, antivortex in $|1\rangle$, vortex in $|2\rangle$, or antivortex in $|2\rangle$. We can associate textures with each of these possibilities, examples of which are shown in Fig. 5.19.

We saw only two of these combinations in the previous section: vortices in $|1\rangle$ and antivortices in $|2\rangle$; the others combining to form the planar defect. Indeed, we have ignored for the moment the lower-likelihood case of a vortex in one component aligning with an antivortex in the other, which we have seen to give rise to a planar defect. The combination of a vortex in one component aligning with a vortex in the other (or two antivortices aligning) has not been observed, but there is no reason to suspect it cannot be created. If such a combination is produced in perfect alignment, simple linear simulations (not presented here) show that no texture defect results. However, this is a degenerate case, and even a small misalignment results in a vortex-skyrmion, so such cases may be worthy of further investigation.

Following the production of vortices, each component individually exhibits the dynamical effects that were described in §4.4.3 and §4.4.5, including the overall breathing mode oscillation (the cause of the overall size variation), vortex cluster dynamics, and vortex-sound interactions. These late-stage dynamics appear not to be affected qualitatively by the inclusion here of the inter-component scattering parameter α_{12} and the change of the initial piece profiles to Gaussian wavepackets.

Whether there is a quantitative change in some detail of the dynamics, due to the inclusion of α_{12}, remains a subject for further study.

Surveying the landscape of textures resulting from our simulation, we see that all defects identified with individual vortices are merons. Vortices and antivortices in $|1\rangle$ correspond to down merons, whereas vortices and antivortices in $|2\rangle$ correspond to up merons. We did not search for cases of planar defects but they are likely to exist fleetingly. We can identify both the hyperbolic and circular merons that were introduced in Fig. 5.17, as well as a third type involving vectors that converge on or diverge from the vortex location. An example of the hyperbolic meron is shown in Fig. 5.19(a). As mentioned above, the vector projection along a contour traced around the meron core determines whether it is circular or hyperbolic. The projection winds in the opposite sense as a circuit around Figs 5.19(b) or (c), which are both examples of circular merons. Figure 5.19(c) has an extra $\pi/2$ rotation of the ϕ coordinate compared to Fig. 5.19(b).

The phase corresponding to the last two frames in Fig. 5.18(a) is shown in Fig. 5.18(b) alongside a map of the z component of the Bloch vectors. The green background of these maps illustrates that most vectors lie on the equator of the Bloch sphere. Because of the large proportion of green in these maps, we are provided with another opportunity to relax the strict definition of topological defects and provide a weaker definition of other skyrmion-like texture defects. In the absence of a boundary defined by the vectors sharing a common single projection direction, this would allow us to still usefully refer to texture clusters. In our pseudo-spinor model, we have the advantage of being able to identify the vortices directly, but without this ability, we might choose to associate textural objects or *texture clusters* with any closed boundary in the green area enclosing vectors that deviate sufficiently toward the poles of the Bloch sphere.

We identify three interesting examples of texture clusters in the z-component map of Fig. 5.18(b) which are labelled regions (i), (ii), and (iii). Corresponding regions with dotted outlines are shown on the phase, allowing identification of the individual vortices and antivortices in each component with the corresponding textures. The details of these regions are shown using Bloch vectors in Fig. 5.20.

Vortex clusters are energetically bound systems that have a natural association with their higher-order texture cluster counterparts. The most common vortex cluster is the vortex-antivortex dipole (VD), with which we are familiar in the single-component BEC. Within a single component, it is energetically favourable for a vortex and antivortex to be bound to form a dynamically stable VD (Crasovan et al., 2003). In a two-component BEC, the vortex and antivortex in a VD need not reside in the same component. If the two reside in different components,

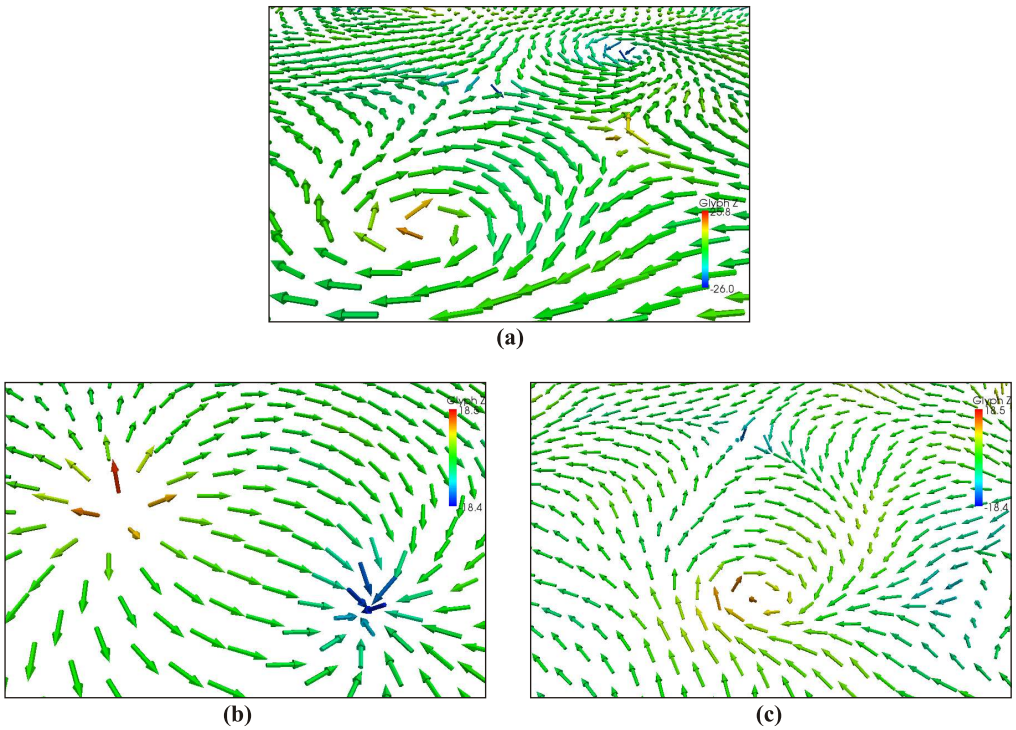

Figure 5.20: (a–c) Examples of defect clusters corresponding respectively to Fig. 5.18(b), regions (i), (ii), and (iii).

it is possible that a dynamically stable pair may still be formed. Such a *vortex molecule* was studied by Kasamatsu et al. (2004) in a rotating two-component BEC and found to be stable in a system with *internal coherent coupling* (see also Kasamatsu et al., 2005). If we assume that such a cluster still requires a vortex and an antivortex for stability, we would expect true vortex-skyrmions, like that shown in Fig. 5.17, which is composed of two antivortices, to be unstable. We are not aware of whether this possible relationship between the VD and vortex-skyrmion has been previously noted. The cluster identified as region (i) has two constituent VDs. It is included here because the resulting visual symmetry of this texture suggests that it may be an interesting object worthy of future investigation.

Region (ii) of Fig. 5.18(b) and its Bloch vector representation in Fig. 5.20(b), shows two circular merons forming a source and sink-like structure reminiscent of the flux lines around a dipolar magnet. This region and region (iii) are both examples where the constituent vortices of a cluster reside in different components. The pair of defects in region (iii) is shown in detail in Fig. 5.20(c) and consists of a circular and hyperbolic meron pair of the same types that form the vortex-skyrmion in Fig. 5.17. It is not clear whether these are part of a bound cluster. Examination of adjacent simulation frames reveals that they are not moving

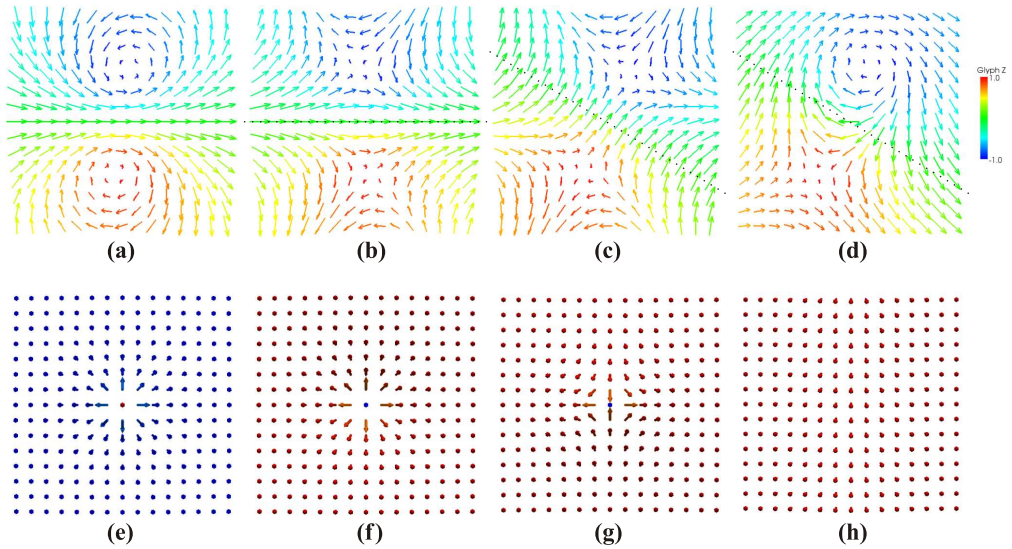

Figure 5.21: Meron pairs comprised of vortices $v \equiv x + i(y + \delta y_1)$ that are transversely displaced from antivortices $av \equiv x - i(y + \delta y_2)$. (a) v in $|1\rangle$ and av in $|2\rangle$, (b) av in $|1\rangle$ and v in $|2\rangle$, (c) av in $|1\rangle$ and v in $|2\rangle$ with x-offsets, (d) av in $|1\rangle$ and av in $|2\rangle$ with x-offsets, (e) two vs in $|2\rangle$ with $|1\rangle$ $(x, y) \equiv 1$, (f) two avs in $|1\rangle$ with $|2\rangle$ $(x, y) \equiv 1$, (g) two vs in $|1\rangle$ with $|2\rangle$ $(x, y) \equiv 1$, (h) a VD composed of a v and an av in $|1\rangle$ with $|2\rangle$ $(x, y) \equiv 1$.

through the condensate, which might be expected if they form a dynamically stable pair by analogy with the VD. Furthermore, the requirement that the boundary map to a single point on the Bloch sphere is not satisfied. The presence of other vortices in the condensate has large-scale (topological) effects on the directions of the vectors.

Figure 5.21 presents some textures that have been modelled in a two-component linear system in which the components are not coupled. The constituent vortices are embedded in approximately the same location in each case, but differ in their signs and the component in which they reside. Flipping the sign of the upper vortex in Fig. 5.17 from − to + has two visible effects, shown in Fig. 5.21(a). The sense of the upper meron is reversed and the lower meron changes type from hyperbolic to circular. We see that the shape of the lower meron is not determined by its constituent vortex, but by its relationship to its neighbour. More generally, we can say that it is determined by the meron's boundary conditions, which are themselves established by the arrangement of neighbouring merons.

Examples corresponding to VDs are shown in Figs 5.21(a–c). Figure 5.21(a) and Fig. 5.21(b) differ only in the signs of the constituent vortices. They demonstrate a dual relationship between circular and hyperbolic merons. In a single component system, flipping the signs of the vortices is equivalent to a mirror reflection about a

plane through the vortices. This mirror symmetry no longer exists when a second component is added and one of the vortices is moved to the second component, as exemplified by the contrasting structure of Figs 5.21(a) and (b). Restoring the symmetry would require an operation, in addition to flipping the signs, that swapped the component assignments $|1\rangle \rightleftharpoons |2\rangle$.

The effect of displacing the vortices along x is shown in Fig. 5.21(c), which differs only in this respect compared to Fig. 5.21(b). Focusing on the vectors along the midline between the merons in (b), which all map to a single point on the Bloch sphere, the simple x-displacement of the merons rotates the midline (dotted line) and the associated vectors to lie along the new perpendicular bisector of the vortex locations; it rotates the background reference frame. It also rotates the projection to a new point on the equator of the Bloch sphere. Similarly, Fig. 5.21(d) is provided for comparison with Fig. 5.17, with the dotted midline shown.

Figure 5.21(d) is the only vortex-skyrmion because, asymptotically far away, the boundary vectors map to a point, whereas Figs 5.21(a–c) have no such boundary. This inability to define a boundary associated with a single vector direction is also true when greater numbers of merons are present, such as in the simulated two-component BEC. Only in specially contrived circumstances will such a boundary exist. Thus the possibility of observing a skyrmion is restricted by the global arrangement of vortices and their associated textures. The study of the restrictions on these arrangements remains yet another subject for future study.

In all cases shown by Figs 5.21(e–h), both vortices reside within one component and the other component is equivalently 1 everywhere. The boundary vectors of these cases map to a single point at one pole of the Bloch sphere, satisfying one of the requirements for the existence of a topological defect. The interiors of Figs 5.21(e–g) appear at first to be merons, but there is a singular point midway between the constituent vortices. That is, the vector at the centre is pointing in the opposite direction, into or out of the page. It is worth remembering that the Bloch vectors here have been normalised to be of equal length and the singular nature of the anomalous vector may be an artefact of normalising it to map it to the order parameter space; these defects require further investigation to understand the anomalous vector. For the case Fig. 5.21(h), the presence of the vortices has surprisingly little effect on the direction of the Bloch vectors, which are only slightly perturbed. Again, further investigation of this case is warranted.

5.5 Summary

In this chapter, we studied the creation of texture defects in the two-component BEC. We began by simulating the experiment of Mertes et al. (2007), which used two internal hyperfine states of ^{87}Rb to model a spin-half system, in order to introduce the concepts and verify the numerical codes used in later simulations. We saw that texture defects were not formed in the modelled system, and attributed this to a lack of vortices in at least one component of the two-component BEC. By basing our simulations on this system, we hope to ensure that they are experimentally realisable.

We exploited the relationship between source phase and lattice translation in the three-piece BEC to create two interleaved honeycomb lattices of vortices and antivortices in 2D simulations of the untrapped pancake BEC. When combined in a pseudo spin-half model, these produced three interleaved lattices of texture defects; one of merons associated with the upper hemisphere of the Bloch sphere, one of merons associated with the lower hemisphere, and one of planar defects. We noted that an equivalent optical experiment could be performed in which the orthogonal polarization components of a monochromatic wavefield take the place of the BEC components.

Noting the turbulent behaviour of vortices and vortex clusters in the single component pancake BEC, we sought to exploit these dynamics to create textures and texture clusters in the trapped two-component pancake BEC. We modelled an interfering three-piece pancake BEC to generate a population of vortices and antivortices and observed the production of associated texture defects and texture clusters. The vortices in individual components were identified with merons. We suggested the possibility of creating dynamically stable VD-like clusters whose constituent vortices reside in different components of the two-component system.

The work presented in this chapter was partly motivated by the desire to produce skyrmions. We discussed two types of skyrmions which are associated with either one or two constituent vortices. According to their formal requirements, as topological defects, skyrmions must satisfy strict boundary conditions. We argued that the boundary conditions are disrupted by the presence of other vortices in the system. Because this disruption reduces the likelihood of their production, we did not observe any skyrmions in our system.

6 Conclusions

We conclude this thesis with a summary of findings and note some open questions and promising avenues for further research.

We began by exploring the vortices and their nodal line structure in 3D in a Young's three-pinhole interferometer modelled by three monochromatic equal-amplitude spherical waves. An analytical description of the vortex structure in the optical far field was obtained as a function of the source locations and phases. A parameter space arose in our description. This showed that the number of vortices generated is finite and allowed an estimate of the number of vortices, which was connected to Gabor's information capacity of a beam. Because counting the vortices amounts to counting lattice points within an ellipse, the problem relates to Gauss's circle problem. The parameter space also led to a natural coordinate system for the vortices, which lie at the intersections of hyperbolic curves.

We made several simplifications in the analytical modelling, the removal of which could lead to new insights or simply a more general model. An early assumption was that the sources are of equal amplitude. Some attempt has been made to avoid this imposition, which would generalise the model. We used delta functions to model spherical wave and Rayleigh-Sommerfeld pinhole propagators. The simple model could be extended by considering diffraction through finite apertures with circular or more general boundaries, generalisation from monochromatic to polychromatic or partially coherent sources, or finite sources with specified coherence properties.

The number of lattice points inside a circle changes in a characteristic way as lattice points cross the circle boundary, such as occurs in the parameter space in response to changing the phase of one of the interferometer sources. This pattern of change, which is related to Gauss's circle problem, may be reflected by the passage of vortices through a circular boundary of the plane in the far field.[1] The study of

[1] Suggested by Mark Dennis, private communication.

the one may give insight to the other.

We studied only the far-field behaviour analytically. The near field and intermediate regime may be amenable to analysis. For example, the point of closest approach of nodal lines to the source plane should be able to be determined.[2]

An obvious generalisation would be to look at vortices from the interference of four, five, or more arbitrarily located sources. The behaviours of various limiting cases could be studied. For example, an infinite line of evenly spaced sources should lead to Bragg diffraction. In this case, a series of spatially isolated peaks should form in the far field, precluding the possibility of vortices in this region. Other limiting cases are those of an aperture, a half-plane, and even no diffracting object. A noteworthy example is that of Berkhout and Beijersbergen (2008), who recently studied the limiting behaviour of n circularly-arranged pinholes illuminated by a Laguerre-Gauss (LG) beam, in an interferometer designed to detect vortices from astronomical sources.

The connection to Gabor's information capacity of a beam was arrived at serendipitously by noting the similarity of form of its description to our expression for the number of vortices produced by three pinholes. It may be possible to derive the relationship directly. There may also be a relationship to the diffracted field from a triangular aperture. With only three sources an unambiguous association exists between the beam cross sectional area and the triangle whose vertices correspond to the source locations. With the addition of a fourth source, ambiguity arises depending on the arrangement of the sources, e.g., if the fourth source lies inside the triangle defined by the other three. If a direct relationship could be found, this ambiguity could be studied.

In deriving the vortex locations for three interfering Gaussian wavepackets evolving in time, we showed that an infinite lattice is produced in the far field, with an overall Gaussian envelope. This is relevant to the evolution of the lattice in the Bose-Einstein condensate (BEC) model, which grows over time, generating vortices within an expanding region. We did not study the growth of the region as a function of time, but it would be worthwhile to do so. The region boundary condition should relate to the local contributions of the three sources, which may not meet the condition of forming a closed triangle of phasors until some time-related condition has been met.

We studied the 3D nodal line structure numerically in the near field for both the spherical point source and the pinhole interferometer cases. The addition of a fourth source within the source plane should allow loops to form away from the

[2] Suggested by Michael Berry, private communication.

source plane. If we shift the source out of this plane, further changes might arise. These cases could also be easily studied numerically.

We applied the numerical superposition of spherical sources to a model of an LG beam diffracting through a ground glass plate (GGP). We presented preliminary results from this model, which reveal an interesting phenomenon in which the speckle and associated vorticity achieved a maximum at a distance that depends on the defining properties of the LG beam and those of the GGP; the wavelength, topological charge and waist radius of the former, and the correlation length and rms deviation roughness of the latter. Future work will be directed at experimentally verifying the numerical findings and developing a physically meaningful model.

The regular vortex-antivortex (VA) honeycomb lattice produced in the linear optics case was predicted to form and studied in the related nonlinear case of a trapped BEC initially separated into three pieces. We showed that the VA honeycomb lattice was produced in both 2D and 3D numerical simulations of BECs, provided the pieces were initially sufficiently well separated. The vortex creation mechanism was explained in terms of a linear theory of the interference of expanding Gaussian wavepackets. We argued that two published experiments to date show indirect evidence of a lattice. However, direct confirmation will require future experiments concentrated on its detection.

The lattice model explains global lattice translations in terms of phase differences between the initially separated pieces. Our model predicts vortex formation even in the case of initially separated pieces with equal phases. This contrasts with the Kibble-Zurek (KZ) mechanism, which was applied to the results of the experiment by Scherer et al. (2007). The relationship with the KZ mechanism, which predicts vortex formation rates in terms of these phases, was noted but not studied in detail. The continued exploration of the connection between these models may be worthwhile. Allowing initial phase gradients within pieces and studying their effect might provide a link.

We applied a crystallographic description of the lattice to a BEC interference experiment performed by Henderson et al. (2009) and verified that their result is consistent with our model. We only presented cases in which a VA lattice formed. Many more simulations would be required to explore and quantify the limits between generation and failure to generate the lattice.

If allowed to expand in the absence of a trapping potential, the honeycomb lattice maintains its form as it expands. In contrast, maintaining the trapping potential allows the lattice to melt and the vortices and antivortices to interact. We observed and described vortex clusters and their dynamics in the trapped

condensate. Direct experimental observation of these dynamics will require the development of improved imaging techniques.

Although we were careful to say that the validity of the 2D model depends on the BEC having a pancake-geometry, 3D simulations showed that the honeycomb lattice is produced even for thick condensates. These simulations also formed structures such as nodal line loops and dynamics involving loop reconnections. Related effects have been noted in linear random wavefields, cosmic string models, and models of turbulence in BECs. Further study of these areas may provide a direction for application of the numerical models to the study of related physics.

The propagation of Kelvin mode excitations in thick condensates leads to the turbulent destruction of Abrikosov lattices in rotating BECs. We discussed the possibility that these excitations may be shielded in the honeycomb lattice, which can be thought of as two interleaved Abrikosov lattices of oppositely charged vortices. It might be possible to measure the propagation of excitations directly or indirectly by the examining the onset of turbulence.

The Berezinskii-Kosterlitz-Thouless (BKT) transition relates the temperature at which a trapped pancaked gas of cold atoms undergoes a transition to a *quasi-condensed* state, associated with superfluidity, with the generation of vortex-antivortex dipoles (VDs) (Hadzibabic et al., 2006). Our model produces a number of vortices that depends on the intensity of the light sheet that initially divides the pieces, and on the angle θ_3 that describes the spacing of two interleaved lattices of vortices and antivortices via Eq. (4.32). It may be possible to relate the initial configuration of the three-piece BEC to an equivalent temperature via these parameters (Simula et al., 2005).

Finite temperature effects are reflected in laboratory experiments as a reduction in the uniformity and coherence of the initial BEC pieces. These effects were ignored in the simple Gross-Pitaevskii equation (GPE) model. In order to model lattice formation in real experimental scenarios, future simulations will incorporate finite temperature effects, perhaps by applying the truncated Wigner approach (Proukakis and Jackson, 2008).

The GPE is a particular example of a nonlinear Schrödinger equation (NLSE) with a cubic nonlinearity. Generalisations to add higher order nonlinear terms can also be considered. For example, fifth order terms often arise in nonlinear optics models involving the NLSE, and allow for the possibility of symmetry breaking potentials. Such terms may also model three-body interactions in BECs, although such interactions are typically also associated with losses. Regardless, modelling of three-wave nonlinear interference with a fifth order term may lead to interesting effects. Although we did not report them in Chap. 4, some numerical simulations

were performed with both positive and negative fifth order terms of the same order of magnitude as the third order term, which were observed to have only small effects on the lattice formation and VA dynamics. That this effect is small is surprising, and hence it may be worthy of further investigation.

Finally, we studied higher order topological texture defects. These may be realised experimentally with a single-species BEC in which the atoms reside in one of two hyperfine states. This model relates texture defects to vortices within one component of a two-component pseudo spin-half model. We exploited the relationship between source phase and lattice translation in the three-piece BEC to create two interleaved honeycomb lattices of vortices and antivortices, which form texture defects in the combined model. We presented numerical 2D simulations of the untrapped pancake BEC with two components and observed that the lattice defects were either *up* merons, *down* merons, or a type of planar defect. Although numerical models produced the expected lattice, experimental observation would test several assumptions of the theory. Production and observation of the texture lattice with orthogonal polarization components in an all-optical analogous system should be more conducive to experimental investigation than the BEC system. In all simulations of the untrapped case, the sources were arranged at the corners of an equilateral triangle. Changing the source arrangement angle away from $\pi/3$ causes the vortex and antivortex lattices within a single component to move relative to one another. This may have interesting effects on the texture defects, which may also be affected by their proximity to their neighbours.

Isolated merons and clusters of merons were also produced in the trapped two-component pancake BEC. As experimental observation of these clusters and associated dynamics in the trapped BEC requires imaging of the individual components; however, the limitations of current optics, which preclude observation of clusters in the single component BEC, also conspire against their direct observation in the two-component system. Baby skyrmions also exist in fully 3D systems, on arbitrary planes perpendicular to nodal lines in one component, and also on compact surfaces such as spheres (Hen and Karliner, 2008a). Some 3D simulations were performed; the results were not presented due to the extra difficulty of computationally detecting and visualising resulting textures.

We produced vortices and their texture counterparts from the interference of three simple coherent waves, in linear and nonlinear systems. The resulting structures, whether static or dynamic, were surprising and beautiful; that they are created at all remains a revelation.

Bibliography

Abrikosov A A (1957). On the magnetic properties of superconductors of the second group. *Soviet Physics JETP* **5**, 1174–1182.

Acheson D J (1990). *Elementary fluid dynamics*. Oxford University Press, Oxford.

Allen L, Beijersbergen M W, Spreeuw R J C and Woerdman J P (1992). Orbital angular momentum of light and the transformation of Laguerre-Gaussian laser modes. *Physical Review A* **45**, 8185–8189.

Allen L J, Faulkner H M L, Oxley M P and Paganin D (2001). Phase retrieval and aberration correction in the presence of vortices in high-resolution transmission electron microscopy. *Ultramicroscopy* **88**, 85–97.

Andrews D L (2008). *Structured Light and its Applications*. Elsevier, Amsterdam.

Andrews G E (1994). *Number Theory*. Dover, New York.

Anglin J R and Zurek W H (1999). Vortices in the wake of rapid Bose-Einstein condensation. *Physical Review Letters* **83**, 1707–1710.

Arlt J, Hitomi T and Dholakia K (2000). Atom guiding along Laguerre-Gaussian and Bessel light beams. *Applied Physics B* **71**, 549–554.

Ball W R (1960). *A Short Account of the History of Mathematics*. Dover, New York.

Bao W, Jaksch D and Markowich P A (2003). Numerical solution of the Gross-Pitaevskii equation for Bose-Einstein condensation. *Journal of Computational Physics* **187**, 318–342.

Barnett S M (2008). On the quantum core of an optical vortex. *Journal of Modern Optics* **55**, 2279–2292.

Bazenhov V Y, Vasnetsov M V and Soskin M S (1990). Laser beams with screw dislocations in their wavefronts. *Soviet Physics JETP* **52**, 429–431.

Beijersbergen M W, Allen L, van der Veen H E L O and Woerdman J P (1993). Astigmatic laser mode converters and transfer of orbital angular momentum. *Optics Communications* **96**, 123–132.

Berkhout G C G and Beijersbergen M W (2008). Method for probing the orbital angular momentum of optical vortices in electromagnetic waves from astronomical objects. *Physical Review Letters* **101**, 100801.

Berry M V (1978). Disruption of wavefronts: statistics of dislocations in incoherent Gaussian random waves. *Journal of Physics A* **11**, 27–37.

Berry M V (1981). Singularities in waves and rays. In R Balian, M Kléman and

J P Poirier, editors, *Les Houches Session XXV - Physics of Defects*, pages 453–543. North-Holland, Amsterdam.

Berry M V (1998). Much ado about nothing: optical distortion lines (phase singularities, zeros, and vortices…). In M S Soskin, editor, *International Conference on Singular Optics*, volume 3487, pages 1–5. SPIE.

Berry M V (2007). Waves near zeros. In *Conference on Coherence and Quantum Optics, OSA Technical Digest (CD) (Optical Society of America, 2007), paper CMB1*.

Berry M V and Dennis M R (2001). Knotted and linked phase singularities in monochromatic waves. *Proceedings of the Royal Society of London, Series A* **457**, 2251–2263.

Berry M V and Dennis M R (2004). Quantum cores of optical phase singularities. *Journal of Optics A* **6**, 178–180.

Berry M V, Nye J F and Wright F J (1979). The elliptic umbilic diffraction catastrophe. *Philosophical Transactions of the Royal Society of London, Series A* **291**, 453–484.

Boivin A, Dow J and Wolf E (1967). Energy flow in the neighborhood of the focus of a coherent beam. *Journal of the Optical Society of America* **57**, 1171–1175.

Bolda E L and Walls D F (1998). Detection of vorticity in Bose-Einstein condensed gases by matter-wave interference. *Physical Review Letters* **81**, 5477–5480.

Born M and Wolf E (1999). *Principles of Optics*. Cambridge University Press, Cambridge, 7th edition.

Brand J and Reinhardt W P (2002). Solitonic vortices and the fundamental modes of the "snake instability": Possibility of observation in the gaseous Bose-Einstein condensate. *Physical Review A* **65**, 43612.

Bransden B H and Joachain C J (2000). *Quantum Mechanics*. Pearson Education, Essex, 2nd edition.

Braunbek W (1951). Zur Darstellung von Wellenfeldern. *Zeitschrift fur Naturforschung A* **6**, 12–15.

Carlsson A H, Malmberg J N, Anderson D, Lisak M, Ostrovskaya E A, Alexander T J and Kivshar Y S (2000). Linear and nonlinear waveguides induced by optical vortex solitons. *Optics Letters* **25**, 660–662.

Carr L D and Clark C W (2006). Vortices and ring solitons in Bose-Einstein condensates. *Physical Review A* **74**, 43613.

Carretero-González R, Anderson B P, Kevrekidis P G, Frantzeskakis D J and Weiler C N (2008a). Dynamics of vortex formation in merging Bose-Einstein condensate fragments. *Physical Review A* **77**, 033625.

Carretero-González R, Whitaker N, Kevrekidis P G and Frantzeskakis D J (2008b).

Vortex structures formed by the interference of sliced condensates. *Physical Review A* **77**, 023605.

Cheng C, Liu C, Zhang N, Jia T, Li R and Xu Z (2002). Absolute measurement of roughness and lateral-correlation length of random surfaces by use of the simplified model of image-speckle contrast. *Applied Optics* **41**, 4148–4156.

Chiofalo M L, Succi S and Tosi M P (2000). Ground state of trapped interacting Bose-Einstein condensates by an explicit imaginary-time algorithm. *Physical Review E* **62**, 7438–7444.

Courtial J, Zambrini R, Dennis M R and Vasnetsov M (2006). Angular momentum of optical vortex arrays. *Optics Express* **14**, 938–949.

Crasovan L C, Vekslerchik V, Pérez-García V M, Torres J P, Mihalache D and Torner L (2003). Stable vortex dipoles in nonrotating Bose-Einstein condensates. *Physical Review A* **68**, 63609.

Curtis J E and Grier D G (2003). Modulated optical vortices. *Optics Letters* **28**, 872–874.

Cushing J T (1998). *Philosophical Concepts in Physics*. Cambridge University Press, Cambridge.

Dalfovo F, Giorgini S, Pitaevskii L P and Stringari S (1999). Theory of Bose-Einstein condensation in trapped gases. *Reviews of Modern Physics* **71**, 463–512.

De Graef M (2003). *Introduction to Conventional Transmission Electron Microscopy*. Cambridge University Press, Cambridge.

Dennis M R (2001). *Topological Singularities in Wave Fields*. Ph.D. thesis, H. H. Wills Physics Laboratory, University of Bristol. http://www.phy.bris.ac.uk/people/dennis_mr/papers/mrdthesis.pdf. Retrieved May 2006.

Dennis M R (2009). On the Burgers vector of a wave dislocation. *Journal of Optics A* **11**, 094002.

Dennis M R, King R P, Jack B, O'Holleran K and Padgett M J (2010). Isolated optical vortex knots. *Nature Physics* **6**, 118–121.

Dennis M R, O'Holleran K and Padgett M J (2009). Singular Optics: Optical Vortices and Polarization Singularities. In E Wolf, editor, *Progress in Optics*, volume 53, chapter 5, pages 293–363. Elsevier, Amsterdam.

Desyatnikov A S, Torner L and Kivshar Y S (2005). Optical Vortices and Vortex Solitons. In E Wolf, editor, *Progress in Optics*, volume 47, chapter 5, pages 291–391. Elsevier, Amsterdam.

Dirac P A M (1931). Quantised singularities in the electromagnetic field. *Proceedings of the Royal Society of London, Series A* **133**, 60–72.

Epstein R I and Baym G (1992). Vortex drag and the spin-up time scale for pulsar glitches. *Astrophysical Journal* **387**, 276–287.

Erf R K, editor (1978). *Speckle Metrology*. Academic Press, New York.

Feder D L, Pindzola M S, Collins L A, Schneider B I and Clark C W (2000). Dark-soliton states of Bose-Einstein condensates in anisotropic traps. *Physical Review A* **62**, 53606.

Fetter A L and Svidzinsky A A (2001). Vortices in a trapped dilute Bose-Einstein condensate. *Journal of Physics: Condensed Matter* **13**, R135–R194.

Feynman R P (1955). Application of quantum mechanics to liquid helium. *Progress in Low Temperature Physics* **1**, 17–53.

Freund I (1999). Critical point explosions in two-dimensional wave fields. *Optics Communications* **159**, 99–117.

Freund I (2000). Optical vortex trajectories. *Optics Communications* **181**, 19–33.

Freund I and Shvartsman N (1994). Wave-field phase singularities: The sign principle. *Physical Review A* **50**, 5164–5172.

Freund I, Shvartsman N and Freilikher V (1993). Optical dislocation networks in highly random media. *Optics Communications* **101**, 247–264.

Friese M E J, Nieminen T A, Heckenberg N R and Rubinsztein-Dunlop H (1998). Optical alignment and spinning of laser-trapped microscopic particles. *Nature* **394**, 348–350.

Fürhapter S, Jesacher A, Bernet S and Ritsch-Marte M (2005a). Spiral interferometry. *Optics Letters* **30**, 1953–1955.

Fürhapter S, Jesacher A, Bernet S and Ritsch-Marte M (2005b). Spiral phase contrast imaging in microscopy. *Optics Express* **13**, 689–694.

Gabor D (1969). Progress in holography. *Reports on Progress in Physics* **32**, 395–404.

Gahagan K T and Swartzlander G A Jr (1996). Optical vortex trapping of particles. *Optics Letters* **21**, 827–829.

Gbur G and Tyson R K (2008). Vortex beam propagation through atmospheric turbulence and topological charge conservation. *Journal of the Optical Society of America A* **25**, 225–230.

Gbur G, Visser T D and Wolf E (2004). Complete destructive interference of partially coherent fields. *Optics Communications* **239**, 15–23.

Ghiglia D C and Pritt M D (1998). *Two-Dimensional Phase Unwrapping: Theory, Algorithms, and Software*. Wiley, New York.

Gibson C G (2003). *Elementary Euclidean Geometry: An Introduction*. Cambridge University Press, Cambridge.

Gibson G, Courtial J, Padgett M, Vasnetsov M, Pas'ko V, Barnett S and Franke-Arnold S (2004). Free-space information transfer using light beams carrying orbital angular momentum. *Optics Express* **12**, 5448–5456.

Goodman J W (2007). *Speckle Phenomena in Optics: Theory and Applications*.

Roberts and Company, Englewood.

Gowers T, Barrow-Green J and Leader I, editors (2008). *The Princeton Companion to Mathematics*. Princeton University Press, New Jersey.

Grier D G (2003). A revolution in optical manipulation. *Nature* **424**, 810–816.

Guenther R D (1990). *Modern Optics*. John Wiley & Sons, New York.

Hadzibabic Z, Krüger P, Cheneau M, Battelier B and Dalibard J (2006). Berezinskii-Kosterlitz-Thouless crossover in a trapped atomic gas. *Nature* **441**, 1118–1121.

He H, Friese M E J, Heckenberg N R and Rubinsztein-Dunlop H (1995). Direct observation of transfer of angular momentum to absorptive particles from a laser beam with a phase singularity. *Physical Review Letters* **75**, 826–829.

Heath T L (1896). *Apollonius, Treatise on Conic Sections*. Cambridge University Press, Cambridge.

Hen I and Karliner M (2008a). Baby Skyrmions on the two-sphere. *Physical Review E* **77**, 36612.

Hen I and Karliner M (2008b). Hexagonal structure of baby Skyrmion lattices. *Physical Review D* **77**, 54009.

Henderson K, Ryu C, MacCormick C and Boshier M G (2009). Experimental demonstration of painting arbitrary and dynamic potentials for Bose–Einstein condensates. *New Journal of Physics* **11**, 043030.

Herman R M and Wiggins T A (1991). Production and uses of diffractionless beams. *Journal of the Optical Society of America A* **8**, 932–942.

Higashiuchi T and Sakaguchi H (2007). Vortex interaction and the two-dimensional dark soliton. *Laser Physics* **17**, 221–225.

Hindmarsh M B and Kibble T W B (1995). Cosmic strings. *Reports on Progress in Physics* **58**, 477–562.

Ho T L and Shenoy V B (1996). Binary mixtures of Bose condensates of alkali atoms. *Physical Review Letters* **77**, 3276–3279.

Holland M and Cooper J (1996). Expansion of a Bose-Einstein condensate in a harmonic potential. *Physical Review A* **53**, 1954–1957.

Inouye S, Gupta S, Rosenband T, Chikkatur A P, Görlitz A, Gustavson T L, Leanhardt A E, Pritchard D E and Ketterle W (2001). Observation of vortex phase singularities in Bose-Einstein condensates. *Physical Review Letters* **87**, 80402.

Jackson B, McCann J F and Adams C S (1998). Vortex formation in dilute inhomogeneous Bose-Einstein condensates. *Physical Review Letters* **80**, 3903–3906.

Kasamatsu K and Tsubota M (2009). Quantized Vortices in Atomic Bose-Einstein Condensates. In *Progress in Low Temperature Physics*, volume 16: Quantum Turbulence, pages 351–404. Elsevier, Amsterdam.

Kasamatsu K, Tsubota M and Ueda M (2004). Vortex molecules in coherently

coupled two-component Bose-Einstein condensates. *Physical Review Letters* **93**, 250406.

Kasamatsu K, Tsubota M and Ueda M (2005). Vortices in multicomponent Bose-Einstein condensates. *International Journal of Modern Physics B* **19**, 1835–1904.

Ketterle W (2002). Nobel lecture: When atoms behave as waves: Bose-Einstein condensation and the atom laser. *Reviews of Modern Physics* **74**, 1131–1151.

Kibble T W B (1976). Topology of cosmic domains and strings. *Journal of Physics A* **9**, 1387–1398.

Kim G H, Jeon J H, Ko K H, Moon H J, Lee J H and Chang J S (1997). Optical vortices produced with a nonspiral phase plate. *Applied Optics* **36**, 8614–8621.

Kishima K, Yoshida N, Osato K and Nakagawa N (2006). Liquid-crystal panel with microdots on an electrode used to modulate optical phase profiles. *Applied Optics* **45**, 3489–3494.

Kittel C (1996). *Introduction to solid state physics*. Wiley, New York, 7th edition.

Kivshar Y S and Agrawal G P (2003). *Optical Solitons: From Fibers to Photonic Crystals*. Academic Press, San Diego.

Kivshar Y S and Luther-Davies B (1998). Dark optical solitons: physics and applications. *Physics Reports* **298**, 81–197.

Klawunn M, Nath R, Pedri P and Santos L (2008). Transverse instability of straight vortex lines in dipolar Bose-Einstein condensates. *Physical Review Letters* **100**, 240403.

Klein A, Jaksch D, Zhang Y and Bao W (2007). Dynamics of vortices in weakly interacting Bose-Einstein condensates. *Physical Review A* **76**, 43602.

Kogelnik H and Li T (1966). Laser beams and resonators. *Applied Optics* **5**, 1550–1567.

Konotop V V (2008). Dark solitons in Bose-Einstein condensates: Theory. In P G Kevrekidis, D J Frantzeskakis and R Carretero-González, editors, *Emergent Nonlinear Phenomena in Bose-Einstein Condensates*, volume 45, chapter 4, pages 64–83. Springer, Berlin.

Kotlyar V V, Khonina S N, Kovalev A A, Soifer V A, Elfstrom H and Turunen J (2006). Diffraction of a plane, finite-radius wave by a spiral phase plate. *Optics Letters* **31**, 1597–1599.

Law C, Zhang X and Swartzlander G A Jr (2000). Waveguiding properties of optical vortex solitons. *Optics Letters* **25**, 55–57.

Lee M D, Morgan S A, Davis M J and Burnett K (2002). Energy-dependent scattering and the Gross-Pitaevskii equation in two-dimensional Bose-Einstein condensates. *Physical Review A* **65**, 43617.

Lee W M, Garcés-Chávez V and Dholakia K (2006). Interference from multiple

trapped colloids in an optical vortex beam. *Optics Express* **14**, 7436–7446.

Leggett A J (2001). Bose-Einstein condensation in the alkali gases: Some fundamental concepts. *Reviews of Modern Physics* **73**, 307–356.

Leggett A J (2006). *Quantum Liquids: Bose Condensation and Cooper Pairing in Condensed-Matter Systems*. Oxford University Press, Oxford.

Leslie L S, Hansen A, Wright K C, Deutsch B M and Bigelow N P (2009). Creation and detection of skyrmions in a Bose-Einstein condensate. *Physical Review Letters* **103**, 250401.

Liu C, Wang D and Zhang Y (2009). Comparison and verification of numerical reconstruction methods in digital holography. *Optical Engineering* **48**, 105802.

Mair A, Vaziri A, Weihs G and Zeilinger A (2001). Entanglement of the orbital angular momentum states of photons. *Nature* **412**, 313–316.

Manton N and Sutcliffe P M (2004). *Topological Solitons*. Cambridge University Press, Cambridge.

Martin A V and Allen L J (2007). Measuring the phase of a Bose-Einstein condensate. *Physical Review A* **76**, 53606.

Masajada J and Dubik B (2001). Optical vortex generation by three plane wave interference. *Optics Communications* **198**, 21–27.

Masajada J, Popiołek-Masajada A and Leniec M (2007). Creation of vortex lattices by a wavefront division. *Optics Express* **15**, 5196–5207.

Masajada J, Popiołek-Masajada A and Wieliczka D M (2002). The interferometric system using optical vortices as phase markers. *Optics Communications* **207**, 85–93.

Matthews M R, Hall D S, Jin D S, Ensher J R, Wieman C E, Cornell E A, Dalfovo F, Minniti C and Stringari S (1998). Dynamical response of a Bose-Einstein condensate to a discontinuous change in internal state. *Physical Review Letters* **81**, 243–247.

Mermin N D (1979). The topological theory of defects in ordered media. *Reviews of Modern Physics* **51**, 591–648.

Mermin N D and Ho T L (1976). Circulation and angular momentum in the *A* phase of superfluid Helium-3. *Physical Review Letters* **36**, 594–597.

Mertes K M, Merrill J W, Carretero-González R, Frantzeskakis D J, Kevrekidis P G and Hall D S (2007). Nonequilibrium dynamics and superfluid ring excitations in binary Bose-Einstein condensates. *Physical Review Letters* **99**, 190402.

Messiah A (1961). *Quantum Mechanics*. North-Holland, Amsterdam.

Mewes M O, Andrews M R, Van Druten N J, Kurn D M, Durfee D S and Ketterle W (1996). Bose-Einstein condensation in a tightly confining dc magnetic trap. *Physical Review Letters* **77**, 416–419.

Minguzzi A, Succi S, Toschi F, Tosi M P and Vignolo P (2004). Numerical methods for atomic quantum gases with applications to Bose-Einstein condensates and to ultracold fermions. *Physics Reports* **395**, 223–355.

Molina-Terriza G, Torres J P and Torner L (2007). Twisted photons. *Nature Physics* **3**, 305–310.

Montgomery W D (1967). Self-imaging objects of infinite aperture. *Journal of the Optical Society of America* **57**, 772–775.

Möttönen M, Virtanen S M M, Isoshima T and Salomaa M M (2005). Stationary vortex clusters in nonrotating Bose-Einstein condensates. *Physical Review A* **71**, 33626.

Mueller E J (2004). Spin textures in slowly rotating Bose-Einstein condensates. *Physical Review A* **69**, 33606.

Mueller E J and Ho T L (2002). Two-component Bose-Einstein condensates with a large number of vortices. *Physical Review Letters* **88**, 180403.

Nascov V and Logofătu P C (2009). Fast computation algorithm for the Rayleigh-Sommerfeld diffraction formula using a type of scaled convolution. *Applied Optics* **48**, 4310–4319.

Nicholls K W and Nye J F (1987). Three-beam model for studying dislocations in wave pulses. *Journal of Physics A* **20**, 4673–4696.

Nielsen M A and Chuang I L (2000). *Quantum Computing and Quantum Information*. Cambridge University Press, Cambridge.

Nieminen T A, Parkin S J, Heckenberg N R and Rubinsztein-Dunlop H (2004). Optical torque and symmetry. *Proceedings of SPIE* **5514**, 254–263.

Nozières P and Pines D (1990). *The Theory of Quantum Liquids, Volume II: Superfluid Bose Liquids*. W. A. Benjamin, New York.

Nye J F (1999). *Natural Focusing and Fine Structure of Light: Caustics and Wave Dislocations*. Institute of Physics Publishing, Bristol.

Nye J F and Berry M V (1974). Dislocations in wave trains. *Proceedings of the Royal Society of London, Series A* **336**, 165–190.

O'Holleran K (2008). *Fractality and Topology of Optical Singularities*. Ph.D. thesis, Department of Physics & Astronomy, University of Glasgow. http://theses.gla.ac.uk/470/01/2008oholleranphd.pdf. Retrieved March 2009.

O'Holleran K, Padgett M J and Dennis M R (2006). Topology of optical vortex lines formed by the interference of three, four, and five plane waves. *Optics Express* **14**, 3039–3044.

Okamoto M and Sasada H (2005). Generation of optical vortices by converting elegant Hermite Gaussian beams. *Japanese Journal of Applied Physics, Part 1* **44**, 1743–7.

Paganin D M (2006). *Coherent X-Ray Optics*. Oxford University Press, Oxford.

Parker N G, Proukakis N P, Barenghi C F and Adams C S (2004). Controlled vortex-sound interactions in atomic Bose-Einstein condensates. *Physical Review Letters* **92**, 160403.

Paterson C (2005). Atmospheric turbulence and orbital angular momentum of single photons for optical communication. *Physical Review Letters* **94**, 153901.

Peele A G and Nugent K A (2003). X-ray vortex beams: A theoretical analysis. *Optics Express* **11**, 2315–2322.

Pethick C J and Smith H (2008). *Bose-Einstein Condensation in Dilute Gases*. Cambridge University Press, Cambridge, 2nd edition.

Phillips R L and Andrews L C (1983). Spot size and divergence for Laguerre Gaussian beams of any order. *Applied Optics* **22**, 643–644.

Pietilä V, Möttönen M, Isoshima T, Huhtamäki J A M and Virtanen S M M (2006). Stability and dynamics of vortex clusters in nonrotated Bose-Einstein condensates. *Physical Review A* **74**, 23603.

Pismen L M (1999). *Vortices in Nonlinear Fields: From Liquid Crystals to Superfluids, From Non-Equilibrium Patterns to Cosmic Strings*. Oxford University Press, Oxford.

Pitaevskii L and Stringari S (2003). *Bose-Einstein Condensation*. Oxford University Press, Oxford.

Pitaevskii L P (1996). Dynamics of collapse of a confined Bose gas. *Physics Letters A* **221**, 14–18.

Press W H, Teukolsky S A, Vetterling W T and Flannery B P (1992). *Numerical recipes in C*. Cambridge University Press, Cambridge.

Proukakis N P and Jackson B (2008). Finite-temperature models of Bose-Einstein condensation. *Journal of Physics B* **41**, 1–66.

Proukakis N P, Parker N G, Frantzeskakis D J and Adams C S (2004). Analogies between dark solitons in atomic Bose Einstein condensates and optical systems. *Journal of Optics B* **6**, S380–S391.

Reijnders J W, van Lankvelt F J M, Schoutens K and Read N (2004). Rotating spin-1 bosons in the lowest Landau level. *Physical Review A* **69**, 23612.

Rhodes D P (2005). *Experimental Studies of Cold Atom Guiding Using Hollow Light Beams*. Ph.D. thesis, University of St Andrews. http://www.st-andrews.ac.uk/atomtrap/papers/Thesis/Daniel(webds).pdf. Retrieved August 2009.

Riley K F, Hobson M P and Bence S J (2006). *Mathematical Methods for Physics and Engineering*. Cambridge University Press, Cambridge, 3rd edition.

Röhrl A, Naraschewski M, Schenzle A and Wallis H (1997). Transition from phase locking to the interference of independent Bose condensates: Theory versus

experiment. *Physical Review Letters* **78**, 4143–4146.

Ruben G and Paganin D M (2007a). Phase vortices from a Young's three-pinhole interferometer. *Physical Review E* **75**, 066613.

Ruben G and Paganin D M (2007b). Erratum: Phase vortices from a Young's three-pinhole interferometer [Phys. Rev. E 75, 066613 (2007)]. *Physical Review E* **76**, 029901(E).

Ruben G and Paganin D M (2007c). Phase vortices from the interference of three spherical waves. In *Conference on Coherence and Quantum Optics, OSA Technical Digest (CD) (Optical Society of America, 2007), paper CSuA40*.

Ruben G, Paganin D M and Morgan M J (2008). Vortex-lattice formation and melting in a nonrotating Bose-Einstein condensate. *Physical Review A* **78**, 013631.

Ruostekoski J, Kneer B, Schleich W P and Rempe G (2001). Interference of a Bose-Einstein condensate in a hard-wall trap: From the nonlinear Talbot effect to the formation of vorticity. *Physical Review A* **63**, 43613.

Sakaguchi H and Higashiuchi T (2006). Two-dimensional dark soliton in the nonlinear Schrödinger equation. *Physics Letters A* **359**, 647–651.

Scherer D R (2007). *Vortex Formation by Merging and Interference of Multiple Trapped Bose-Einstein Condensates*. Ph.D. thesis, University of Arizona. http://www.optics.arizona.edu/Anderson/DRSchererPhDdissertation.pdf. Retrieved August 2007.

Scherer D R, Weiler C N, Neely T W and Anderson B P (2007). Vortex formation by merging of multiple trapped Bose-Einstein condensates. *Physical Review Letters* **98**, 110402.

Schumer P D (2004). *Mathematical Journeys*. Wiley, New Jersey.

Sethna J P (2006). *Statistical Mechanics: Entropy, Order Parameters, and Complexity*. Oxford University Press, Oxford.

Simula T P, Lee M D and Hutchinson D A W (2005). Transition from the Bose-Einstein condensate to the Berezinskii-Kosterlitz-Thouless phase. *Philosophical Magazine Letters* **85**, 395–403.

Simula T P, Mizushima T and Machida K (2008). Vortex waves in trapped Bose-Einstein condensates. *Physical Review A* **78**, 53604.

Sirohi R S, editor (1993). *Speckle metrology*. Marcel Dekker, New York.

Skyrme T H R (1961). A non-linear field theory. *Proceedings of the Royal Society of London, Series A* **260**, 127–138.

Snyder J P (1987). Map Projections: A Working Manual. Technical Report 1395, U.S. Geological Survey.

Soskin M S and Vasnetsov M V (2001). Singular Optics. In E Wolf, editor, *Progress in Optics*, volume 42, chapter 4, pages 219–276. Elsevier, Amsterdam.

Swartzlander G A Jr (2001). Peering into darkness with a vortex spatial filter. *Optics Letters* **26**, 497–499.

Swartzlander G A Jr (2009). The optical vortex coronagraph. *Journal of Optics A* **11**, 094022.

Takeuchi H, Kasamatsu K and Tsubota M (2009). Spontaneous radiation and amplification of Kelvin waves on quantized vortices in Bose-Einstein condensates. *Physical Review A* **79**, 33619.

Tan Y R E, Paganin D M, Yu R P and Morgan M J (2003). Wave-function reconstruction of complex fields obeying nonlinear parabolic equations. *Physical Review E* **68**, 66602.

Tanatar B, Minguzzi A, Vignolo P and Tosi M P (2002). Density profile of a Bose-Einstein condensate inside a pancake-shaped trap: observational consequences of the dimensional cross-over in the scattering properties. *Physics Letters A* **302**, 131–136.

Theocharis G, Frantzeskakis D J, Kevrekidis P G, Malomed B A and Kivshar Y S (2003). Ring dark solitons and vortex necklaces in Bose-Einstein condensates. *Physical Review Letters* **90**, 120403.

Thomson W (1867). On vortex atoms. *Philosophical Magazine* **34**, 15–24.

ThorLabs (2009). ThorLabs catalogue data on Ground Glass Diffusers, p.785. http://www.thorlabs.com/catalogPages/785.pdf. Retrieved 30 Jul 2008.

Tilley D R and Tilley J (1990). *Superfluidity and Superconductivity*. Institute of Physics Publishing, Bristol, 3rd edition.

Timm C (2009). A new twist in a ferromagnet. *Physics* **2**, 35.

Tsubota M (2009). Quantum turbulence: from superfluid helium to atomic Bose-Einstein condensates. *Contemporary Physics* **50**, 463–475.

Tsubota M, Araki T and Barenghi C F (2003). Rotating superfluid turbulence. *Physical Review Letters* **90**, 205301.

Tsubota M, Barenghi C F, Araki T and Mitani A (2004). Instability of vortex array and transitions to turbulence in rotating helium II. *Physical Review B* **69**, 134515.

Turner L D, Domen K F E M and Scholten R E (2005). Diffraction-contrast imaging of cold atoms. *Physical Review A* **72**, 31403.

Tyler G A and Boyd R W (2009). Influence of atmospheric turbulence on the propagation of quantum states of light carrying orbital angular momentum. *Optics Letters* **34**, 142–144.

Vaughan J M and Willetts D V (1979). Interference properties of a light beam having a helical wave surface. *Optics Communications* **30**, 263–267.

Volovik G E (2003). *The Universe in a Helium Droplet*. Oxford University Press, Oxford.

Vyas S and Senthilkumaran P (2007). Interferometric optical vortex array generator. *Applied Optics* **46**, 2893–2898.

Wang W, Chiba K, Hanson S G and Takeda M (2008). Vortex sheets in optical and coherence fields. volume 6905, page 690506. SPIE.

Weiler C N, Neely T W, Scherer D R, Bradley A S, Davis M J and Anderson B P (2008). Spontaneous vortices in the formation of Bose-Einstein condensates. *Nature* **455**, 948–951.

Weisstein E W (2009). Ball – From MathWorld–A Wolfram Web Resource. http://mathworld.wolfram.com/Ball.html. Retrieved 25 Nov 2009.

Whewell W (1836). On the results of an extensive system of tide observations made on the coasts of Europe and America in June 1835, in Researches on the tides, 6th series. *Philosophical Transactions of the Royal Society* **126**, 289–34.

Wolter H (1950). Zur Frage des Lichtweges bei Totalreflexion. *Zeitschrift fur Naturforschung A* **5**, 276.

XmdS (2007). eXtensible multi-dimensional Simulator. http://www.xmds.org. Retrieved 9 May 2007.

Xu X, Minogin V G, Lee K, Wang Y and Jhe W (1999). Guiding cold atoms in a hollow laser beam. *Physical Review A* **60**, 4796–4804.

Yepez J, Vahala G, Vahala L and Soe M (2009). Superfluid turbulence from quantum Kelvin wave to classical Kolmogorov cascades. *Physical Review Letters* **103**, 84501.

Young T (1804). The Bakerian lecture: Experiments and calculations relative to physical optics. *Philosophical Transactions of the Royal Society of London* **94**, 1–16.

Zhang P, Naidon P and Ueda M (2009). Independent control of scattering lengths in multicomponent quantum gases. *Physical Review Letters* **103**, 133202.

Zurek W H (1985). Cosmological experiments in superfluid helium? *Nature* **317**, 505–508.

A

Detecting vortices and nodal lines in phase data

This appendix describes the techniques used to numerically detect the presence of vortices and nodal lines in 2D and 3D phase data. This was applied to the modelled and experimentally obtained data for the three-pinhole interferometer, the modelled data of the Laguerre-Gauss (LG) beam passing through a ground glass plate (GGP), and the nodal line structures in the 3D Bose-Einstein condensate (BEC) model.

Figure A.1 shows the phase at pixel locations of the prototypical vortex-carrying function $\Psi(x, y) = x + iy$. Although the phase is multivalued at the origin, it is calculated here using the quadrant-preserving arctan2 function, which evaluates to 0 at this location. Four discrete contour integrals (a–d) of the phase gradient

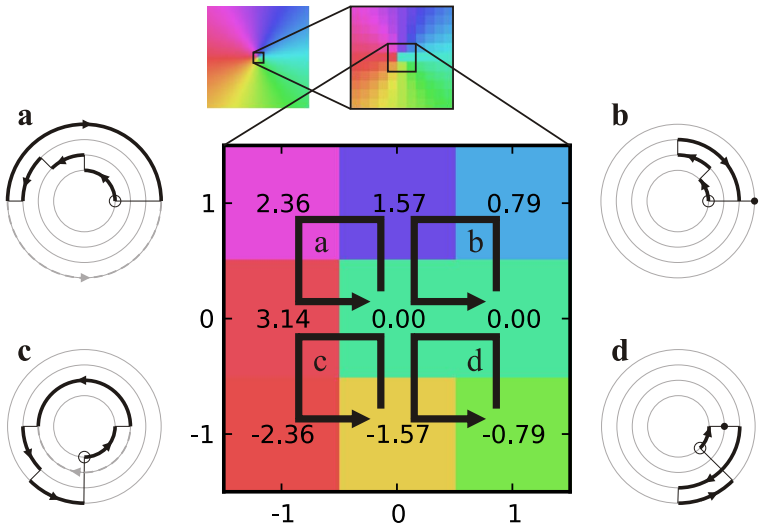

Figure A.1: Phase unwrapping in 2D. Phase values of $\Psi(x, y) = x + iy$ are shown on the pixel faces. Four 2×2 discrete integrals are shown with the corresponding path on a 1D compact manifold indicating the presence of a vortex in (c).

are shown, corresponding to the four possible positions of a 2×2 square on a 3×3 discretely sampled phase map. These are taken in the conventional counter-clockwise sense. The vortex detection algorithm steps around the 2×2 square, summing the phase gradients, i.e. the difference in values. When the modulus of this difference $|\Delta\chi|$ exceeds π, the phase is *unwrapped*, meaning that the shortest phase change path is always taken, ignoring all branch cuts. p is found such that the phase gradient is $2p\pi - \Delta\chi \mapsto \Delta\xi$, where $p \in \mathbb{Z}$ and $\Delta\xi \in (-\pi, \pi]$. p is then the detected winding number.

The decision to use a 2×2 square to sample the phase limits the possible detected charge s to $-1, 0$, or $+1$. In order to detect higher-charge vortices, the Nyquist sampling theorem requires us to sample the phase in any π-interval of the order parameter space twice, so to detect vortices up to $|s| = 1$ requires four samples. To detect $|s| = 2$ vortices requires eight samples, which can be achieved by measuring at points on the perimeter of a 3×3 square, and so on. Limiting the magnitude of the possible detected charge to 1 is justified because we do not expect vortices of higher charge, except in Chap. 3, where the LG beam charge may be greater. As explained in §1.5, three linearly interfering sources can only produce $|s| = 1$ vortices as there are fewer than the 6 degrees of freedom required for $|s| = 2$ vortex production. Any higher-charge vortices in the nonlinear fields modelled in the remaining parts of this thesis will decay into $|s| = 1$ vortices due to their sensitivity to perturbation. Finally, for a charge-ℓ vortex in the LG beam in Chap. 3 or randomly created in a nonlinear field, we will detect a cluster of ℓ vortices with $s = \operatorname{sgn} \ell$, which is adequate for our purposes; we can evaluate a vorticity metric over an area and identify the presence of an axial LG beam vortex.

If one thinks of the phase as being sampled at the pixel centres, any detected vortex lies at the vertex of the four phase pixels. For $n \times m$ phase pixels, we produce an $(n-1) \times (m-1)$ map of vortices. Only in Fig. A.1(c) does the unwrapped phase form a closed contour in the accompanying diagram, which represents the path traced in the order parameter space when the order parameter in physical space (the phase) is sampled by the contour integral of the phase gradient. The order parameter space is an S^1-sphere (i.e. a circle) since the first homotopy group of the circle is the set of all integers $\mathbb{Z}$. Mathematically, this is written $\pi(S^1) = \mathbb{Z}$. The four concentric circles allow us to show the four discrete subpaths in the order traversed on the phase map, with the initial position indicated by an open circle on the innermost circle. In Fig. A.1(c) the path taken on this manifold winds once, indicating the presence of a charge-1 vortex. This is because the third subpath has been unwrapped from $3.14 - (-2.36)$ to $2\pi - (3.14 + 2.36)$. The direction is counter-clockwise corresponding to a vortex as opposed to an antivortex. The

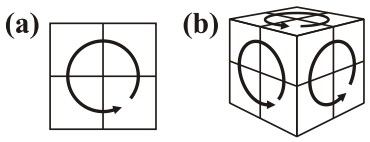

Figure A.2: Phase unwrapping in (a) 2D, and (b) 3D. A simple method was applied in 3D where the Boolean results indicating the presence or absence of a vortex on the three orthogonal contours over the three 2×2 faces were logically combined with a Boolean-OR operation to indicate the presence or absence of a vortex.

integral is performed for every vertex in the phase map. The effect of changing the condition on the magnitude of the phase-difference from $|\Delta\chi| > \pi$ to $|\Delta\chi| \geq \pi$ is shown by the dashed paths in Figs A.1(a) and (c); the vortex location shifts from contour (c) to (a) under this change.

For the three-pinhole interferometer, a spherical background envelope was subtracted from the phase data prior to application of the vortex detection algorithm, as this does not affect the location of the detected vortices yet allows detection of any vortices in 2D rather than 3D. Similarly, a Gaussian envelope was subtracted from the LG beam prior to detection. However, for any more complicated wavefield shape, it is necessary to detect the vortices in 3D. A simple extension to 3D allows the detection of a disconnected set of points on any nodal lines which, when visualised, lie at neighbouring points in space. Figure A.2 shows the extension in which every vertex of three faces of a cube of voxels is sampled. The phase unwrapping algorithm is applied on each of these faces independently and, by ignoring the charge of any detected vortices, a Boolean result indicating the presence or absence of a vortex on these faces is obtained by logically combining the three results using a Boolean-OR operation. An implicit assumption is made that only charge +1 and −1 vortices will exist and we were not concerned with the winding orientation. More sophisticated algorithms allow for traversal of the cube face in a unified manner, the detection of higher-charge nodal lines and their orientation through the cube, and exploitation of the restriction on possible topologies of a nodal line passing through a cube. These were not applied here, where the purpose was only for simple visualisation of nodal-line structures. The shape of the vortex detection kernel here is not a cube, as it does not include the back faces, and only involves seven out of the eight voxels.

It is also common to choose an integration contour larger than 2×2. For example, 3×3 is commonly applied, but could potentially miss an enclosed vortex and antivortex pair whose charges would cancel, whilst having the previously stated advantage of allowing detection of higher-charge vortices.

B

Three spherical waves reconsidered as one perturbed spherical wave

Here we show that the sum of three spherical waves may be thought of as a perturbed background spherical wave whose centre coincides with the centroid of the component waves.

Consider three spheres of radius r, centred at (x_j, y_j, z_0), where $j = 1, 2, 3$.

$$S_j : (x - x_j)^2 + (y - y_j)^2 + (z - z_0)^2 - r^2 = 0, \qquad j = 1, 2, 3. \tag{B.1}$$

These represent the wavefronts of radius r emanating from three sources, lying in the z_0 plane. Summing these and subtracting a sphere of radius r_0 where ${r_0}^2 \equiv 3r^2$, that is centred at (x_0, y_0, z_0)

$$\begin{aligned} 0 &= \sum_{j=1,2,3} S_j - 3[(x - x_0)^2 + (y - y_0)^2 + (z - z_0)^2 - r_0^2] \\ &= 2x[3x_0 - (x_1 + x_2 + x_3)] + 2y[3y_0 - (y_1 + y_2 + y_3)] \\ &\quad + [({x_1}^2 + {x_2}^2 + {x_3}^2) - 3{x_0}^2] + [({y_1}^2 + {y_2}^2 + {y_3}^2) - 3{y_0}^2]. \end{aligned} \tag{B.2}$$

allows us to solve for the unknown coordinates (x_0, y_0). This may be thought of as a 2D regression equation of the form $mx + ny + c = 0$, in which eliminating any dependence on x and y will produce the fixed background upon which perturbations operate. We thus want to fix m and n such that $mx + ny = 0$, which is the case when $x_0 = (x_1 + x_2 + x_3)/3$ and $y_0 = (y_1 + y_2 + y_3)/3$. This establishes the coordinates of the centre of a background sphere of radius $r_0 = \sqrt{3}r$, which is seen to lie at the centroid of the three spherical sources.

Mathematica GPE derivations

C

This appendix contains Mathematica notebooks demonstrating the derivation of the 2D Gross-Pitaevskii equation (GPE) from the 3D form. As with many "obvious" derivations, this is not always well described in the literature. Part of the problem is that various choices exist for normalisation conditions and length scaling factors. The clearest descriptions of the method adopted in this thesis are found in Lee et al. (2002) and Leggett (2006).

The first two notebooks present two alternatives to obtaining the dimensionless (2+1)D GPE. The first notebook demonstrates reduction from 3D to 2D followed by transformation to dimensionless quantities, whereas the second notebook follows the alternative sequence of transformation to dimensionless quantities followed by reduction from 3D to 2D. Both follow the approach adopted by Lee et al. (2002) of integrating a Gaussian z-profile to obtain the reduced-dimensional governing equation. The approach is discussed in detail in §4.3, which refers back to the relevant derivations in this Appendix. An alternative approach to reducing the dimensionality from 3D to 2D is simply to evaluate the 3D GPE in the $z = 0$ plane, as discussed in §4.3.2. This is shown in the third Mathematica notebook. In the fourth notebook, which we apply in §5.3.1, two coupled GPEs are reduced to dimensionless form and then to 2D, in the absence of an axial trap.

It is necessary to tightly control the operation of Mathematica to prevent it from mixing terms in the GPE that we wish to keep separate. We deal with the terms individually before finally combining them, rather than first forming the GPE and allowing Mathematica to operate on it as a whole.

Notebook 1

Reduction from 3D to 2D of the GPE

In[1]:=
```
$Assumptions = {m > 0, ω > 0, ωz > 0, t > 0, ħ > 0, r > 0, a > 0, N > 0, z ∈ Reals};
```

In[2]:=
```
θ[z_] = (m ωz / (π ħ))^(1/4) Exp[-(m ωz / (2 ħ)) z^2];
```

In[3]:=
```
∫_-∞^∞ Abs[θ[z]]^2 dz
```

Out[3]= 1

In[4]:=
```
subs = {Ψ[r, θ, z, t] → Φ[r, θ, t] θ[z],
    Ψ*[r, θ, z, t] → Φ*[r, θ, t] θ[z], ∂t Ψ[r, θ, z, t] → θ[z] ∂t Φ[r, θ, t],
    Laplacian[Ψ[r, θ, z, t]] → θ[z] PLapl[Φ[r, θ, t]] + Φ[r, θ, t] ∂z,z θ[z]};
```

In[5]:=
```
TDGP1 = i ħ ∂t Ψ[r, θ, z, t] /. subs
```

Out[5]= $\frac{i\, e^{-\frac{m r^2 \omega}{2\hbar}} \sqrt{\frac{m\omega z}{\hbar}}\ \hbar\, \Phi^{(0,0,1)}(r,\theta,t)}{\sqrt[4]{\pi}}$

In[6]:=
```
ATDGP1 = μ Ψ[r, θ, z, t] /. subs
```

Out[6]= $\frac{e^{-\frac{m r^2 \omega}{2\hbar}}\, \mu \sqrt{\frac{m\omega z}{\hbar}}\ \Phi(r,\theta,t)}{\sqrt[4]{\pi}}$

In[7]:=
```
TDGP2 = -(ħ^2 / (2 m)) Laplacian[Ψ[r, θ, z, t]] /. subs // Simplify
```

Out[7]= $-\frac{e^{-\frac{m r^2 \omega}{2\hbar}} \sqrt{\frac{m\omega z}{\hbar}}\ (\text{PLapl}(\Phi(r,\theta,t))\,\hbar^2 + m\omega z\,(m r^2 \omega z - \hbar)\,\Phi(r,\theta,t))}{2\, m \sqrt[4]{\pi}}$

In[8]:=
```
TDGP3a = (1/2) m ω^2 r^2 Ψ[r, θ, z, t] /. subs
```

Out[8]= $\frac{e^{-\frac{m r^2 \omega}{2\hbar}}\, m r^2 \omega^2 \sqrt{\frac{m\omega z}{\hbar}}\ \Phi(r,\theta,t)}{2\sqrt[4]{\pi}}$

In[9]:=
```
TDGP3b = (1/2) m ω^2 z^2 (ωz^2 / ω^2) Ψ[r, θ, z, t] /. subs
```

Out[9]= $\frac{e^{-\frac{m r^2 \omega}{2\hbar}}\, m z^2 \omega z^2 \sqrt{\frac{m\omega z}{\hbar}}\ \Phi(r,\theta,t)}{2\sqrt[4]{\pi}}$

In[10]:=
```
TDGP4 = N U0 Abs[Ψ[r, θ, z, t]]^2 Ψ[r, θ, z, t] /. subs // Simplify
```

Out[10]= $\frac{e^{-\frac{3 m r^2 \omega}{2\hbar}}\, N \left(\frac{m\omega z}{\hbar}\right)^{3/4} |\Phi(r,\theta,t)|^2\, U_0\, \Phi(r,\theta,t)}{\pi^{3/4}}$

In[11]:=
```
IGP1 = ∫_-∞^∞ θ[z]* TDGP1 dz // Simplify
```

Out[11]= $i\,\hbar\,\Phi^{(0,0,1)}(r,\theta,t)$

In[12]:=
```
AIGP1 = ∫_-∞^∞ θ[z]* ATDGP1 dz // Simplify
```

Out[12]= $\mu\,\Phi(r,\theta,t)$

In[13]:=
```
IGP2 = ∫_-∞^∞ θ[z]* TDGP2 dz // Simplify
```

Out[13]= $\frac{\hbar\,(m\,\omega z\,\Phi(r,\theta,t) - 2\,\hbar\,\text{PLapl}(\Phi(r,\theta,t)))}{4\,m}$

In[14]:=
```
IGP3a = ∫_-∞^∞ θ[z]* TDGP3a dz // Simplify
```

Out[14]= $\frac{1}{2}\, m\, r^2\, \omega^2\, \Phi(r,\theta,t)$

In[15]:=
```
IGP3b = ∫_-∞^∞ θ[z]* TDGP3b dz // Simplify
```

Out[15]= $\frac{1}{4}\,\omega z\,\hbar\,\Phi(r,\theta,t)$

In[16]:=
```
IGP4 = ∫_-∞^∞ θ[z]* TDGP4 dz // Simplify
```

Out[16]= $\frac{N \sqrt{\frac{m\omega z}{\hbar}}\ |\Phi(r,\theta,t)|^2\, U_0\, \Phi(r,\theta,t)}{\sqrt{2\,\pi}}$

In[17]:=
```
gammafactor = (m ωz / (2 π ħ))^(1/2);
```

In[18]:=
```
TDGP := IGP1 - IGP3b == IGP2 + IGP3a + IGP4 /. gammafactor → γ
```

In[19]:=
```
TDGP
```

Out[19]= $i\,\hbar\,\Phi^{(0,0,1)}(r,\theta,t) - \frac{1}{4}\,\omega z\,\hbar\,\Phi(r,\theta,t) = \frac{1}{2}\, m\, r^2\, \Phi(r,\theta,t)\,\omega^2 + N\,\gamma\,|\Phi(r,\theta,t)|^2\, U_0\, \Phi(r,\theta,t) + \frac{\hbar\,(m\,\omega z\,\Phi(r,\theta,t) - 2\,\hbar\,\text{PLapl}(\Phi(r,\theta,t)))}{4\,m}$

In[20]:=
```
ATDGP := AIGP1 - IGP3b == IGP2 + IGP3a + IGP4 /. gammafactor → γ
```

In[21]:=
```
ATDGP
```

Out[21]= $\mu\,\Phi(r,\theta,t) - \frac{1}{4}\,\omega z\,\hbar\,\Phi(r,\theta,t) = \frac{1}{2}\, m\, r^2\, \Phi(r,\theta,t)\,\omega^2 + N\,\gamma\,|\Phi(r,\theta,t)|^2\, U_0\, \Phi(r,\theta,t) + \frac{\hbar\,(m\,\omega z\,\Phi(r,\theta,t) - 2\,\hbar\,\text{PLapl}(\Phi(r,\theta,t)))}{4\,m}$

Make dimensionless

In[22]:=
```
dsubs = {t → τ / ω, r → ρ l, a → α l, Ψ[r, θ, t] → l^-1 φ[ρ, θ, τ],
    ∂t Ψ[r, θ, t] → ω l^-1 ∂τ φ[ρ, θ, τ], PLapl[Ψ[r, θ, t]] → l^-2 l^-1 DLapl[φ[ρ, θ, τ]]};
```

In[23]:=
```
l = Sqrt[ħ / (2 m ω)];
```

In[24]:=
```
U0 = 4 π ħ^2 a / m;
```

In[25]:=
```
commonfactor2 = 2^(2/4) ω^(6/4) ħ^(2/4) m^(2/4);
```

In[26]:= **DGP1 = IGP1 / commonfactor2 /. dsubs // Simplify**

Out[26]= $i\,\varphi^{(0,0,1)}(\rho,\theta,\tau)$

In[27]:= **ADGP1 = AIGP1 / commonfactor2 /. dsubs // Simplify**

Out[27]= $\frac{\mu\,\varphi(\rho,\theta,\tau)}{\omega\,\hbar}$

In[28]:= **DGP2 = IGP2 / commonfactor2 /. dsubs // Simplify**

Out[28]= $\frac{\omega z\,\varphi(\rho,\theta,\tau)}{4\,\omega} - \text{DLapl}(\varphi(\rho,\theta,\tau))$

In[29]:= **DGP3a = IGP3a / commonfactor2 /. dsubs // Simplify**

Out[29]= $\frac{1}{4}\,\rho^2\,\varphi(\rho,\theta,\tau)$

In[30]:= **DGP3b = IGP3b / commonfactor2 /. dsubs // Simplify**

Out[30]= $\frac{\omega z\,\varphi(\rho,\theta,\tau)}{4\,\omega}$

In[31]:= **DGP4 = IGP4 / commonfactor2 /. dsubs // Simplify**

Out[31]= $4\,N\,\sqrt{\pi}\;\alpha\,\sqrt{\frac{\omega z}{\omega}}\;|\varphi(\rho,\theta,\tau)|^2\,\varphi(\rho,\theta,\tau)$

In[32]:= **DTDGP := DGP1 - DGP3b == DGP2 + DGP3a + DGP4**

In[33]:= **DTDGP**

Out[33]= $i\,\varphi^{(0,0,1)}(\rho,\theta,\tau) - \frac{\omega z\,\varphi(\rho,\theta,\tau)}{4\,\omega} = \frac{1}{4}\,\varphi(\rho,\theta,\tau)\,\rho^2 - \text{DLapl}(\varphi(\rho,\theta,\tau)) + 4\,N\,\sqrt{\pi}\;\alpha\,\sqrt{\frac{\omega z}{\omega}}\;|\varphi(\rho,\theta,\tau)|^2\,\varphi(\rho,\theta,\tau) + \frac{\omega z\,\varphi(\rho,\theta,\tau)}{4\,\omega}$

In[34]:= **ADTDGP := ADGP1 - DGP3b == DGP2 + DGP3a + DGP4**

In[35]:= **ADTDGP**

Out[35]= $\frac{\mu\,\varphi(\rho,\theta,\tau)}{\omega\,\hbar} - \frac{\omega z\,\varphi(\rho,\theta,\tau)}{4\,\omega} = \frac{1}{4}\,\varphi(\rho,\theta,\tau)\,\rho^2 - \text{DLapl}(\varphi(\rho,\theta,\tau)) + 4\,N\,\sqrt{\pi}\;\alpha\,\sqrt{\frac{\omega z}{\omega}}\;|\varphi(\rho,\theta,\tau)|^2\,\varphi(\rho,\theta,\tau) + \frac{\omega z\,\varphi(\rho,\theta,\tau)}{4\,\omega}$

Notebook 2

Make dimensionless

In[1]:=
```
$Assumptions = {m > 0, ω > 0, ωz > 0, t > 0, ħ > 0, r > 0, a > 0, N > 0, z ∈ Reals};
```

In[2]:=
```
subs = {t → τ / ω, r → ρ l, z → ζ l, a → α l,
    Ψ[r, θ, z, t] → l^-3/2 ψ[ρ, θ, ζ, τ], ∂t Ψ[r, θ, z, t] → ω l^-3/2 ∂τ ψ[ρ, θ, ζ, τ]};
```

In[3]:=
```
l = Sqrt[ħ / (2 m ω)];
```

In[4]:=
```
MyLapl = l^-2 l^-3/2 Lapl[ψ[ρ, θ, ζ, τ]]
```

Out[4]=
$$\frac{2\, 2^{3/4}\, m\, \omega\, \text{Lapl}(\psi(\rho, \theta, \zeta, \tau))}{\hbar \left(\frac{\hbar}{m\omega}\right)^{3/4}}$$

In[5]:=
```
TDGP1 = i ħ ∂t Ψ[r, θ, z, t] /. subs // Simplify
```

Out[5]=
$$i\, 2^{3/4} \sqrt[4]{m^3 \omega^7 \hbar}\ \psi^{(0,0,0,1)}(\rho, \theta, \zeta, \tau)$$

In[6]:=
```
TDGP2 = -ħ^2 / (2 m) MyLapl /. subs // Simplify
```

Out[6]=
$$-2^{3/4} \sqrt[4]{m^3 \omega^7 \hbar}\ \text{Lapl}(\psi(\rho, \theta, \zeta, \tau))$$

In[7]:=
```
TDGP3a = 1/2 m ω^2 r^2 Ψ[r, θ, z, t] /. subs // Simplify
```

Out[7]=
$$\frac{\rho^2 \sqrt[4]{m^3 \omega^7 \hbar}\ \psi(\rho, \theta, \zeta, \tau)}{2\sqrt[4]{2}}$$

In[8]:=
```
TDGP3b = 1/2 m ω^2 z^2 ωz^2 / ω^2 Ψ[r, θ, z, t] /. subs // Simplify
```

Out[8]=
$$\frac{\zeta^2\, \omega z^2 \sqrt{\frac{m^3 \hbar}{\omega}}\ \psi(\rho, \theta, \zeta, \tau)}{2\sqrt[4]{2}}$$

In[9]:=
```
U0 = 4 π ħ^2 a / m /. subs;
```

In[10]:=
```
TDGP4 = N U0 Abs[Ψ[r, θ, z, t]]^2 Ψ[r, θ, z, t] /. subs // Simplify
```

Out[10]=
$$8\, 2^{3/4}\, N \pi \alpha \sqrt[4]{m^3 \omega^7 \hbar}\ |\psi(\rho, \theta, \zeta, \tau)|^2\, \psi(\rho, \theta, \zeta, \tau)$$

In[11]:=
```
commonfactor = ħ^1/4 m^3/4 ω^7/4 2^3/4
```

Out[11]=
$$2^{3/4}\, m^{3/4}\, \omega^{7/4} \sqrt[4]{\hbar}$$

In[12]:=
```
GP1 = TDGP1 / commonfactor // Simplify
```

Out[12]=
$$i\, \psi^{(0,0,0,1)}(\rho, \theta, \zeta, \tau)$$

In[13]:=
```
GP2 = TDGP2 / commonfactor // Simplify
```

Out[13]=
$$-\text{Lapl}(\psi(\rho, \theta, \zeta, \tau))$$

In[14]:=
```
GP3a = TDGP3a / commonfactor // Simplify
```

Out[14]=
$$\frac{1}{4} \rho^2 \psi(\rho, \theta, \zeta, \tau)$$

In[15]:=
```
GP3b = TDGP3b / commonfactor // Simplify
```

Out[15]=
$$\frac{\zeta^2\, \omega z^2\, \psi(\rho, \theta, \zeta, \tau)}{4\, \omega^2}$$

In[16]:=
```
GP4 = TDGP4 / commonfactor // Simplify
```

Out[16]=
$$8\, N \pi \alpha\, |\psi(\rho, \theta, \zeta, \tau)|^2\, \psi(\rho, \theta, \zeta, \tau)$$

In[17]:=
```
TDGP := GP1 - GP3b == GP2 + GP3a + GP4
```

In[18]:=
```
TDGP
```

Out[18]=
$$i\, \psi^{(0,0,0,1)}(\rho, \theta, \zeta, \tau) - \frac{\zeta^2\, \omega z^2\, \psi(\rho, \theta, \zeta, \tau)}{4\, \omega^2} = \frac{1}{4} \psi(\rho, \theta, \zeta, \tau)\, \rho^2 - \text{Lapl}(\psi(\rho, \theta, \zeta, \tau)) + 8\, N \pi \alpha\, |\psi(\rho, \theta, \zeta, \tau)|^2\, \psi(\rho, \theta, \zeta, \tau)$$

Reduction from 3D to 2D of the GPE

In[19]:=
```
Θ[ξ_] = (m ωz / (π ħ) l^2)^1/4 Exp[-m ωz / (2 ħ) l^2 ξ^2];
```

In[20]:=
```
∫_-∞^∞ Abs[Θ[ξ]]^2 dξ
```

Out[20]=
$$1$$

In[21]:=
```
dsubs = {ψ[ρ, θ, ξ, τ] → φ[ρ, θ, τ] Θ[ξ],
    ψ*[ρ, θ, ξ, τ] → φ*[ρ, θ, τ] Θ[ξ], ∂τ ψ[ρ, θ, ξ, τ] → Θ[ξ] ∂τ φ[ρ, θ, τ],
    Lapl[ψ[ρ, θ, ξ, τ]] → Θ[ξ] DLapl[φ[ρ, θ, τ]] + φ[ρ, θ, τ] ∂ξ,ξ Θ[ξ]};
```

In[22]:=
```
TDGP1 = GP1 /. dsubs
```

Out[22]=
$$\frac{i\, e^{-\frac{\zeta^2 \omega z}{4\omega}} \sqrt{\frac{\omega z}{\omega}}\ \varphi^{(0,0,1)}(\rho, \theta, \tau)}{\sqrt[4]{2\pi}}$$

In[23]:=
```
TDGP2 = GP2 /. dsubs // Simplify
```

Out[23]=
$$-\frac{e^{-\frac{\zeta^2 \omega z}{4\omega}} \sqrt{\omega z}\ (4\, \text{DLapl}(\varphi(\rho, \theta, \tau))\, \omega^2 + \omega z\, (\zeta^2\, \omega z - 2\, \omega)\, \varphi(\rho, \theta, \tau))}{4 \sqrt[4]{2\pi}\ \omega^{9/4}}$$

In[24]:=
```
TDGP3a = GP3a /. dsubs // Simplify
```

Out[24]=
$$\frac{e^{-\frac{\zeta^2 \omega z}{4\omega}} \rho^2 \sqrt{\frac{\omega z}{\omega}}\ \varphi(\rho, \theta, \tau)}{4 \sqrt[4]{2\pi}}$$

In[25]:=
```
TDGP3b = GP3b /. dsubs // Simplify
```

Out[25]=
$$\frac{e^{-\frac{\zeta^2 \omega z}{4\omega}} \zeta^2 \left(\frac{\omega z}{\omega}\right)^{9/4} \varphi(\rho, \theta, \tau)}{4 \sqrt[4]{2\pi}}$$

Printed by Mathematica for Students

In[26]:= **TDGP4 = GP4 /. dsubs // Simplify**

Out[26]= $4\, e^{-\frac{\omega z\left(\zeta^2+2\,\mathrm{Re}[\zeta^2]\right)}{4\omega}}\, N\, \sqrt{2\pi}\ \alpha \left(\frac{\omega z}{\omega}\right)^{3/4} |\varphi(\rho,\theta,\tau)|^2\, \varphi(\rho,\theta,\tau)$

In[27]:= **IGP1 = $\left(\int_{-\infty}^{\infty} \theta[\zeta]^*\, \mathbf{TDGP1}\, d\zeta\right)$ // Simplify**

Out[27]= $i\, \varphi^{(0,0,1)}(\rho,\theta,\tau)$

In[28]:= **IGP2 = $\left(\int_{-\infty}^{\infty} \theta[\zeta]^*\, \mathbf{TDGP2}\, d\zeta\right)$ // Simplify**

Out[28]= $\frac{\omega z\, \varphi(\rho,\theta,\tau)}{4\omega} - \mathrm{DLapl}(\varphi(\rho,\theta,\tau))$

In[29]:= **IGP3a = $\left(\int_{-\infty}^{\infty} \theta[\zeta]^*\, \mathbf{TDGP3a}\, d\zeta\right)$ // Simplify**

Out[29]= $\frac{1}{4}\, \rho^2\, \varphi(\rho,\theta,\tau)$

In[30]:= **IGP3b = $\left(\int_{-\infty}^{\infty} \theta[\zeta]^*\, \mathbf{TDGP3b}\, d\zeta\right)$ // Simplify**

Out[30]= $\frac{\omega z\, \varphi(\rho,\theta,\tau)}{4\omega}$

In[31]:= **IGP4 = $\left(\int_{-\infty}^{\infty} \theta[\zeta]^*\, \mathbf{TDGP4}\, d\zeta\right)$ // Simplify**

Out[31]= $\frac{4\, N\, \sqrt{\pi}\ \alpha\, \omega z\, |\varphi(\rho,\theta,\tau)|^2\, \varphi(\rho,\theta,\tau)}{\sqrt{\omega\, \omega z}}$

In[32]:= **DTDGP := IGP1 - IGP3b == IGP2 + IGP3a + IGP4**

In[33]:= **DTDGP**

Out[33]= $i\, \varphi^{(0,0,1)}(\rho,\theta,\tau) - \frac{\omega z\, \varphi(\rho,\theta,\tau)}{4\omega} = \frac{1}{4}\, \varphi(\rho,\theta,\tau)\, \rho^2 - \mathrm{DLapl}(\varphi(\rho,\theta,\tau)) + \frac{4\, N\, \sqrt{\pi}\ \alpha\, \omega z\, |\varphi(\rho,\theta,\tau)|^2\, \varphi(\rho,\theta,\tau)}{\sqrt{\omega\, \omega z}} + \frac{\omega z\, \varphi(\rho,\theta,\tau)}{4\omega}$

Notebook 3

Reduction from 3D to 2D of the GPE

In[1]:=
```
$Assumptions = {m > 0, ω > 0, ωz > 0, t > 0, ħ > 0, r > 0, a > 0, N > 0, z ∈ Reals};
```

In[2]:=
```
θ[z_] = (m ωz / (π ħ))^(1/4) Exp[-(m ωz / (2 ħ)) z^2];
```

In[3]:=
```
∫_-∞^∞ Abs[θ[z]]^2 dz
```

Out[3]= 1

In[4]:=
```
subs = {Ψ[r, θ, z, t] → Φ[r, θ, t] θ[z],
    Ψ*[r, θ, z, t] → Φ*[r, θ, t] θ[z], ∂t Ψ[r, θ, z, t] → θ[z] ∂t Φ[r, θ, t],
    Laplacian[Ψ[r, θ, z, t]] → θ[z] PLapl[Φ[r, θ, t]] + Φ[r, θ, t] ∂z,z θ[z]};
```

In[5]:=
```
TDGP1 = i ħ ∂t Ψ[r, θ, z, t] /. subs
```

Out[5]= $\frac{i\, e^{-\frac{m r^2 \omega}{2\hbar}} \sqrt[4]{\frac{m\omega z}{\hbar}}\ \hbar\, \Phi^{(0,0,1)}(r,\theta,t)}{\sqrt[4]{\pi}}$

In[6]:=
```
ATDGP1 = μ Ψ[r, θ, z, t] /. subs
```

Out[6]= $\frac{e^{-\frac{m r^2 \omega}{2\hbar}}\, \mu \sqrt[4]{\frac{m\omega z}{\hbar}}\ \Phi(r,\theta,t)}{\sqrt[4]{\pi}}$

In[7]:=
```
TDGP2 = -(ħ^2 / (2 m)) Laplacian[Ψ[r, θ, z, t]] /. subs // Simplify
```

Out[7]= $-\frac{e^{-\frac{m r^2 \omega}{2\hbar}} \sqrt[4]{\frac{m\omega z}{\hbar}}\ (\text{PLapl}(\Phi(r,\theta,t))\,\hbar^2 + m\,\omega z\,(m z^2 \omega z - \hbar)\,\Phi(r,\theta,t))}{2\, m \sqrt[4]{\pi}}$

In[8]:=
```
TDGP3a = (1/2) m ω^2 r^2 Ψ[r, θ, z, t] /. subs
```

Out[8]= $\frac{e^{-\frac{m r^2 \omega}{2\hbar}}\, m r^2 \omega^2 \sqrt[4]{\frac{m\omega z}{\hbar}}\ \Phi(r,\theta,t)}{2\sqrt[4]{\pi}}$

In[9]:=
```
TDGP3b = (1/2) m ω^2 z^2 (ωz^2 / ω^2) Ψ[r, θ, z, t] /. subs
```

Out[9]= $\frac{e^{-\frac{m r^2 \omega}{2\hbar}}\, m z^2 \omega z^2 \sqrt[4]{\frac{m\omega z}{\hbar}}\ \Phi(r,\theta,t)}{2\sqrt[4]{\pi}}$

In[10]:=
```
TDGP4 = N U0 Abs[Ψ[r, θ, z, t]]^2 Ψ[r, θ, z, t] /. subs // Simplify
```

Out[10]= $\frac{e^{-\frac{3 m r^2 \omega}{2\hbar}}\, N \left(\frac{m\omega z}{\hbar}\right)^{3/4} |\Phi(r,\theta,t)|^2\, U_0\, \Phi(r,\theta,t)}{\pi^{3/4}}$

In[11]:=
```
commonfactor = ħ^-1/4 m^1/4 π^-1/4 ωz^1/4;
```

In[12]:=
```
IGP1 = TDGP1 / commonfactor /. z → 0 // Simplify
```

Out[12]= $i\,\hbar\,\Phi^{(0,0,1)}(r,\theta,t)$

In[13]:=
```
AIGP1 = ATDGP1 / commonfactor /. z → 0 // Simplify
```

Out[13]= $\mu\,\Phi(r,\theta,t)$

In[14]:=
```
IGP2 = TDGP2 / commonfactor /. z → 0 // Simplify
```

Out[14]= $\frac{\hbar\,(m\,\omega z\,\Phi(r,\theta,t) - \hbar\,\text{PLapl}(\Phi(r,\theta,t)))}{2\,m}$

In[15]:=
```
IGP3a = TDGP3a / commonfactor /. z → 0 // Simplify
```

Out[15]= $\frac{1}{2}\, m\, r^2\, \omega^2\, \Phi(r,\theta,t)$

In[16]:=
```
IGP3b = TDGP3b / commonfactor /. z → 0 // Simplify
```

Out[16]= 0

In[17]:=
```
IGP4 = TDGP4 / commonfactor /. z → 0 // Simplify
```

Out[17]= $\frac{N \sqrt{\frac{m\omega z}{\hbar}}\ |\Phi(r,\theta,t)|^2\, U_0\, \Phi(r,\theta,t)}{\sqrt{\pi}}$

In[18]:=
```
gammafactor = (m ωz / (π ħ))^1/2;
```

In[19]:=
```
TDGP := IGP1 - IGP3b == IGP2 + IGP3a + IGP4
```

In[20]:=
```
TDGP /. gammafactor → γ
```

Out[20]= $i\,\hbar\,\Phi^{(0,0,1)}(r,\theta,t) = \frac{1}{2}\, m\, r^2\, \Phi(r,\theta,t)\,\omega^2 + N\,\gamma\,|\Phi(r,\theta,t)|^2\, U_0\, \Phi(r,\theta,t) + \frac{\hbar\,(m\,\omega z\,\Phi(r,\theta,t) - \hbar\,\text{PLapl}(\Phi(r,\theta,t)))}{2\,m}$

In[21]:=
```
ATDGP := AIGP1 - IGP3b == IGP2 + IGP3a + IGP4 /. gammafactor → γ
```

In[22]:=
```
ATDGP
```

Out[22]= $\mu\,\Phi(r,\theta,t) = \frac{1}{2}\, m\, r^2\, \Phi(r,\theta,t)\,\omega^2 + N\,\gamma\,|\Phi(r,\theta,t)|^2\, U_0\, \Phi(r,\theta,t) + \frac{\hbar\,(m\,\omega z\,\Phi(r,\theta,t) - \hbar\,\text{PLapl}(\Phi(r,\theta,t)))}{2\,m}$

Make dimensionless

In[23]:=
```
dsubs = {t → τ / ω, r → ρ l, a → α l, Ψ[r, θ, t] → l^-1 φ[ρ, θ, τ],
    ∂t Ψ[r, θ, t] → ω l^-1 ∂τ φ[ρ, θ, τ], PLapl[Ψ[r, θ, t]] → l^-2 l^-1 DLapl[φ[ρ, θ, τ]]};
```

In[24]:=
```
l = Sqrt[ħ / (2 m ω)];
```

In[25]:=
```
U0 = 4 π ħ^2 a / m;
```

In[26]:=
```
commonfactor2 = 2^2/4 ω^6/4 ħ^2/4 m^2/4;
```

In[27]:=
```
DGP1 = IGP1 / commonfactor2 /. dsubs // Simplify
```

Out[27]= $i\,\varphi^{(0,0,1)}(\rho,\theta,\tau)$

Printed by Mathematica for Students

In[28]:=
```
ADGP1 = AIGP1 / commonfactor2 /. dsubs // Simplify
```

Out[28]=
$$\frac{\mu\,\varphi(\rho,\,\theta,\,\tau)}{\omega\,\hbar}$$

In[29]:=
```
DGP2 = IGP2 / commonfactor2 /. dsubs // Simplify
```

Out[29]=
$$\frac{\omega z\,\varphi(\rho,\,\theta,\,\tau)}{2\,\omega} - \text{DLapl}(\varphi(\rho,\,\theta,\,\tau))$$

In[30]:=
```
DGP3a = IGP3a / commonfactor2 /. dsubs // Simplify
```

Out[30]=
$$\frac{1}{4}\,\rho^2\,\varphi(\rho,\,\theta,\,\tau)$$

In[31]:=
```
DGP3b = IGP3b / commonfactor2 /. dsubs // Simplify
```

Out[31]=
$$0$$

In[32]:=
```
DGP4 = IGP4 / commonfactor2 /. dsubs // Simplify
```

Out[32]=
$$4\,N\,\sqrt{2\,\pi}\;\alpha\,\sqrt{\frac{\omega z}{\omega}}\;|\varphi(\rho,\,\theta,\,\tau)|^2\,\varphi(\rho,\,\theta,\,\tau)$$

In[33]:=
```
DTDGP := DGP1 - DGP3b == DGP2 + DGP3a + DGP4
```

In[34]:=
```
DTDGP
```

Out[34]=
$$i\,\varphi^{(0,0,1)}(\rho,\,\theta,\,\tau) = \frac{1}{4}\,\varphi(\rho,\,\theta,\,\tau)\,\rho^2 - \text{DLapl}(\varphi(\rho,\,\theta,\,\tau)) + 4\,N\,\sqrt{2\,\pi}\;\alpha\,\sqrt{\frac{\omega z}{\omega}}\;|\varphi(\rho,\,\theta,\,\tau)|^2\,\varphi(\rho,\,\theta,\,\tau) + \frac{\omega z\,\varphi(\rho,\,\theta,\,\tau)}{2\,\omega}$$

In[35]:=
```
ADTDGP := ADGP1 - DGP3b == DGP2 + DGP3a + DGP4
```

In[36]:=
```
ADTDGP
```

Out[36]=
$$\frac{\mu\,\varphi(\rho,\,\theta,\,\tau)}{\omega\,\hbar} = \frac{1}{4}\,\varphi(\rho,\,\theta,\,\tau)\,\rho^2 - \text{DLapl}(\varphi(\rho,\,\theta,\,\tau)) + 4\,N\,\sqrt{2\,\pi}\;\alpha\,\sqrt{\frac{\omega z}{\omega}}\;|\varphi(\rho,\,\theta,\,\tau)|^2\,\varphi(\rho,\,\theta,\,\tau) + \frac{\omega z\,\varphi(\rho,\,\theta,\,\tau)}{2\,\omega}$$

Notebook 4

Make coupled 3D GPEs dimensionless

```
In[1]:= $Assumptions = {m > 0, ω > 0, ωz > 0, t > 0, ħ > 0, r > 0,
          a11 > 0, a22 > 0, a12 > 0, N1 > 0, N2 > 0, {m, t, r, z, ω, ωz} ∈ Reals};
```

For the moment, assume we only have one mass m because we only have one species of atom.

```
In[2]:= m1 = m; m2 = m;
```

```
In[3]:= m11 = m1 m1 / (m1 + m1)
```

$$\text{Out[3]}= \frac{m}{2}$$

```
In[4]:= m22 = m2 m2 / (m2 + m2)
```

$$\text{Out[4]}= \frac{m}{2}$$

```
In[5]:= m12 = m1 m2 / (m1 + m2)
```

$$\text{Out[5]}= \frac{m}{2}$$

```
In[6]:= subs = {t → τ / ω,  r → ρ l, z → ξ l, a11 → α11 l, a22 → α22 l, a12 → α12 l,
          Ψ1[r, θ, z, t] → l^-3/2 ψ1[ρ, θ, ξ, τ], ∂t Ψ1[r, θ, z, t] → ω l^-3/2 ∂τ ψ1[ρ, θ, ξ, τ],
          Ψ2[r, θ, z, t] → l^-3/2 ψ2[ρ, θ, ξ, τ], ∂t Ψ2[r, θ, z, t] → ω l^-3/2 ∂τ ψ2[ρ, θ, ξ, τ]};
```

```
In[7]:= l = Sqrt[ħ / (2 m ω)] ;
```

```
In[8]:= MyLapl1 = l^-2 l^-3/2 Lapl[ψ1[ρ, θ, ξ, τ]]
```

$$\text{Out[8]}= \frac{2\, 2^{3/4}\, m\, \omega\, \text{Lapl}(\psi_1(\rho,\theta,\zeta,\tau))}{\hbar \left(\frac{\hbar}{m\omega}\right)^{3/4}}$$

```
In[9]:= MyLapl2 = l^-2 l^-3/2 Lapl[ψ2[ρ, θ, ξ, τ]]
```

$$\text{Out[9]}= \frac{2\, 2^{3/4}\, m\, \omega\, \text{Lapl}(\psi_2(\rho,\theta,\zeta,\tau))}{\hbar \left(\frac{\hbar}{m\omega}\right)^{3/4}}$$

```
In[10]:= TDGP11 = i ħ ∂t Ψ1[r, θ, z, t] /.  subs // Simplify
```

$$\text{Out[10]}= i\, 2^{3/4} \sqrt[4]{m^3 \omega^7 \hbar}\ \psi_1^{(0,0,0,1)}(\rho,\theta,\zeta,\tau)$$

```
In[11]:= TDGP12 = -ħ^2 / (2 m) MyLapl1 /. subs // Simplify
```

$$\text{Out[11]}= -2^{3/4} \sqrt[4]{m^3 \omega^7 \hbar}\ \text{Lapl}(\psi_1(\rho,\theta,\zeta,\tau))$$

```
In[12]:= TDGP13a = 1/2 m ω^2 r^2 Ψ1[r, θ, z, t] /. subs // Simplify
```

$$\text{Out[12]}= \frac{\rho^2 \sqrt[4]{m^3 \omega^7 \hbar}\ \psi_1(\rho,\theta,\zeta,\tau)}{2\sqrt{2}}$$

```
In[13]:= TDGP13b = 1/2 m ω^2 z^2 ωz^2 / ω^2 Ψ1[r, θ, z, t] /. subs // Simplify
```

$$\text{Out[13]}= \frac{\zeta^2 \omega z^2 \sqrt[4]{\frac{m^3\hbar}{\omega}}\ \psi_1(\rho,\theta,\zeta,\tau)}{2\sqrt[4]{2}}$$

```
In[14]:= U11 = 2 π ħ^2 a11 / m11 /. subs
```

$$\text{Out[14]}= \frac{2\sqrt{2}\ \pi \hbar^2 \sqrt{\frac{\hbar}{m\omega}}\ \alpha_{11}}{m}$$

```
In[15]:= U22 = 2 π ħ^2 a22 / m22 /. subs
```

$$\text{Out[15]}= \frac{2\sqrt{2}\ \pi \hbar^2 \sqrt{\frac{\hbar}{m\omega}}\ \alpha_{22}}{m}$$

```
In[16]:= U12 = 2 π ħ^2 a12 / m12 /. subs
```

$$\text{Out[16]}= \frac{2\sqrt{2}\ \pi \hbar^2 \sqrt{\frac{\hbar}{m\omega}}\ \alpha_{12}}{m}$$

```
In[17]:= TDGP14 = U11 Abs[Ψ1[r, θ, z, t]]^2 Ψ1[r, θ, z, t] /. subs // Simplify
```

$$\text{Out[17]}= 8\, 2^{3/4}\, \pi \sqrt{m^3 \omega^7 \hbar}\ |\psi_1(\rho,\theta,\zeta,\tau)|^2\, \alpha_{11}\, \psi_1(\rho,\theta,\zeta,\tau)$$

```
In[18]:= TDGP15 = U12 Abs[Ψ2[r, θ, z, t]]^2 Ψ1[r, θ, z, t] /. subs // Simplify
```

$$\text{Out[18]}= 8\, 2^{3/4}\, \pi \sqrt{m^3 \omega^7 \hbar}\ |\psi_2(\rho,\theta,\zeta,\tau)|^2\, \alpha_{12}\, \psi_1(\rho,\theta,\zeta,\tau)$$

```
In[19]:= commonfactor = ħ^1/4 m^3/4 ω^7/4 2^3/4
```

$$\text{Out[19]}= 2^{3/4}\, m^{3/4}\, \omega^{7/4} \sqrt[4]{\hbar}$$

```
In[20]:= GP11 = TDGP11 / commonfactor // Simplify
```

$$\text{Out[20]}= i\, \psi_1^{(0,0,0,1)}(\rho,\theta,\zeta,\tau)$$

```
In[21]:= GP12 = TDGP12 / commonfactor // Simplify
```

$$\text{Out[21]}= -\text{Lapl}(\psi_1(\rho,\theta,\zeta,\tau))$$

```
In[22]:= GP13a = TDGP13a / commonfactor // Simplify
```

$$\text{Out[22]}= \frac{1}{4}\rho^2 \psi_1(\rho,\theta,\zeta,\tau)$$

```
In[23]:= GP13b = TDGP13b / commonfactor // Simplify
```

$$\text{Out[23]}= \frac{\zeta^2 \omega z^2 \psi_1(\rho,\theta,\zeta,\tau)}{4\omega^2}$$

```
In[24]:= GP14 = TDGP14 / commonfactor // Simplify
```

$$\text{Out[24]}= 8\pi\, |\psi_1(\rho,\theta,\zeta,\tau)|^2\, \alpha_{11}\, \psi_1(\rho,\theta,\zeta,\tau)$$

```
In[25]:= GP15 = TDGP15 / commonfactor // Simplify
```

$$\text{Out[25]}= 8\pi\, |\psi_2(\rho,\theta,\zeta,\tau)|^2\, \alpha_{12}\, \psi_1(\rho,\theta,\zeta,\tau)$$

Printed by Mathematica for Students

In[26]:= **TDGP1 := GP11 - GP13b == GP12 + GP13a + GP14 + GP15**

In[27]:= **TDGP1**

Out[27]= $i\,\psi_1^{(0,0,0,1)}(\rho,\theta,\zeta,\tau) - \frac{\zeta^2\,\omega z^2\,\psi_1(\rho,\theta,\zeta,\tau)}{4\,\omega^2} =$

$$\frac{1}{4}\psi_1(\rho,\theta,\zeta,\tau)\,\rho^2 - \text{Lapl}(\psi_1(\rho,\theta,\zeta,\tau)) + 8\,\pi\,|\psi_1(\rho,\theta,\zeta,\tau)|^2\,\alpha_{11}\,\psi_1(\rho,\theta,\zeta,\tau) + 8\,\pi\,|\psi_2(\rho,\theta,\zeta,\tau)|^2\,\alpha_{12}\,\psi_1(\rho,\theta,\zeta,\tau)$$

This is the first GPE. To get the second (coupled) GPE, swap all the 1 and 2 indices.

Reduce coupled GPEs from 3D to 2D with axial trap removed at t=0

The freely expanding wavepacket description from Bransden and Joachain is used as an Ansatz for the axial profile of the untrapped condensate in the z-dimension. This assumes a non-interacting gas that starts in a sufficiently pancake-confined state that it can be described by a single Gaussian mode.

In[28]:= **θ[ζ_] = $\left(\frac{m\,\omega z}{\pi\,\hbar}\,l^2\right)^{1/4}$ $(1 + i\,\omega z\,t)^{-1/2}$ Exp$\left[-\frac{m\,\omega z}{2\,\hbar\,(1 + i\,\omega z\,t)}\,l^2\,\zeta^2\right]$;**

In[29]:= $\int_{-\infty}^{\infty}$ **Abs[θ[ζ]]^2 dζ /. t → 0**

Out[29]= 1

In[30]:=
```
dsubs = {ψ1[ρ, θ, ζ, τ] → φ1[ρ, θ, τ] θ[ζ],
    ψ1*[ρ, θ, ζ, τ] → φ1*[ρ, θ, τ] θ[ζ], ψ2[ρ, θ, ζ, τ] → φ2[ρ, θ, τ] θ[ζ],
    ψ2*[ρ, θ, ζ, τ] → φ2*[ρ, θ, τ] θ[ζ], ∂τ ψ1[ρ, θ, ζ, τ] → θ[ζ] ∂τ φ1[ρ, θ, τ],
    ∂τ ψ2[ρ, θ, ζ, τ] → θ[ζ] ∂τ φ2[ρ, θ, τ],
    Lapl[ψ1[ρ, θ, ζ, τ]] → θ[ζ] DLapl[φ1[ρ, θ, τ]] + φ1[ρ, θ, τ] ∂ζ,ζ θ[ζ],
    Lapl[ψ2[ρ, θ, ζ, τ]] → θ[ζ] DLapl[φ2[ρ, θ, τ]] + φ2[ρ, θ, τ] ∂ζ,ζ θ[ζ]};
```

In[31]:= **CF = $(i\,t\,\omega z + 1)^{-1/2}$**

Out[31]= $\frac{1}{\sqrt{i\,t\,\omega z + 1}}$

In[32]:= **GP2D11 = GP11 /. dsubs**

Out[32]= $\frac{i\,e^{-\frac{\zeta^2\,\omega t}{4\,\omega\,(i\,t\,\omega t+1)}}\,\sqrt[4]{\frac{\omega z}{\omega}}\,\varphi_1^{(0,0,1)}(\rho,\theta,\tau)}{\sqrt[4]{2\,\pi}\,\sqrt{i\,t\,\omega z + 1}}$

In[33]:= **GP2D12 = GP12 /. dsubs // Simplify**

Out[33]= $-\frac{e^{-\frac{\zeta^2\,\omega t}{4\,(i\,t\,\omega t\omega+\omega t}}\,\sqrt{\omega z}\,\left(4\,\omega^2\,\text{DLapl}(\varphi_1(\rho,\theta,\tau))\,(t\,\omega z - i)^2 + \omega z\,(\omega\,(2\,i\,t\,\omega z + 2) - \zeta^2\,\omega z)\,\varphi_1(\rho,\theta,\tau)\right)}{4\,\sqrt[4]{2\,\pi}\,\omega^{9/4}\,\sqrt{i\,t\,\omega z + 1}\,(t\,\omega z - i)^2}$

In[34]:= **GP2D13a = GP13a /. dsubs**

Out[34]= $\frac{e^{-\frac{\zeta^2\,\omega t}{4\,\omega\,(i\,t\,\omega t+1)}}\,\rho^2\,\sqrt[4]{\frac{\omega z}{\omega}}\,\varphi_1(\rho,\theta,\tau)}{4\,\sqrt[4]{2\,\pi}\,\sqrt{i\,t\,\omega z + 1}}$

In[35]:= **GP2D13b = GP13b /. dsubs**

Out[35]= $\frac{e^{-\frac{\zeta^2\,\omega t}{4\,\omega\,(i\,t\,\omega t+1)}}\,\zeta^2\,\omega z^2\,\sqrt{\frac{\omega z}{\omega}}\,\varphi_1(\rho,\theta,\tau)}{4\,\sqrt[4]{2\,\pi}\,\omega^2\,\sqrt{i\,t\,\omega z + 1}}$

In[36]:= **GP2D14 = GP14 /. dsubs**

Out[36]= $\frac{4\,e^{-\frac{\omega t\,\zeta^2}{4\,\omega\,(i\,t\,\omega t+1)}-\frac{1}{2}\,\text{Re}\left(\frac{\zeta^2\,\omega t}{\omega\,(i\,t\,\omega t+1)}\right)}\,\sqrt{2\,\pi}\,\sqrt[4]{\frac{\omega z}{\omega}}\,\left|\frac{\sqrt[4]{\frac{\omega t}{\omega}}\,\varphi_1(\rho\beta,\tau)}{\sqrt{i\,t\,\omega z+1}}\right|^2\,\alpha_{11}\,\varphi_1(\rho,\theta,\tau)}{\sqrt{i\,t\,\omega z + 1}}$

In[37]:= **GP2D15 = GP15 /. dsubs**

Out[37]= $\frac{4\,e^{-\frac{\omega t\,\zeta^2}{4\,\omega\,(i\,t\,\omega t+1)}-\frac{1}{2}\,\text{Re}\left(\frac{\zeta^2\,\omega t}{\omega\,(i\,t\,\omega t+1)}\right)}\,\sqrt{2\,\pi}\,\sqrt[4]{\frac{\omega z}{\omega}}\,\left|\frac{\sqrt[4]{\frac{\omega t}{\omega}}\,\varphi_2(\rho\beta,\tau)}{\sqrt{i\,t\,\omega z+1}}\right|^2\,\alpha_{12}\,\varphi_1(\rho,\theta,\tau)}{\sqrt{i\,t\,\omega z + 1}}$

In[38]:= **IGP11 = $\left(\int_{-\infty}^{\infty}$ ComplexExpand[θ[ζ]* GP2D11] dζ$\right)$ // Simplify**

Out[38]= $i\,\varphi_1^{(0,0,1)}(\rho,\theta,\tau)$

In[39]:= **IGP12 = $\left(\int_{-\infty}^{\infty}$ θ[ζ]* GP2D12 dζ$\right)$ // Simplify**

Out[39]= $-\frac{\sqrt{\omega - i\,t\,\omega\,\omega z}\,\left(\frac{1}{\sqrt{i\,t\,\omega t+1}}\right)^*\,(4\,\omega\,\text{DLapl}(\varphi_1(\rho,\theta,\tau)) - \omega z\,\varphi_1(\rho,\theta,\tau))}{4\,\omega^{3/2}}$

In[40]:= **IGP13a = $\left(\int_{-\infty}^{\infty}$ ComplexExpand[θ[ζ]* GP2D13a] dζ$\right)$ // Simplify**

Out[40]= $\frac{1}{4}\,\rho^2\,\varphi_1(\rho,\theta,\tau)$

In[41]:= **IGP13b = $\left(\int_{-\infty}^{\infty}$ θ[ζ]* GP2D13b dζ$\right)$ // Simplify**

Out[41]= $\frac{\omega z\,(t^2\,\omega z^2 + 1)\,\varphi_1(\rho,\theta,\tau)}{4\,\omega}$

In[42]:= **IGP14 = $\left(\int_{-\infty}^{\infty}$ ComplexExpand[θ[ζ]* GP2D14] dζ$\right)$ // Simplify**

Out[42]= $\frac{4\,\pi\,\omega z\,|\varphi_1(\rho,\theta,\tau)|^2\,\alpha_{11}\,\varphi_1(\rho,\theta,\tau)}{\sqrt{\pi\,t^2\,\omega\,\omega z^3 + \pi\,\omega\,\omega z}}$

In[43]:= **IGP15 = $\left(\int_{-\infty}^{\infty}$ ComplexExpand[θ[ζ]* GP2D15] dζ$\right)$ // Simplify**

Out[43]= $\frac{4\,\pi\,\omega z\,|\varphi_2(\rho,\theta,\tau)|^2\,\alpha_{12}\,\varphi_1(\rho,\theta,\tau)}{\sqrt{\pi\,t^2\,\omega\,\omega z^3 + \pi\,\omega\,\omega z}}$

In[44]:= **D2DGP := IGP11 - IGP13b == IGP12 + IGP13a + IGP14 + IGP15**

Finally, we form the dimensionless, time-dependent 2D coupled GPE for φ_1 (component 1)

In[45]:= **D2DGP**

Out[45]= $$i\,\varphi_1^{(0,0,1)}(\rho,\theta,\tau)-\frac{\omega z\,(t^2\,\omega z^2+1)\,\varphi_1(\rho,\theta,\tau)}{4\,\omega}=\frac{1}{4}\varphi_1(\rho,\theta,\tau)\,\rho^2+\frac{4\,\pi\,\omega z\,|\varphi_1(\rho,\theta,\tau)|^2\,\alpha_{11}\,\varphi_1(\rho,\theta,\tau)}{\sqrt{\pi\,t^2\,\omega\,\omega z^3+\pi\,\omega\,\omega z}}+$$
$$\frac{4\,\pi\,\omega z\,|\varphi_2(\rho,\theta,\tau)|^2\,\alpha_{12}\,\varphi_1(\rho,\theta,\tau)}{\sqrt{\pi\,t^2\,\omega\,\omega z^3+\pi\,\omega\,\omega z}}-\frac{\sqrt{\omega-i\,t\,\omega\,\omega z}\;\left(\frac{1}{\sqrt{i\,t\,\omega z+1}}\right)^{*}\,(4\,\omega\,\mathrm{DLapl}(\varphi_1(\rho,\theta,\tau))-\omega z\,\varphi_1(\rho,\theta,\tau))}{4\,\omega^{3/2}}$$

Verify that this reduces to the known case at t=0 - it does!

In[46]:= **D2DGP /. t → 0**

Out[46]= $$i\,\varphi_1^{(0,0,1)}(\rho,\theta,\tau)-\frac{\omega z\,\varphi_1(\rho,\theta,\tau)}{4\,\omega}=\frac{1}{4}\varphi_1(\rho,\theta,\tau)\,\rho^2+\frac{4\sqrt{\pi}\;\omega z\,|\varphi_1(\rho,\theta,\tau)|^2\,\alpha_{11}\,\varphi_1(\rho,\theta,\tau)}{\sqrt{\omega\,\omega z}}+$$
$$\frac{4\sqrt{\pi}\;\omega z\,|\varphi_2(\rho,\theta,\tau)|^2\,\alpha_{12}\,\varphi_1(\rho,\theta,\tau)}{\sqrt{\omega\,\omega z}}-\frac{4\,\omega\,\mathrm{DLapl}(\varphi_1(\rho,\theta,\tau))-\omega z\,\varphi_1(\rho,\theta,\tau)}{4\,\omega}$$

Contents of optical disk

D

A list of contents of the optical disk included inside the back cover of this thesis.

readme.txt Contents file

GaryRuben_PhDThesis_screen.pdf Adobe Acrobat pdf with coloured hyperlinks of thesis with amendments.
GaryRuben_PhDThesis_print.pdf Adobe Acrobat pdf with invisible hyperlinks of thesis with amendments.

examined_thesis
- GaryRuben_PhDThesis.pdf Adobe Acrobat pdf of thesis provided for examination.
- GaryRuben_PhDThesisAddendum.pdf Adobe Acrobat pdf of amendments to the examined version.

bec_movies

These are various .avi and .wmv animations of BEC dynamics produced during the PhD.

gist800.avi a personal favourite

The following animations correspond to figures in the thesis:

Fig. 4.1 20071205_op8_two_symmetric_parts_straight_g_amp.wmv

Fig. 4.3 jet800.avi (a similar but not identical movie)

Fig. 4.6(a,b) 20071129_op8_g_amp.avi (pinks800.avi is computed on a 1024x1024 grid)
Fig. 4.6(a,c) 20080428_op8_peakgamma_notrap squaredamp_g_amp.wmv

Fig. 4.9(a,b) 20071130_op8_rotated_g_amp.wmv
Fig. 4.9(a,c) 20080428_op8_peakgamma_notraprotated_squaredamp_g_amp.wmv

Fig. 4.10(a,b) 20071201_op3_g_amp.wmv
Fig. 4.10(a,c) 20071130_op3_rotated_g_amp.wmv
Fig. 4.10(a,d) 20080428_op3_peakgamma_notraprotated_squaredamp_g_amp.wmv
Fig. 4.10(a,e) 20071201_op3_biowalls_g_amp.wmv
Fig. 4.10(a,f) 20071201_op8_90degwalls_g_amp.wmv

Fig. 4.17 20090314_3D_trapped_a_i.avi

Fig. 4.19(upper) a3_q.avi

Fig. 4.21(a) a3_a.avi
Fig. 4.21(b) a3_b.avi
Fig. 4.21(c) a3_p.avi
Fig. 4.21(d) v3.avi

Fig. 4.22 a2_d.avi

bec_sims

Selected xmds and Python files for BEC simulations.

texture_sims

Selected xmds and Python files for texture defect simulations.

conference posters

pdf files of conference posters.

thesis

Full source of this thesis, including CorelDRAW11 files, Python files, and source data.

Publications arising from thesis

E

This appendix contains three papers, based on the work undertaken during the PhD. The first was published in *Physical Review E* and a short Erratum was later published in the same journal, correcting an erroneous minor claim made in the first paper. The second paper is a short peer-reviewed conference paper of work presented at The Ninth Rochester Conference on Coherence and Quantum Optics (CQO9). The third paper was published in *Physical Review A*.

G Ruben and D M Paganin. Phase vortices from a Young's three-pinhole interferometer. *Physical Review E* **75**, 066613, (2007). "Copyright (2007) by the American Physical Society."

G Ruben and D M Paganin. Erratum: Phase vortices from a Young's three-pinhole interferometer [Phys. Rev. E 75, 066613 (2007)]. *Physical Review E* **76**, 029901(E), (2007). "Copyright (2007) by the American Physical Society."

G Ruben and D M Paganin. Phase vortices from the interference of three spherical waves. In *Conference on Coherence and Quantum Optics, OSA Technical Digest (CD) (Optical Society of America, 2007), paper CSuA40*, (2007)

G Ruben, D M Paganin and M J Morgan. Vortex-lattice formation and melting in a nonrotating Bose-Einstein condensate. *Physical Review A* **78**, 013631, (2008). "Copyright (2008) by the American Physical Society."

PHYSICAL REVIEW E **75**, 066613 (2007)

Phase vortices from a Young's three-pinhole interferometer

Gary Ruben* and David M. Paganin
School of Physics, Monash University, Victoria 3800, Australia
(Received 17 December 2006; revised manuscript received 17 April 2007; published 27 June 2007)

An analysis is presented of the phase vortices generated in the far field by an arbitrary arrangement of three monochromatic point sources of complex spherical waves. In contrast with the case of three interfering plane waves, in which an infinitely extended vortex lattice is generated, the spherical sources generate a finite number of phase vortices. Analytical expressions for the vortex core locations are developed and shown to have a convenient representation in a discrete parameter space. Our far-field analysis may be mapped onto the case of a coherently illuminated Young's interferometer, in which the screen is punctured by three rather than two pinholes.

DOI: 10.1103/PhysRevE.75.066613 PACS number(s): 42.25.Hz, 03.65.Vf, 07.60.Ly

I. INTRODUCTION

In a seminal paper, Dirac [1] considered vortical screw-type dislocations in the phase of complex wave fields, noting the one-dimensional nature of the associated vortex cores (nodal lines) in three dimensions (3D). Such phase vortices exist in a variety of linear and nonlinear physical systems that may be described via complex fields, including the angular momentum eigenstates of the hydrogen atom [2], the Meissner state of type-II superconductors [3,4], vortex states of superfluids [5,6] and Bose-Einstein condensates (BECs) [7], optical vortex solitons [8], propagating electron wave functions diffracting through crystalline slabs [9], Gaussian random wave fields [10], and optical speckle fields [11].

In continuous complex scalar fields, to which the considerations of the present paper are restricted, vortical behavior is manifest as screw-type dislocations in the field's multivalued surfaces of constant phase [12–14]. More precisely, consider a stationary-state, complex spatial wave function or order-parameter field $\Psi(\mathbf{r})=A(\mathbf{r})\exp[i\chi(\mathbf{r})]$. Here, $A(\mathbf{r})$ is the non-negative real amplitude, $\chi(\mathbf{r})$ is the phase, and $\mathbf{r}=(x,y,z)$ is a position vector in 3D. Note that harmonic time dependence on angular frequency ω and time t, via the usual multiplicative factor of $\exp(-i\omega t)$, is suppressed throughout. To determine whether a phase vortex exists at a point p in a plane Π over which $\Psi(\mathbf{r})$ is defined, a line integral of the phase gradient is evaluated along a smooth infinitesimally small closed path Γ that encircles p. This path is assumed to have a winding number of unity with respect to p and to be such that the modulus of $\Psi(\mathbf{r})$ is strictly positive at each point on Γ. One may then write the following expression for the "circulation" of the phase over Γ (see, e.g., Nye [15]):

$$\oint_\Gamma d\chi = \oint_\Gamma \nabla\chi\cdot\mathbf{t}\,ds = 2\pi n. \tag{1}$$

Here, $\mathbf{t}$ is a unit tangent vector to Γ, ds is an infinitesimal line element along Γ, and n is an integer corresponding to the number of phase windings about p. Any nonzero n indicates the presence of a vortex core threading the path Γ, with the nonzero value for n being referred to as its topological charge. The sign of this charge distinguishes between a vortex (+) and an antivortex (−).

In an optical setting, a common way to generate such phase vortices is to pass coherent laser light or soft x rays through a spiral phase plate or forked transmission diffraction grating [16–21]. Kim *et al.* [22] generated optical vortices with a curved glass plate as an alternative to the spiral phase plate. Other means for creating optical phase vortices in coherent light include the use of spatial light modulators [23], liquid crystal panels patterned with microdots [24], the use of aberrated lenses to create vortices in a distorted focal volume [25], and diffraction from random phase screens [10].

Alternatively, one can forego the use of diffractive or refractive optical elements, seeking instead to create phase vortices by the superposition of a small number of nonvortical fields. For example, Nicholls and Nye [26] showed that a lattice of vortices may be generated by interfering three plane waves. Later, Masajada and Dubik [27] showed analytically and experimentally that this is a minimum requirement, reformulating the analysis in terms of phasors. The interference of higher numbers of plane waves has also been investigated in a study of the resulting 3D structure of nodal lines [28]. Furthermore, by directly interfering vortical beams, a looped and knotted nodal line network may be created [29].

Here, we generalize the idea of vortex formation from three plane waves by considering the creation of phase vortices from the superposition of three outgoing spherical waves, generated by three distinct monochromatic equal-energy point sources.

We see that the resulting system of nodal lines (vortex cores) exhibits a rich geometry, by developing approximate analytical expressions for the far-field behavior of this nodal-line network. The 3D space, into which the sources radiate, is foliated using a family of observation planes that are parallel to the plane containing the three point sources. When one observes the wave field over any such foliating plane, a 2D pattern of point vortices may be seen, the cores of which coincide with the points at which a nodal line punctures the plane.

Interestingly, the problem of three interfering spherical waves may be mapped onto a Young-type experiment, in

*Electronic address: gary.ruben@sci.monash.edu.au

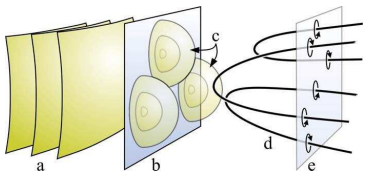

FIG. 1. (Color online) In this schematic of a Young's three-pinhole interferometer, incident illumination (a) impinges upon a punctured screen (b), producing three divergent waves (c), which interfere, giving rise to a network of nodal lines (d). These are observed as phase vortices over a plane (e).

which a black screen with three small pinholes is coherently illuminated by a propagating complex scalar field (see Fig. 1). Note that this identification is only possible when one is both sufficiently far from the screen and sufficiently close to the optic axis, in which case the radiation transmitted by each of the pinholes is approximately spherical.

In two recent experiments, vortex generation has been demonstrated in systems related to the one we describe. Lee *et al.* [30] illuminated three (and more) "microspheres" with a laser and observed vortices in the resulting interference pattern. More recently, Scherer *et al.* [31] have observed vortices resulting from the merging of three nonrotating BEC clouds. Disregarding nonlinear effects and reconsidering the three-spatial-dimensional system described here in 2+1 dimensions by replacement of the z dimension with time t, the BEC vortex generation may be understood as arising from the linear interference of propagating, expanding waves.

We close this Introduction with a brief outline of the remainder of the paper: We begin by reviewing the manner in which the superposition of three plane waves may be used to generate an infinite lattice of phase vortices. The generalization of this idea to the superposition of three outgoing spherical waves is then given. We describe the application of a phasor approach to the spherical-wave arrangement, applying this in the far-field region asymptotically far from the sources. Approximate analytical expressions are derived for the vortex locations. A representation in terms of a certain parameter space arises, allowing estimates of the number of vortices and description of a natural coordinate system for the vortices at the intersections of a certain family of hyperbolas. A specific case of collinear sources is explored in detail. We then show how the theory, which has been derived for spherical point sources, may be mapped onto the case of a Young's interferometer in which the illuminated screen contains three rather than two pinholes. Finally, the 3D nodal line structure is examined for both the spherical point source and the pinhole interferometer cases.

II. PHASE VORTICES FROM THE INTERFERENCE OF THREE PLANE WAVES

Consider the following superposition of three planar spatial wave functions:

$$\Psi(\mathbf{r}) = \sum_{j=1}^{3} A_j \exp[i(\mathbf{k}_j \cdot \mathbf{r} + \phi_j)], \tag{2}$$

where the non-negative real constants A_j denote the amplitude of the jth wave, $\mathbf{k}_j$ are wave vectors corresponding to the same wavelength $\lambda_0 = 2\pi/|\mathbf{k}_j|$, and ϕ_j are global phase factors. Notwithstanding the fact that the constituent plane waves do not have a vortical character, the above superposition may yield a regular lattice of phase vortices and antivortices [26,27].

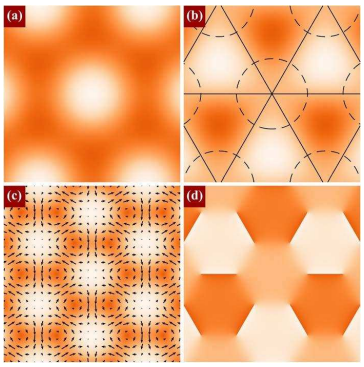

FIG. 2. (Color online) Interference of three plane waves giving rise to an infinite, regular vortex lattice [see Eq. (2)]. Here, the wave vectors are oriented symmetrically with respect to the z axis, with $\mathbf{k}_1 = (\sqrt{3}, -1, 10)$, $\mathbf{k}_2 = (-\sqrt{3}, -1, 10)$, and $\mathbf{k}_3 = (0, 2, 10)$. The real (a) and imaginary (b) parts, amplitude (c), and phase (d) of the wave function $\Psi(x, y, z=0)$ are shown. In (b), zero contours of the real (dashed lines) and imaginary (solid lines) parts are overlaid. In (c) is overlaid the vector field of the probability current density, which is seen to rotate counterclockwise around vortices and clockwise around antivortices. In (d), vortices are visible as the ends of branch cuts indicated by dark to light ($-\pi \rightarrow \pi$) steps. Values in (a)–(c) are represented by linear levels from dark to light (minimum to maximum).

A numerical example of this phenomenon is given in Fig. 2, corresponding to the parameters $A_1 = A_2 = A_3 = 1$ and $\phi_1 = \phi_2 = \phi_3 = 0$, with all fields being evaluated over the plane $z = 0$. This example illustrates the three interfering plane waves giving rise to an infinitely extended lattice of straight, parallel nodal lines (vortex cores). These nodal lines intersect the plane $z = 0$, to give the location of the point vortices that are visible as screw dislocations in the phase map of Fig. 2(d). The locations of these point vortices coincide with both (i) the intersections of the zero contours in Fig. 2(b) and (ii) the points at which $|\Psi| = 0$ in the amplitude plot of Fig. 2(c). Indeed, continuity of the wave function implies that the probability density vanishes at each vortex core, since these are branch points at which the phase ceases to be differentiable. The topological charge or phase winding number n of each of these point defects is seen to be equal to ± 1, as the phase increases by $\pm 2\pi$ as one traverses a circuit that encloses a given vortex core. In this context, we note that higher-charge vortices are not observed in the case of three sources. To form a charge n nodal line in a field locally obeying the Helmholtz equation, $n(n+1)/2$ complex conditions must be specified [32]. A factor of 2, accounting for separation of the real and imaginary parts, gives $n(n+1)$ real conditions which must be satisfied. Evidently, a minimum of five point sources lying in a plane, requiring a total of seven

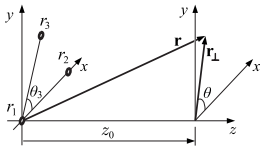

FIG. 3. Coordinate system. The point sources r_1, r_2, and r_3 lie in the plane $z=0$. The position vector $\mathbf{r}$ is to a point with cylindrical-polar coordinates $(r_\perp, \theta, z_0)$.

coordinates for the specification of their position (up to irrelevant translations and rotations), is the minimum requirement to form $n=2$ charges.

III. PHASE VORTICES FROM THE INTERFERENCE OF THREE SPHERICAL WAVES

Given that the superposition of three complex plane-wave spatial wave functions may lead to phase vortices [26,27], it is natural to enquire whether the superposition of three outgoing spherical waves may not also lead to phase vortices. This latter case is investigated here.

A. Extending the plane-wave case to spherical waves

The complex spatial wave function $\Psi_j(\mathbf{r})$, due to a point source at position $\mathbf{r}_j$ that is radiating outgoing spherical waves *in vacuo*, is given by

$$\Psi_j(\mathbf{r}) = \frac{A_j}{|\mathbf{r}-\mathbf{r}_j|}\exp[i(k|\mathbf{r}-\mathbf{r}_j|+\phi_j)] \equiv \frac{A_j}{|\mathbf{r}-\mathbf{r}_j|}\exp(i\chi), \tag{3}$$

where $k \equiv 2\pi/\lambda_0$. For all $\mathbf{r} \neq \mathbf{r}_j$, such spherical waves obey the free-space Helmholtz equation. This applies to monochromatic complex scalar electromagnetic waves, to nonrelativistic spinless particles in the form of the time-independent free-space Schrödinger equation, and to relativistic spinless particles in the form of the time-independent free-space Klein-Gordon equation. As such, the following discussions are applicable to all of these physical systems. For example, experimental application involving a high-energy transmission electron microscope might be envisaged using the paraxial form of the time-independent free-space Klein-Gordon equation, which ignores the typically small effects of electron spin in this setting [33].

Now, consider an assembly of three point sources, all of which have the same wave number k. Without loss of generality, we may consider these sources to occupy the same plane $z=0$, with source locations $\mathbf{r}_j \equiv (x_j, y_j, 0)$, where $j=1,2,3$. The resulting spatial wave function $\Psi(\mathbf{r})$ may thus be written as

$$\Psi(\mathbf{r}) = \sum_{j=1}^{3} \frac{A_j}{|\mathbf{r}-\mathbf{r}_j|}\exp[i(k_j|\mathbf{r}-\mathbf{r}_j|+\phi_j)], \tag{4}$$

where $|\mathbf{r}-\mathbf{r}_j| \equiv \sqrt{(x-x_j)^2+(y-y_j)^2+z^2}$ is the distance from the jth source to a given observation point $\mathbf{r}$.

Referring to Fig. 3, we label both the jth source and its distance from the coordinate origin by the same symbol r_j. The position vector $\mathbf{r}$ and its perpendicular component $\mathbf{r}_\perp$ have lengths $r \equiv |\mathbf{r}|$ and $r_\perp \equiv |\mathbf{r}_\perp|$, respectively.

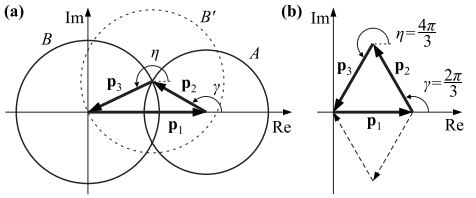

FIG. 4. Phasor diagram from which vortex solution conditions are established [27]. Three phasors $\mathbf{p}_1$, $\mathbf{p}_2$, and $\mathbf{p}_3$—which, respectively, correspond to the three terms on the right-hand side of Eq. (4), at a given point $\mathbf{r}$ on a nodal line—form a closed triangle corresponding to a resultant zero amplitude. Two angles γ and η arise in the construction, as indicated. (a) In the case of arbitrary amplitudes for $\mathbf{p}_1$, $\mathbf{p}_2$, and $\mathbf{p}_3$, the tip of $\mathbf{p}_2$ is constrained to lie on circle A of radius $|\mathbf{p}_2|$, with the tail of $\mathbf{p}_3$ being constrained to lie on circle B of radius $|\mathbf{p}_3|$. (b) For equal amplitudes $|\mathbf{p}_1|=|\mathbf{p}_2|=|\mathbf{p}_3|$ an equilateral triangle is formed. The dashed construction represents another of the six equivalent alternatives formed by permutating the phasor order.

To determine the locations of the vortices which result from the superposition of the three spherical waves, we utilize the fact that vortex cores lie at points of zero amplitude. Given that the problem is restricted to two degrees of freedom, due to the complex wave-field representation, a geometric phasor diagram can be constructed with one phasor for each wave component in Eq. (4) (see Fig. 4). We follow the phasor approach of Masajada and Dubik [27] (see also [34]). At any point coinciding with a vortex core, the phasor components must sum to zero when placed tip to tail. Note that if the source amplitudes differ sufficiently, it is possible that no closed triangle of phasors may be formed; i.e., circles A and B in Fig. 4 cannot intersect if $|\mathbf{p}_1| > |\mathbf{p}_2| + |\mathbf{p}_3|$. In this case, no vortices will be produced.

Consider a given point $\mathbf{r}$ in space, corresponding to the special case of Eq. (4) where $A_1=A_2=A_3=1$. Let $\mathbf{p}_1$, $\mathbf{p}_2$, and $\mathbf{p}_3$ denote the three complex terms that are summed on the right-hand side of this equation. These three numbers are represented as phasors in Fig. 4. Here, we set $\phi_1=0$, which implies no loss of generality, since the invariance of the equations of motion under a shift in the origin of time implies global phase factors to have no physical meaning. The circle B' represents the possible orientations of $\mathbf{p}_3$, constrained by the tip of $\mathbf{p}_2$. The zero sum condition is easier to construct if $\mathbf{p}_3$ is notionally flipped to give circle B whose center coincides with the tail of $\mathbf{p}_1$. The resulting vortex solutions correspond to the phasors $\mathbf{p}_2$ and $\mathbf{p}_3$ meeting at the intersections of the circles A and B. Note that there are two such "closed-triangle" intersections and hence two apparent solutions. In the case of equal amplitudes, where $|\mathbf{p}_1|=|\mathbf{p}_2|=|\mathbf{p}_3|$, symmetry dictates that there are only two unique solution angles. We consider the triangle in the first quadrant of the complex plane, which is an arbitrary choice, as any of the six equivalent constructions formed by permutating the phasor order will lead to the same solution. Relaxing the equal-

amplitude condition will require consideration of extra solutions.

B. Vortices in the far-field regime

We evaluate Eq. (4) in the "far-field" regime—namely, in the half-space $z > z_0$ in which z_0 is sufficiently large that

$$|\mathbf{r} - \mathbf{r}_j| \sim r - \frac{\mathbf{r}_\perp \cdot \mathbf{r}_j}{r}, \quad r \equiv |\mathbf{r}| \gg r_j. \tag{5}$$

Here, we are making a paraxial approximation to the wave function. This approximation is applied to the phase term in the exponent of Eq. (4). In an alternative approach, one might seek solutions of the paraxial wave equation in restricting attention to the far field (see, e.g., [34]). The wave function Ψ depends linearly on the amplitude term $A_j/|\mathbf{r} - \mathbf{r}_j|$, so for large r the divisor varies much more slowly with $|\mathbf{r} - \mathbf{r}_j|$ than the phase argument. Consequently, the stronger approximation $|\mathbf{r} - \mathbf{r}_j| \sim r$ is made to this term (see, e.g., [35]). Thus, Eq. (4) becomes

$$\begin{aligned}\Psi(\mathbf{r}) = \sum_{j=1}^{3} \frac{1}{r} \exp\left\{ i\left[k_j\left(r - \frac{\mathbf{r}_\perp \cdot \mathbf{r}_j}{r} \right) + \phi_j \right] \right\} &= \frac{1}{r}\exp(ikr) \\ &+ \frac{1}{r}\exp\left\{ i\left[k\left(r - \frac{r_\perp r_2}{r}\cos\theta \right) + \phi_2 \right] \right\} \\ &+ \frac{1}{r}\exp\left\{ i\left[k\left(r - \frac{r_\perp r_3}{r}\cos(\theta - \theta_3) \right) + \phi_3 \right] \right\},\end{aligned} \tag{6}$$

where we have made use of the assumptions that $A_1 = A_2 = A_3 = 1$ and that the sources share a single wave number k. This expression vanishes when

$$\begin{aligned}1 + \exp\left[i\left(-k\frac{r_\perp r_2}{r}\cos\theta + \phi_2 \right) \right] \\ + \exp\left[i\left(-k\frac{r_\perp r_3}{r}\cos(\theta - \theta_3) + \phi_3 \right) \right] = 0.\end{aligned} \tag{7}$$

Geometrically, the above condition reduces to the addition of three unit-length phasors in the complex plane, such that they form an equilateral triangle when placed tip to tail [27]. This construction is shown in Fig. 4(b), with the arguments of the two exponentials in Eq. (7) being denoted by γ and η, respectively. These phase angles are uniquely defined to within an integer multiple of 2π, so that

$$\gamma = -k\frac{r_\perp r_2}{r}\cos\theta + \phi_2 = \frac{2\pi}{3} + 2m\pi \tag{8a}$$

and

$$\eta = -k\frac{r_\perp r_3}{r}\cos(\theta - \theta_3) + \phi_3 = \frac{4\pi}{3} + 2n\pi, \tag{8b}$$

where m and n are integers.

C. Vortex locations

Here, we show how the construction of the previous subsection can be used to determine the polar coordinates $r_{\perp mn}$ and θ_{mn} of a given point vortex in the plane $z = z_0$ that is specified by the integer indices (m,n) (cf. Fig. 3).

Dividing Eq. (8b) by Eq. (8a) gives

$$\frac{r_3\cos(\theta - \theta_3)}{r_2\cos\theta} = \frac{\frac{4\pi}{3} + 2n\pi - \phi_3}{\frac{2\pi}{3} + 2m\pi - \phi_2} = \frac{2(2+3n)\pi - 3\phi_3}{2(1+3m)\pi - 3\phi_2}. \tag{9}$$

We denote the denominator and numerator, on the right-hand side, as

$$M(m) \equiv 2(1+3m)\pi - 3\phi_2 \tag{10a}$$

and

$$N(n) \equiv 2(2+3n)\pi - 3\phi_3, \tag{10b}$$

respectively. Next, making the substitution

$$\begin{aligned}\frac{\cos(\theta - \theta_3)}{\cos\theta} &= \frac{\cos\theta\cos\theta_3 + \sin\theta\sin\theta_3}{\cos\theta} \\ &= \cos\theta_3 + \tan\theta\sin\theta_3\end{aligned} \tag{11}$$

gives

$$\frac{r_3}{r_2}(\cos\theta_3 + \tan\theta\sin\theta_3) = \frac{N(n)}{M(m)}. \tag{12}$$

Finally, isolating θ and labeling it with an mn subscript, to identify it with the (m,n)th vortex core, gives the desired expression for the polar angle to the (m,n)th vortex core,

$$\theta_{mn} = \arctan\left[\frac{1}{\sin\theta_3}\left(\frac{r_2}{r_3}\frac{N(n)}{M(m)} - \cos\theta_3 \right) \right]. \tag{13}$$

With a view to obtaining the radial coordinate $r_{\perp mn}$ of the vortex core, take Eq. (8a) and write the denominator r in terms of its components z_0 and $r_\perp$ (see Fig. 3). Hence,

$$-k\frac{r_\perp r_2}{\sqrt{z_0^2 + r_\perp^2}}\cos\theta_{mn} = \frac{1}{3}M(m). \tag{14}$$

Squaring and then solving for $r_\perp$, we obtain

$$r_{\perp mn}^2 = \frac{z_0^2}{\left(\frac{3kr_2\cos\theta_{mn}}{M(m)} \right)^2 - 1}, \tag{15}$$

where an mn subscript has been added to $r_\perp$. Applying the identity

$$\cos^2\theta_{mn} = \frac{1}{1 + \tan^2\theta_{mn}} \tag{16}$$

and making use of Eq. (13), we obtain our final expression for the radial coordinate $r_{\perp mn}$ of the (m,n)th vortex core:

$$r_{\perp mn} = \frac{\pm z_0}{\sqrt{\dfrac{(3kr_2/M(m))^2}{1+\dfrac{1}{\sin^2\theta_3}\left(\dfrac{r_2}{r_3}\dfrac{N(n)}{M(m)}-\cos\theta_3\right)^2}-1}}. \quad (17)$$

The positive and negative solutions correspond to two separate vortices. Note that these coincide with an extra branch of the arctan function in Eq. (13). Note, also, that Eq. (17) is only valid for integers (m,n) that yield a real number for $r_{\perp mn}$ (cf. Sec. III D).

The polar equations (13) and (17) specify the vortex core locations for all allowed m and n parameter values, in the far-field regime. Note that $r_{\perp mn}$ is proportional to z_0, as one would expect in the far field. This corresponds to a 3D nodal-line structure of asymptotically straight lines radiating from a single point in the source plane. This may be contrasted with the case of three superposed plane waves, where the nodal lines are mutually parallel [26,27].

D. Parameter space

For real solutions, the argument of the square root in Eq. (17) must be positive, imposing a condition on the allowable (m,n) values for a given source arrangement. In what follows, we set $\phi_j=0$, corresponding to all three point sources radiating in phase with one another. The integers m and n must therefore satisfy the inequality

$$[(1+3m)\sin\theta_3]^2+\left((2+3n)\frac{r_2}{r_3}-(1+3m)\cos\theta_3\right)^2 < \left(\frac{3kr_2\sin\theta_3}{2\pi}\right)^2. \quad (18)$$

We claim that this describes the interior of an ellipse in the Cartesian (m,n) plane for all noncollinear arrangements of the three sources.

To prove the above claim, first note that the boundary curve, of the open region defined by Eq. (18), is obtained by replacing the inequality in this expression with an equality. The resulting equation form is consistent with a general conic section in the (m,n) plane: namely (see, e.g., [36]),

$$Q(m,n) = am^2+2hmn+bn^2+2gm+2fn+c=0, \quad (19)$$

where a, h, b, g, f, and c are real numbers given by

$$a = 9r_3^2,$$

$$h = -9r_2r_3\cos\theta_3,$$

$$b = 9r_2^2,$$

$$g = 3r_3^2-6r_2r_3\cos\theta_3,$$

$$f = 6r_2^2-3r_2r_3\cos\theta_3,$$

$$c = r_3^2+4r_2^2-4r_2r_3\cos\theta_3-\left(\frac{3kr_2r_3\sin\theta_3}{2\pi}\right)^2. \quad (20)$$

Introduce the invariants [36]

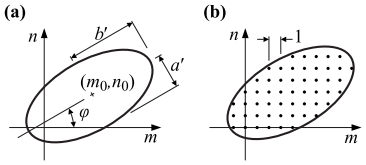

FIG. 5. A parameter-space ellipse, in the (m,n) plane, sets an upper limit on the number of vortices that are created by the interfering radiation from three point sources. (a) The bounding ellipse has center (m_0,n_0), makes an angle φ to the positive m axis, and has semiaxis lengths a' and b'. (b) The enclosed (m,n) pairs lie on a discrete square lattice of unit spacing. Each of these interior points corresponds to two vortices.

$$\Delta = \begin{vmatrix} a & h & g \\ h & b & f \\ g & f & c \end{vmatrix}, \quad (21a)$$

$$\delta = \begin{vmatrix} a & h \\ h & b \end{vmatrix}, \quad (21b)$$

and

$$\tau = a+b. \quad (21c)$$

Substituting Eqs. (20) into Eqs. (21) and evaluating gives

$$\Delta = -\left(\frac{27k}{2\pi}(r_2r_3\sin\theta_3)^2\right)^2, \quad (22a)$$

$$\delta = (9r_2r_3\sin\theta_3)^2, \quad (22b)$$

and

$$\tau = 9(r_2^2+r_3^2). \quad (22c)$$

In order for Eq. (19) to correspond to an ellipse, the discriminant conditions $\Delta\neq 0$, $\delta>0$, and $\Delta/\tau<0$ must be satisfied. These three conditions are met when (i) $r_2,r_3\neq 0$ and (ii) $\theta_3\neq p\pi$, $p\in\mathbb{Z}$. This will always be true for noncollinear arrangements of three distinct sources. Since the area of the corresponding ellipse is finite, for three noncollinear sources, each of which is separated by a finite distance, we have a finite number of vortices labeled by the integer pairs (m,n) obeying Eq. (18).

The parameter-space ellipse has center (m_0,n_0), is rotated anticlockwise at an angle φ, and has semiaxis lengths a' and b' (Fig. 5). These ellipse parameters are given by well-known expressions in terms of the coefficients in Eq. (20). The center and rotation angle are given by [36]

$$(m_0,n_0) = \left(\frac{bg-hf}{h^2-ab},\frac{af-hg}{h^2-ab}\right) = \left(-\frac{1}{3},-\frac{2}{3}\right),$$

$$\varphi = \frac{1}{2}\operatorname{arccot}\left(\frac{b-a}{2h}\right) = \frac{1}{2}\operatorname{arccot}\left(\frac{r_3^2-r_2^2}{2r_2r_3\cos\theta_3}\right). \quad (23)$$

The semiaxis lengths $a'\equiv s_+$ and $b'\equiv s_-$ are given by

$$s_{\pm} = \sqrt{\left|\frac{\Delta}{\lambda_{\pm}\delta}\right|}, \tag{24}$$

where $\lambda_{\pm}$ denotes the two solutions to the quadratic

$$\lambda^2 - \tau\lambda + \delta = 0. \tag{25}$$

Thus

$$\lambda_{\pm} = \frac{9}{2}[r_2^2 + r_3^2 \pm \sqrt{(2r_2r_3\cos\theta_3)^2 + (r_2^2 - r_3^2)^2}], \tag{26}$$

so that the semiaxis lengths are given by

$$s_{\pm} = \frac{|kr_2r_3\sin\theta_3|}{\pi\sqrt{2}\sqrt{|(2r_2r_3\cos\theta_3)^2 + (r_2^2 - r_3^2)^2 \pm (r_2^2 + r_3^2)|}}. \tag{27}$$

For fixed k, r_2, and r_3 and variable θ_3, Eqs. (23) and (27) define a family of ellipses. A "bounding rectangle" may be constructed as the envelope of this continuum of ellipses. Any one ellipse in this family, corresponding to a particular value of θ_3, touches each side of this bounding rectangle exactly once. The bounding rectangle is centered at (m_0, n_0) and has dimensions of kr_2/π and kr_3/π in the m and n directions, respectively. [Note that these dimensions are found by setting $\theta_3 = \pi/2$ in Eq. (27).] As θ_3 is varied from 0 to π, while keeping k, r_2, and r_3 fixed, the parameter-space ellipse transforms from (i) a line at 45° to the m axis, identified with the positive-gradient diagonal to the bounding rectangle, to (ii) a series of nondegenerate ellipses, each of which touches each side of the bounding rectangle exactly once, to (iii) a line at −45°—namely, the negative-gradient diagonal to the bounding rectangle. Note that no vortices are produced in the limit cases (i) and (iii) above, since the open region bounded by a straight line is an empty set [cf. Eq. (18)]. The change in shape of the ellipse with θ_3 is symmetric about $\theta_3 = \pi$ [corresponding to case (iii)], so that the ellipse for $\theta_3 = \pi - \xi$ is coincident with that for $\pi + \xi$ for any angle ξ.

Figures 6 and 7 present simulations with various source geometries showing predicted vortex locations for the far-field case. The corresponding parameter-space ellipses are shown in Fig. 8. The fields of view of the intensity and phase plots do not show the outermost vortex cores in most cases. This is evident from a count of the lattice points enclosed by the corresponding ellipse in Fig. 8. Only Figs. 7(c) and 7(d) have all the generated vortices within the visible region. The corresponding parameter-space ellipse, near −45° in Fig. 8, encloses six lattice points—this corresponds to the $6 \times 2 = 12$ phase vortices in Figs. 7(c) and 7(d).

Note that, to aid visualization in all of the phase plots in Figs. 6 and 7, a constant spherical background has been subtracted. Indeed, far from the three point sources, one may meaningfully write the wave function as a single expanding "background" spherical wave, multiplied by an envelope whose functional form depends on the particular local arrangement of the sources. By subtracting the phase of this spherical background from all of the displayed phase maps, the structure of the envelope alone—including any vortical structure—may be examined without the distraction of a large number of concentric phase contours from the background wave. Note also that this background spherical wave corresponds to an effective source located at the geometric centroid of the real sources, with amplitude $A = A_1 + A_2 + A_3$.

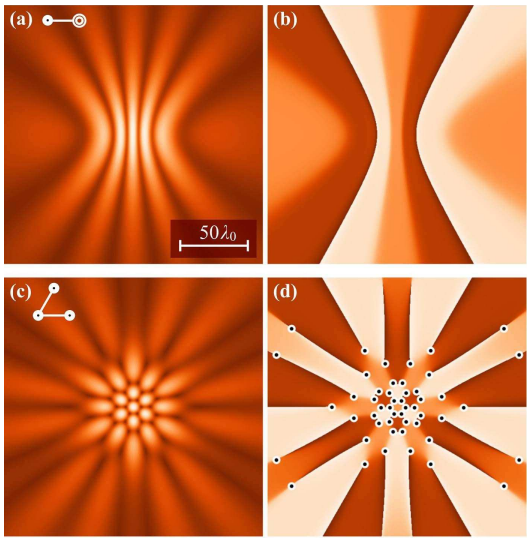

FIG. 6. (Color online) (a), (c) Amplitude $|\Psi|$ and (b), (d) associated phase χ from Eq. (4) at $z_0 = 25\lambda_0$ with different source arrangements, shown pictographically alongside the (a) and (c) labels. Small circles overlaid on numerical simulations show the vortex locations as approximated by Eqs. (13) and (17). Values in (a) and (c) are represented by linear levels from dark to light (minimum to maximum). The phase ranges from $-\pi$ (dark) to π (light). All sources are in phase (i.e., $\phi_2 = \phi_3 = 0$), $\lambda_0 = \pi$, and the source arrangements are (a), (b) $r_2 = r_3 = 3\lambda_0$, $\theta_3 = 0°$ and (c), (d) $r_2 = r_3 = 3\lambda_0$, $\theta_3 = 60°$. Note that a spherical background has been subtracted from all phase maps, as described in the main text.

Let us return consideration to Figs. 6(a) and 6(b), which exhibits a degenerate case in which two of the point sources are colocated, thereby reducing the system to two in-phase spherical sources with one having twice the amplitude of the other. As expected for only two sources, no vortices are generated. Rather, one has a series of Young-type fringes. In the case of two equal-amplitude sources, in 3D, a series of nodal planes or "domain walls" is generated, coinciding with the amplitude minima. Domain walls separate regions of space where the phase changes discontinuously [6]. Changing the amplitude of the second source or adding a third source as in Fig. 7(e), dissolves the nodal planes, allowing the phase to change rapidly but smoothly between the regions. In Fig. 6(b), the phase is not left-right mirror symmetric, due to the positioning of the geometric centroid for three sources being to the right of center. Thus, there is a global tilt to the phase, which is observed to cycle through two branch cuts. For this example, the parameter-space ellipse (not shown) is the limiting case of a line at 45°. The complementary limiting case is Fig. 7(e) where the three sources are collinear; the ellipse (not shown) is a line at −45° and again no vortices are generated. The phase here is mirror symmetric since (i) the ini-

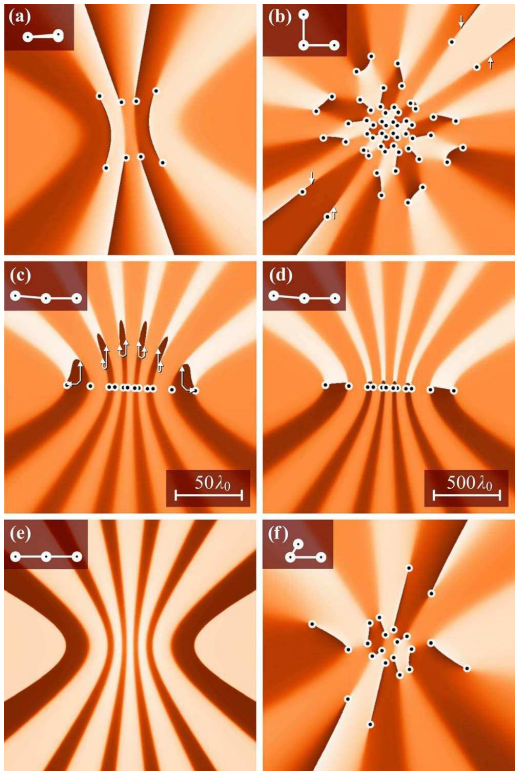

FIG. 7. (Color online) Phase χ from Eq. (4) and vortex-core locations approximated by Eqs. (13) and (17), with variation in source arrangement. The representation and parameters are as described in Fig. 6. The scale bar in (c) applies to all images and corresponds to $z_0=25\lambda_0$, except for (d) which corresponds to $z_0=250\lambda_0$. Small arrows in (b), (c) point to the exact vortex locations, to indicate their deviation from the far-field predictions. $\lambda_0=\pi$ and source arrangements are (a) $r_2=r_3=3\lambda_0$, $\theta_3=10°$, (b) $r_2=r_3=3\lambda_0$, $\theta_3=90°$, (c) $r_2=r_3=3\lambda_0$, $\theta_3=175°$, (d) $r_2=r_3=3\lambda_0$, $\theta_3=175°$, $z_0=250\lambda_0$, (e) $r_2=r_3=3\lambda_0$, $\theta_3=180°$, and (f) $r_2=3\lambda_0$, $r_3=1.5\lambda_0$, $\theta_3=60°$. A spherical background has been subtracted from all phase maps (see main text).

tial field configuration is mirror symmetric and (ii) the wavefield propagator is rotationally symmetric. In Fig. 7(a), one of the sources has been moved just enough from coincidence with another so that the corresponding ellipse just encompasses some lattice points and vortices are created. There are four points clearly within the ellipse, giving rise to the vortices seen in the panel. If the additional two points near the boundary are just inside the ellipse, more vortices will be present at large $r_\perp$ and these will lie at the other ends of the branch-cut lines; otherwise, the branch-cut lines will extend to infinity. Figure 7(b) shows the case for $\theta_3=90°$, giving a circle in parameter space. The number of vortices will therefore be close to the maximum for fixed values of r_2 and r_3.

The far-field solution is usually considered valid for a Fresnel number $N_F \equiv a^2/\lambda_0 z \ll 1$, where a is the largest

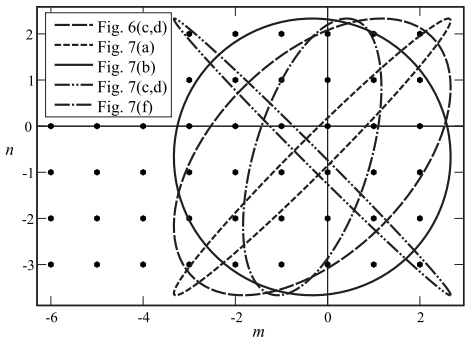

FIG. 8. Parameter-space ellipses corresponding to Figs. 6 and 7. Enclosed lattice points define vortex locations.

transverse length scale present in the system (see, e.g., [34]). We take this to be the maximum pinhole-pinhole spacing. The far-field condition corresponding to Fig. 6 is then $(3\lambda_0)^2/\lambda_0 z \ll 1$ or, say, $z > 100\lambda_0$. The value of z_0 for numerical simulations in Fig. 7 was deliberately chosen as $25\lambda_0$ to show up visual disagreements between the vortices in the numerically determined phase map and their analytically determined locations. Small arrows illustrate the true vortex positions for some vortices which do not coincide with their predicted far-field positions. The discrepancy between numerical and analytical results is highlighted in Fig. 7(c), a case arising from all parameter space lattice points lying close to the ellipse boundary. In Fig. 7(d), the Fresnel number is smaller and the correspondence is improved because the observation is being made further into the far field, where nodal lines have asymptotically approached closer to the straight lines predicted in Sec. III C. Note that, for any finite z_0, there will be some angle θ_3, close to π, at which the numerical and analytical prediction disagree by an arbitrarily large amount. Predictions are more reliable for (m,n) lattice points closer to the ellipse center. In contrast with the far-field prediction that vortices may abruptly appear and disappear with infinitesimal changes in source arrangement as lattice points cross the ellipse boundary, we observe through simulations at finite z_0 that the vortex location becomes highly sensitive to the source arrangement, with vortices arriving from and escaping transversely to an infinite $r_\perp$ distance. This point is further explored in Sec. III H.

E. Source phase variation

We now consider the effects of source phase variation on the geometric parameter space description.

The functions $M(m)$ and $N(n)$ [Eqs. (10)] contain the vortex coordinate dependence on the source phase via Eqs. (13) and (17), where ϕ_j is the relative phase of the jth source and $\phi_1=0$. These may be rewritten as

$$M(m) \equiv 2\pi[1+3(m-\phi_2/2\pi)] \tag{28a}$$

and

$$N(n) \equiv 2\pi[2 + 3(n - \phi_3/2\pi)], \tag{28b}$$

to highlight the 2π phase periodicity.

We see that a 2π change in relative phases ϕ_2 or ϕ_3 may be absorbed as an integer change in an associated parameter-space coordinate m or n, respectively. By allowing the lattice point coordinates to correspond to discrete real values, spaced at intervals of 2π, the coordinates specified by m and n may then also absorb fractional parts of the relative phase. The subtraction of a value from m or n therefore corresponds geometrically to a translation of the (m,n) lattice points along the associated axis, with a relative phase change of 2π effecting a translation of one lattice unit.

In summary, parameters defining the source configuration or the wave-number map to the parameter space as different ellipse constructions, whereas source phase variations correspond to translations of the lattice itself.

F. Estimate of number of vortices

In contrast to the case of three interfering plane waves reviewed in Sec. II, in which infinitely many nodal lines are produced, the analysis of the preceding subsections implies that only a finite number of vortices are produced by three overlapping spherical waves, provided that there is a finite spacing between the three corresponding point sources. Here, we give a simple means to estimate the number of vortices over a given plane in the far field, as a function of the geometry of the three point sources.

As mentioned earlier, the two-valued nature of Eq. (17) implies that each (m,n) pair gives rise to a pair of vortices. Because the m and n values have unit spacing [see Fig. 5(b)], the number of vortices n_v may be approximated by twice the area $\pi a' b'$ of the ellipse. Thus

$$n_v \approx 2\pi a' b' \tag{29}$$

or

$$n_v \approx \frac{k^2}{2\pi}|r_2 r_3 \sin\theta_3| = \frac{k^2 \mathcal{A}}{\pi}, \tag{30}$$

where $\mathcal{A}$ is the area of a triangle whose vertices coincide with the locations of the three point sources.

This is exactly the expression $N=\mathcal{A}\Omega/\lambda^2$ found by Gabor [37] and attributed by him as a restatement of an earlier result of Max von Laue, for the degrees of freedom N—a measure of the information carrying capacity—of a light beam of area $\mathcal{A}$. Here, Ω is the solid angle of any beamlet, equal to 2π, corresponding to a forward-propagating spherical wave front, and $\lambda=2\pi/k$. Each lattice point determines two vortices as Eq. (17) has positive and negative solutions; hence, $N=n_v/2$. Correspondingly, $\mathcal{A}$ is found to be the area of the triangle whose vertices coincide with the pinholes.

One may ask whether it is possible to develop an exact expression for the number of lattice points enclosed by our parameter-space ellipse, thereby improving on the approximation for n_v given in Eq. (30). Indeed, this question is addressed by a famous problem in number theory known as "Gauss's circle problem." With $\phi_2=2\pi/3$, $\phi_3=-2\pi/3$, and $\theta_3=\pi/2$, the conditions corresponding to the common form of Gauss's circle problem are established; the ellipse is a circle and is centered on a lattice point. The resulting solution for this case is both involved and well known, and so will not be given here (see, e.g., Andrews [38]).

We note that two unexpected and beautiful connections have arisen between the physical system considered here, a result from information theory, and a certain problem in the theory of numbers.

G. Vortex trajectories from phase variation

In most of the preceding discussion, the phases ϕ_1, ϕ_2, and ϕ_3 of the sources were all set to zero. Here, we consider how vortices move in response to varying the phase of one of the sources.

The equations of these curves are found by eliminating the phase ϕ_j corresponding to the source r_j in Eqs. (13) and (17). For example, the trajectories for variation of source r_2 are found by solving Eq. (13) for ϕ_2 and substituting this into Eq. (17). Repeating this for ϕ_3 gives a second set of trajectories along which the vortices move with ϕ_3 variation. The resulting equations are

$$r_{\perp m} = \frac{M(m) z_0}{\sqrt{(3kr_2 \cos\theta_m)^2 - M(m)^2}} \tag{31a}$$

and

$$r_{\perp n} = \frac{N(n) z_0}{\sqrt{[3kr_3 \cos(\theta_n - \theta_3)]^2 - N(n)^2}}, \tag{31b}$$

where the subscripts mn have been changed to m or n to highlight the independence of the equations with respect to the complementary parameter space coordinate. Note that Eq. (31a) is the same as Eq. (15), with minor manipulation.

Figure 9 shows the trajectories overlaying the numerical simulation results for the source arrangement seen in Fig. 7(f).

We have seen (Sec. III E) that variation of ϕ_2 (or ϕ_3) corresponds to a translation of the m (or n) lattice alone. Thus, our choice to eliminate the respective phase has led to the separation of the m and n dependences. The equations describe hyperbolas, where the polar coordinate system origin is centered between the two hyperbola branches. Note that this polar form is less common than that typically seen in the study of conics, in which the origin is placed at the focus of one branch. Equations (31) may be thought of as a (one-to-many) mapping from lines of constant m or n in parameter space to hyperbolas in real space.

The angle θ_3 in Eq. (31b) corresponds to the rotation of the n-indexed hyperbola axes with respect to the coordinate system axes. The square-root limits the range of real solutions, hence the number of hyperbolas and the number of vortices. The domain of the parameter-space variable m (or n) is restricted to match that determined by the parameter-space ellipse. Thus, these equations may be applied to determine the valid domains of m or n independently, without recourse to the ellipse solution.

Fixing the source phases defines two particular hyperbolas corresponding to the parameter space coordinates m and

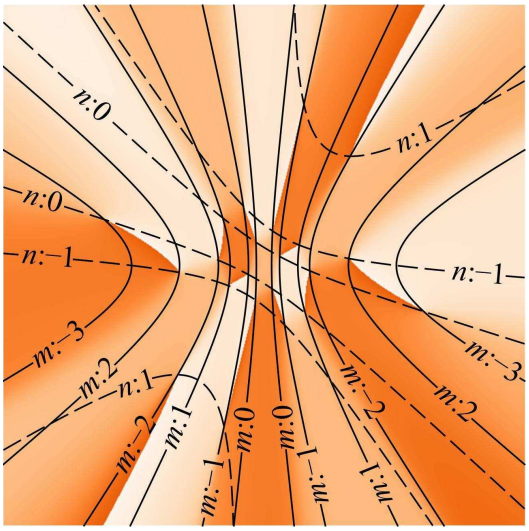

FIG. 9. (Color online) Vortices move with varying source phase along trajectories and lie at the intersections of two independent sets of hyperbolas. Two independent phases give rise to two sets of hyperbolas indexed by m (solid lines) and n (dashed lines), respectively. The hyperbolas are shown overlaying the phase χ from Eq. (6). Note that the result of this equation is ≥ 0 for arbitrary $(r_\perp, \theta)$. The parameters are the same as Fig. 7(f).

n, respectively, with vortices located at the intersections of an m and an n curve. Both branches are included, giving four separate curves. Where one branch of an m (or n) hyperbola intersects both branches of an n (or m) hyperbola, only one intersection is observed to correspond to a physical vortex solution.

These equations also describe an intersecting curvilinear coordinate system. The location of a vortex on the phase map may be thought of as addressable by selection of a particular patch having coordinates (m,n) and then finely addressable within that patch by variation of the source phases. Variation of the phases from 0 to 2π shifts the vortices along one of the two families of curvilinear trajectories within the patch. When there are a moderate or large number of vortices present, the patches in the central region of the phase map are correspondingly small. In this case, the vortices shift a small distance with changing phase. In the outer, sparsely populated regions, small changes in phase lead to arbitrarily large distance changes since the outermost patches have boundaries at infinity.

It is not unexpected that vortices should lie along intersecting hyperbolas. Two point sources naturally give rise to surfaces of constant phase that are hyperboloids of two sheets having the sources as their foci. The difference in path length being constant establishes the condition for constant phase and is equivalent to the well-known geometric construction method for hyperboloids. The intersections of hyperboloids of two sheets with the $z=z_0$ plane will be hyperbolas of two branches. These will not have phase values at the amplitude maxima or minima due to any individual pair, but will be at some other value $\chi=a+ib$ on one set and $-\chi=-a-ib$ on the other, summing to zero at the vortex locations.

H. Parameter space near collinearity

Here, we examine the behavior of the nodal lines as θ_3 approaches π (three collinear sources) when $\phi_2=\phi_3=0$, since we observe a marked deviation between numerical simulation and analytical results in this regime [see Fig. 7(c), which clearly illustrates this discrepancy].

An analysis around $\theta_3=\pi$ may be performed by substituting $\theta_3=\pi+\varepsilon$ into Eq. (12), where ε is small:

$$\frac{r_3}{r_2}(\cos(\pi+\varepsilon)+\tan\theta\sin(\pi+\varepsilon))=\frac{N(n)}{M(m)}. \tag{32}$$

Applying the small-angle approximations $\cos\varepsilon\sim 1$ and $\sin\varepsilon\sim\varepsilon$, Eq. (32) yields

$$\tan\theta_{mn}(\varepsilon)=\frac{1}{\varepsilon}\left(\frac{r_2}{r_3}\frac{N(n)}{M(m)}+1\right) \tag{33}$$

for the θ_{mn} coordinate of the vortex core. Substituting into Eq. (15) and applying Eq. (16) gives $r_{\perp mn}$ for our special case

$$r_{\perp mn}^2=\frac{z_0^2}{\left(\frac{3kr_2}{M(m)}\right)^2\frac{1}{1+\tan^2\theta_{mn}}-1}. \tag{34}$$

Finally, substituting Eq. (33), we get

$$r_{\perp mn}(\varepsilon)=\pm\frac{z_0}{\sqrt{\frac{(3kr_2/M(m))^2}{1+\frac{1}{\varepsilon^2}\left(\frac{r_2}{r_3}\frac{N(n)}{M(m)}+1\right)^2}-1}}. \tag{35}$$

In the limit $\varepsilon\to 0$, we now see that $\theta_{mn}(\varepsilon)\to\pi/2$ and $r_{\perp mn}(\varepsilon)\to\mp iz_0$. Regarding the latter limit, $r_{\perp mn}(\varepsilon)$ first approaches infinity and then becomes imaginary.

We may widen the context of this result by realizing that it is but one example of a lattice point crossing an ellipse boundary. Whenever this occurs, the far-field prediction is that associated vortices will be created or destroyed instantaneously. In contrast, in numerical simulations, which are at some finite distance from the source, vortices rapidly enter from or escape to infinity.

I. Relation to the Young's three-pinhole interferometer

Here, we show how to map our far-field results for three spherical point sources, hitherto the main subject of this paper, onto a three-pinhole Young's interferometer. In this interferometer, coherent radiation illuminates a black screen that is punctured with three small pinholes, with the resulting transmitted radiation being observed at a distance that is large compared to the spacing between the pinholes (see Fig. 1). Note that the assumptions of equal amplitude and a single wave number, applied in Eq. (6), correspond to uniform co-

herent illumination of the screen. The following argument is based on the Rayleigh-Sommerfeld diffraction theory (see, e.g., [39]).

The Rayleigh-Sommerfeld diffraction integral of the first kind yields a rigorous solution to the Helmholtz equation (time-independent free-space Schrödinger equation) in a vacuum-filled half-space for a field that obeys the Sommerfeld radiation condition. For a field $U^{(i)}$ incident on an aperture A centered on the plane $z=0$, the wave function U may be determined at an arbitrary point (x,y,z) in the half-space $z \geq 0$. With the boundary conditions that $U(x,y,z=0) \approx U^{(i)}(x,y,z=0)$ when $(x,y,z=0)$ is in A and $U(x,y,z=0) \approx 0$ when $(x,y,z=0)$ is not in A, the diffraction integral reads

$$U(x,y,z) = \int \int_A U^{(i)}(x',y',0) K(x,y,x',y') dx' dy', \quad (36)$$

where

$$K \equiv \frac{1}{2\pi} \frac{\partial}{\partial z} \left(\frac{\exp(ikr)}{r} \right) \quad (37)$$

is a propagator and $r = \sqrt{(x-x')^2+(y-y')^2+z^2}$. Evaluation of the derivative gives

$$K = \frac{1}{2\pi} \frac{z}{r} \left(\frac{ik}{r} - \frac{1}{r^2} \right) \exp(ikr). \quad (38)$$

For a pinhole aperture, $U^{(i)} \equiv \delta(x-x',y-y',z)$, and the wave field $U(x,y,z)$ takes the form of the propagator, Eq. (38). In general, the pinhole aperture does not produce spherical waves. However, when the observation point is such that $r \gg \lambda_0$, the first term inside the parentheses dominates the second, giving

$$K \approx \frac{ikz}{2\pi r^2} \exp(ikr). \quad (39)$$

It can now be seen that Eq. (7), which resulted from factoring out a common term of $\exp(ikr)/r$ from the simplified three-spherical-source wave field [Eq. (6)], also results from instead factoring out a common term of $ikz \exp(ikr)/2\pi r^2$ from a superposition of three "illuminated pinhole" waves of the form in Eq. (39). Similarly, when one is both in the far field and close to the z axis, $z \approx r$, so Eq. (39) reduces to a spherical wave function with a constant multiplier, as asserted.

We conclude that the analysis of the preceding sections may be mapped onto the case of a Young's three-pinhole interferometer in the far field. The nodal planes of the two-pinhole Young's experiment, which are unstable with respect to perturbations, therefore decay into a nodal-line network of vortex cores when the third pinhole is added.

J. Three-dimensional nodal-line structure

As previously mentioned, our far-field analysis implies the nodal lines—produced by either the superposition of three spherical waves or by coherent illumination of a Young's three-pinhole interferometer—to be asymptotically straight [see Eqs. (13) and (17)]. When one is not in the far field, the nodal lines are curved. Here, we examine this point in more detail by presenting simulations of the 3D structure of nodal lines for both the spherical waves and the pinhole interferometer wave functions [Eqs. (3) and (38)].

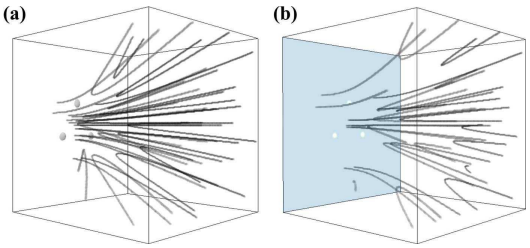

FIG. 10. (Color online) Numerical simulations of nodal line structures developed by three sources arranged symmetrically at the corners of an equilateral triangle of side length $r_2=r_3=3\lambda_0$ [cf. Figs. 6(c) and 6(d)]. The region shown is $z=0-5\lambda_0$ for a source wavelength of $\lambda_0=\pi$. (a) Three spherical wave sources. (b) Three pinholes.

With reference to Fig. 10, the nodal-line structures are shown within a volume close to the sources and not corresponding to the far field. Here, the relative phases of the three sources have been set to zero. The contrast between the simulations, resulting from the differing forms of the source waves, is strikingly apparent. Comparing the positions of the nodal lines between the two figures as they intersect the volume face at $z_0=5\lambda_0$, both are asymptotically approaching the same set of straight lines predicted for the far field (Sec. III C). In the case of spherical sources [Fig. 10(a)], the simulation is over the positive z half-space, on the implicit understanding that the nodal structure is mirror symmetric about the virtual plane in which the sources lie. In this case, nodal lines are of two general types: those that pass through the virtual plane and those that approach the source plane and without reaching it retreat again. The latter features, commonly known as "hairpins", correspond to annihilating vortex-antivortex pairs when observed in any plane which is a tangent to the associated nodal line [40] and are well known to exist in fields near focal points [41]. For the case of pinholes [Fig. 10(b)], nodal lines either attach to the source plane or contain a hairpin structure.

Regions devoid of nodal structure arise close to the source plane and near a source, where the intensity from that source dominates the contributions from the others. This may be understood in terms of the phasor diagram in Fig. 4(a) as an inability to form a closed triangle. Nodal lines approaching these regions join in hairpins.

In summary, the 3D nodal-line simulations reveal both the asymptotic behavior toward the analytically described far-field structure and, in regions close to the sources, display a structure of nodal lines distinguished by the different source descriptions of spherical sources and pinholes.

IV. CONCLUSION

A network of phase vortices was seen to be generated by the superposition of three stationary-state sources of outgo-

ing complex spherical waves. We presented an analysis of the structure of the associated vortex cores (nodal lines) in the far-field regime. A finite number of vortices was seen to be generated. Determination of the number of such vortices was mapped onto the problem of determining how many points, on a two-dimensional square lattice, lie within a given ellipse. The equation of the ellipse depends in a known way on the geometry of the sources. The parameter-space description also gives some insight into the effects of varying both the arrangement of the three sources and their relative phase. Indeed, phase variation of two of the sources provides a means for precisely positioning one or several vortex cores. We showed how to map all of the preceding analyses onto the problem of determining the far-field disturbance that results when a three-pinhole Young's interferometer is coherently illuminated. Last, we relaxed the far-field approximation to study numerically the curved nodal lines which arise when one is not in the far field. In contrast to the classical two-pinhole Young's interferometer, in which the resulting diffracted field vanishes over a series of nodal planes, the three-pinhole interferometer yields a quite different phase topology, permeated with a rich structure of nodal lines that thread vortex cores.

ACKNOWLEDGMENTS

The authors thank M.J. Morgan and R.A. Bartnik for their fruitful insights related to this work. G.R. is supported by an Australian Postgraduate Award. D.M.P. acknowledges support from the Australian Research Council.

[1] P. A. M. Dirac, Proc. R. Soc. London, Ser. A **133**, 60 (1931).
[2] A. Messiah, *Quantum Mechanics* (North-Holland, Amsterdam, 1961), Vol. I, Chap. 11, pp. 412–420.
[3] A. A. Abrikosov, Sov. Phys. JETP **5**, 1174 (1957).
[4] D. R. Tilley and J. Tilley, *Superfluidity and Superconductivity*, 3rd ed. (Institute of Physics, Bristol, 1990).
[5] R. P. Feynman, Prog. Low Temp. Phys. **1**, 17 (1955).
[6] L. M. Pismen, *Vortices in Nonlinear Fields: From Liquid Crystals to Superfluids, From Non-Equilibrium Patterns to Cosmic Strings* (Oxford University Press, Oxford, 1999).
[7] L. Pitaevskii and S. Stringari, *Bose-Einstein Condensation* (Oxford University Press, Oxford, 2003).
[8] A. S. Desyatnikov, L. Torner, and Y. S. Kivshar, in *Progress in Optics*, edited by E. Wolf (Elsevier, Amsterdam, 2005), Vol. 47, Chap. 5, pp. 291–391.
[9] L. J. Allen, H. M. L. Faulkner, M. P. Oxley, and D. Paganin, Ultramicroscopy **88**, 85 (2001).
[10] M. V. Berry, J. Phys. A **11**, 27 (1978).
[11] I. Freund, N. Shvartsman, and V. Freilikher, Opt. Commun. **101**, 247 (1993).
[12] J. Riess, Phys. Rev. D **2**, 647 (1970).
[13] J. F. Nye and M. V. Berry, Proc. R. Soc. London, Ser. A **336**, 165 (1974).
[14] J. O. Hirschfelder, C. J. Goebel, and L. W. Bruch, J. Chem. Phys. **61**, 5456 (1974).
[15] J. F. Nye, *Natural Focusing and Fine Structure of Light: Caustics and Wave Dislocations* (Institute of Physics, Bristol, 1999).
[16] N. Heckenberg, R. McDuff, C. Smith, H. Rubinsztein-Dunlop, and M. Wegener, Opt. Quantum Electron. **24**, 951 (1992).
[17] N. Heckenberg, R. McDuff, C. Smith, and A. White, Opt. Lett. **17**, 221 (1992).
[18] H. He, M. E. J. Friese, N. R. Heckenberg, and H. Rubinsztein-Dunlop, Phys. Rev. Lett. **75**, 826 (1995).
[19] A. G. Peele and K. A. Nugent, Opt. Express **11**, 2315 (2003).
[20] M. Okamoto and H. Sasada, Jpn. J. Appl. Phys., Part 1 **44**, 1743 (2005).
[21] V. V. Kotlyar, S. N. Khonina, A. A. Kovalev, V. A. Soifer, H. Elfstrom, and J. Turunen, Opt. Lett. **31**, 1597 (2006).
[22] G.-H. Kim, J.-H. Jeon, K.-H. Ko, H.-J. Moon, J.-H. Lee, and J.-S. Chang, Appl. Opt. **36**, 8614 (1997).
[23] J. E. Curtis and D. G. Grier, Opt. Lett. **28**, 872 (2003).
[24] K. Kishima, N. Yoshida, K. Osato, and N. Nakagawa, Appl. Opt. **45**, 3489 (2006).
[25] A. Boivin, J. Dow, and E. Wolf, J. Opt. Soc. Am. **57**, 1171 (1967).
[26] K. W. Nicholls and J. F. Nye, J. Phys. A **20**, 4673 (1987).
[27] J. Masajada and B. Dubik, Opt. Commun. **198**, 21 (2001).
[28] K. O'Holleran, M. J. Padgett, and M. R. Dennis, Opt. Express **14**, 3039 (2006).
[29] J. Leach, M. R. Dennis, J. Courtial, and M. J. Padgett, Nature (London) **432**, 165 (2004).
[30] W. M. Lee, V. Garcés-Chávez, and K. Dholakia, Opt. Express **14**, 7436 (2006).
[31] D. R. Scherer, C. N. Weiler, T. W. Neely, and B. P. Anderson, Phys. Rev. Lett. **98**, 110402 (2007).
[32] M. V. Berry and M. R. Dennis, Proc. R. Soc. London, Ser. A **457**, 2251 (2001).
[33] M. De Graef, *Introduction to Conventional Transmission Electron Microscopy* (Cambridge University Press, Cambridge, England, 2003).
[34] D. M. Paganin, *Coherent X-Ray Optics* (Oxford University Press, Oxford, 2006).
[35] A. Messiah, *Quantum Mechanics* (North-Holland, Amsterdam, 1961), Vol. II, Chap. 19, p. 811.
[36] C. G. Gibson, *Elementary Euclidean Geometry: An Introduction* (Cambridge University Press, Cambridge, England, 2003).
[37] D. Gabor, Rep. Prog. Phys. **32**, 395 (1969).
[38] G. E. Andrews, *Number Theory* (Dover, New York, 1994).
[39] M. Born and E. Wolf, *Principles of Optics*, 7th ed. (Cambridge University Press, Cambridge, England, 2003).
[40] M. V. Berry, in *Proceedings of the International Conference on Singular Optics*, edited by M. S. Soskin (SPIE, Partenit, Ukraine, 1998), Vol. 3487, pp. 1–5.
[41] M. V. Berry, J. F. Nye, and F. J. Wright, Philos. Trans. R. Soc. London, Ser. A **291**, 453 (1979).

PHYSICAL REVIEW E **76**, 029901(E) (2007)

Erratum: Phase vortices from a Young's three-pinhole interferometer [Phys. Rev. E 75, 066613 (2007)]

Gary Ruben and David M. Paganin

(Received 20 July 2007; published 2 August 2007)

DOI: 10.1103/PhysRevE.76.029901 PACS number(s): 42.25.Hz, 03.65.Vf, 07.60.Ly, 99.10.Cd

It is incorrectly stated that domain walls (nodal planes) are produced in the complex scalar wave field of the uniformly illuminated two-pinhole Young's interferometer. This statement is made in the last paragraph on p. 6, and again in the final sentence of the Conclusion. If a paraxial approximation is made to the diverging wave functions emanating from each pinhole, domain walls may be produced in the resulting wave field expression. However, in the physical system considered in the present paper, and without stating this qualification, true domain walls are not produced. The remaining conclusions of the paper are unaffected by this minor correction.

We thank Ari T. Friberg for alerting us to this error.

Phase Vortices from the Interference of Three Spherical Waves

Gary Ruben and David M. Paganin
School of Physics, Monash University, Victoria 3800, Australia
gary.ruben@sci.monash.edu.au

Abstract: We study the phase vortices arising from the interference of three complex spherical waves. Expressions are developed for vortex positions in the far field, as a function of source arrangement.

OCIS codes: (260.3160) Interference; (270.1670) Coherent optical effects; (350.7420) Waves; (999.9999) Optical vortices

1. Introduction

Phase vortices exist in a variety of linear and non-linear physical systems that may be described using complex fields, including the angular-momentum eigenstates of the hydrogen atom, the Meissner state of type-II superconductors, vortex states of superfluids and Bose–Einstein condensates, optical vortex solitons, electron wavefunctions diffracting through crystalline slabs, Gaussian random wavefields and optical speckle fields (see, e.g., [1,2]).

We restrict ourselves to continuous complex scalar fields, where vortical behavior manifests itself as screw-type dislocations in the field's multi-valued surfaces of constant phase [3,4]. Vortices arise naturally in almost all fields of this type when there are interfering plane wave components [4,5]. Masajada and Dubik [6] showed that three plane waves is the minimum requirement to produce a vortex lattice by means of direct interference of the constituent waves, and applied phasor analysis to describing this lattice. We have taken an analogous approach – analyzing vortices arising from the interference of three spherical waves, generated by three distinct monochromatic equal-energy point sources. We develop a description of the vortex positions in the far field and see that, in contrast with the case of plane waves, in which an infinitely-extended vortex lattice is generated, the spherical sources generate a finite number of phase vortices. Analytical expressions for the vortex core locations, as a function of source arrangement, are presented and a representation in terms of a discrete parameter space arises, allowing estimates of the number of vortices and a description of a natural coordinate system in terms of a family of hyperbolas.

A more comprehensive account of this work is presented in [7].

2. Summary of results

Consider three spherical sources of unit amplitude and equal wavenumber *k*, located at coordinates $\mathbf{r}_1 \equiv \vec{0}, \mathbf{r}_2, \mathbf{r}_3$ [Fig. 1(a)]. We express the wavefield $\Psi(\mathbf{r})$ as a function of position $\mathbf{r}$ over the plane $z = z_0$.

$$\Psi(\mathbf{r}) = \sum_{j=1}^{3} \frac{1}{|\mathbf{r} - \mathbf{r}_j|} \exp\left[i\left(k|\mathbf{r} - \mathbf{r}_j| + \phi_j\right)\right], \tag{1}$$

where ϕ_j is the relative phase of the *j*th source and $|\mathbf{r} - \mathbf{r}_j| \equiv \sqrt{(x - x_j)^2 + (y - y_j)^2 + z^2}$.

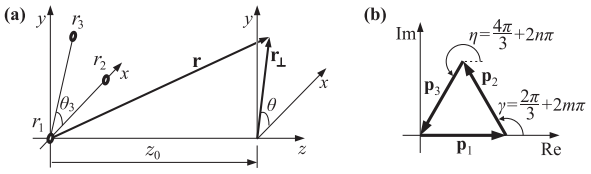

Fig. 1. (a) Coordinate system. (b) Phasor construction of three interfering waves.

At any point coinciding with a vortex core, the phasors $\mathbf{p}_1, \mathbf{p}_2, \mathbf{p}_3$, corresponding to the three waves, must sum to zero [Fig. 1(b)]. To determine the conditions giving rise to vortices, Eq. (1) is therefore equated to zero, with

simplifications such as $|\mathbf{r}-\mathbf{r}_j| \approx |\mathbf{r}| - (\mathbf{r}_\perp \cdot \mathbf{r}_j)/|\mathbf{r}|$ corresponding to the far-field regime being made. As a result, vortex positions are described in polar coordinates $(r_\perp, \theta)$ [Fig. 1(a)] by

$$r_\perp = \frac{\pm z_0}{\sqrt{\dfrac{(3kr_2/M(m))^2}{1+\dfrac{1}{\sin^2\theta_3}\left(\dfrac{r_2}{r_3}\dfrac{N(n)}{M(m)}-\cos\theta_3\right)^2}-1}}, \quad \theta = \arctan\left[\frac{1}{\sin\theta_3}\left(\frac{r_2}{r_3}\frac{N(n)}{M(m)}-\cos\theta_3\right)\right], \tag{2}$$

where $r_2 \equiv |\mathbf{r}_2|, r_3 \equiv |\mathbf{r}_3|$, θ_3 is the angle between $\mathbf{r}_2$ and $\mathbf{r}_3$, m and n are integers arising from angular periodicity of the phasors [Fig. 1(b)], $M(m) = 2(1+3m)\pi - 3\phi_2$, and $N(n) = 2(2+3n)\pi - 3\phi_3$.

For real solutions, the argument of the square root in Eq. (2) must be positive, imposing a condition on the allowable (m, n) values for a given source arrangement. This condition corresponds to permitting only those values which lie in the interior of a related ellipse in the 2D parameter space formed by the (m, n) coordinates. Changes in source arrangement correspond to different parameter-space ellipses, examples of which are shown in Fig. 2(d). Translations of the lattice points along each axis correspond to independent source phase variations. Lines of constant m or n map to hyperbolas lying in the z_0 plane. Thus, vortices indexed by particular (m, n) values lie at the intersection of two of these hyperbolas (not shown). This knowledge provides a means for precisely positioning one or several vortex cores by control of the source phases.

The area A of the ellipse, corresponding to an estimate of the number of enclosed points, gives an estimate of the number of vortices n_v:

$$n_v \approx \frac{k^2}{2\pi}|r_2 r_3 \sin\theta_3| = \frac{k^2 A}{\pi}. \tag{3}$$

Fig. 2 presents a visual summary of the correspondence between simulated wavefields, predicted vortex locations and the parameter space description.

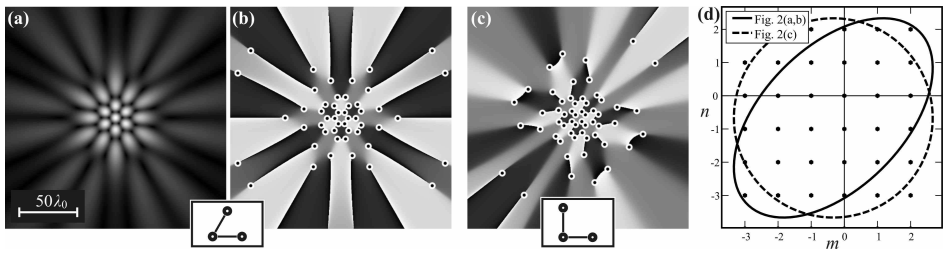

Fig. 2. Observed amplitude and phase observed in the plane $z_0 = 25\pi$ and overlaid with vortex cores given by Eq. (2). A spherical background has been subtracted from the phase maps. (a) Amplitude and (b) associated phase for sources arranged in an equilateral triangle (small glyph at bottom of figure). (c) Phase for sources arranged at three corners of a square. (d) Corresponding parameter space ellipses.

In contrast to the case of two spherical sources, exemplified by the two-pinhole Young's interferometer, in which the resulting field vanishes over a series of nodal planes, interference from three spherical sources yields a quite different phase topology, permeated with a rich structure of nodal lines that thread vortex cores.

3. References

[1] D. M. Paganin, *Coherent X-Ray Optics*, (Oxford University Press, Oxford, 2006), Chap. 5.
[2] A. S. Desyatnikov, L. Torner, and Y. S. Kivshar, in *Progress in Optics*, edited by E. Wolf (Elsevier B. V., Amsterdam, 2005), vol. 47, chap. 5, pp. 291–391.
[3] J. Riess, "Nodal Structure, Nodal Flux Fields, and Flux Quantization in Stationary Quantum States," Phys. Rev. D 2, 647 (1970).
[4] J. F. Nye and M. V. Berry, "Dislocations in Wave Trains," Proc. R. Soc. London, A 336, 165 (1974).
[5] K. W. Nicholls and J. F. Nye, "Three-beam model for studying dislocations in wave pulses," J. Phys. A: Math. Gen. 20, 4673 (1987).
[6] J. Masajada and B. Dubik, "Optical vortex generation by three plane wave interference," Opt. Commun. 198, 21 (2001).
[7] G. Ruben and D. M. Paganin, "Phase vortices from a Young's three-pinhole interferometer", arXiv:quant-ph/0612148v1.
* We acknowledge M. J. Morgan for helpful discussions and insights related to this work. G.R. is supported by an Australian Postgraduate Award. D.M.P. acknowledges support from the Australian Research Council.

PHYSICAL REVIEW A **78**, 013631 (2008)

Vortex-lattice formation and melting in a nonrotating Bose-Einstein condensate

Gary Ruben,* David M. Paganin, and Michael J. Morgan
School of Physics, Monash University, Clayton, Victoria 3800, Australia
(Received 2 January 2008; published 24 July 2008)

Numerical simulations of the interference of a three-way segmented nonrotating Bose-Einstein condensate reveal the production of a honeycomb vortex lattice containing significant numbers of vortices and antivortices. If confined within a trap, the lattice subsequently melts, exhibiting a rich assortment of vortex-antivortex interactions. In contrast with nonlinear vortex production mechanisms previously described for Bose-Einstein condensates, the process here is shown to be primarily one of linear superposition, with initial vortex locations approximately described by a linear theory of wave packet interference.

DOI: 10.1103/PhysRevA.78.013631 PACS number(s): 03.75.Lm, 03.75.Dg, 03.75.Kk

I. INTRODUCTION

The production of vortices has attracted great interest in the study of Bose-Einstein condensates (BECs) (see, e.g., [1–4]). Typically, production has been through bulk rotation of the condensate cloud, such as with a "laser spoon," or by laser phase imprinting. These rotating systems form an Abrikosov lattice [5] of vortices with hexagonal symmetry. In contrast with the rotating BEC, in which the number of vortices is governed by the net angular momentum of the system, the nonrotating BEC can also give rise to vortices due to the reconciliation of initial random phase variations via the Kibble-Zurek mechanism [6].

Interference of two nonrotating BEC pieces with a repulsive nonlinearity has also been shown to give rise to vortices [7]. In this system, analogous to the Young's two-pinhole interferometer, the interference fringes—also known as dark stripe solitons—decay via a "snake instability" into a string of vortices [7–9]. This vortex formation mechanism relies on the nonlinearity of the BEC self-interaction.

Recently, Scherer *et al.* [10] performed an experiment in which vortices were observed as a result of the interference of a three-way segmented BEC. An oblate spheroidal BEC was formed in an asymmetric trap partitioned into three regions by shining a laser light sheet on the condensate (see Fig. 1).The partition walls were then removed at varying rates and vortices were sought after different elapsed times, during which the three pieces were allowed to expand and interfere. Both two- and three-dimensional numerical simulations of this experiment have also been performed by Carretero-González *et al.* [11].

In this paper, we demonstrate with numerical simulations that vortices are produced by a three-segment BEC devoid of initial phase variations and show that this mechanism is, in contrast with the two-piece case, predicted by a linear theory, the development of which is related to previous work on the three-pinhole Young's interferometer [12]. In contrast with Carretero-González *et al.* [11], we have not sought to replicate the aforementioned experiment exactly. By instead focusing attention on those initial states characterized by a constant phase, we aim to demonstrate that initial phase variations are unnecessary for vortex formation. In addition, we demonstrate interference and vortex production in the absence of a confining transverse trap, thereby reducing the requirement for the nonlinear processes at play in two-fragment condensate interference, and providing deeper insight into the argument that the vortex generation mechanism for three symmetrically arranged, well-separated, pieces is, by contrast, primarily a linear process.

By increasing the intensity of the light sheet, we have also been able to generate a lattice comprised of significant numbers of vortices and antivortices. In the trapped system, the regular vortex-antivortex lattice subsequently melts, exhibiting a diversity of interactions by, for example, self-propelling vortex-antivortex dipoles (VDs) [11,13–18], and rotating vortex tripoles and quadrupoles [15,17]. These interactions between vortices and vortex clusters in the condensate include dipole scattering and annihilation events. The large vortex population produced in the trapped system makes it an excellent environment for the study of vortex dynamics, VDs, and vortex-sound interactions [1].

The remainder of this paper is structured as follows. We describe the production of vortices via the phasor approach in Sec. II. In Sec. III we describe the numerical BEC model, focusing on the time-dependent and ground state models, the reduction from three to two dimensions, and a vorticity metric for the order parameter field. We present the simulation results in Sec. IV, highlighting the effects of light-sheet intensity, different light-sheet geometries, and phase variation between the condensate pieces in the trapped and untrapped cases, while making connections to the linear theory. We

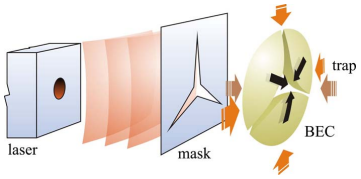

FIG. 1. (Color online) A laser-illuminated mask separates a pancake-shaped BEC, formed in an asymmetric trap, into three pieces. Upon removal of the illumination—and optionally the trap—the pieces interfere, forming a lattice of vortices and antivortices.

*Electronic address: gary.ruben@sci.monash.edu.au

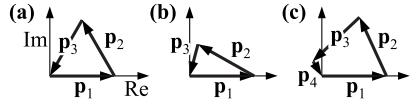

FIG. 2. Representing the sources with a phasor diagram, vortices lie at locations corresponding to a closed loop of phasors. (a) Three sources linearly superposed. (b) Two sources and a nonlinear interaction term. (c) Four sources linearly superposed or three sources plus a nonlinear interaction term.

provide a visualization of the lattice formation and melting, and in Sec. V, describe the rich vortex-antivortex dynamics that arise after the lattice has melted. Finally, we summarize our findings in Sec. VI.

II. PHASOR DESCRIPTION OF VORTEX PRODUCTION

In weakly nonlinear systems, typical of experimentally realistic BEC systems, we expect to observe phenomena approximately predicted by the linear theory. The creation of a vortex-antivortex lattice is one such observation, whose geometry is described in the Appendix. We include this short section to explain the production of vortices by linear interference, from which the lattice is formed.

In order to form vortices by a linear interference process, at least three source waves are required [19]. This may be understood with reference to the phasor diagram Fig. 2(a) in which each phasor represents a source wave. The probability amplitude is zero at a vortex core, corresponding to a closed loop comprised in general of three or more phasors. Although two phasors may sum to zero, such a case corresponds to a domain-wall defect rather than a vortex. Vortex formation from linear superposition of higher numbers of sources has also been demonstrated [20], corresponding to a loop of four or more phasors.

In the following, the individual terms of a sum of complex scalar waves $\Psi_1+\Psi_2+\cdots$ are represented graphically as phasors $\mathbf{p}_1+\mathbf{p}_2+\cdots$ in Fig. 2. Figure 2(a) is a representation of the linear interference of three sources $\Psi_1+\Psi_2+\Psi_3$ evaluated at the vortex location. Alternatively, Fig. 2(b) represents a nonlinear system in which the third contribution is now associated with the interaction term in the sum $\Psi_1+\Psi_2+\mathrm{f}(\Psi_1,\Psi_2)$. The production of vortices by the snake instability might be represented by the latter picture. Thus, a loop of n phasors may correspond either to the interference of n sources in a linear system, or to $n-1$ sources plus a nonlinear interaction term. For example, Fig. 2(c) may represent either four sources $\Psi_1+\Psi_2+\Psi_3+\Psi_4$ in the case of a linear system, or three sources plus a nonlinear interaction term $\Psi_1+\Psi_2+\Psi_3+\mathrm{f}(\Psi_1,\Psi_2,\Psi_3)$ in the case of a nonlinear system.

Recently, the results of the interference of two-dimensional (2D) condensates sliced into two and four pieces have been studied [21]. Examination of these results for the case of four pieces suggests that sufficient contributions from at least three of the four source pieces have combined in the manner just described, which we refer to as a primarily linear process. For the system we study in this paper, we present further evidence for the role of the linear interference mechanism in Sec. IV.

III. NUMERICAL MODEL

In this section we describe the derivation and parameters of our numerical model for the interference of a three-way segmented nonrotating BEC. We model an experiment similar to that conducted by Scherer *et al.* [10].

We note the following features that distinguish our simulation from the experiment and its modeling by Carretero-González *et al.* [11]. First, in establishing the initial condition prior to time evolution we obtain the ground state with a uniform global phase, so that no initial phase variation is allowed within or between the three pieces, in order to demonstrate vortex production as predicted by the linear theory. In contrast, Carretero-González *et al.* [11] apply phase variations within their numerical scheme to obtain their initial condition. Although we subsequently also apply an example of different relative phases to the three pieces following establishment of the ground state, this is presented to demonstrate how the linear theory applies to this case. The second distinguishing feature is the instantaneous removal of the light sheet at $t=0$. In contrast, Scherer *et al.*[10] remove the light sheet at varying finite rates, but report a maximum efficiency of vortex generation for the maximum observable rate of removal. Third, we exclusively model the system in 2D. As such, our simulation results are most pertinent to pancake-shaped condensate clouds, in which the ratio of the axial to transverse trap frequencies is large in the sense outlined below. Because nonpancake condensates admit the existence of vortex lines with more complex geometries, investigation of these systems would have to be performed separately to assess the applicability of the results reported here. A final difference is that we present simulations with and without the transverse trap to demonstrate that lack of transverse confinement is not an impediment to vortex production, consistent with predictions from the linear theory.

The production of vortices in pancake-shaped condensates may be numerically modeled in two rather than three spatial dimensions. In this case the evolution of the macroscopic wave function or order parameter Ψ of the BEC is considered to be governed by the Gross-Pitaevskii equation (GPE) in (2+1)D,

$$i\hbar\partial_t\Psi = \left[-\frac{\hbar^2}{2m}\nabla_\perp^2 + V(r,\theta) + \gamma N U_0|\Psi|^2\right]\Psi, \qquad (1)$$

where we have adopted plane-polar coordinates for space (r,θ) and t denotes time. The GPE takes the form of the (2+1)D time-dependent Schrödinger equation with an additional nonlinear self-interaction term $\gamma N U_0|\Psi|^2\Psi$ for a condensate containing N atoms, each of mass m. Here $U_0=4\pi\hbar^2 a/m$ depends on the s-wave scattering length a, which in this case is positive in order to permit the BEC pieces to expand and interfere. The multiplication factor γ arises as a result of reduction from the full 3D description to 2D in the manner described below. In this form of the GPE, the normalization condition is $2\pi\int_0^\infty|\Psi(r,\theta)|^2 r\,dr=1$ (see, e.g., [22–24]).

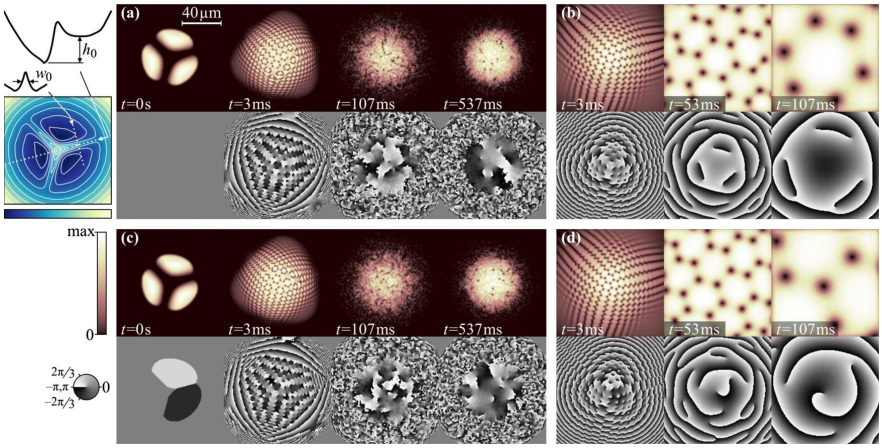

FIG. 3. (Color online) Amplitude (upper) and associated phase plots (lower) for the ground-state trap potential shown as a contour plot at left, which is a 2D harmonic trap with a superposed three-way light sheet of dimensionless amplitude $I_0=0.8$. The trap profiles identifying wall height h_0 and width w_0 are taken along the dotted paths. (a) Three-segment BEC interference with a harmonic confining trap showing progression from the ground state, through lattice formation to a late stage characterized by complex vortex-antivortex (VA) dynamics. (b) Honeycomb lattice formation and free expansion in the absence of a confining trap. (c),(d) The initial piece phases are rotated to 0, $2\pi/3$, and $-2\pi/3$. The effect is to shift the lattice so that an antivortex coincides with the trap center.

The axial dimension of the BEC is determined by the axial trap component $m\omega_z^2 z^2/2$, whose angular frequency ω_z provides a characteristic length $a_z=[\hbar/(m\omega_z)]^{1/2}$. When a_z is much greater than the scattering length a, the multiplication factor γ may be found by separating the 3D order parameter into a product of independent axial and transverse components $\Psi_{3D}(r,\theta,z)\approx\Phi_0(z)\Psi(r,\theta)$ and evaluating the expectation value of the transverse component $\Psi(r,\theta)$ along the axial direction z [23,25]. The axial condensate profile is assumed to be the well-known ground-state solution $\Phi_0(z)=(\pi a_z^2)^{-1/4}\exp[-z^2/(2a_z^2)]$ to the 1D time-independent Schrödinger equation. The 2D Laplacian operator arises from separation of the full 3D Laplacian into its transverse and axial components, $\nabla^2\equiv\nabla_\perp^2+\partial_z^2$. The final result is a (2+1)D GPE with a nonlinear multiplication factor $\gamma=[m\omega_z/(2\pi\hbar)]^{1/2}$ that represents the averaged value of the 3D nonlinear factor over all z. An alternative approach, and that presented here, is to directly evaluate the nonlinearity occurring at $z=0$, corresponding to the location of the peak density of the axial profile, and assign this value to γ. Since the nonlinearity achieves a maximum in this plane, it arguably represents a good choice for modeling the vortex dynamics. In this case $\gamma=|\Phi_0(0)|^2=[m\omega_z/(\pi\hbar)]^{1/2}$. We have performed simulations with both approaches and find no qualitative difference with any of the effects reported here. The reader preferring the former approach may note that the factor of $\sqrt{2}$ by which the γ factors differ may be absorbed as a change in the number of condensate atoms N.

The BEC ground state is determined in the presence of a trapping potential $V(r,\theta)$ formed from the combination of a harmonic trap and light-sheet potential $V(r,\theta)=m\omega^2r^2/2+L(r,\theta)$, where ω is the angular frequency of the radial trap component. By assuming that the light sheet $L(r,\theta)$ is instantaneously removed at $t=0$, the light-sheet potential term appears only in the time-independent GPE used to determine the ground state. The harmonic trap term is included in the time-dependent GPE for the trapped condensate simulations, but it is removed for the untrapped simulations. The parameter values used in our simulations were $a=5.77\times10^{-9}$m for ^{87}Rb [2], $N=2.6\times10^5$, $\omega=46.5$ rad s^{-1}, and $\omega_z=88.6$ rad s^{-1}.

We define a vorticity metric for the order parameter field Ψ according to

$$(\text{vorticity})=\frac{1}{V}\int\int|\nabla\times\mathbf{j}|dx\,dy, \tag{2}$$

where the integral represents integration over the numerical field of volume V, and $\mathbf{j}$ is the probability current $\mathbf{j}\equiv(\Psi^*\nabla\Psi-\Psi\nabla\Psi^*)\hbar/(2m)$.

This metric is similar to the usual vorticity measure in fluids, $\boldsymbol{\omega}=\nabla\times\mathbf{v}$, of the velocity field $\mathbf{v}=\mathbf{j}/\rho$ where $\rho=|\Psi|^2$ is the local probability density. By not dividing the probability current by ρ, extra weighting is conferred upon vortices located within a locally increased density over vortices in regions of lower density. The metric sums the modulus of the local measure over the whole field.

IV. RESULTS

In Fig. 3 we present simulation snapshots for the segmented BEC showing the initial state, the vortex-antivortex lattice that forms after the three pieces have interfered, and later stages that, in the trapped cases, follow the disintegration of the lattice. For corresponding movies, see [26]. The intensity of the laser light sheet relative to the trap is repre-

sented by a dimensionless quantity I_0, where the trap potential contour plots (shown to the left of the time series) indicate the magnitude relative to the trap. We have chosen to present results for $I_0=0.3$ and 0.8, as these values allow exposition of the different behaviors of poorly and well-separated BEC pieces, respectively. The walls are characterized, as shown in the trap profile plots, by wall height h_0, expressed in units of energy, and full width at half maximum w_0. $I_0=0.3$ and 0.8 correspond to $h_0 \approx k_B \times 70$ and $k_B \times 180$ nK, respectively; both higher than the $k_B \times 26$ nK barrier produced by Scherer *et al.* [10]. Our wall width $w_0 \approx 9$ μm may be challenging to produce experimentally. A comparison value is not given in [10], although the condensate profiles are indicative of wider walls. The upper time series show the evolution of the BEC beginning from the global ground state. The probability density and phase are also shown in Fig. 3. The expansion and interference occur both within a confining harmonic trap [Figs. 3(a) and 3(c)] following instantaneous removal of the light sheet, and in the absence of a transverse confining trap [Figs. 3(b) and 3(d)]. In the latter case, the condensate would expand beyond a finite simulation region. To allow for this in the numerical model, a damping term is added to the time evolution equation to absorb the outward-propagating matter. Since these are 2D simulations, and as such are applicable to pancake-shaped condensates, experimental realization would most likely require maintenance of the axial trap component in both cases, not just to allow for establishment of the lattice, but also for any free-expansion stage prior to imaging.

Scherer *et al.* [10] observed vortices consistent with production by the Kibble-Zurek mechanism. They reported that 10% of nonsegmented condensates contain vortices. In our simulations, by starting from a ground state, no vortices may be produced by this mechanism.

Previous work [12] has shown that the linear interference of three expanding monochromatic spherical waves generates a distorted honeycomb vortex-antivortex (VA) lattice. In the Appendix, we present a related linear theory for the case of three Gaussian wave packets, evolving in (2+1)D, clarifying the effect of source phase variation on the predicted vortex locations. In this case, an infinite, regular, honeycomb VA lattice is formed, with a Gaussian probability density envelope. The formation of vortices by a three-piece BEC may be understood as arising from the same mechanism, albeit now in a highly nonlinear system. The linear theory applies most directly to the untrapped system. For observing interaction dynamics, the trap presence must be maintained. However, if the interference is instead performed with the transverse trap switched off, experimental measurement of the position of any central vortex with respect to the center and lattice parameter should allow determination of the phases of the initial BEC pieces to within a global phase factor. Figures 3(b) and 3(d) show the formation of an extremely regular lattice, which compares favorably with that formed by linear superposition shown in Fig. 4.

If the three BEC pieces are sufficiently isolated from each other, they may acquire random relative phases [27]. Scherer *et al.* [10] describe the presence or absence of a central vortex according to reconciliation of these phases. The linear theory instead describes an equivalent effect, which predicts

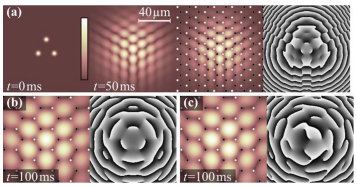

FIG. 4. (Color online) Three linearly superposed wave packets lying at the corners of an equilateral triangle [cf. Figs. 3(b) and 3(d)]. The amplitude, with analytically determined vortices (dark) and antivortices (light) overlaid [see Eqs. (A10) and (A11)], and phase of Eq. (A2) are shown. (a) Equal-phase wave packets shown at 0 ms, after interference at 50 ms (with and without the overlaid lattice), and (b) after 100 ms. (c) Phases 0, $2\pi/3$, and $-2\pi/3$ cause a lattice translation.

the presence of a central vortex as resulting from translation of the lattice as a whole. Röhrl *et al.* [27] state that the pieces are "virtually degenerate," allowing them to be treated as coherent pieces whose relative phases may vary randomly. For a lower-intensity light sheet, tunneling through the light-sheet walls ensures that the phases of the separate pieces remain coupled. The interference pattern is said to become "locked." In our case, the lattice translation becomes locked in an equivalent sense to give the result in Figs. 3(a) and 3(b). To simulate the effect of decoupling between the pieces, we apply global phase factors by rotating the phase of the BEC pieces, following establishment of the ground state but prior to time evolution.

In Figs. 3(c) and 3(d), the relative phases of two of the regions have been rotated from 0 to $2\pi/3$ and $-2\pi/3$, as shown in the $t=0$ s phase plot. The $t=53$ and 107 ms cases without a transverse trap show a vortex at the center. This may be understood by evaluating the predicted vortex locations using the linear theory. To illustrate this, Fig. 4 provides linear simulation results for the equal [Figs. 4(a) and 4(b)] and rotated [Fig. 4(c)] phase cases for the model described in the Appendix. For these examples, the source positions r_2 and r_3, and the momentum uncertainty Δp were determined by fitting Gaussian profiles to the leading (innermost) edges of the probability density of the three BEC pieces at $t=0$ for the $I_0=0.8$ case, i.e., from the first frame in Fig. 3(a). Because the model assumes that the BEC pieces are well described by circularly symmetric Gaussian pieces, which is not the case here, this approach was found to be better than fitting to the whole BEC pieces. However, because of this departure, illustrated by the poor match of the lattice scale to that of the nonlinear results, the linear model is best applied qualitatively. Although the nonlinear dynamics of the BEC do not allow the analytically predicted vortex locations to be mapped directly onto the nonlinear simulation results, the linear theory nevertheless provides useful predictions of the generation of the central vortex and the lattice symmetry.

If the phases are such that a vortex is created sufficiently close to the center of the trap, in the case where few other vortices are produced, such as when the wall heights are low [as in Figs. 5(a)–5(d)], the vortex may migrate to take up residence in the center of the trap. Figure 5(b) illustrates this

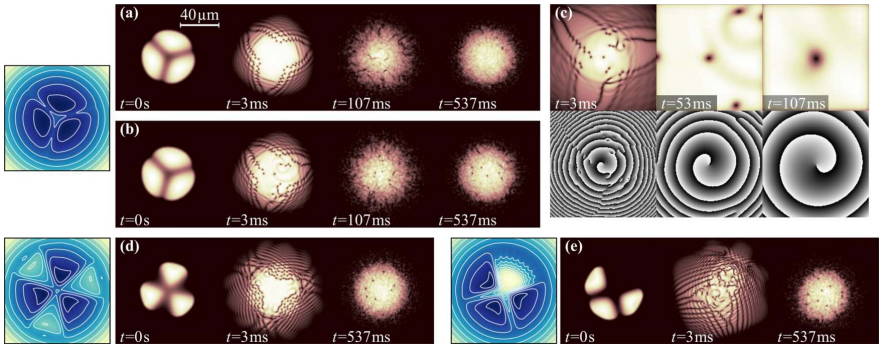

FIG. 5. (Color online) Amplitude [and associated phase plots for (c)] for light sheets characterized by the trapping potentials shown as adjacent contour plots. (a)–(c) When compared with Fig. 3, the lower-intensity light sheet (I_0=0.3) allows vortices to propagate outward with the condensate matter. In (a), the central region of the lattice is left devoid of vortices. In the trapped (b) and untrapped (c) cases—in which the relative phases of the initial pieces are set to 0, $2\pi/3$, and $-2\pi/3$—the central vortex is clearly visible. (d),(e) Two alternative arrangements with (d) propeller-shaped pieces, and (e) pieces at three corners of a square, discussed in the main text.

behavior. Since flows associated with phase gradients cancel there, any resident vortex occupies a privileged position and is allowed to remain there until perturbed by a local change, such as might be caused by a passing vortex set in motion following melting of the lattice.

The vorticity metric is plotted against time for four different initial conditions in Fig. 6(a). Figures 6(b) and 6(c) are time-series plots of the vortices in the side-on condensate slices. In these figures, period (i) denotes the initial formation of the regular vortex-antivortex lattice. In the subsequent period (ii), the regular lattice melts, as the condensate matter washes back toward the center due to confinement by the harmonic trap. During this period, the high population of vortices and antivortices promotes a high interaction rate characterized by a rich variety of vortex interaction dynamics. VA annihilation reduces the vortex population to a level where this rate slows and dynamics involving VDs begin to dominate in the final period (iii). The washing in and out is roughly circularly symmetric, cyclically increasing and decreasing the probability density in the center. These global oscillations are visible in Fig. 6(a) due to the vorticity measure giving extra weight to vortices embedded in a locally increased condensate probability density. The predicted frequency of the radial breathing mode of a harmonically trapped 2D condensate is twice the trap frequency ω [28] (in our simulations ω=46.5 rad s^{-1}). The measured frequency from the lower three plot series, whose condensates have centroids coinciding with the trap center, is 93.6 ± 0.6 rad s^{-1}, in agreement with theory. From Figs. 6(b) and 6(c) we see that the vortices themselves are carried in and out by the bulk motion of the condensate matter, presumably changing the vortex interaction rate in turn. The interaction dynamics are discussed in more detail in Sec. V.

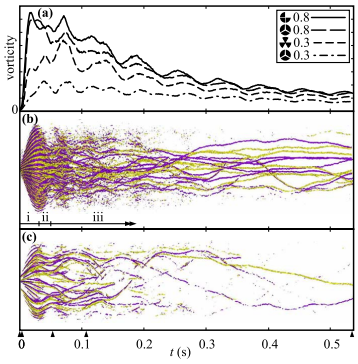

FIG. 6. (Color online) Vorticity plots for selected BEC segmentation schemes with a harmonic trap. Small arrows along the time axis correspond to the times selected in Figs. 3 and 5. (a) Vorticity measure [Eq. (2)] for I_0=0.3 and 0.8 and for sources at three corners of an equilateral triangle, a square, and a propeller-shaped scheme (see main text). (b) Vortices (dark) and antivortices (light) generated from the equilateral triangle scheme with I_0=0.8. Regions (i), (ii), and (iii) are described in the main text. (c) Fewer vortices are produced with a lower-intensity I_0=0.3 light sheet.

A lower wall height results in the pieces starting closer together. In the linear theory in [12], correspondingly smaller r values generate smaller numbers of vortices. This is clearly illustrated by the smaller vorticity values in Fig. 6(a) and the reduced population of vortices in Fig. 6(c) over Fig. 6(b). In Figs. 5(a) and 5(b), we see that the matter expanding from the center carries most of the vortices to the outer parts of the trap as the lattice is forming, where they may be lost altogether, further reducing the vortex population.

The propeller shape in Fig. 5(d) is included to show an alternative mask, which also produces BEC pieces at 120° angles to each other, but which pushes the centers of the condensate pieces further apart. Accordingly, higher numbers of vortices are predicted by the BEC created from this mask. Indeed, this is the case, as can be seen by comparing the bottom two results in Fig. 6(a), which plot vorticity for the same light sheet intensity I_0=0.3 for the two 120° alternatives.

In the linear theory in [12], the maximum number of vortices is predicted for a source arrangement in which the

pieces are initially arranged at three corners of a square. This prediction guided investigation of a new source configuration, shown in Fig. 5(e), which may be realized by a cross-shaped light-sheet mask with one quadrant open to the passage of light from the illuminating laser. Confirmation of the prediction is apparent by comparing the top two results in Fig. 6(a), which are for the same light-sheet intensity. In fact, the spacing of the condensate centroids for the 90° arrangement is smaller than for the 120° case. Thus the increase in vorticity due to the angular arrangement more than offsets the decrease in vorticity-generating capacity caused by reducing the piece spacing. While we have shown a geometry with an increased capacity to generate vortices, it is possible that nonlinearity causes the absolute maximum to be achieved for another angle close to 90°. Evidence of nonlinear effects is visible in this case: the snake instability [8,9] is visible as a curvature of some fringes of the second frame in Fig. 5(e). On close inspection we see that the linear vortex generation mechanism dominates in this region, as disturbances from the third BEC piece propagate through and interfere with these fringes prior to the snake instability evolving to form vortices directly. The initial displacement of the condensate centroid from the center of the trap results in the merged condensate oscillating back and forth along the initial mirror symmetry plane, in addition to the radial oscillation mode. In a previous investigation the ability to suppress the snake instability was reported in a system containing a ring dark soliton (RDS)—a dark stripe soliton formed into a closed loop—that shared the circular symmetry of the confining harmonic trap [29]. Depending on the RDS parameters, this structure could preferentially decay by emission of radiation instead of the snake instability. In the three-segment BEC system, the intervention of linear interference can be seen as another means for suppressing the onset of the snake instability in dark stripe solitons.

A possible explanation for Scherer *et al.*[10] not observing the production of large numbers of vortices along with a regular lattice in experiments may be their application of light-sheet intensities below our lower intensity results. Blurring and possible nonuniformity of the light-sheet walls is related to the size and manufacturing process used for the mask—attention to the design of the mask optics and optical path may permit the creation of more uniform, sharper walls, leading to the lattice structures we see in our simulations. Also, real experimental initial conditions with a nonzero-temperature chemical potential introduce some phase randomness which would disrupt the lattice. Finally (as noted in [11]), if the condensate is more spheroidal than pancakelike, the probability of observing vortices in the projected 2D image is reduced due to the extra freedom of possible vortex line geometries.

V. VORTEX DYNAMICS

In this section we focus attention on the striking interactions seen to occur between those vortices and antivortices remaining in the condensate following the disintegration of the lattice. The vortices and antivortices are propelled and evolve within a seething background sea of sound waves.

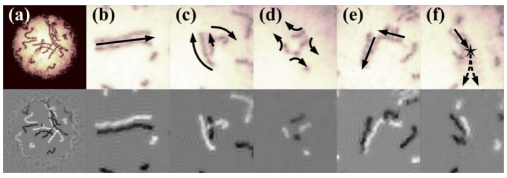

FIG. 7. (Color online) Vortex interaction dynamics for the 120°, I_0=0.8 arrangement. In the lower frames vortices (dark) and antivortices (light) are shown. (a) Vortex trails corresponding to the range t=323–429 ms. (b) A propagating vortex-antivortex dipole (VD). t=430–471 ms. (c) Vortex-vortex-antivortex tripole rotating through ≈90°. t=471–517 ms. (d) Two VDs meet to form a quadrupole. VA partners are exchanged and the new VDs move off orthogonally to the original directions. t=526–537 ms. (e) A VD meets a lone vortex. The antivortex exchanges its vortex partner and the new VD moves off on a new trajectory. t=285–328 ms. (f) VA annihilation resulting from passing by a lone vortex. t=342–366 ms.

Due to the complexity of these interactions, we provide a phenomenological description of just some of the rich dynamics, making observations of structures previously described by other investigators. A fuller appreciation of the complexity will be gained by viewing the accompanying movies [26].

The dynamics described in this section will be exhibited primarily in 2D pancake-shaped condensates. In 3D, vortices are stringlike objects, either forming closed loops (e.g., ring solitons) or terminating at two points on the condensate surface [4,30]. In this case, the interaction dynamics are instead characterized by string intercommutation or formation of smaller loops.

Most of the BEC vortex literature has focused on vortices (or antivortices) in rotating traps, in which antivortices (vortices) are expelled from the condensate. The complex interactions described here instead rely on the presence of a population of vortices and antivortices and hence are best observed in a nonrotating system. Interfering condensates comprised of two, three, or more pieces will all generate the required conditions, provided they are nonrotating. Another example of a nonrotating system able to generate an equal population is the ring dark soliton system [29]. Experimentally, phase contrast imaging with detuned light may leave the BEC sufficiently undisturbed to allow observation of these dynamics [31].

A vortex generates a local circulating velocity field and associated phase gradient which falls off rapidly with distance. Another vortex or antivortex in this field experiences a force in the direction of flow [13]. Similarly, VDs travel at a velocity determined by their distance apart. In Fig. 7(a), the paths of several VDs, are shown over a 106 ms period. The dipoles in which the partners are more widely spaced have shorter paths, illustrating the predicted behavior (see also accompanying movies [26]). In contrast, rotating vortex-vortex (or antivortex-antivortex) molecules are rarely and only fleetingly seen. Two equal-charge vortices can circulate around a common point, midway between them, like a facing pair of figure skaters. However, these structures have been

shown to be unstable in radiative media [1,32] and would also be disturbed by the more mobile VDs, or prevented from rotating by (countering) field gradients due to the presence of nearby antivortices (vortices).

In Fig. 7(b), a VD approaches a lone, near-stationary antivortex, with which it couples to form the tripole shown in Fig. 7(c). The net angular momentum of the tripole subsequently causes it to rotate through approximately 90° before it interacts again [15,17]. In Fig. 7(d), a rare event is shown, in which two counterpropagating VDs approach and momentarily meet, forming a quadrupole, before exchanging partners and moving off orthogonally to the original directions. In Fig. 7(e), a VD approaches a stationary vortex, which is swapped for the partnered vortex. The new VD continues on a new trajectory. This case may be contrasted with the formation of the tripole. In both cases, a VD approached a stationary (anti)vortex. However, the different interaction geometries resulted in the two different examples of dynamics shown.

The spacing of VDs changes in response to local field gradient perturbations, causing them to slow, speed up, separate completely, or annihilate. An example of annihilation, promoted by the proximity of another vortex, is shown in Fig. 7(f). Following the annihilation, scattered remnant waves travel ahead of the event location, dissipating the residual VD kinetic energy. Such interactions of the vortex with field perturbations and radiation of energy as waves are examples of vortex-sound interactions [1]. As already mentioned, vortex-vortex molecules are unstable, emitting spiral waves as they travel apart. Indeed, the sound waves emitted by all dynamical vortex interactions travel outwards and are reflected by the trap, recombining to form a chaotic fluctuating background that affects the ongoing condensate evolution.

Parker *et al.* [33] analyzed a BEC containing a lone vortex within a harmonic trap that was carefully modified to control the emission of spiral waves from a confinement region near the trap center. When spiral wave radiation was permitted to escape confinement and prevented from reinteracting with the vortex, the local energy was thus reduced, manifesting as a migration of the vortex away from the condensate center and its precession around the trap. Although our system is complex in comparison, we nevertheless observe sound emission from isolated vortices in the form of spiral waves. As our system evolves, a reduction in the number and associated energy of the vortices also occurs, consistent with the conversion of this energy to sound.

Vortices residing in the outer parts of the trap spiral helically about the center in a right-hand screw sense. Antivortices spiral in the opposite sense and are therefore likely to meet the aforementioned vortices. These often form VDs, which then move inward toward the trap center.

VI. CONCLUSION

A nonrotating pancake-shaped Bose-Einstein condensate fragmented into three pieces, with a repulsive nonlinearity, forms significant numbers of vortices and antivortices after merging. We have demonstrated, with numerical 2D simulations of this system, that the vortex creation mechanism may be explained in terms of a linear theory of the interference of expanding wave packets. This was contrasted with the vortex creation mechanism from a two-fragment BEC, in which dark stripe solitons decay into necklaces of vortices and antivortices; an intrinsically nonlinear physical process. With the three pieces separated sufficiently and arranged symmetrically, the formation of a distorted honeycomb lattice containing equal numbers of vortices and antivortices was demonstrated and explained via the linear theory. Moreover, this theory shows that phase differences between the initially separated pieces manifest as a global lattice translation. If allowed to expand in the absence of a trapping potential, the honeycomb lattice maintains its form as it expands. If instead the BEC evolves within a trap, the lattice was shown to melt, exhibiting a diversity of vortex interactions, including the formation of vortex-antivortex dipoles and other vortex clusters.

ACKNOWLEDGMENTS

The authors thank S. Clarke, L. D. Turner, and A. M. Martin for helpful discussions. G.R. is supported by the Australian Government Department of Education, Science, and Training. D.M.P. acknowledges support from the Australian Research Council.

APPENDIX: VORTEX LATTICE PRODUCTION

In this appendix we provide an analytical description of the vortices generated through linear superposition of three wave function fragments expanding from concentrated Gaussian distributions. The exposition here follows a similar approach to that reported in [12], which studied the vortices in the interference pattern from the Young's three-pinhole interferometer. In that work, an analytical description of the far-field vortex locations was derived as a function of source arrangement for three equal-amplitude complex scalar waves represented as either spherical waves or pinhole secondary sources. A representation in terms of a discrete parameter space arose, allowing estimates of the number of vortices—shown to relate to the information capacity of a beam—and the description of a natural coordinate system in terms of a family of hyperbolas.

Consider three (2+1)D Gaussian wave packets, each of unit mass, whose position expectation values are stationary and centered about coordinates $\mathbf{r}_1 \equiv \mathbf{0}, \mathbf{r}_2, \mathbf{r}_3$. This is shown in the polar coordinate system schematic, Fig. 8(a). The normalized probability amplitude for a Gaussian centered at the origin, as a function of position $\mathbf{r}$ and time t is given by [34]

$$\Psi(\mathbf{r},t) = \frac{\pi^{-1/2}\Delta p/\hbar}{1 + i(\Delta p)^2 t/(m\hbar)} \exp\left(\frac{-(\Delta p/\hbar)^2|\mathbf{r}|^2}{2[1 + i(\Delta p)^2 t/(m\hbar)]}\right), \tag{A1}$$

where m is the mass of an atom of the atomic species, Δp is the momentum uncertainty that defines the wave packet width, and $\mathbf{r}_t = (\mathbf{r},t)$ is a (2+1)D position vector covering the xy plane, whose origin lies at $(\mathbf{r},t) = (\mathbf{0},0)$. The total prob-

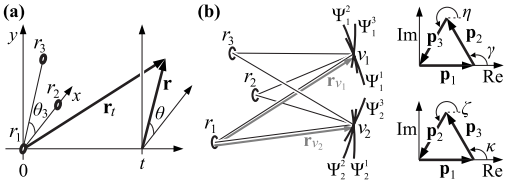

FIG. 8. (a) Coordinate system. Three Gaussians lie in the xy plane, centered at points $\mathbf{r}_1$, $\mathbf{r}_2$, and $\mathbf{r}_3$. Vortex positions are parametrized by polar coordinates (r,θ) at time t where $\mathbf{r}_t$ is a (2+1)D position vector. (b) Phasor construction of three interfering waves. Two possible phasor orderings, corresponding to a vortex and antivortex, may be produced by three given wave functions $\Psi_v^s, s\in\{r_1,r_2,r_3\}, v\in\{v_1,v_2\}$.

ability amplitude arising from the three superposed Gaussians is then

$$\Psi(\mathbf{r},t)=\sum_{j=1}^{3}\frac{\pi^{-1/2}\Delta p/\hbar}{1+i(\Delta p)^2t/(m\hbar)}\times\exp\left(\frac{-(\Delta p/\hbar)^2|\mathbf{r}-\mathbf{r}_j|^2}{2[1+i(\Delta p)^2t/(m\hbar)]}+i\phi_j\right), \quad \text{(A2)}$$

where $|\mathbf{r}-\mathbf{r}_j|\equiv\sqrt{(x-x_j)^2+(y-y_j)^2}$ is the distance from the center of the jth Gaussian to a given observation point $(\mathbf{r},t)$ and ϕ_j is the relative phase of the jth Gaussian. Separating the amplitude and phase terms of the wave field components $\Psi_j(\mathbf{r},t)=A_j(\mathbf{r},t)\exp[i\chi_j(\mathbf{r},t)]$, we get

$$A_j(\mathbf{r},t)=\frac{\pi^{-1/2}\Delta p/\hbar}{1+i(\Delta p)^2t/(m\hbar)}\exp\left(\frac{-(\Delta p)^2m^2|\mathbf{r}-\mathbf{r}_j|^2}{2[(\Delta p)^4t^2+m^2\hbar^2]}\right) \quad \text{(A3)}$$

and

$$\chi_j(\mathbf{r},t)=\frac{(\Delta p)^4mt|\mathbf{r}-\mathbf{r}_j|^2}{2[(\Delta p)^4t^2\hbar+m^2\hbar^3]}+\phi_j. \quad \text{(A4)}$$

Vortices lie at points of the phase $\chi(\mathbf{r},t)$, at which a line integral of $\nabla_\perp\chi$ along a closed path Γ about such a point evaluates to a nonzero value. More formally $\oint_\Gamma d\chi=2\pi n$ for some integer $n\neq 0$. At any point coinciding with a vortex core, the phasors $\mathbf{p}_1,\mathbf{p}_2,\mathbf{p}_3$ corresponding to the three wave packets must sum to zero. Equivalently, Eq. (A2) is equated to zero. With reference to Fig. 8(b), if the phasors are of equal length—corresponding to equal-amplitude contributions from the three Gaussians—an equilateral triangle is formed, allowing the angles at the vertices to be specified simply.

As the amplitude contributions from the Gaussians are not unconditionally equal we must make an appropriate approximation to the amplitude term. By restricting consideration to some finite region of the xy plane defined by $|\mathbf{r}-\mathbf{r}_j|\leq|\mathbf{r}_{\max}-\mathbf{r}_j|$, the exponential term in Eq. (A3) will be approximately unity, provided its argument is small, or $(\Delta p)^4t^2+m^2\hbar^2\gg(\Delta p)^2m^2|\mathbf{r}_{\max}-\mathbf{r}_j|^2/2$. For a given $\mathbf{r}_{\max}$, this is always true after sufficient time has elapsed. The amplitude term may now be factored out of the probability amplitude expression. Expanding the term $|\mathbf{r}-\mathbf{r}_j|^2=r^2-2\mathbf{r}\cdot\mathbf{r}_j+\mathbf{r}_j\cdot\mathbf{r}_j$ and remembering that $\mathbf{r}_1=\mathbf{0}$, the probability amplitude $\Psi(\mathbf{r},t)$ from Eq. (A2) vanishes when

$$1+\exp\{i[\alpha(r_2^2-2r_2r\cos\theta)+\phi_2]\}+\exp\{i[\alpha(r_3^2-2r_3r\cos(\theta-\theta_3))+\phi_3]\}=0, \quad \text{(A5)}$$

where $\alpha=m\hbar t/[2(\hbar t)^2+2m^2(\hbar/\Delta p)^4]$. The three summands are associated with the three phasors in Fig. 8(b). Whereas the first summand, 1, is uniquely identified with the horizontal phasor $\mathbf{p}_1$, the association of the sources with the other two phasors allows two permutations, corresponding to the two phasor diagrams; one for each vortex, v_1 and v_2. In fact one will be a vortex and the other an antivortex.

The arguments of the two exponentials in Eq. (A5) are denoted by γ and η, respectively. These phase angles are uniquely defined to within an integer multiple of 2π, so that

$$\gamma=\alpha(r_2^2-2r_2r\cos\theta)+\phi_2=\frac{2\pi}{3}+2m\pi, \quad \text{(A6a)}$$

$$\eta=\alpha[r_3^2-2r_3r\cos(\theta-\theta_3)]+\phi_3=\frac{4\pi}{3}+2n\pi, \quad \text{(A6b)}$$

where m and n are integers. The association of the m and n indices with the vertices is arbitrary. The choice is made here to match m with r_2 and n with r_3. The alternative phasor association is thus

$$\zeta=\alpha(r_2^2-2r_2r\cos\theta)+\phi_2=\frac{4\pi}{3}+2m\pi, \quad \text{(A7a)}$$

$$\kappa=\alpha[r_3^2-2r_3r\cos(\theta-\theta_3)]+\phi_3=\frac{2\pi}{3}+2n\pi. \quad \text{(A7b)}$$

Forming the fraction γ/η or ζ/κ yields

$$\frac{r_3}{r_2}(\cos\theta_3+\tan\theta\sin\theta_3)=\frac{r_3^2-\beta N(n)}{r_2^2-\beta M(m)}, \quad \text{(A8)}$$

where $\beta=1/(3\alpha)=2[(\hbar t)^2+m^2(\hbar/\Delta p)^4]/(3m\hbar t)$. For the fraction γ/η, we get

$$M(m)=2\pi[1+3(m-\phi_2/2\pi)],\quad N(n)=2\pi[2+3(n-\phi_3/2\pi)], \quad \text{(A9a)}$$

and for the fraction ζ/κ we instead have

$$M(m)=2\pi[2+3(m-\phi_2/2\pi)],\quad N(n)=2\pi[1+3(n-\phi_3/2\pi)]. \quad \text{(A9b)}$$

Examination of these expressions reveals that a 2π change in relative phase ϕ_2 or ϕ_3 may be absorbed as an integer change in the associated parameter-space coordinate m or n, respectively. By allowing m and n to correspond to discrete real values instead of integer values, they may then also absorb fractional parts of the relative phase. Consequently, the vortex lattice may be continuously translated by a single lattice cell for each 2π change in the source phase. The position of any vortex in a cell coinciding with the BEC trap center is

thus understood as resulting from a translation of the entire lattice. Isolating θ in Eq. (A8) yields

$$\theta = \arctan\left[\frac{1}{\sin\theta_3}\left(\frac{r_3 - \beta N(n)/r_3}{r_2 - \beta M(m)/r_2}\right) - \cos\theta_3\right]. \quad \text{(A10)}$$

Finally, the expression for the radial coordinate r of the (m,n)th vortex core is obtained from Eq. (A6a) or Eq. (A7a) by applying the identity $\cos^2\theta = 1/(1+\tan^2\theta)$ and making use of Eq. (A10):

$$r = \frac{1}{2}\sqrt{\frac{1}{\sin^2\theta}\left[r_3 - \frac{\beta N(n)}{r_3} - \left(r_2 - \frac{\beta M(m)}{r_2}\right)\cos\theta_3\right]^2 + 1}. \quad \text{(A11)}$$

Together with Eq. (A10), we have the vortex coordinates (r,θ,t), with the sign of the vortex charge—i.e., whether they describe the positions of vortices or antivortices—depending on the choice of Eq. (A9a) or (A9b) and the value of θ_3. If $\theta_3 \in (0,\pi)$, vortices are indicated by Eq. (A9a) and antivortices by Eq. (A9b). If $\theta_3 \in (\pi, 2\pi)$, the association is reversed, with vortices indicated by Eq. (A9b) and antivortices by Eq. (A9a).

Note that, in contrast with the case described in [12], in which the allowed range of integers (m,n) was restricted, here there are no restrictions and an infinite, uniform vortex-antivortex lattice is generated. However, the amplitude term Eq. (A3) applies a Gaussian envelope to the probability density $|\Psi|^2 = |\Sigma_{j=1}^3 A_j(\mathbf{r})|^2$, effectively limiting the lattice. For sources arranged at the three corners of an equilateral triangle, the lattice has a symmetric honeycomb symmetry, with regular hexagonal cells. Changing the angle θ_3 or the side lengths r_2 or r_3 distorts the cells and the lattice.

[1] L. M. Pismen, *Vortices in Nonlinear Fields: From Liquid Crystals to Superfluids, from Non-Equilibrium Patterns to Cosmic Strings* (Oxford University Press, Oxford, 1999).
[2] F. Dalfovo, S. Giorgini, L. P. Pitaevskii, and S. Stringari, Rev. Mod. Phys. **71**, 463 (1999).
[3] A. L. Fetter and A. A. Svidzinsky, J. Phys.: Condens. Matter **13**, R135 (2001).
[4] A. Minguzzi, S. Succi, F. Toschi, M. P. Tosi, and P. Vignolo, Phys. Rep. **395**, 223 (2004).
[5] A. A. Abrikosov, Sov. Phys. JETP **5**, 1174 (1957).
[6] J. R. Anglin and W. H. Zurek, Phys. Rev. Lett. **83**, 1707 (1999).
[7] D. L. Feder, M. S. Pindzola, L. A. Collins, B. I. Schneider, and C. W. Clark, Phys. Rev. A **62**, 053606 (2000).
[8] Y. S. Kivshar and B. Luther-Davies, Phys. Rep. **298**, 81 (1998).
[9] J. Brand and W. P. Reinhardt, Phys. Rev. A **65**, 043612 (2002).
[10] D. R. Scherer, C. N. Weiler, T. W. Neely, and B. P. Anderson, Phys. Rev. Lett. **98**, 110402 (2007); D. R. Scherer, Ph.D. thesis, University of Arizona, 2007,eprint arXiv:0704.2054v1.
[11] R. Carretero-González, B. P. Anderson, P. G. Kevrekidis, D. J. Frantzeskakis, and C. N. Weiler, Phys. Rev. A **77**, 033625 (2008).
[12] G. Ruben and D. M. Paganin, Phys. Rev. E **75**, 066613 (2007); G. Ruben and D. M. Paganin, *ibid.* **76**, 029901(E) (2007).
[13] P. Nozières and D. Pines, *The Theory of Quantum Liquids, Volume II: Superfluid Bose Liquids* (Addison-Wesley, Reading, MA, 1990).
[14] L. C. Crasovan, V. Vekslerchik, V. M. Pérez-García, J. P. Torres, D. Mihalache, and L. Torner, Phys. Rev. A **68**, 063609 (2003).
[15] M. Möttönen, S. M. M. Virtanen, T. Isoshima, and M. M. Salomaa, Phys. Rev. A **71**, 033626 (2005).
[16] H. Sakaguchi and T. Higashiuchi, Phys. Lett. A **359**, 647 (2006); T. Higashiuchi and H. Sakaguchi, Laser Phys. **17**, 221 (2007).
[17] V. Pietilä, M. Möttönen, T. Isoshima, J. A. M. Huhtamäki, and S. M. M. Virtanen, Phys. Rev. A **74**, 023603 (2006).
[18] A. Klein, D. Jaksch, Y. Zhang, and W. Bao, Phys. Rev. A **76**, 043602 (2007).
[19] J. Masajada and B. Dubik, Opt. Commun. **198**, 21 (2001).
[20] K. O'Holleran, M. J. Padgett, and M. R. Dennis, Opt. Express **14**, 3039 (2006).
[21] R. Carretero-González, N. Whitaker, P. G. Kevrekidis, and D. J. Frantzeskakis, Phys. Rev. A **77**, 023605 (2008).
[22] M. Holland and J. Cooper, Phys. Rev. A **53**, R1954 (1996).
[23] M. D. Lee, S. A. Morgan, M. J. Davis, and K. Burnett, Phys. Rev. A **65**, 043617 (2002).
[24] W. Bao, D. Jaksch, and P. A. Markowich, J. Comput. Phys. **187**, 318 (2003).
[25] B. Tanatar, A. Minguzzi, P. Vignolo, and M. P. Tosi, Phys. Lett. A **302**, 131 (2002).
[26] See EPAPS Document No. E-PLRAAN-78-066807 for movies corresponding to Figs. 3(a) and 5(b), and a trapped two-piece BEC. For more information on EPAPS, see http://www.aip.org/pubservs/epaps.html.
[27] A. Röhrl, M. Naraschewski, A. Schenzle, and H. Wallis, Phys. Rev. Lett. **78**, 4143 (1997).
[28] L. P. Pitaevskii, Phys. Lett. A **221**, 14 (1996).
[29] G. Theocharis, D. J. Frantzeskakis, P. G. Kevrekidis, B. A. Malomed, and Y. S. Kivshar, Phys. Rev. Lett. **90**, 120403 (2003).
[30] L. D. Carr and C. W. Clark, Phys. Rev. A **74**, 043613 (2006).
[31] L. D. Turner, K. F. E. M. Domen, and R. E. Scholten, Phys. Rev. A **72**, 031403(R) (2005).
[32] N. P. Proukakis, N. G. Parker, D. J. Frantzeskakis, and C. S. Adams, J. Opt. B: Quantum Semiclassical Opt. **6**, S380 (2004).
[33] N. G. Parker, N. P. Proukakis, C. F. Barenghi, and C. S. Adams, Phys. Rev. Lett. **92**, 160403 (2004).
[34] B. H. Bransden and C. J. Joachain, *Quantum Mechanics*, 2nd ed. (Prentice Hall, Harlow, England, 2000), Chap. 2, p. 65.